Université Libanaise
École Doctorale
Sciences et Technologies

Laboratoire Physique et Chimie Théoriques

UNIVERSITÉ DE LORRAINE

THESE de doctorat en Cotutelle

Pour obtenir le grade de Docteur délivré par

L'Université Libanaise Et l'Université de Lorraine

Spécialité : Chimie

Présentée et soutenue publiquement par

BERRO Youssef

Le 22 Novembre 2019

Elaboration de Formulations Catalytiques Optimisées pour la Valorisation de la Biomasse par une Approche Combinée Théorie/Expérience.

Membre du Jury

M. Sébastien Royer, Pr, UCCS UMR 8181, Université de Lille	*Rapporteur*
M. Ahmed Naitabdi, McF HDR, LCPMR UMR 7614, Sorbonne Université	*Rapporteur*
M. Fawaz El Omar, Pr, Doyen EDST, Université Libanaise	*Examinateur*
Mme Karine Thomas, McF, LCS UMR 6506, Université de Caen	*Examinatrice*
Mme Emilie Gaudry, Pr, IJL UMR 7198, Université de Lorraine	*Examinatrice*
M. Sébastien Lebègue, DR, LPCT UMR 7019, Université de Lorraine	*Directeur de thèse*
M. Fouad El Haj Hassan, Pr, directeur PRASE, Université Libanaise	*Directeur de thèse*
M. Michael Badawi, McF, LPCT UMR 7019, Université de Lorraine	*Co-directeur de thèse/Invité*
M. Mounir Kassir, McF, PRASE, Université Libanaise	*Co-directeur de thèse/Invité*
Mme Andreea Pasc, Pr, L2CM UMR 7053, Université de Lorraine	*Invitée*

Acknowledgments

First, I would like to express my humble thanks to God for the wise both fear and love.
Special and warm thanks to my parents and my family for their encouragement where the success of this work would have not light into existence with the absence of their love.

I would like to thank all the teaching stuff at the Lebanese University (Faculty of Engineering) who taught me. A special thanks to the dean of the faculty Dr. Rafic Younes, who was my master thesis supervisor and helped me to continue my dream in doing a Ph.D. I am also very grateful for the Lebanese University and the CNRS-Lebanon for giving me a Ph.D. grant.

My deepest appreciation and thanks to my supervisors, Dr. Fouad El Haj Hassan, Dr. Sébastien Lebègue, Dr. Mounir Kassir and Dr. Michael Badawi. I thank them for their recommendations, suggestions and support. I gained much knowledge from them, and for that, I am very grateful.

Then, I would like to express my sincere appreciation to Dr. Andreea Pasc, Dr. Anthony Dufour and Dr. Nadia Canilho for their continuous guidance, encouragement and support throughout my Ph.D. period. They provided counsel and assistance that greatly enhanced my skills.

I would like to thank also all the people that worked with me and helped me during those three years for their efforts: Dr. El Eulmi Bendeif, Dr. Christine Bellouard, Dr. Vanessa Fierro, Dr. Frederik Tielens, Dr. Axel Ganzmuller, Dr. Alain Celzard, Dr. Bernard Malaman, Dr. Mohammed El-Miloud Bettahar, Dr. Ghouti Medjahdi, Dr. Marie-antoinette Dziurla, Dr. Sarah Rogers, Dr. Saber Gueddida, Dr. Younès Bouizi, Dr. Ovidiu Ersen, Dr. Dris Ihiawakrim, Stephan Parant, Michel Mercy, Séverine Bonenberger, and Paule Bazard.

I am also grateful to all my friends from the laboratories (Laboratoire Lorrain de Chimie Moléculaire L2CM, Laboratoire de Physique et Chimie Théoriques LPCT, Laboratoire de Réacteurs et Génie Chimique LRGP, Plateforme de Recherche et d'Analyse des Sciences de l'Environnement PRASE) who encouraged me along the path.

Finally, I want to express a sense of love to all my friends for supporting me.

Thank You All
Youssef Berro

Résumé

La valorisation de la biomasse lignocellulosique est l'un des piliers de l'économie du futur. La lignine est un polymère polyphénolique, dont le clivage conduit à des monomères de phénol et de méthoxyphénol. Sa pyrolyse produit des bio-huiles à haute teneur en oxygène (20 à 45%), telles que des composés phénoliques, des aldéhydes, des cétones, des esters, des acides et des alcools. Ces bio-huiles, qui présentent un mauvais rendement énergétique peuvent être valorisées par hydrodésoxygénation (HDO), un procédé thermo-catalytique sous pression d'H_2, qui conduit à des molécules non-oxygénées. Notre étude vise à élaborer de nouvelles formulations catalytiques pour l'HDO, en combinant des calculs utilisant la théorie de la fonctionnelle de la densité (DFT), et des études expérimentales (synthèse, caractérisation et tests catalytiques). L'HDO peut se faire suivant deux voies : (i) l'hydrogénation du cycle aromatique avant la rupture de la liaison C-O (HYD) ou (ii) la rupture directe de la liaison C-O - Désoxygénation directe (DDO). Le but de ce travail est de favoriser la voie DDO afin d'augmenter la production d'aromatiques et de limiter la consommation d'H_2. La littérature montre que les catalyseurs Fe@silice sont potentiellement actifs et sélectifs (aromatiques) avec une moindre désactivation. Ainsi, nous avons focalisés sur la synthèse de catalyseurs métalliques Fe (ou bimétallique Fe-Cu) sur un support silice permettant une meilleure performance en HDO.

Les énergies d'adsorption du phénol (molécule modèle représentant les bio-huiles) et de molécules inhibitrices (CO et eau) sur différentes surfaces de silice amorphe et cristalline, ayant différentes densités et types de silanols, ont été obtenues par DFT. Trois modes d'interaction du phénol ont été étudiés : «O perpendiculaire», «π plat» et «O plat». Les surfaces cristallines favorisent préférablement la voie HYD étant donné que l'interaction «π plat» prédomine. Sur la silice amorphe, des énergies d'adsorption plus élevées ont été mises en évidence pour le mode «O plat», et une interaction spécifique de 120 kJ/mol (avec une liaison C-Si et déformation du phénol) est observée sur les surfaces ayant une densité de silanol comprise entre 2 et 3,3 OH/nm^2. La compétition du CO est négligeable sur toutes les surfaces, ce qui rend la silice plus attractive que les catalyseurs sulfurés classiques. L'eau présente un effet inhibiteur sur les surfaces ayant une densité de silanol supérieure à 5 OH/nm^2. Par conséquent, ces résultats ont motivé la synthèse de catalyseurs sur silice avec une densité de silanol allant de 2 à 4 OH/nm^2.

Des catalyseurs avec des atomes de fer "Single Atom Catalysts" (SACs) supportés par de la silice mésoporeuse ont été élaborés par procédé sol-gel en utilisant des tensioactifs non-ioniques (P123), et métalliques (CTAF) comme agents porogènes. La distribution des atomes de fer dans les micelles mixtes P123/CTAF permet la dispersion fine de ces atomes sur les mésopores de la silice. Le rapport molaire P123/CTAF permet de contrôler la charge de fer, ainsi que les propriétés structurelles de la silice. Par conséquent, différentes solutions micellaires ont été préparées et analysées (concentration micellaire critique CMC, diffusion de lumière dynamique DLS, diffusion de neutrons aux petits angles SANS, études magnétiques) afin de comprendre leur structuration en fonction de ce rapport. L'absence d'agrégats de fer et des nanoparticules a été confirmée par les mesures synchrotrons - fonction de distribution des paires PDF, résonance magnétique nucléaire RMN, magnétiques, et par cartographie de la microscopie électronique à balayage en transmission STEM. Les résultats expérimentaux et les calculs DFT ont confirmé que ces atomes sont principalement du Fe (III) à haut spin. Cette méthode augmente le nombre de sites actifs, ce qui améliore la performance catalytique. Cependant, les résultats des tests catalytiques n'ont pas été satisfaisants à cause de la difficulté à réduire le Fe(III).

Les catalyseurs métalliques (Fe et Cu) et bimétalliques (Fe-Cu) sur support de silice synthétisés par la méthode d'imprégnation et d'autres catalyseurs Fe élaborés selon la méthode de co-précipitation avec décomposition d'urée sous température permettant d'obtenir du Fe (II) ont été testés pour l'HDO du guaiacol (molécule modèle représentant les bio-huiles). Le catalyseur bimétallique Fe-Cu/SiO_2 présente une meilleure performance (90 % conversion, 70% sélectivité en phénol) que les catalyseurs à base de fer, car l'incorporation de cuivre facilite la réduction du fer en Fe(0). De même, les catalyseurs synthétisés par décomposition d'urée dont le fer est réduit plus facilement se sont révélés plus performant que ceux préparés par imprégnation.

Mots Clés : Hydrodésoxygénation (HDO), Théorie de la fonctionnelle de la densité (DFT), Catalyseurs à atome isolée (SACs), Propriétés d'adsorption.

Abstract

As a major source of renewable resources, the valorization of lignocellulosic biomass is one pillar of the future economy. Lignin consists of aryl ether units connected by ether and alkyl bonds, whose cleavage yields monomeric phenols and methoxy phenols. Thus, the pyrolysis of lignin produces oxygenated bio-oils (20-45%) with poor fuel efficiency, such as phenols, aromatics, aldehydes, ketones, esters, acids and alcohols. Hence, those bio-oils have to be upgraded, mainly through hydrodeoxygenation (HDO), which is a thermal catalytic process under H_2 pressure leading to the production of oxygen-free molecules and water as by-product. Our objective is to elaborate new catalytic formulations for the HDO process by combining Density Functional Theory (DFT) calculations with experimental studies (synthesis, characterization, and catalytic tests). HDO of phenolic compounds includes two deoxygenation routes: (i) the hydrogenation of aromatic ring before C-O bond cleavage (HYD) or (ii) the direct C-O bond cleavage - Direct DeOxygenation (DDO). The present work aims to promote the second route in order to increase the production of aromatics under lower H_2 pressure. As described in the literature, Fe@silica catalysts show a good activity and selectivity toward aromatics, with being rather resistant towards deactivation. Thus, our work focused on designing silica-supported metallic Fe (or bimetallic Fe-Cu) catalysts with specific properties allowing higher performances.

The adsorption energies of phenol (as a model molecule of bio-oils) and inhibitors (CO and water) over several amorphous and crystalline silica surfaces, with various silanol densities and types, were computed by DFT. Three interaction modes were investigated for phenol: the “perpendicular O-interaction”, the “flat π-interaction”, and the “flat O-interaction”. Results show that crystalline surfaces promote the HYD route since the “flat π-interaction” dominates. For amorphous silica, the highest adsorption energies were found for the “flat O-interaction” mode, and a specific interaction of 120 kJ/mol (including a C-Si bond and phenol deformation) was observed for surfaces with a silanol density between 2 and 3.3 OH/nm^2. The CO competitive adsorption is negligible for all silica surfaces, which make them more attractive than conventional sulfide catalysts. Water shows an inhibiting effect for all surfaces whose silanol density is higher than 5 OH/nm^2. Hence, these results motivated the synthesis of silica-supported catalysts with a silanol density between 2 and 4 OH/nm^2.

Single iron atom catalysts (SACs) supported on mesoporous silica were elaborated following the Sol-gel mechanism using non-ionic (P123) and metallic (CTAF) surfactants as porogens. Iron distribution within mixed P123/CTAF micelles, which is used as template for the silica framework polymerization, allows the fine dispersion of those atoms within silica mesopores. Tuning the P123/CTAF molar ratio enables to control the iron load, as well as the silica structural properties.

Therefore, different micellar solutions were prepared and analyzed (critical micellar concentration CMC, dynamic light scattering DLS, small angle neutron scattering SANS, magnetic studies) in order to understand their structuration depending on this ratio. The lack of iron clusters and nanoparticles was confirmed by synchrotrons - pair distribution function PDF, scanning transmission electron microscopy STEM mapping, magnetic and nuclear magnetic resonance NMR measurements. Both experimental results and DFT calculations confirmed that those atoms are predominately present as Fe(III) with high spin. Obtaining single metallic iron atoms increases the number of active sites, which improves the catalytic performance. However, the results of catalytic tests were unsatisfactory because the reduction of Fe(III) appeared to be difficult.

Silica-supported metallic (Fe & Cu) and bimetallic (Fe-Cu) catalysts were synthesized by simple impregnation, and Fe catalysts were elaborated following the co-precipitation method with urea decomposition under heating, enabling obtaining Fe(II) species. Catalysts were tested for guaiacol (as a model molecule of bio-oils) HDO conversion and results proved that bimetallic Fe-Cu have a better performance (90% conversion, 70% phenol selectivity) than iron-based catalysts since incorporation of Cu facilitates the reduction of Fe(III) species into Fe(0). Similarly, catalysts prepared by co-precipitation with urea decomposition proved a better performance than those prepared by impregnation since the reduction of iron species was easier.

Keywords: Hydrodeoxygenation (HDO), Density Functional Theory (DFT), Single Atom Catalysts (SACs), Adsorption Properties.

Table of Content

Table of Content

Figures and Tables

Résumé de la Thèse en Français

Chap1. Bibliographic Review

Chap 2. Theoretical and Experimental Methods

Chap 3. Atomistic Description of Phenol, CO and H_2O Adsorption over Crystalline and Amorphous Silica Surfaces for Hydrodeoxygenation Applications

Chap 4. Synthesis of Metal@silica Catalysts

Chap 5. Hydrodeoxygenation Catalytic Tests

Annexes

Résumé de la Thèse en Français

Cette thèse vise à développer de nouveaux catalyseurs à base de silice pour valoriser la biomasse qui est l'une des plus larges sources d'énergie renouvelable. L'augmentation néfaste de l'effet de serre et la déplétion des ressources fossiles et pétrolières, accompagnés par la forte croissance de la demande en carburant et en molécules pétrochimiques nécessite le développement et l'amélioration de sources d'énergie durables et renouvelables.

La biomasse lignocellulosique est l'objet de nombreuses études scientifiques de la dernière décennie. Notre étude concerne le procédé d'hydrodéoxygénation (HDO) des bio-huiles dérivées de la pyrolyse directe de la lignine.[1] Comparée aux autres composants de la biomasse lignocellulosique (cellulose et hémicellulose), la lignine possède plus de noyaux aromatiques et un rapport oxygène/carbone moins élevé, ce qui en fait un bon candidat pour la production de molécules aromatiques.

Le procédé HDO implique une réaction catalytique en phase gazeuse sous pression d'hydrogène pour réduire le pourcentage d'oxygène des bio-huiles, produisant des hydrocarbures et de l'eau, suivant plusieurs mécanismes réactionnels.[2] La quantité d'hydrogène consommée et les produits obtenus dépendent de la voie réactionnelle suivie. Suivant la voie de désoxygénation directe (DDO), la consommation d'hydrogène est plus faible, et la production de molécules d'intérêt énergétique (phénol et benzène) est plus grande, qu'avec la voie d'hydrogénation du noyau aromatique (HYD) (**Figure R.1**).

Cette thèse traite le procédé HDO par une approche combinée théorique/expérimentale, dans le but de comprendre le fonctionnement des catalyseurs, et de développer de nouvelles formulations catalytiques pour réduire la consommation d'H_2, et par conséquent obtenir une meilleure balance énergétique à moindre coût (coûts opérationnels d'H_2, coûts de stockage et des équipements de pressurisation d'H_2, coût du catalyseur...). Dans ce but, notre stratégie d'investigation inclut trois aspects :

- Le premier, théorique, se base sur des calculs de la théorie de la fonctionnelle de la densité (DFT) pour évaluer l'interaction entre les molécules oxygénées, les inhibiteurs (eau et CO) et la surface catalytique, pour mieux comprendre les phénomènes d'adsorption et pour proposer des formulations catalytiques optimisées.
- Le second aspect considère la synthèse des catalyseurs abordables par des méthodes avancées pour augmenter le nombre des sites actifs et leur dispersion dans le matériau.
- Le troisième aspect consiste à réaliser des tests expérimentaux de conversion du guaiacol pour déterminer l'activité HDO, la sélectivité, ainsi que les avantages et inconvénients des matériaux synthétisés, afin de proposer des nouveaux catalyseurs optimisés.

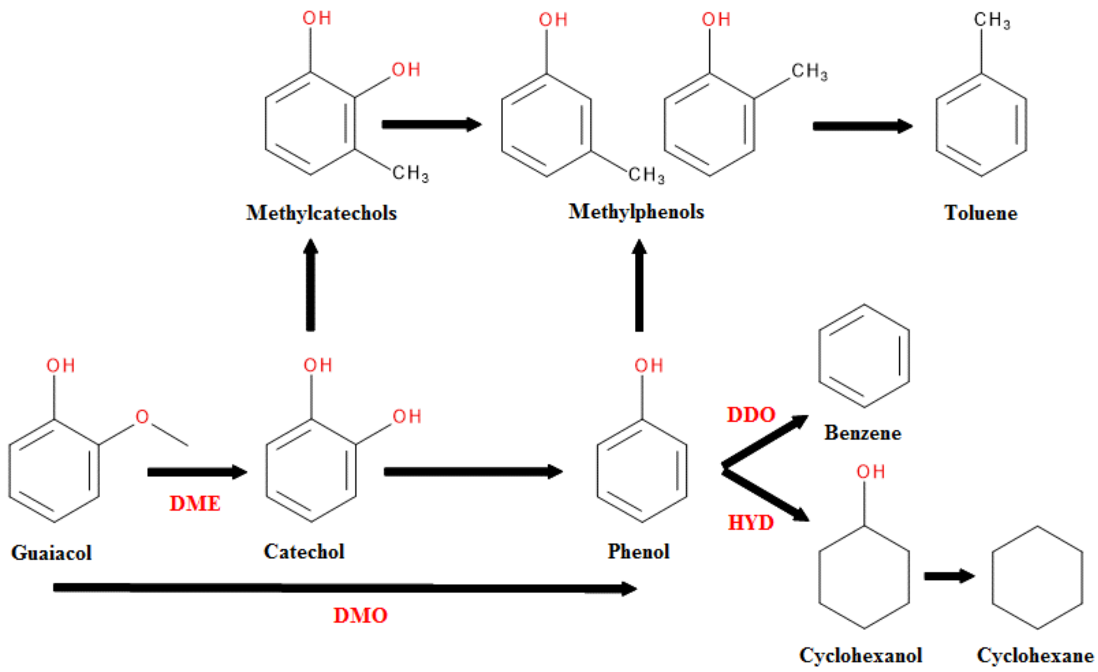

Figure R.1 *Voies réactionnelles de la conversion d'HDO catalytique du guaiacol : DDO vs HYD.*

Dans la littérature, plusieurs types des catalyseurs ont été étudiés pour la valorisation des bio-huiles dérivées de la pyrolyse de la lignine par le procédé d'HDO, tels que les sulfures de métaux de transition (CoMoS, NiMoS, MoS_2…), les métaux nobles (Pd, Pt…) et les métaux non-précieux (Fe, Cu, Ni…) supportés sur différents matériaux (TiO_2, Al_2O_3, SiO_2 et charbon). Notre objectif est d'améliorer les performances des catalyseurs à base de fer supporté par de la silice mésoporeuse (Fe/SiO_2) qui ont déjà prouvé leur efficacité dans ce domaine ces dernières années.[3]

Le présent rapport de thèse sera structuré comme suit :

- Le chapitre 1 décrira le sujet et les principales problématiques, en passant en revue les différents procédés de valorisation de la biomasse, plus spécifiquement le processus HDO. L'adsorption de molécules oxygénées (première étape du mécanisme réactionnel) et les performances catalytiques de Fe/SiO_2 (conditions réactionnelles et effet des sous-produits) y seront discutées à partir des données bibliographiques.
- Le chapitre 2 présentera les méthodes théoriques et expérimentales utilisées dans ce travail comme suit :
    - En décrivant en détail la théorie de la fonctionnelle de la densité, ses fondements et ses applications aux systèmes périodiques.
    - En examinant et en discutant la synthèse et les applications des catalyseurs à base de métaux non précieux supportés sur l'oxyde de silice, ainsi que le procédé sol-gel utilisé pour la synthèse des silicates mésoporeux.

  - enfin, en décrivant le procédé HDO et les équipements d’analyse (**Figure R.2**).
- Les chapitres 3, 4 et 5 présenteront les résultats obtenus, en les discutant.
- Les conclusions et perspectives seront ensuite présentées, suivi des annexes.

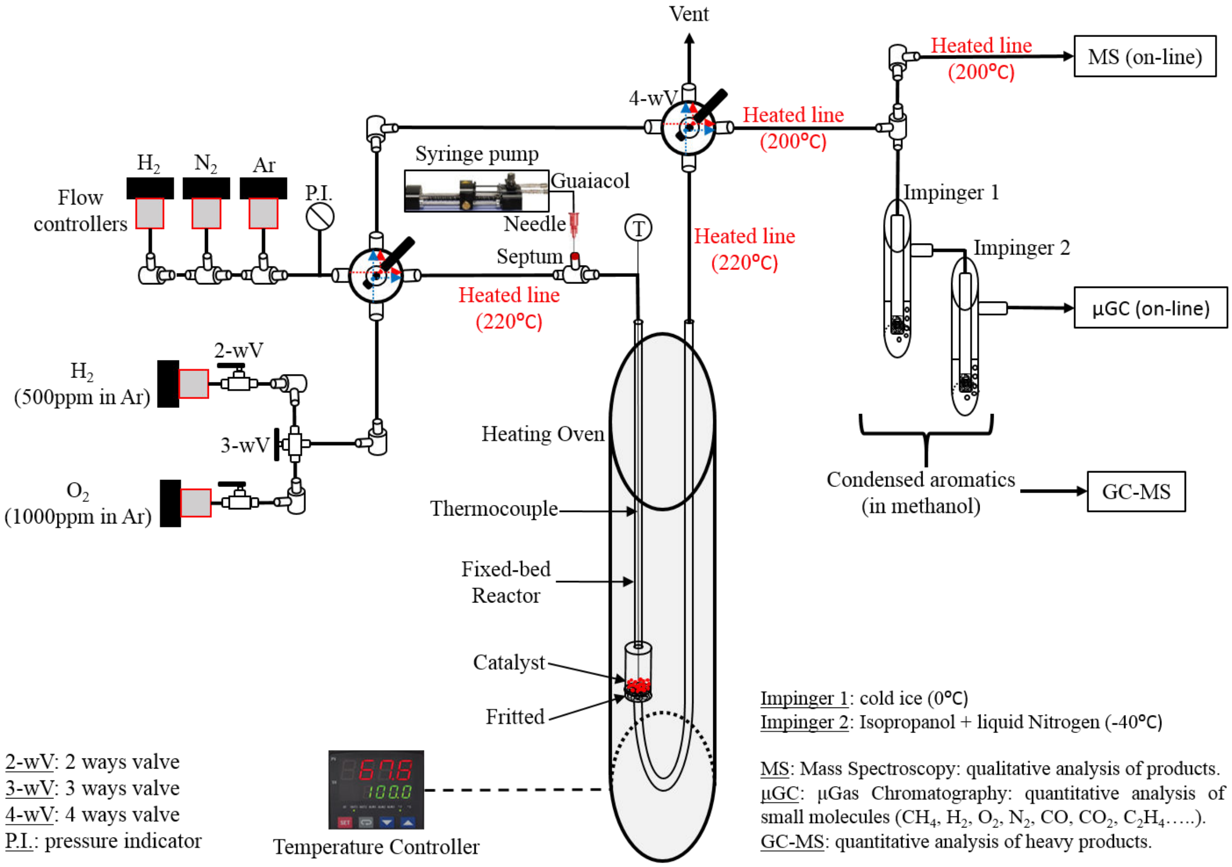

Figure R.2 *Présentation schématique du procédé d’HDO et des équipements d’analyse des produits.*

La suite de ce résumé de thèse décrit les différents objectifs de notre travail, la démarche adoptée pour les atteindre, et les résultats obtenus.

L’adsorption des molécules oxygénées sur les catalyseurs, plus spécifiquement sur les groupes silanols de la surface de silice, constitue la première étape du mécanisme réactionnel. Des calculs DFT ont été réalisés pour déterminer les énergies d’adsorption du phénol (comme molécule modèle des bio-huiles) et des co-produits inhibiteurs (eau et CO)[4], suivant différents modes d’interaction, sur plusieurs surfaces de silice amorphe et cristalline. Les calculs DFT sont effectués avec le code VASP, en prenant en compte les forces de dispersion (vdW) par la méthode Grimme D2.

L’interaction des molécules oxygénées et inhibiteurs sur les surfaces de silice varient selon la densité, la distribution et le type de groupes silanols qui caractérisent chaque surface. Trois modes d’interaction du phénol avec la surface de silice ont été mis en évidence : « perpendicular

O-interaction », « flat π-interaction » et « flat O-interaction » (**Figure R.3**). Neuf surfaces de silice ont été étudiées dont quatre cristallines ((111) β-cristobalite ayant 4.29 OH/nm^2 (de type isolé), (101) β-cristobalite ayant 5.24 OH/nm^2 (de type vicinal), (001à β-cristobalite ayant 7.24 OH/nm^2 (de type géminal), et la (001) α-quartz ayant 8.28 OH/nm^2 de type géminal) et cinq amorphes ayant une densité qui varie de 7.2 à 1.1 OH/nm^2 avec plusieurs types de silanols (SiO_2-7.2, SiO_2-5.9, SiO_2-4.6, SiO_2-3.3, SiO_2-2, SiO_2-1.1). Les résultats obtenus montrent que pour les surfaces cristallines, le mode « flat π-interaction » domine, ce qui peut favoriser la voie HYD plutôt que la voie DDO. Sur les surfaces amorphes, les énergies d'adsorption du phénol sont plus élevées selon le mode « flat O-interaction » qu'avec les autres modes (**Figure R.4**). Une interaction spécifique du phénol selon le mode « flat O-interaction » égale à 120 kJ/mol, a été identifiée avec les surfaces SiO_2-3.3 et SiO_2-2. Celle-ci comporte une liaison C-Si entre un atome de carbone du phénol et un atome de silice, ce qui provoque la déformation de la molécule de phénol. Ce phénomène peut être favorable aux réactions catalytiques. L'effet compétitif du CO est négligeable sur toutes les surfaces de silice, ce qui les rend bien plus intéressantes que les catalyseurs sulfurés conventionnelles selon ce critère. L'eau présente un effet inhibiteur intense sur l'adsorption du phénol sur les surfaces amorphes ayant une densité de silanols supérieure à 5 OH/nm^2. Cependant, de très faibles énergies d'adsorption de l'eau par rapport au phénol ont été déterminées pour les surfaces SiO_2-3.3 et SiO_2-2. Ces résultats ont motivé la synthèse de silices amorphes ayant une densité de silanols entre 2 et 4 OH/nm^2, qui d'après nos calculs devraient présenter des performances catalytiques intéressantes.[5]

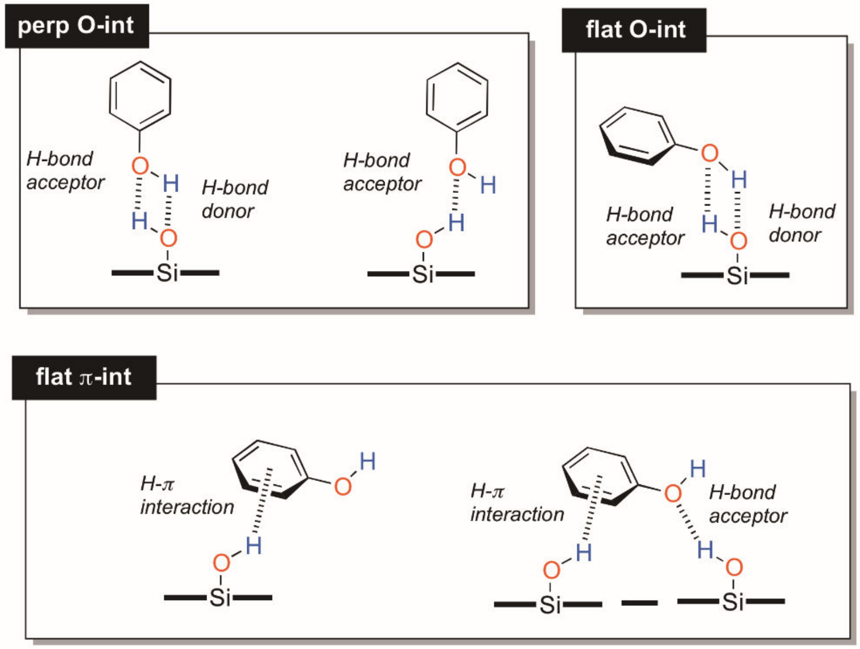

Figure R.3 *Différents types d'interaction (H-bond donor, H-bond acceptor et π-interaction) se produisant durant l'adsorption du phénol suivant les 3 modes (perpendicular O-interaction, flat O-interaction et flat π-interaction) sur la surface de la silice.*

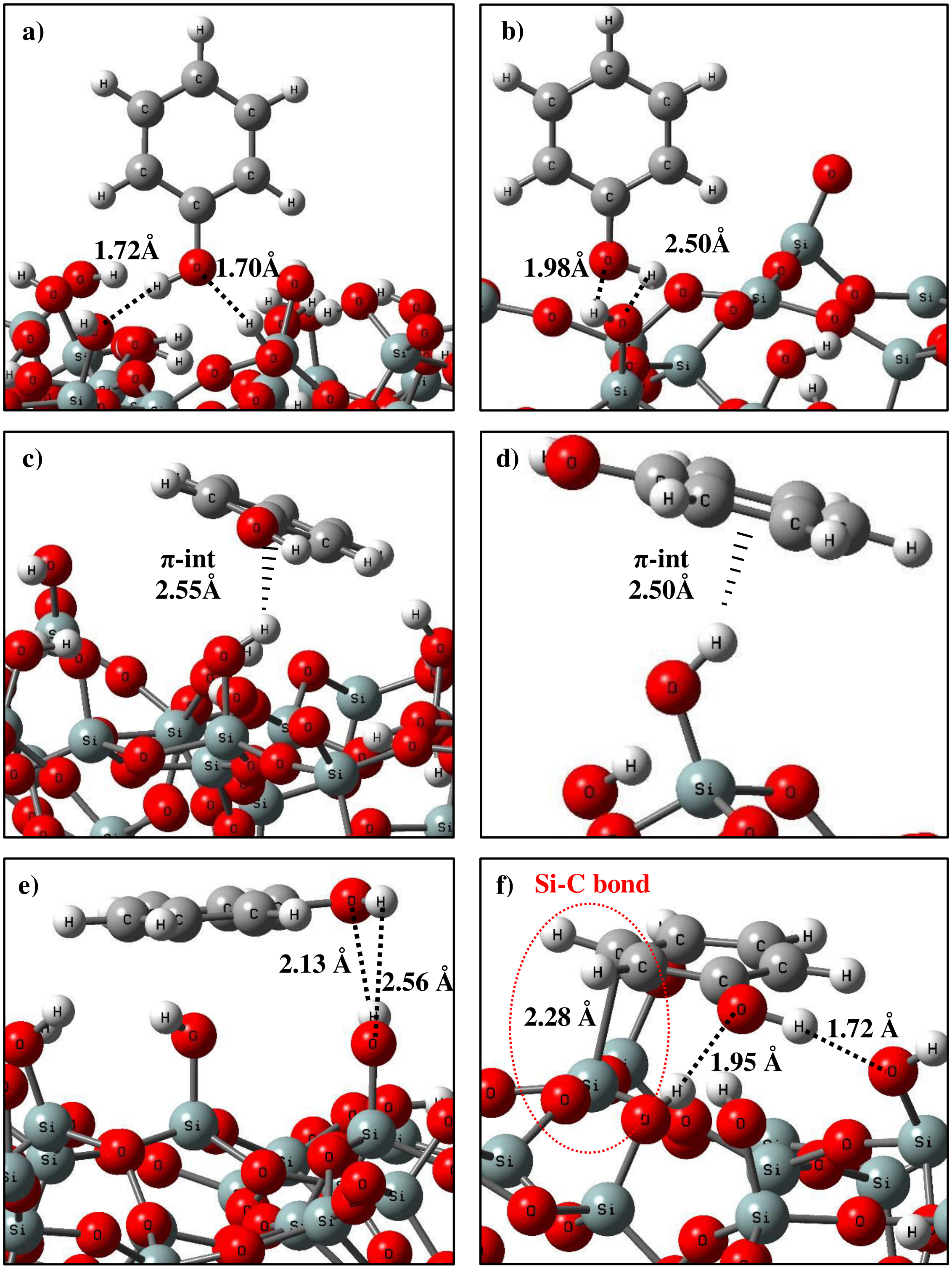

Figure R.4 *Mécanismes d'adsorption du phénol sur les différents sites des surfaces de la silice amorphe:* ***a)*** *perp O-int sur le site nid-2 de* SiO_2*-7.2,* ***b)*** *perp O-int sur le site vicinal de* SiO_2*-2.0,* ***c)*** *flat π-int sur le site vicinal de* SiO_2*-5.9,* ***d)*** *flat π-int sur le site isolé de* SiO_2*-1.1,* ***e)*** *flat O-int sur le site nid-2 de* SiO_2*-3.3.* ***f)*** *flat O-int sur le site nid-1 de* SiO_2*-2.0.*

Considérant la synthèse de catalyseurs de silice contenant des nanoparticules métalliques, des matériaux monométalliques (Fe/SiO_2 et Cu/SiO_2) et bimétalliques Fe-Cu/SiO_2 ont été élaborés par des méthodes conventionnelles basées sur l'imprégnation de silice par une solution métallique. Trois matériaux siliciques ont été synthétisés par la méthode « Sol-Gel » sous des conditions similaires à celles de la synthèse du SBA-15.[6] Leur caractérisation structurale a été réalisée par différentes méthodes (diffraction des rayons X pour confirmer la structure hexagonale ; isothermes d'adsorption et de désorption sous N_2 pour déterminer le diamètre, le volume de pores et la surface active ; thermogravimétrie pour déterminer la densité de silanols). Deux méthodes de précipitation ont été testées, l'imprégnation à température ambiante de silice par une solution de nitrate de fer(III) (catalyseur Fe)[7] ou de chlorure de cuivre (catalyseur Cu) ou d'un mélange des deux (catalyseur Fe-Cu), et la co-précipitation de la silice et du sulfate de fer(II) à pH contrôlé par la décomposition d'urée à chaud (jusqu'à 80°C).[8]

La **Figure R.5** présente la structure des micelles mixtes utilisées comme "templates" durant la synthèse hydrothermale de silice par la méthode « Sol-Gel ». Ces micelles mixtes sont constituées de surfactants non-ioniques (pluronic P123) et de surfactants métalliques cationiques contenants le fer (cetyltrimethylammoniumtrichloromonobromoferrate CTAF), avec plusieurs rapports CTAF/P123. Le changement de structuration des micelles a été étudié pour différents rapports CTAF/P123. Des solutions micellaires pures (P123 et CTAF) et mixtes (rapports molaires CTAF/P123 de 0.1, 0.2, 0.5, 1, 2, 5, et 10) ont été préparées à différentes concentrations. La concentration micellaire critique de chaque solution a été déterminée en analysant la différence de tension de surface. La taille des micelles (diffusion dynamique de la lumière (DLS, **Figure R.6**) et leur potentiel zêta ont été déterminés. L'analyse de la diffusion de neutrons aux petits angles (SANS)[9] des micelles ainsi que celle d'autres micelles (mixtes P123/CTAB et micelles deutérées P123/CTAFd) dans l'H_2O, le D_2O et un mélange D_2O/H_2O, a permis de mesurer les diamètres de gyration et d'identifier des formes structurales pour chaque mélange micellaire. L'ajout de CTAF réduit la taille des micelles et perturbe leur forme sphérique.

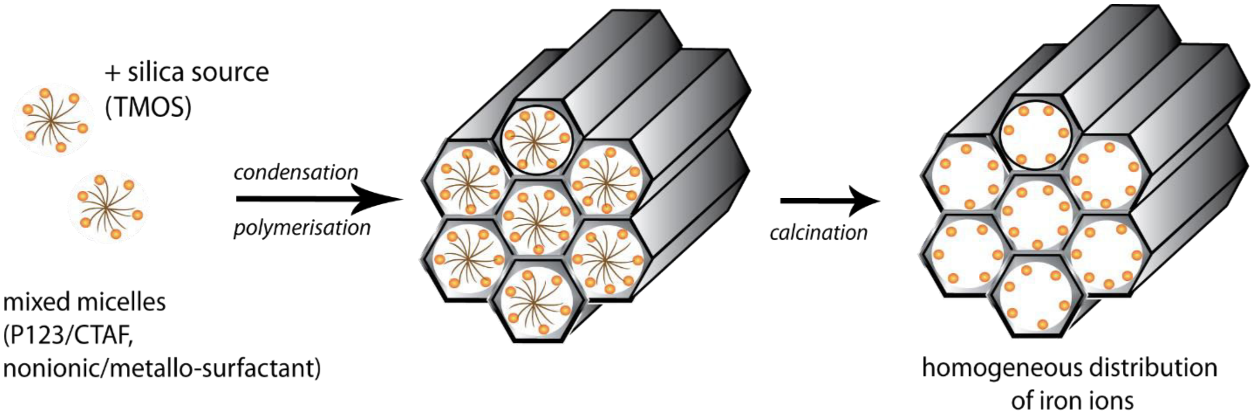

Figure R.5 *La synthèse hydrothermale des catalyseurs Fe/SiO$_2$ suivant le procédé Sol-Gel en utilisant les micelles mixtes non-ionique/métallique (P123/CTAF).*

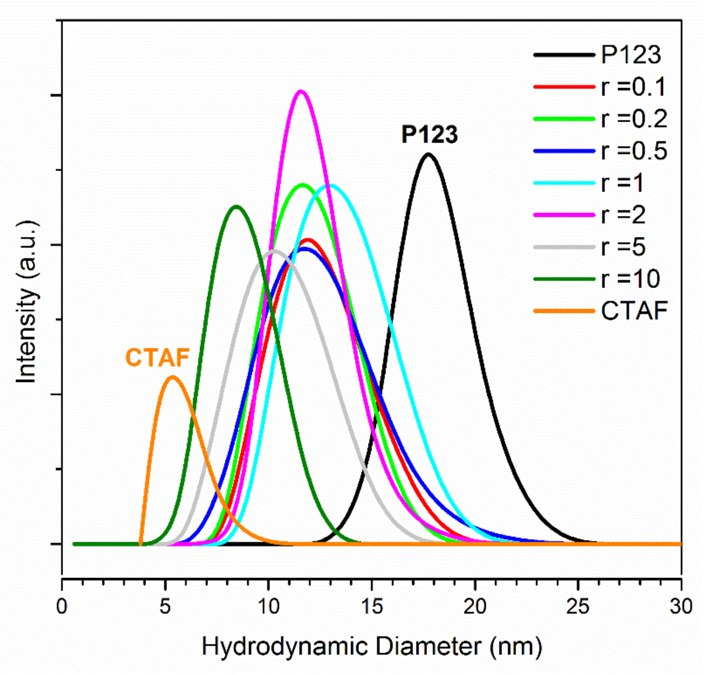

Figure R.6 *Distribution de la taille des micelles pour les solutions micellaires (P123, CTAF, et mélange des deux à proportion variable).*

Notre méthode de synthèse innovante consiste à incorporer le fer durant la formation de la structure de la silice en utilisant les micelles mixtes non-ionique/métallique (CTAF/P123) pour empêcher l'agglomération des atomes de fer et la formation des nanoparticules. Cette méthode permet de bien disperser les atomes de fer sur la surface de la silice dans le but d'obtenir des « Single Atom Catalysts (SACs) » et donc d'augmenter le nombre des sites catalytiques réellement actifs.[10] La dispersion des atomes de fer résulte de leur distribution fine dans la structure micellaire qui sert de matrice autour de laquelle la polycondensation de la chaine silicique se produit. Le rapport des surfactants métallique/non-ionique CTAF/P123 permet de contrôler non seulement le pourcentage de fer dans le matériau final mais encore les propriétés structurales de la silice. Quatre matériaux ont été synthétisés avec un rapport molaire CTAF/P123 égal à 1, 2, 5 et 10. Les propriétés texturales de ces matériaux ont été déterminées par plusieurs méthodes telles que la diffusion de rayons X aux petits angles (SAXS), les isothermes d'adsorption et de désorption d'azote (BET, BJH), et la microscopie électronique à transmission (TEM). L'absence d'agglomération des atomes de fer et de nanoparticules a été confirmée par des mesures magnétiques Squid, des mesures de résonnance magnétique nucléaire (NMR), des mesures de rayons X réalisées en synchrotron « pair-ditribution function » (PDF), et par cartographie des éléments obtenus par microscopie électronique a transmission (TEM). Les calculs DFT+U confirment les résultats trouvés durant les mesures magnétiques Squid à propos de l'état d'oxydation du fer (Fe(III) haut spin 5/2). Ces résultats suggèrent que les « SACs » préparés présentent une performance catalytique améliorée par rapport aux matériaux conventionnels.[11]

Pour déterminer la performance des matériaux synthétisés, des tests catalytiques ont été réalisés sur l'HDO du guaiacol (molécule modèle représentant les bio-huiles), dans des conditions expérimentales (température, pression partielle d'H_2….) similaires à celles utilisées par *Olcese et al.*[3,12–14] dans des études précédentes. Des analyses de réduction à température programmée (TPR) et de spectroscopie Mössbauer ont été effectuées pour déterminer l'état d'oxydation du fer et le pourcentage du fer métallique Fe(0). Ces mesures permettent de régler les conditions de réduction (température et temps) dans le but d'augmenter le pourcentage de sites Fe(0) et limiter l'effet négatif d'agglomération. Un spectromètre de masse (MS) a été monté en ligne pour suivre qualitativement la conversion du guaiacol, et la formation des produits de réaction (eau, phénol, benzène, CO, CO_2) en temps réel (**Figure R.7**). Les résultats de ces expériences peuvent permettre de proposer des mécanismes réactionnels et de prédire la stabilité du catalyseur au cours du temps. Les grandes molécules produites en sortie de réacteur ont été condensées (à -40°C) et analysées quantitativement par chromatographie en phase gaz couplée à la spectrométrie de masse (GCMS). Un chromatographe phase gaz (µGC) a aussi été installé en ligne dans le but d'analyser quantitativement les petites molécules non-condensées (CO, CO_2, O_2, N_2, H_2, C_2H_2, C_2H_4, C_2H_6…). La performance catalytique des matériaux synthétisés a été évaluée en déterminant le taux de conversion du guaiacol (en fin de réaction, 30 min), l'activité et la sélectivité des matériaux par rapport aux fonctions aromatiques. De plus, un bilan élémentaire molaire (C, O, et H) a été établi pour déterminer la sélectivité du procédé en termes de carbones aromatiques.

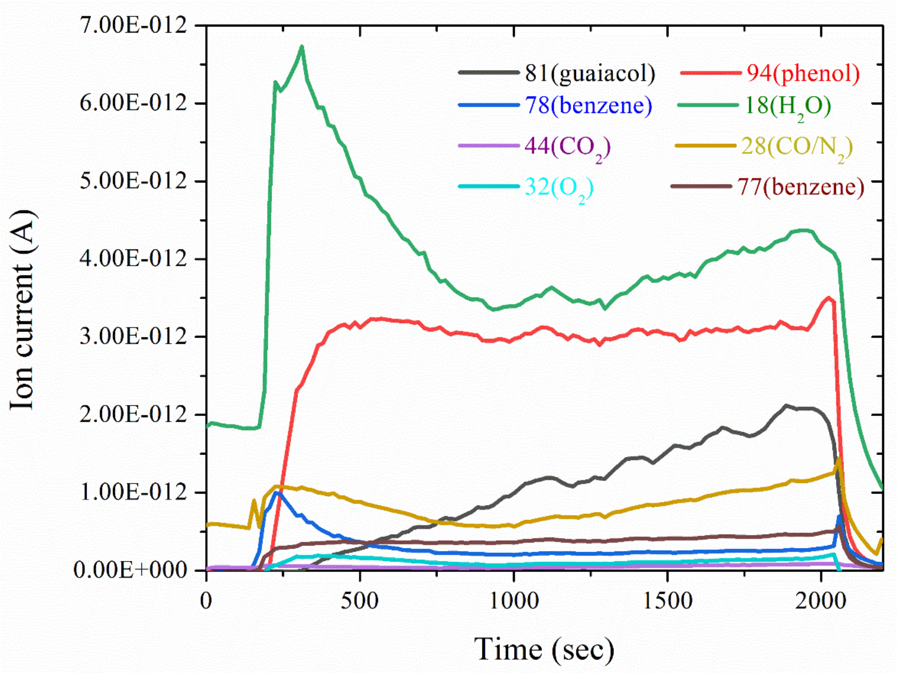

Figure R.7 *Analyse en temps réel du flux sortant du réacteur d'HDO contenant le guaiacol non-converti et les produits formés (H_2O, CO, CO_2, phénol, benzène).*

Les analyses TPR et Mössbauer ont montré que pour les matériaux SACs, les atomes de Fe(III) fortement attachés à la surface de la silice restent sous forme Fe(III) au cours de l'HDO du guaiacol. Par conséquent, la performance catalytique de ces matériaux n'est pas satisfaisante. Par contre, des modifications de synthèse telles que l'incorporation de cuivre (en utilisant des metallosurfactants de cuivre), peuvent faciliter la réduction des atomes de fer (III).

Les catalyseurs bimétalliques Fe-Cu/SiO_2 et les autres catalyseurs synthétisés à pH contrôlé par dégradation d'urée à chaud (conduisant au Fe(II))[8] sont réduits plus facilement que les catalyseurs Fe/silice, conduisant à un plus grand nombre des sites actifs en fer métallique Fe(0). Le catalyseur Fe-Cu/SiO_2 a montré les meilleurs taux de conversion du guaiacol et sélectivités en aromatiques (en fin de réaction, 30 min) : 87% et 72%, respectivement (**Tableau R.1**). Les catalyseurs à support de silice avec une densité de silanols de 8 OH/nm^2 montrent une sélectivité en aromatiques nulle. L'effet de la taille des pores du support est critique : les catalyseurs à double porosité (porosité de 5 et 8 nm) sont moins sélectifs que ceux ayant uniquement de grands pores (porosité de 8 nm), ce qui pourrait être dû à l'obstruction des pores par les grandes molécules. Les catalyseurs synthétisés par la méthode de co-précipitation (donnant du Fe(II)) montrent une meilleure performance que ceux synthétisés par l'imprégnation simple à température ambiante. Par conséquent, des catalyseurs bimétalliques Fe-Cu doivent être synthétisés par la méthode de co-précipitation (à pH contrôlé, par dégradation d'urée) ce qui permet de les réduire dans des conditions moins sévères (température plus basse) et ainsi d'obtenir de plus petites nanoparticules, aboutissant à une meilleure performance catalytique.

Tableau R.1 *Performance catalytique des matériaux à 400 ^{o}C: conversion du guaiacol (X_{gua}), HDO sélectivité (S_{HDO}), et activité catalytique (A_{HDO}) à la fin de la réaction (après30 min).*

Catalyseur	Caractéristique	Conversion du guaiacol après 30 min (X_{gua} %)	Sélectivité en aromatiques après 30 min (S_{HDO} %)	Activité catalytique A_{HDO} ($mmol.h^{-1}.g_{cat}^{-1}$)
15%Fe@ SBA-15- 1SC	Silice (pores 8 nm, 2 OH/nm^2)	82	56	5.61
15%Fe@ SBA-15-3S	Silice (pores 5-8 nm, 8 OH/nm^2)	55	0	0
15%Fe@ SBA-15-3SC	Silice (pores 5-8 nm, 2 OH/nm^2)	52	26	1.75
15%Cu@ SBA-15-3SC	Cuivre sur silice (pores 5-8 nm, 2 OH/nm^2)	71	80	7.24
15%Fe3%Cu@ SBA-15-3SC	Bimétallique Fe-Cu sur silice (pores 5-8 nm, 2 OH/nm^2)	87	72	7.39
15%Fe@ SBA-15-3SC-DPU	Fe(II) (contrôlé par DPU imprégnation	73	52	4.82

Références

(1) Bu, Q.; Lei, H.; Zacher, A. H.; Wang, L.; Ren, S.; Liang, J.; Wei, Y.; Liu, Y.; Tang, J.; Zhang, Q.; Ruan, R. A Review of Catalytic Hydrodeoxygenation of Lignin-Derived Phenols from Biomass Pyrolysis. *Bioresour. Technol.* **2012**, *124*, 470–477.
(2) Furimsky, E. Catalytic Hydrodeoxygenation. *Appl Catal A* **2000**, *199(2)*, 147–190.
(3) Olcese, R.; Bettahar, M. M.; Malaman, B.; Ghanbaja, J.; Tibavizco, L.; Petitjean, D.; Dufour, A. Gas-Phase Hydrodeoxygenation of Guaiacol over Iron-Based Catalysts. Effect of Gases Composition, Iron Load and Supports (Silica and Activated Carbon). *Appl. Catal. B Environ.* **2013**, *129*, 528–538.
(4) Badawi, M.; Paul, J. F.; Cristol, S.; Payen, E.; Romero, Y.; Richard, F.; Brunet, S.; Lambert, D.; Portier, X.; Popov, A.; Kondratieva, E.; Goupil, J.M.; El Fallah, J.; Gilson, J.P.; Mariey, L.; Travert, A.; Mugé, F. Effect of Water on the Stability of Mo and CoMo Hydrodeoxygenation Catalysts: A Combined Experimental and DFT Study. *J. Catal.* **2011**, *282* (1), 155–164.
(5) Berro, Y.; Gueddida, S.; Lebègue, S.; Pasc, A.; Canilho, N.; Kassir, M.; El Haj Hassan, F.; Badawi, M. Atomistic Description of Phenol, CO and H_2O Adsorption over Crystalline and Amorphous Silica Surfaces for Hydrodeoxygenation Applications. *Appl. Surf. Sci.* **2019**, *494*, 721–730.
(6) Zhao, D. Triblock Copolymer Syntheses of Mesoporous Silica with Periodic 50 to 300 Angstrom Pores. *Science* **1998**, *279* (5350), 548–552.
(7) Huang, H.; Ji, Y.; Qiao, Z.; Zhao, C.; He, J.; Zhang, H. Preparation, Characterization, and Application of Magnetic Fe-SBA-15 Mesoporous Silica Molecular Sieves. *J. Autom. Methods Manag. Chem.* **2010**, *2010*, 1–7.

(8) Shi, D.; Yang, Q.; Peterson, C.; Lamic-Humblot, A.-F.; Girardon, J.-S.; Griboval-Constant, A.; Stievano, L.; Sougrati, M. T.; Briois, V.; Bagot, P. A.J.; Wojcieszak, R.; Paul, S.; Marceau, E. Bimetallic Fe-Ni/SiO_2 Catalysts for Furfural Hydrogenation: Identification of the Interplay between Fe and Ni during Deposition-Precipitation and Thermal Treatments. *Catal. Today* **2019**, *334*, 162–172.

(9) Kim, S.; Bellouard, C.; Pasc, A.; Lamouroux, E.; Blin, J.-L.; Carteret, C.; Fort, Y.; Emo, M.; Durand, P.; Stébé, M.-J. Nanoparticle-Free Magnetic Mesoporous Silica with Magneto-Responsive Surfactants. *J. Mater. Chem. C* **2013**, *1* (42), 6930–6934.

(10) Thomas, J. M.; Raja, R. The Advantages and Future Potential of Single-Site Heterogeneous Catalysts. *Top. Catal.* **2006**, *40* (1–4), 3–17.

(11) Chen, Y.; Ji, S.; Wang, Y.; Dong, J.; Chen, W.; Li, Z.; Shen, R.; Zheng, L.; Zhuang, Z.; Wang, D.; Li, Y. Isolated Single Iron Atoms Anchored on N-Doped Porous Carbon as an Efficient Electrocatalyst for the Oxygen Reduction Reaction. *Angew. Chem.* **2017**, *129* (24), 7041–7045.

(12) Olcese, R. N.; Bettahar, M.; Petitjean, D.; Malaman, B.; Giovanella, F.; Dufour, A. Gas-Phase Hydrodeoxygenation of Guaiacol over Fe/SiO_2 Catalyst. *Appl. Catal. B Environ.* **2012**, *115–116*, 63–73.

(13) Olcese, R. N.; Lardier, G.; Bettahar, M.; Ghanbaja, J.; Fontana, S.; Carré, V.; Aubriet, F.; Petitjean, D.; Dufour, A. Aromatic Chemicals by Iron-Catalyzed Hydrotreatment of Lignin Pyrolysis Vapor. *ChemSusChem* **2013**, *6* (8), 1490–1499.

(14) Olcese, R. N.; Francois, J.; Bettahar, M. M.; Petitjean, D.; Dufour, A. Hydrodeoxygenation of Guaiacol, A Surrogate of Lignin Pyrolysis Vapors, Over Iron Based Catalysts: Kinetics and Modeling of the Lignin to Aromatics Integrated Process. *Energy Fuels* **2013**, *27* (2), 975–984.

Introduction

Introduction

Climate change, depletion of oil reserves, and the high increase in the energy demand requires the development of new efficient and sustainable processes for bio-fuels production from lignocellulosic biomass, which is one of the largest sources of renewable energies. The low O/C and H/C ratio found in the lignin component, comparing to cellulose and hemi-cellulose, and its aromatic structure make him more attractive for fuels and chemicals production. However, those ratios are higher than that of conventional crude oil, thus further processing is needed to reduce its oxygen content. This study treats the gas phase hydrodeoxygenation (HDO) of lignin pyrolysis bio-oils. Lignin pyrolysis occurs at temperatures varying from 500 to 800 ^{o}C in absence of oxygen, and produces char, oligomers, non-condensable gases and lignin aromatic bio-oil vapors (mainly phenols, guaiacol, anisole, cresol….). The HDO process is a thermal catalytic conversion in presence of dihydrogen which convert those bio-oils in hydrocarbons and water as a by-product.

HDO includes two principal deoxygenation routes, (i) the hydrogenation of the aromatic ring before C-O bond cleavage (HYD), or (ii) the direct C-O bond cleavage, Direct Deoxygenation (DDO). Researches in this field aim to promote the DDO route in order to decrease the H_2 consumption (decrease the working pressure and costs) and produce valuable aromatics. In addition to the enormous number of experimental studies in this field, Density Functional Theory (DFT) calculations are used in order to complement the experimental studies and provide new perspectives in this domain. Several catalysts and supports were tested for biomass conversion under HDO conditions; among them, Fe/SiO_2 showed an interesting selectivity to aromatics.

This thesis aims to develop new mesoporous silica-supported metal catalysts in order to promote the DDO route, thus increasing aromatics production. To achieve this goal, we applied a theoretical/experimental approach where DFT calculations, materials synthesis, and catalytic tests were performed. Results obtained, using this approach, allow to understand the effect of various parameters and characteristics on the catalytic performance of synthesized materials, and to propose new modifications for further investigations.

In the following, we detail the structure of this manuscript, giving a brief descriptive of the content of each chapter.

The first chapter gives a bibliographic review on biomass upgrading, especially on the hydrodeoxygenation HDO reaction of lignin-derived bio-oils, highlighting the relevance of combined theoretical and experimental studies and the performances of non-noble metal catalysts supported on mesoporous silica.

The second chapter presents the theoretical and experimental methods I have used during my PhD thesis. It is composed of three parts where the first one focuses on presenting the density functional theory (DFT), the second part introduces the synthesis methods used to elaborate the mesoporous ferrisilicate materials, and the third part presents the HDO process and equipment.

In chapter 3, we investigated, using DFT, the adsorption properties of various crystalline and amorphous silica surfaces. Phenol (model molecule of bio-oils) interaction modes with silanols were interpreted and adsorption energies were computed in order to choose the more appropriate surface favoring the DDO route and limiting the inhibiting effect of by-products (water and CO).

In chapter 4, we presented the elaboration of the metal@silica materials where the first part describes the synthesis of metallic Fe and bimetallic Fe-Cu silica supported catalysts, with various structural properties, using conventional methods as the impregnation of pre-synthetized silica and the co-precipitation with decomposition of urea (DPU). In the second part of this chapter, we studied the micelles structuration of non-ionic/metallo surfactants into mixed micelles. Finally, in the third part, we presented the direct hydrothermal synthesis of mesoporous ferrisilicate single atom catalysts (SACs), using those mixed micelles as templates, where various characterizations proved the well dispersion of iron species on the silica mesopores.

In Chapter 5, we presented the catalytic performance of the synthetized materials when tested for guaiacol hydrodeoxygenation (HDO) conversion. The conversion, aromatics selectivity, catalytic activity, and aromatics carbon selectivity of SACs and conventionally synthesized (Fe, Cu, and Fe-Cu@SiO_2) catalysts were discussed showing the effect of the synthesis method, the silica textural properties, and the incorporation of copper as a bi-metal catalyst.

Finally, we gave conclusions on the theoretical and experimental results obtained in this work, and their importance in this field. We gave some perspectives for future studies.

Chapter 1

Bibliographic Review

Chap. 1 Bibliographic Review

According to the Renewable Energy Policy Network for the 21th Century (REN21 report), renewable energy sources covered about 19% of the total world energy consumption in 2013, where biomass contributes with nearly half of the energy supplied from renewable sources.[1] The most popular way to obtain energy from biomass is the direct burning of plants; however, this method produces a copious amount of carbon dioxide and contribute to the formation of unhealthy environmental areas. Rising energy demand, climate change, and depletion of gas and oil reserves require the development of cleaner and efficient processes to convert biomass into bio-fuels. **Figure 1.1** shows some sources of lignocellulosic biomass and the main valorization process. We are interested in the route highlighted by a red line, and leading to bio-fuels production.

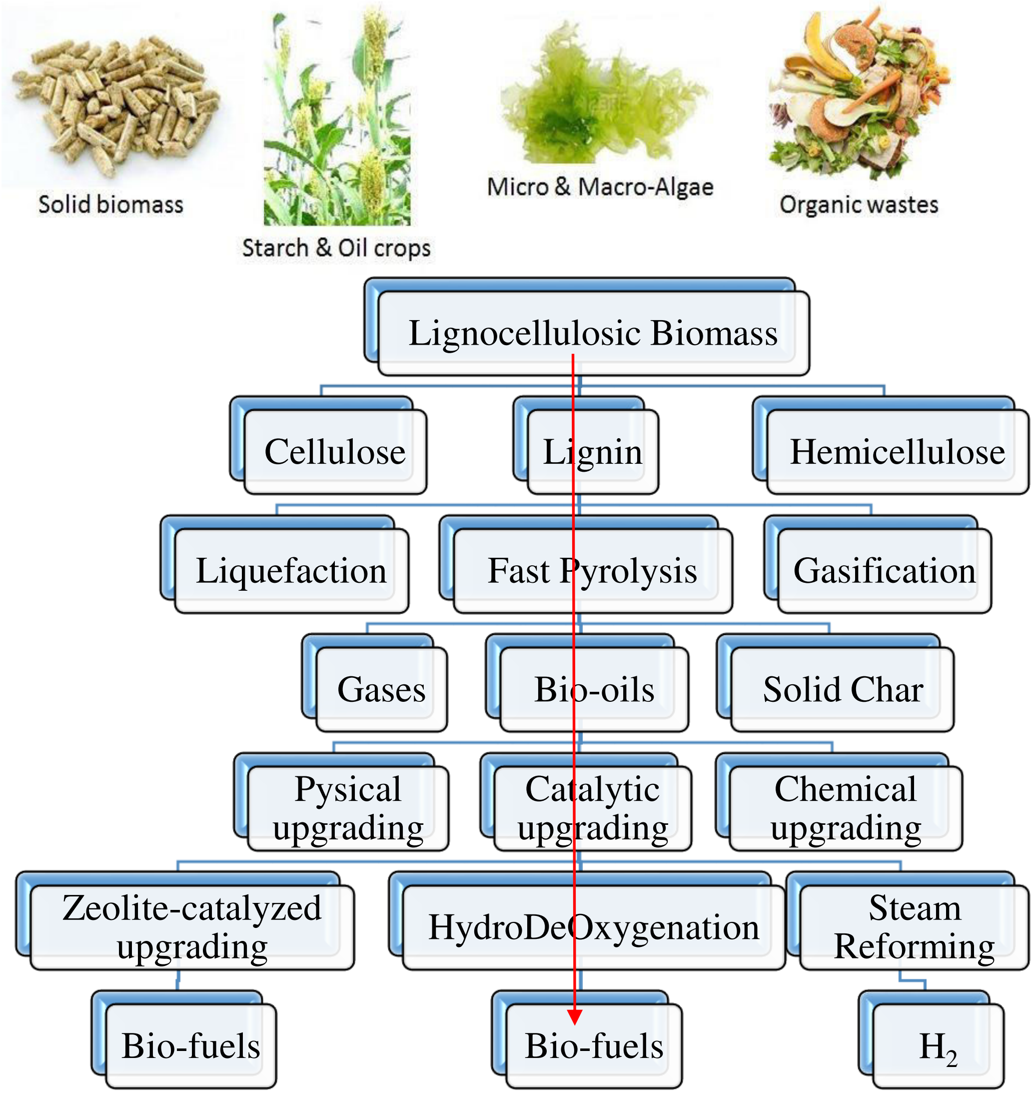

***Figure 1.1** Biomass sources and processing technologies leading to bio-fuels production.*

1.1 Lignocellulosic Biomass

The lignocellulosic biomass is considered as one of the main alternative sources to petroleum for the production of bio-fuels and chemicals ; it comprises about 30-50% cellulose, 15-25 % hemicellulose, and 15-30% lignin depending on its origin.[2] Those components, found in the plant cell wall, are presented in **Figure 1.2**. Cellulose is made of linear homo-polysaccharides with a high degree of polymerization. Hemicellulose is a mixture of various polymerized monosaccharides (branched polymers with a low degree of polymerization). Lignin consists of aromatic units linked in large polymeric structure and acts as a resin to strengthen the lignocellulose matrices. It has the lowest Oxygen/Carbon and Hydrogen/Carbon ratios in comparison with cellulose and hemicellulose, but these ratios are still much higher than those of conventional crude oil. Therefore, studies focus on upgrading lignin by several processes in order to reduce its oxygen content and obtain valuable aromatic bio-fuels.

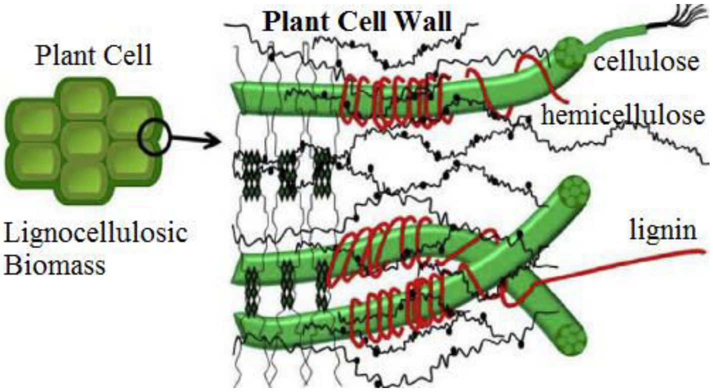

***Figure 1.2** Lignocellulosic biomass components.*

The main structure of lignin (***Figure 1.3***) involves several types of monomer alcohols, mainly the p-coumoryl (Hydroxyphenyl), the coniferyl (Guaiacyle) and the sinapyl (Syringyle). Softwood contains the highest level of lignin (around 30%) in comparison with hardwood, energy crop, and agricultural waste. The separation of lignin from other biomass components is performed throughout various methods including Kraft, soda pulping, Organosolv, steam explosion…[3] The organosolv pulping technique[4] consists of the solvent extraction of lignin (ethanol, ethylene glycol, acetic acid…) at 140 to 220 ºC, leading to the production of a high purity dry sulfur-free solid lignin with a molecular weight of about 5000 g/mol.

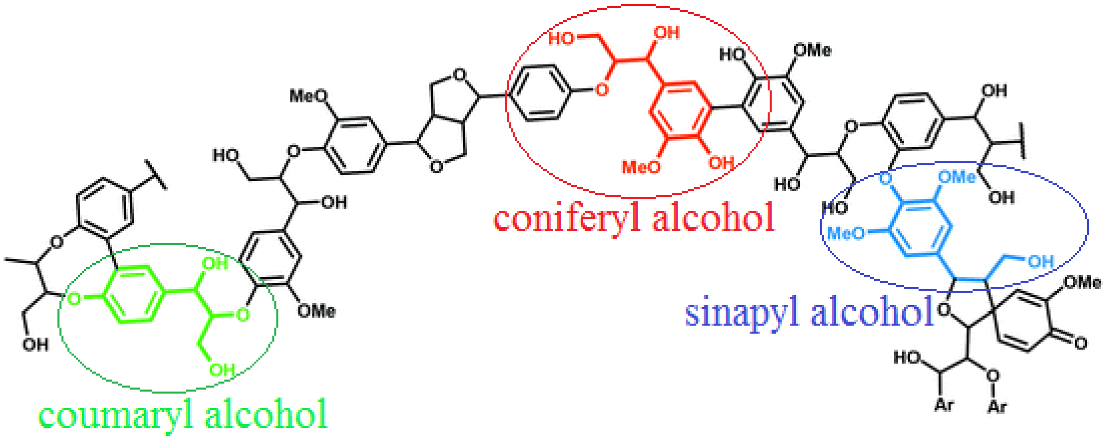

Figure 1.3 *Lignin main structure and building blocks.*

1.2 Lignin Valorization and Market Products

Currently, Kraft lignin produced from the Kraft pulping process is used directly as a fuel for Kraft pulp mills,[5] while lignosulfonate produced by the sulfite pulping process have many applications as plasticizer or emulsifier, animal feed pellets, pesticides, and oil-well drilling mud additives.[6] The strategies of lignin valorization include gasification to produce syngas,[7] slow pyrolysis to produce carbon-based materials[8] (activated carbon and carbon fibers[9]), controlled oxidation to produce valuable chemicals (as vanillin and eugenol),[10] and catalytic fast pyrolysis using zeolites to produce bio-oils.[11]

The most interesting economic technique for lignin valorization is HydroDeOxygenation of bio-oil vapors produced from pyrolysis or hydrothermal conversion. In 2007, Holladay *et al.*[12] studied the economic scenario of lignin valorization in USA. They showed that the income of BTX (benzene, toluene, and xylene) production was more than twice as high as the income of power production through lignin combustion. Haveren *et al.*[13] discussed a similar case study for biorefineries located in the port of Rotterdam, which is one of the most important ports in Europe for biomass handling, storage and valorization.

According to the Global Market Insights, the lignin market will increase from 650 M$ in 2016 to exceed 960 M$ by 2024, and the size of aromatic lignin market will register gains at over 4.5 %.[14] BTX are produced conventionally from naphtha reforming, coal pyrolysis, and methanol-to-gasoline MTG processes; they are used as fuel additives and as starting blocks for several molecules. Phenol is conventionally produced from cumene oxidation and used as starting block for resin and antioxidants synthesis. Therefore, researchers focus on the development of processes for lignin conversion into aromatic hydrocarbons (BTX and phenol). **Figure 1.4** presents the volume distribution of lignin products and their corresponding income values.

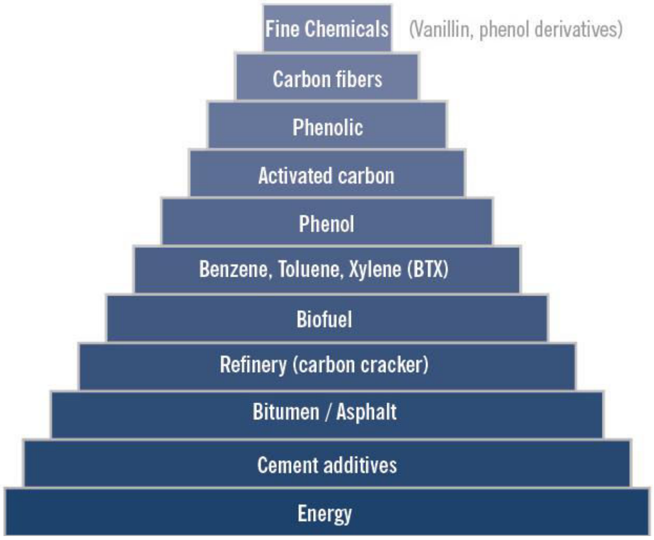

Figure 1.4 *Lignin applications and products: the base of the histogram present a high volume of low value revenue while the top present low volume of high value revenue.*

1.3 Lignin Pyrolysis and Hydrothermal Conversion

Various processes are adopted for lignin depolymerization in order to obtain valuable aromatic chemicals. ***Table 1.1*** summarizes literature data about those processes.

Table 1.1 *Main lignin-to-aromatics upgrading processes, their advantages and drawbacks.*

Process Description	Advantages	Drawbacks
Base catalyzed depolymerization and HDO of phenol produced (50 bar H_2, transition metal catalyzed)[15]	High yield of hydrocarbons (64w.% of dry lignin)	Difficulty of phenols extraction procedure
Pyrolysis and HDO of condensed pyrolysis vapors (100 bar H_2, catalyzed by noble metals)[16]	Phenols are well separated from char before the catalytic treatment	Low yield of heavy HCs (C_6+)
Catalytic Pyrolysis[17,18]	Low pressure (no H_2 consumption)	Difficult regeneration of catalyst (Char agglomeration)
Noguchi process ;[19] Catalytic hydrotreatment of lignin dissolved on lignin-based phenolic mixture	High yield of monophenols	Expensive reactors for hydrotreatment at T>673K, complex distillation of products
Lignol process;[20] catalytic ellubated bed	Production of phenol and cresols	Formation of carbonaceous solid and clogging of the bed
Pyrolysis and low pressure, gas phase, HDO of phenolic bio-oil vapors (this work)[21–27]	HDO catalysts not in contact with char, low pressure, cheap and regenerated catalysts	Need the development of steady state lignin pyrolysis reactor

The type of process applied depends on the lignin source (ex. water content) and on the product needed. Our work focuses on hydrodeoxygenation (HDO) of bio-oil vapors produced from lignin pyrolysis, in order to obtain BTX and phenol. **Figure 1.5** shows the main molecules found among the bio-oil derived from the pyrolysis of lignin.

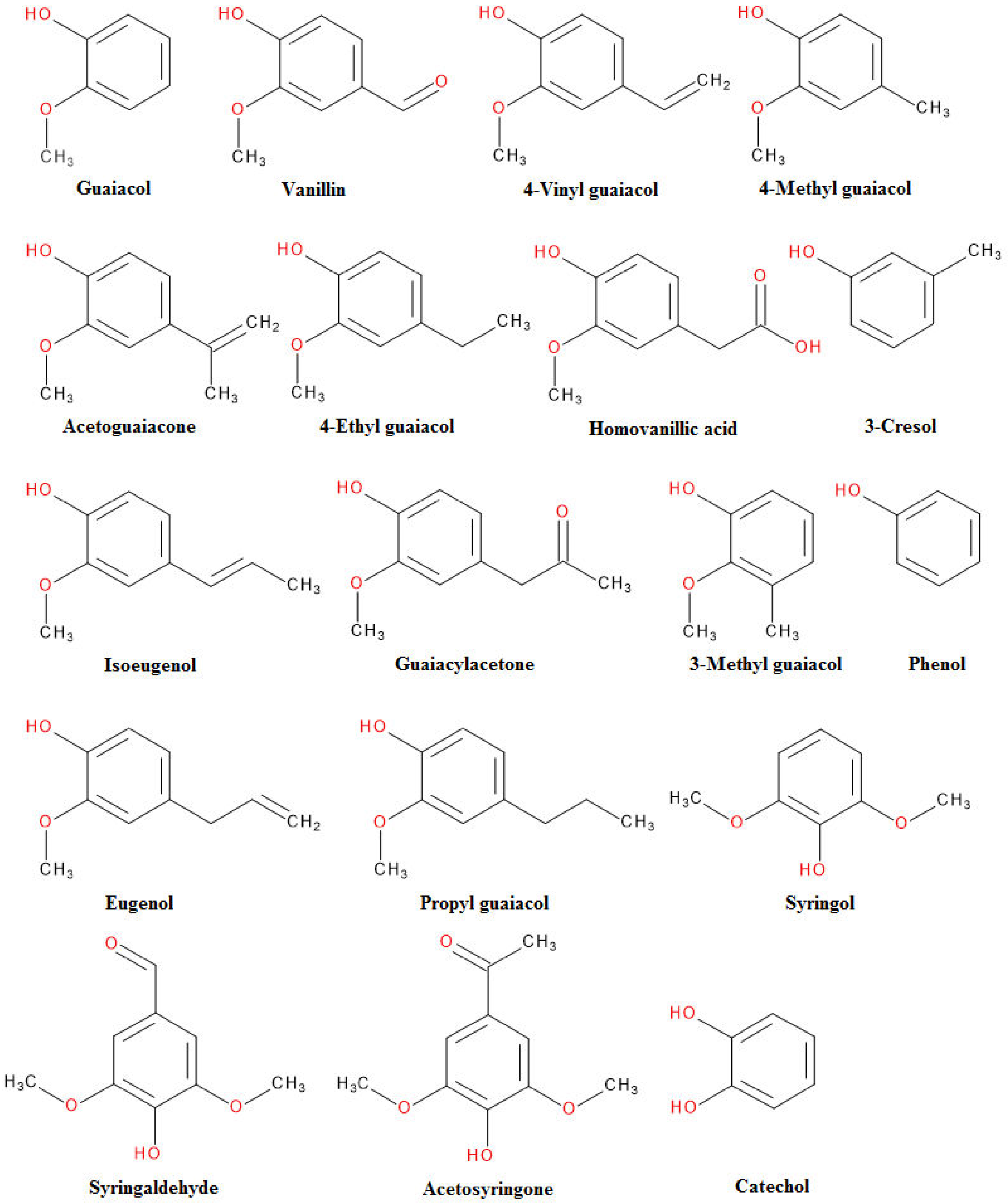

Figure 1.5 *Principal bio-oil vapors obtained from the pyrolysis of lignin.*

Lignin pyrolysis,[28–34] which is a thermochemical process under moderate temperature (623-873K) in absence of oxygen, produces char, oligomers, non-condensable gases (CO, CO_2, CH_4, light HCs) and aromatic bio-oil vapors (mainly phenols, guaiacol, anisole, cresol….). Several studies focused on the analysis of lignin pyrolysis products and their quantities, depending on the source of lignin,[31,35] pyrolysis temperature,[16,35] and various other conditions.[33] Depending on lignin source, the production of bio-oil vapors reaches about 15 to 30 wt.% in a pyroprobe reactor at 873K,[35] whereas it is only about 9 wt.% in a fluidized bed reactor at 673K.[16]

Because bio-oils produced through lignin pyrolysis are have a high content in oxygenated compounds(up to 40%), they display bad fuel properties such as high viscosity, thermal and chemical instability, low heating value, acidic and corrosive nature, and bad motor efficiency….[36] The major catalytic treatments studied for upgrading these bio-oils[37] are (i) the steam reforming of bio-oils for hydrogen production,[38–40] (ii) the zeolite catalyzed cracking which doesn't require H_2 supply but leads to high coke yield and fast catalyst deactivation,[41–43] and (iii) Hydrodeoxygenation (HDO) which is the subject of the present thesis.[44–50]

1.4 HydroDeOxygenation of Pyrolysis Bio-oils

The gas phase HDO of lignin-derived pyrolysis bio-oil vapors, refers to high temperature (623-873K) chemical conversion to obtain oxygen-free molecules, and water as a by-product. It consists in several reactions, mainly hydrocracking, hydrogenation, dehydration, hydrogenolysis, demethylation (DME), demethoxylation (DMO) and decarboxylation.[49] Pyrolysis coupled with online HDO process results in optimizing the heat integration, and reducing the problem of condensed bio-oil feeding.[51,52] In 2000, as a brief literature review on HDO, Furimsky[44] studied the kinetics and reaction networks of HDO, and concluded that more stable catalysts are needed to make fuel production more attractive. In 2007, Elliott[45] reviewed the historical development of catalytic hydroprocessing of bio-oils, while Choudhary and Phillips[46] reviewed the applications of HDO from an industrial perspective, using different bio-oil feeds, catalysts, and operating conditions. More recently, Bu *et al.*[47] reviewed the HDO of phenols derived from lignin pyrolysis. The kinetics and reactions mechanisms of the process were investigated and analyzed using different model compounds and the performance of various conventional ($CoMo/Al_2O_3$ and $NiMo/Al_2O_3$) and noble catalysts were discussed. They concluded that for various techno-economic problems, future investigations should be performed on improving catalysts, optimizing catalytic conditions, and understanding reaction kinetics. He & Wang[48] considered advances in HDO using various bio-oil models and catalysts (noble and non-precious metals, sulfides, nitrides, metal oxides…). They also studied the importance of the support, and proved that O from oxy-compounds is adsorbed on H in -OH of non-metal oxides (such as SiO_2).

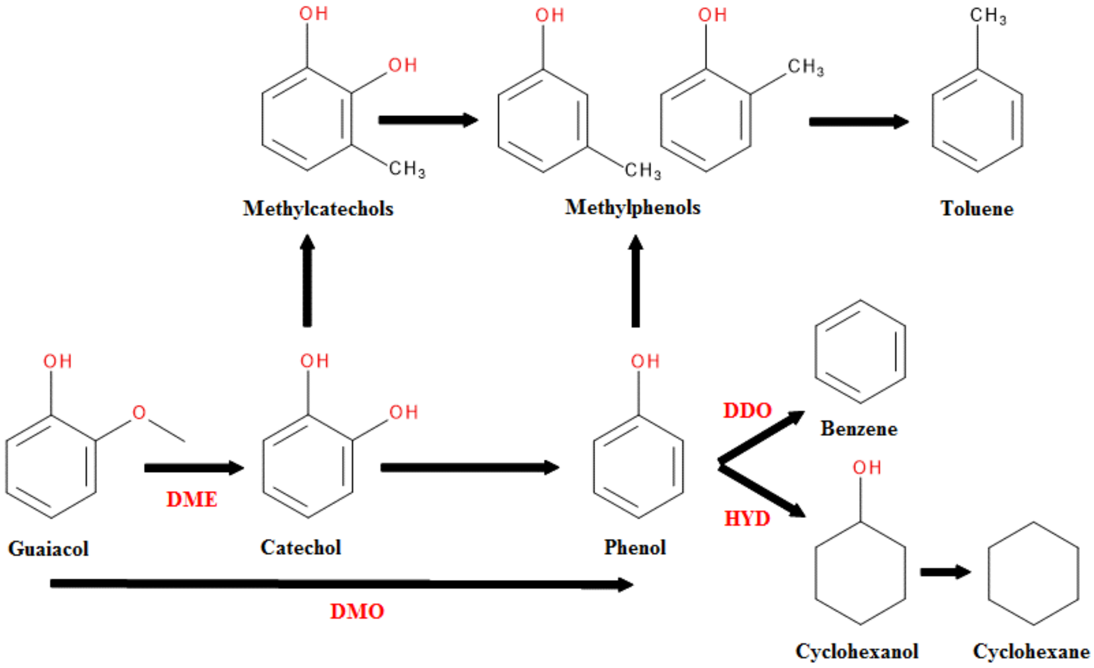

Figure 1.6 *Schematic description of guaiacol HDO reactions and pathways: DDO vs. HYD routes.*

The HDO process includes two main deoxygenation routes, (i) the hydrogenation of the aromatic ring before C-O bond cleavage (HYD), or (ii) the direct C-O bond cleavage, Direct Deoxygenation (DDO) (see **Figure 1.6**). Most investigations in this field aim to promote the DDO route, in order to avoid hydrogenation of the aromatic ring, and therefore to reduce H_2 consumption (which in consequence, decreases the working pressure and costs) and to produce more valuable aromatics (BTX). In addition to the enormous number of experimental studies in this field, theoretical Density Functional Theory (DFT) calculations are frequently used to study the adsorption of oxygenated molecules on the catalyst surface under HDO conditions, and the effect of inhibitors, for understanding the reaction pathways and mechanisms.[53–55]

1.5 Reaction Mechanisms of HDO Model Molecules

1.5.a Conversion of phenol

Containing an aromatic ring and a hydroxyl group, phenol has been widely investigated as the simplest representative model of bio-oil compounds. The two major routes for HDO conversion of phenol are the hydrogenolysis, known as the Direct DeOxygenation route DDO, and the hydrogenation route HYD. The DDO route includes the direct cleavage of the C-O bond before hydrogenation of the aromatic ring. It occurs preferentially at high temperatures, while hydrogenation of the aromatic ring occurs first in the HYD route as described in **Figure 1.7**.[56–58]

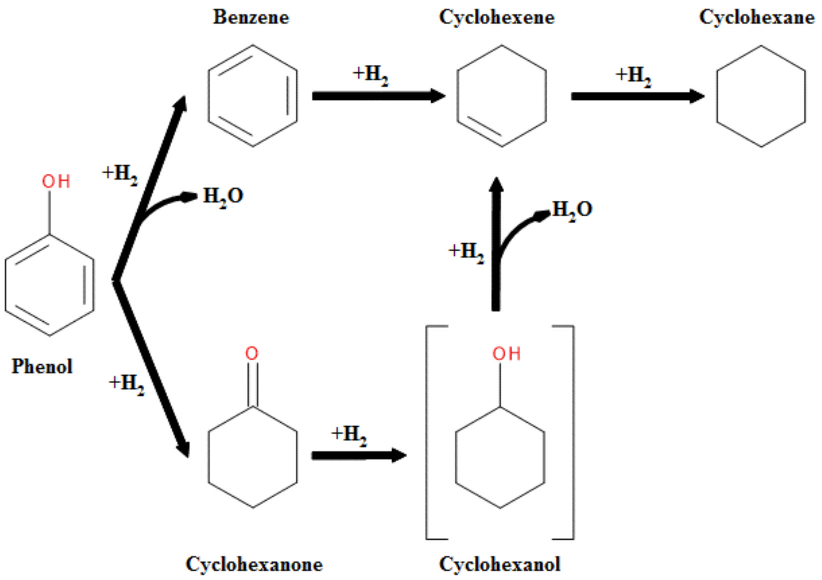

Figure 1.7 Possible routes for phenol conversion during HDO process.

1.5.b Conversion of guaiacol

Because of its two C-O bonds, present in the hydroxy (C_{sp2}-OH) and methoxy (C_{sp2}-OCH_3) groups, guaiacol is the most preferred model molecule of lignin-derived bio-oils.[59,60] A wide range of pathways for guaiacol conversion are presented in **Figure 1.8**. Three main mechanisms occur: (i) the demethylation DME (hydrogenolysis of the O-CH_3 bond) leading to the formation of catechol and methane. Catechol usually loses one of its OH groups under H_2 pressure, producing phenol and water as by-product, (ii) the demethoxylation DMO, by direct cleavage of $C_{aromatic}$-OCH_3 bond leading to phenol and methanol, and (iii) the hydrogenolysis of the $C_{aromatic}$-OH bond producing water and anisole.[61] This last molecule can exhibit four reaction pathways, (i) the DME producing phenol and methane, (ii) the DMO or direct deoxygenation route producing benzene and methanol, (iii) the hydrogenation of the aromatic ring leading to the formation of methoxycyclohexane, and (iv) the methyl group transfer (transalkylation) producing toluene and xylenes as final products.[62,63] The DME route is kinetically more favorable than the DMO route because the C_{methyl}-O bond is weaker then the $C_{aromatic}$-O bond.[64] Zhu *et al.*[63] demonstrated that when the catalyst incorporates an acidic function (as an acidic support), the transalkylation pathway is kinetically the most significant. They concluded that both methyl transfer and HDO occur at higher rates on bifunctional metallic-acidic catalysts than on monofunctional metallic catalysts, leading to the formation of phenol and BTX products with a lower H_2 consumption.

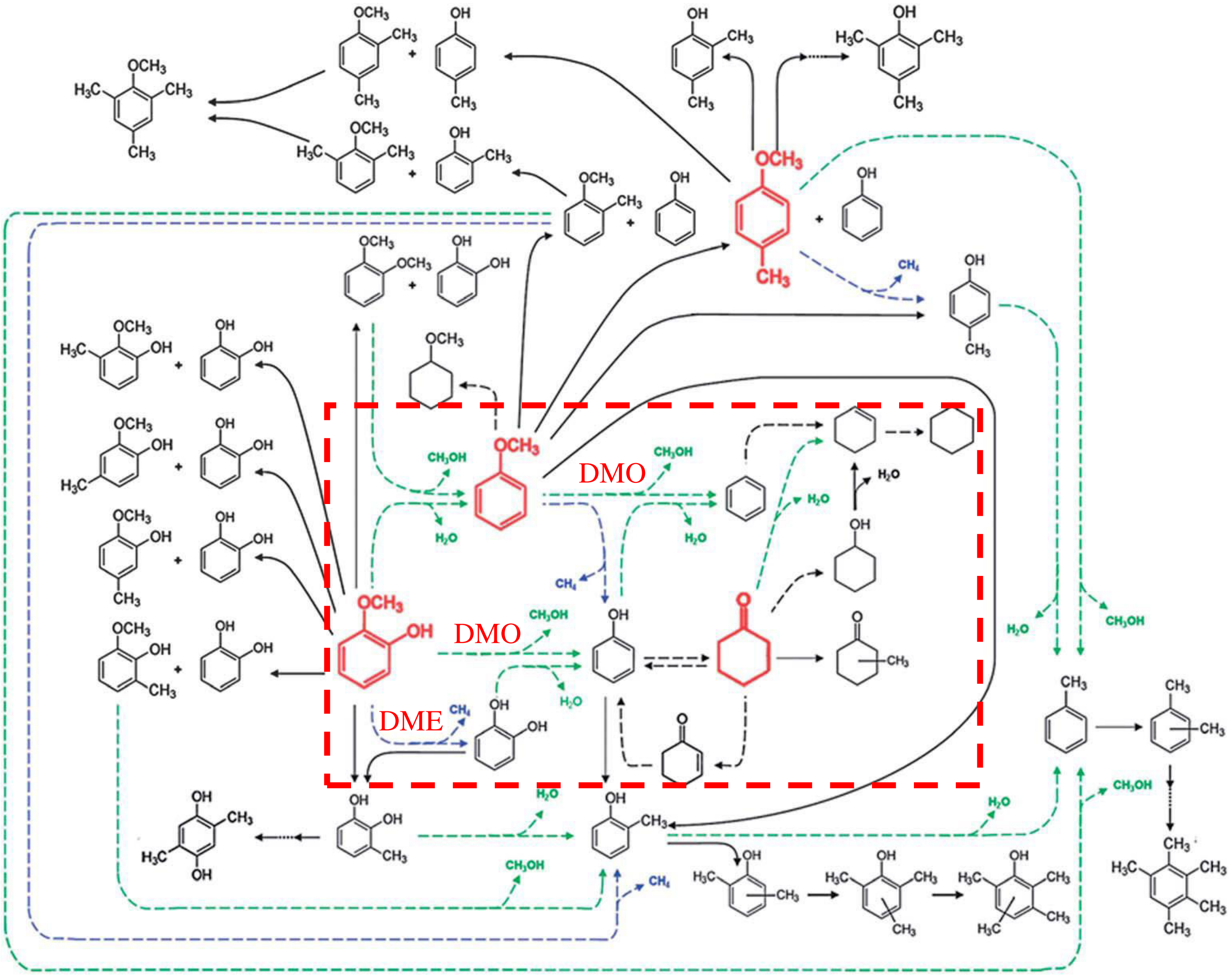

Figure 1.8 Map of possible reaction mechanisms and pathways during the HDO process for the conversion of guaiacol.

1.6 Catalysts and Supports for HDO Reaction

Several catalysts and supports have been tested for biomass conversion under HDO conditions;[46–49,65] ***Table 1.2*** shows some examples under various operating conditions while ***Table 1.3*** compares the conversion yield of guaiacol and selectivity of some catalysts. The choice of the appropriate catalyst depends on its activity and selectivity toward aromatics (DDO route), its deactivation rate under operating conditions and its suitability for environmental use. Noble metals showed a high activity but they are expensive and suffer from high deactivation and reactor clogging at high temperatures.[34] Conventional metal sulfides are very active and selective toward aromatics but their stability depends on the H_2S/H_2O pressure ratio, which requires feeding with H_2S, and in consequence poisoning the product.[54] Low-price transition metals showed an optimal activity/selectivity ratio.

Table 1.2 *Examples of catalysts and supports used in HDO of lignin-derived bio-oils under different conditions.*

Catalyst	**Support**	**Reactor**	**Operating Conditions (P, T) and reactant**	**Major products**	**Reference**
Transition Metal Catalysts					
Fe	SiO2	Fixed bed	1bar, 623- 723K Guaiacol	benzene, toluene	Olcese *et al.* 2012-2013
CoMo	Al_2O_3	Flow reactor	15bar, 573K Anisole	Tol., Benz., phenol, 2-methylphenol	Ryymin *et al.* 2010
NiCu	CeO_2-ZrO_2	Batch	170bar, 593K Guaiacol	cyclohexane, cyclohexanone	Bykova *et al.* 2012
Ga	H-beta zeolite	Packed-bed	1bar, 673-823K 3-methylphenol	BTX	Ausavasukhi *et al.* 2012
Noble Metal Catalysts					
Pt	SiO_2-Al_2O_3	Packed-bed	1.4bar, 573K 4-methylanisole	4-methylphenol, Toluene	Runnebaum *et al.* 2012
Pt-Sn	Inconel	Quartz tube	1bar, 673K Guaiacol	phenol, benzene	Gonzalez-Borja *et al.* 2011
Pd	Carbon, HZSM-5	Batch	50bar, 473K Guaiacol	cycloalkanes	Zhao *et al.* 2012
Metal Sulfide Catalysts					
CoMoWS	SBA-16	Fixed bed	30bar, 583K Anisole	phenol, cresol, xylenol	Loricera *et al.* 2011
CoMoS	Al_2O_3	Batch	50bar, 573K Phenol	benzene	Jongerius *et al.* 2012
NiMoS	γ-Al_2O_3	Batch	28bar, 723K Guaiacol	benzene, toluene	Kallury *et al.* 1985
MoS2	Carbon	Batch	50bar, 573K Guaiacol	phenol, catechol	Ruiz *et al.* 2012

Alumina support, which are highly acidic, lead to a significant formation of coke and to a rapid deactivation of the catalyst. In presence of water, alumina is converted to boehmite, which decreases its activity by 2/3 in less than 60 hours.[66] Small-pores materials such as zeolites are highly affected by coke and rapidly deactivated.[67] Silica and Carbon supports show a lower coke formation, a better selectivity but lower activity towards aromatics than alumina.[49]

Table 1.3 *Comparison of the activity and selectivity of different catalysts and supports used for the HDO of guaiacol.*

Catalyst	**Operating conditions (P, T)**	**Conversion**	**Selectivity**	**Reference**
55 wt.% Ni/SiO_2	170 bar, 320°C	97.5%	Cyclic C_5-C_7 HCs & benzene (93%)	Bykova *et al.* 2011
Ni_2P/SiO_2	1 bar, 300°C	80%	Phenol (30%), benzene (60%), anisole (10%)	Zhao *et al.* 2011
Ru/Al_2O_3	40 bar, 250°C	100%	Cyclohexane (22%), cyclohexanol (35%)	Lee *et al.* 2012
CoMoS	40 bar, 300°C	50%	Benzene (42%)	Bui *et al.* 2011
CoMoS/TiO_2	40 bar, 300°C	100%	Phenol (61%), light compounds (14%), O-free products (18%)	Bui *et al.* 2011
Ni_2P/SiO_2	1 bar, 300°C	99.5%	Benzene (72%), phenol (2%)	Wu *et al.* 2013
Ni_2P/Al_2O_3	1 bar, 300°C	99.6%	Benzene (31%), phenol (14%)	Wu *et al.* 2013
Ni_2P/ZrO_2	1 bar, 300°C	96.5%	Benzene (33%), phenol (26%)	Wu *et al.* 2013

Olcese *et al.*[24,25,51,52] studied the competition between DDO and HYD pathways using non-noble metals. They showed that silica support have higher selectivity towards BTX products than activated carbon, and that Fe/SiO_2 is more selective but less active than Co/SiO_2. The effect of temperature, hydrogen partial pressure and contact time on guaiacol conversion and catalyst deactivation (iron oxidation into Fe_2O_3, coke accumulation, or formation of metallic carbon Fe_5C_2) was also studied. The catalytic mechanism of guaiacol adsorption on surfaces was interpreted by Popov *et al.*,[68] demonstrating also that silica is more stable than alumina or silica-alumina supports.

1.7 Fe@SiO_2 Catalyst

The essential roles of Fe-based catalysts for bio-oils HDO applications was reported in 2016 by Hong *et al.*[69] with perspectives towards performance improvement. As reported by by Olcese *et al.*[24], Fe@SiO_2 catalysts have a good selectivity for guaiacol conversion into benzene and toluene. In their proposed mechanism for guaiacol HDO oxygenated compounds interact with acidic silanols (Si-OH) sites of the silica surface, while H_2 is activated by metallic functions of the catalyst and spills over to adsorbed oxygen atoms, leading to C-O bond cleavage (**Figure 1.9**).[24,68]

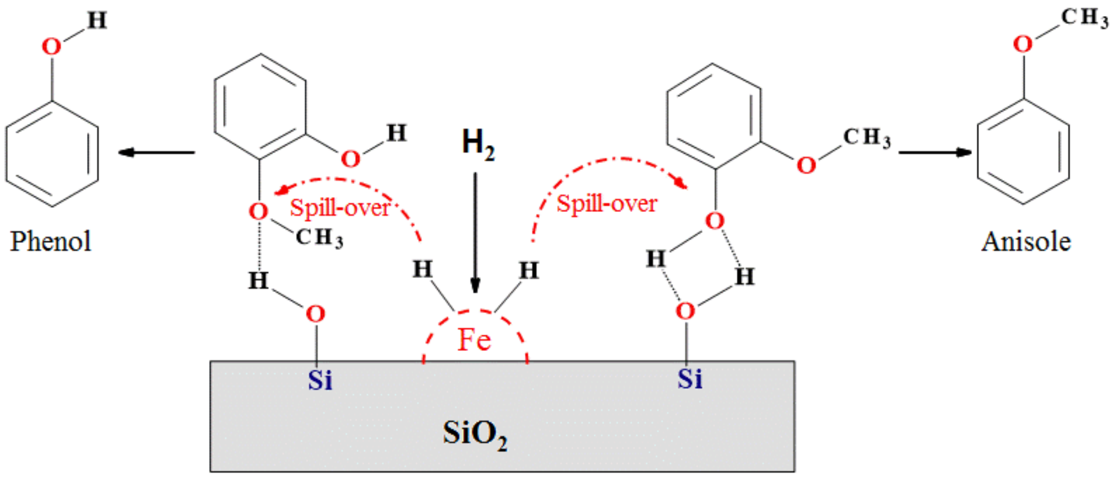

Figure 1.9 Guaiacol HDO spill over mechanism and resulting products.

1.7.a Silica surface support

Because of their large pore size, mesoporous silica such as Santa Barbara Amorphous (SBA) and Mobil Composition of Matter (MCM) allow a high molecular diffusion speed.[70] This characteristic in addition to their high surface area and the presence of acidic silanols active sites make them compelling supports for catalytic applications.[71] Silica-based metallic catalysts showed better performance than alumina-based catalysts because of weaker metal-support interactions and acidity.[72] Due to its acidity, silica support represents a potential candidate for bio-oils HDO with better catalytic stability and lower affinity for carbon formation.[23] The acidity of silica surface depends on the silanol density and on silanol defect types that can donate or accept hydrogen bonds with different strengths.[73–75] Four main groups of silanols defects have been defined and are presented in **Figure 1.10**.[76]

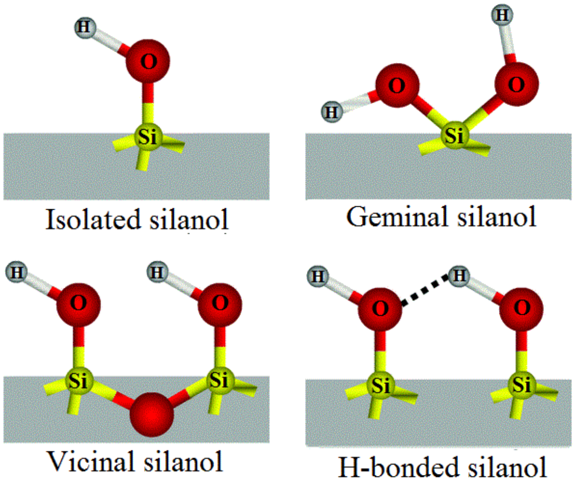

Figure 1.10 Silanols defects of the silica surface.

1.7.b Adsorption mechanisms of oxygenated molecules on silica surface

Popov *et al.*[68] studied the adsorption of phenolic molecules on oxide supports, which is the first step of HDO mechanism. Infrared spectroscopy investigations revealed that phenolic compounds interact mainly with the silica surface via H-bonds with silanols groups. Their study confirms that carbon deposition takes place on alumina support due to the presence of Lewis acid-base pairs on this surface, and that phenates are produced at high HDO operating temperatures. This study therefore suggests that silica support is a potential candidate with high stability.[23] The adsorption of phenol, anisole and guaiacol on silica was studied by following the perturbations of the IR spectra of the Si-OH peak. Corresponding adsorption mechanisms are proposed (see **Figure 1.11**).

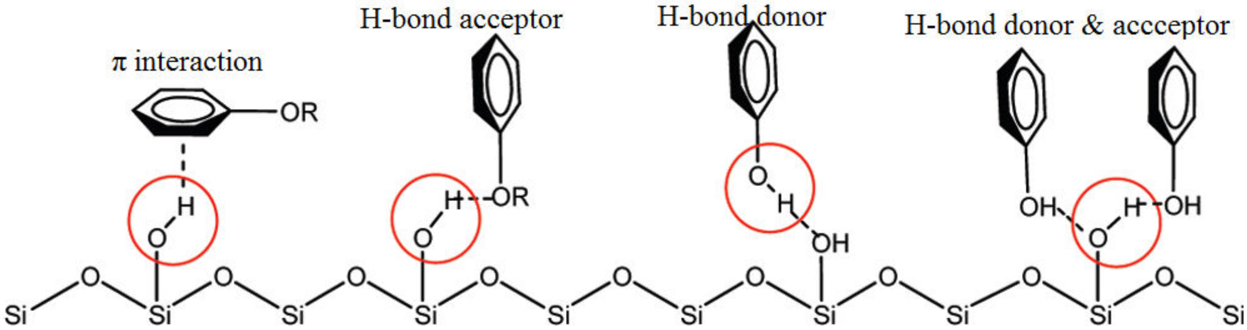

Figure 1.11 *Adsorption modes of phenol and anisole on the silica surface.*

1.7.c Performance of Fe@SiO2 for guaiacol HDO conversion

Olcese *et al.*[24] studied the catalytic HDO conversion of guaiacol in a fixed-bed reactor using Fe@SiO_2 catalyst synthetized by simple impregnation of commercial silica (Aerosil 130, Degussa) in an iron nitrate solution. They have studied the effect of operating conditions such as the reaction temperature, H_2 partial pressure and catalyst contact time, and have compared their results with those obtained using a commercial cobalt-based catalyst. Guaiacol conversion yield without hydrogen was about 30%, while it became about 70% with a H_2 partial pressure of 0.2 bar; however, for a higher H_2 partial pressure (0.2-0.9 bar), HDO conversion remained almost unchanged, and the benzene yield increased slightly. As the reaction temperature increased, guaiacol conversion (activity) and benzene production (selectivity) increased; however, in the same time, the production of undesirable by-products such as CO and CH_4 increased. Different contact times from 0.11 to 1.5 hours were tested, showing that at a contact time of 0.8 hr., guaiacol is totally converted with the highest phenol yield being 60 vol.%, and with the benzene yield being about 14 vol.%. At a contact time of 1.5 hr., 673 K and 90% H_2, the guaiacol HDO conversion on Fe@SiO_2 catalyst achieved a yield of about 74% with a BTX yield of 38%. Comparing these values with those obtained with Co-based catalyst, Fe@SiO_2 catalysts show lower guaiacol HDO conversion but much higher BTX yield (selectivity) and lower coke deposition than Co-based catalysts, making Fe@SiO_2 an attractive inexpensive environmental-friendly catalyst.

The effect of by-products (CH_4, CO, CO_2 and water) was investigated on guaiacol conversion for iron-supported catalysts. These studies showed that water and CO have negative effects, as water inhibits the production of benzene and reduce the overall activity, and CO promotes coke formation due to the carburization of iron particles. While methane has negligible effects, CO_2 has a positive effect as it reduces the catalyst deactivation.[25] Coke deposits were observed near iron particles, which suggests that the reaction occurs at the metal-silica interface. The composition and type of iron species were identified using Mössbauer spectra before and after catalysis. The results showed the existence of residual Fe(III), Fe_2O_3, γ-Fe_5C_2 in addition to α-Fe particles. The comparison of different iron loads (5, 10 and 15%) showed that the guaiacol conversion is proportional to the exposed iron surface, with similar yields of aromatics and phenols. In order to understand the effect of silanol defects, the silica support was replaced with activated carbon. The activity was similar but no benzene or toluene were produced. The hydrotreatment of lignin pyrolysis vapors using Fe@SiO_2 catalyst was reported, and the lignin to BTX process was simulated based on the kinetic model integrated in Aspen Plus as shown in **Figure 1.11**.[51,52]

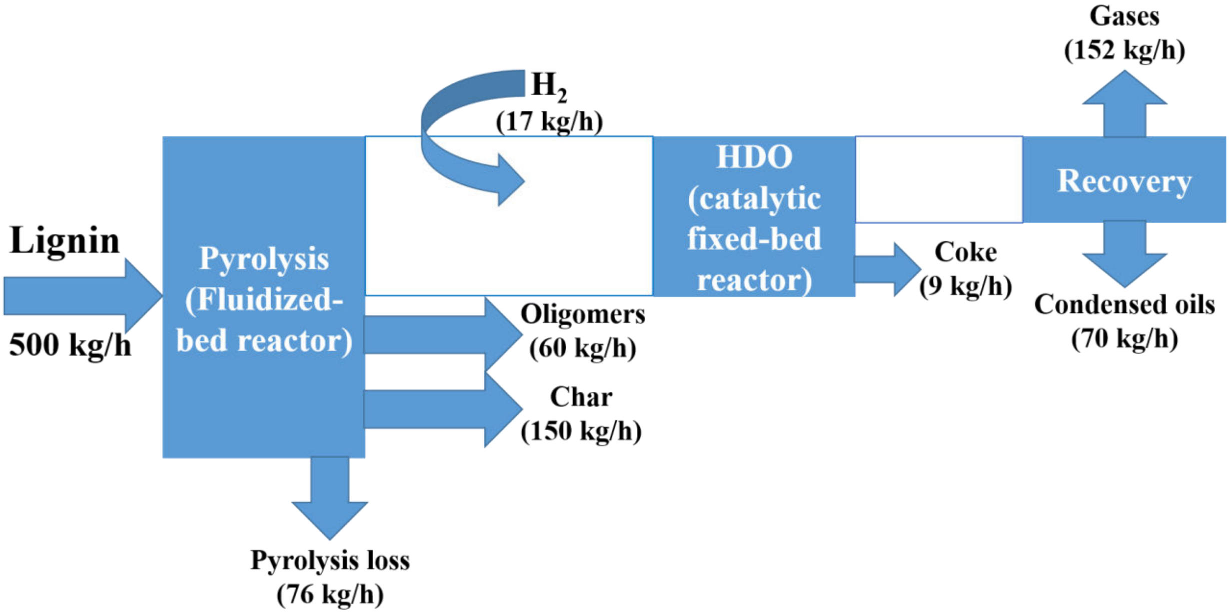

Figure 1.12 *Mass flows from Aspen Plus simulation of the lignin to BTX process. The 70 kg/h of condensed species are composed of 43.9 kg/h of water, 17.8 kg/h of benzene, and 4.3 kg/h of toluene (rest: methanol, cresols, etc).*

1.8 DFT for Chemical Applications

1.8.a DFT for HDO studies

Density functional theory (DFT) has been applied extensively for HDO applications, in order to complement experimental studies and to provide new perspectives in this area.[77–79] The objectives of theoretical studies are to compute and interpret the reaction mechanisms, the effect of inhibitors, and the catalysts adsorption properties.[80–84] The HDO reaction pathways and schemes have been investigated for the interaction of various model molecules with different types of catalyst, for describing the occurrence of the C-O bond cleavage and for identifying the most favorable reaction pathway and mechanism.[79,85–89] The recent investigations of Zhang *et al.*[84] on anisole decomposition using bi-functional acidic metallic catalysts established the role of the metallic function and the Bronsted acid sites of the support. Studies of Mian *et al.*[90–92] on the adsorption of catechol on cristobalite silica surface in the presence of competitive water molecules showed that catechol molecules displaces pre-adsorbed water, and adsorbs preferentially on the catalyst surface. Badawi *et al.*[53,54,93,94] applied DFT methods on HDO reactions in order to elucidate the role of sulfide catalysts. Their studies about furan (as model molecule for bio-oil vapors) adsorption on a stable molybdenum sulfide catalyst under HDO conditions demonstrated that MoS_2 stability depends on the H_2S/H_2O ratio during the reaction. They showed that H_2S must be fed into the reaction in order to prevent the partial oxidation of the sulfur edge. Furan adsorption on the catalyst surface occurs through its oxygen atom (η^1) after creating a vacancy by removing a sulfur atom from the metallic edge.[53] Later, these authors investigated the adsorption of guaiacol, its derivatives (phenol and anisole), and inhibitors (H_2S, H_2O, and CO) on MoS_2 and CoMoS catalysts. They showed that the η^1 adsorption mode promotes the DDO route, and that the adsorption of inhibitors is stronger than the adsorption of oxygenated compounds. Therefore, inhibitors could reduce the catalyst activity.[54] Another DFT/experimental study about the impact of water molecules on sulfide Mo and Co Mo catalysts (Badawi *et al.*, 2011) [94] showed that MoS_2 catalyst is very sensitive to water molecules and is deactivated through the exchange of edge sulfur atoms with oxygen atoms of water. Water poisoning is much lower and reversible on the CoMoS catalyst, as Co atoms prevent sulfur-oxygen exchanges. Hence, Co provides a passivation effect (stabilization of the active phase towards water) in addition to its promotion effect (increase in activity).

1.8.b DFT for adsorption and catalysis on silica models

Various crystalline and amorphous silica models have been suggested, constructed, and relaxed using DFT calculations.[95–99] DFT has been widely used for investigating the catalytic and adsorption properties of silica and silica-based materials.[100–108] Tielens *et al.*[109–112] applied theoretical methods to investigate different aspects and characteristics of amorphous silica-based materials. Their physico-chemical properties are ruled by the presence of silanol groups.[113,114] Prediction of those properties (such as hydrophobicity, or acidity) is challenged by the statistical distribution of silanol groups depending on the local environment and surface concentration.[115–117] The water-silanol interaction was computed on crystalline and amorphous surfaces in order to understand the effect of silanol groups on the adsorption properties of the surface.[118–123]

The interaction of small molecules (as CO_2/CH_4,[124] CO/CO_2/CH_4,[125] argon/nitrogen[126]…) and large molecules (as catechol,[90] 2,2,2-triflueroethanol,[127] aldehydes,[128] organometallic platinum complex,[129] benzothiophene/naphthalene[130]…) with various silica surfaces were also reported.

1.9 Synthesis of Porous Silica Materials

The porosity of a material influences its surface area, and in consequence, its applications for catalysis, storage, and molecule separation. The International Union of Pure and Applied Chemistry (IUPAC) admitted the classification of porous materials proposed by Dubinin in 1960 [131,132] based on the pore size. Mesoporous materials are those having a pore width between 2 and 50 nm.

1.9.a Surfactants and metallosurfactants

Surfactants are amphiphilic molecules, which have at least one hydrophilic and one hydrophobic part. Being divided into two classes, the ionic (cationic, anionic, or zwitterion) and non-ionic surfactants, they are characterized by their surface tension, they segregate on the water-air surface and associate into micelles above a certain concentration, called critical micelles concentration CMC. Above the CMC, surfactants are self-assembled into various micellar structures (spherical, cylindrical, lamellar….) in order to avoid the interaction of their hydrophobic part with water molecules.[133] Non-ionic pluronic copolymers, such as pluronic P123®, consist of two hydrophilic poly(ethylene oxide) blocks separated by one hydrophobic poly(propylene oxide) block. With the cationic surfactant cetrimonium bromide (CTAB), they are the most popular surfactants used as templates for the synthesis of mesoporous materials.[134]

The term metallosurfactant refers to metals-containing surfactants. Several publications describe their elaboration and three-dimensional structure, which can be in the form of micelles, vesicles or aggregates.[135–142] Metallosurfactants have been reported as being templates for the synthesis of mesoporous silicates containing metallic nanoparticles.[143–148]

1.9.b Mesoporous silica materials

During the last decade, many studies focused on the development of mesoporous materials in order to overcome diffusion problems which occur in catalytic applications[149] with zeolites, because of the small pore size of these materials[71]. In 1992, Mobil Research and Development Corporation has produced the M41 mesoporous silica family, which has an organized structure and large surface area (around 1000m^2/g).[150,151] Its synthesis, based on the Sol-Gel process, is performed either through the Liquid Crystal Templating (LCT) mechanism or through the Cooperative Self-Assembling (CSA) Mechanism.[151,152] The materials MCM-41, MCM-48 and MCM-50 (Mobil Crystalline Materials), with hexagonal, cubic *Ia3d* and lamellar structures respectively, are synthesized with using CTAB as template.[153,154] Several years later, the Santa Barbara Amorphous (SBA) mesoporous silica series was discovered by Zhao *et al.*[155,156] at the University of California. In particular, these authors discovered the well-ordered hexagonal SBA-15 silica structure, which has a larger pore size and higher wall thickness than MCM-41. It displays two types of pores, primary mesopores interconnected with intrawall micropores, resulting in a higher mechanical strength and a greater hydrothermal stability.[157]

1.9.c Sol-Gel process

The Sol-Gel process, discovered by Ebelmen[158] in 1846, allows the synthesis of mesoporous materials using inorganic precursors at various temperatures (20-150ºC).[159,160] During the process, alkoxysilane precursors Si(OR)$_4$ such as tetramethyl orthosilicate (TMOS, Si(OCH$_3$)$_4$), first hydrolyze to give silanols (Si-OH) and the corresponding alcohol (R-OH, CH$_3$OH when using TMOS), as described in the following equation:

$$Si(OR)_4 + n\,H_2O \rightarrow Si(OR)_{4-n}(OH)_n + n\,ROH \qquad (1)$$

The second step is the condensation leading to the formation of a siloxane bridge Si-O-Si and the gelification of the system. It occurs either by the condensation of two silanol groups with the production of water (*equation 2*), or by the condensation of a silanol group with a non-hydrolyzed alkoxy group with the production of one alcohol molecule (*equation 3*).[161]

$$Si(OR)_4 + Si(OR)_3(OH) \rightarrow Si(OR)_3Si - O - Si(OR)_3 + H_2O \qquad (2)$$

$$Si(OR)_4 + Si(OR)_4 \rightarrow Si(OR)_3Si - O - Si(OR)_3 + ROH \qquad (3)$$

The silica framework produced is a series of tetrahedral silica SiO_4^{4-}, with the silica atom in the center. These small size clusters constitute a colloidal suspension called Sol. The Gel is formed when clusters bind together to give a three-dimensional interconnected framework. Structural properties of the material depend on the competition between hydrolysis and condensation reactions, and can therefore be adjusted by varying the pH of the solution, the temperature of the reaction, and other parameters.[134,162,163]

1.9.d Corporative Self-Assembly (CSA) mechanism

According to this mechanism, inorganic precursors are self-assembled into micelles, and polymerize around themselves, leading to the organization of the silica framework. First, the polar head of the surfactants interacts with the silica precursor through hydrogen or electrostatic bonding, depending on its nature; this step is called the intramicellar polymerization. Then, the intermicellar condensation occurs, where silica-covered micelles aggregate and produce the hybrid material. Finally, the surfactant is removed in order to obtain the mesoporous silica structure.[134]

For ionic surfactants, electrostatic interactions occur between surfactants and precursors. They can be direct in the case of opposite charges (S^+I^- or S^-I^+), or indirect through involving an intermediate X in the case of same charges ($S^+X^-I^+$ or $S^-X^+I^-$).[164] For non-ionic surfactants, weak hydrogen bonds are present S^0I^0, which can be advantageous for the surfactant removal step.[165] **Table 1.4** presents different mesoporous silica materials, their synthesis conditions and surfactant precursors.

Table 1.4 *Different mesoporous materials depending on the synthesis conditions (pH, surfactant) and the surfactant-precursor interactions.*

Surfactant type	**Interaction**		**Conditions**		**Examples**
			pH	**Surfactant**	
Ionic	Electrostatic direct	S^+I^-	basic	CTAB	MCM-41 (hexagonal) MCM-48 (cubic) MCM-50 (lamellar)
	Electrostatic indirect	$S^+X^-I^+$	acidic	CTAB	SBA-1 (cubic) SBA-2 (hex) SBA-3 (hex)
Non-ionic	Hydrogen bonds	S^0I^0	neutral	primary amine	HMS
		$(S^0H^+)(X^-I^+)$	very acidic	$C_m(EO)_nOH$	SBA-11 (cubic) SBA-12 (hex)
				pluronic	SBA-15 (hex) SBA-16 (cubic)

References

(1) Sawin, J. L.; Renewable Energy Policy Network for the 21st Century e.V. (REN21). *Renewables 2013: Global Status Report*; Paris, **2013**.

(2) Ragauskas, A. J.; Beckham, G. T.; Biddy, M. J.; Chandra, R.; Chen, F.; Davis, M. F.; Davison, B. H.; Dixon, R. A.; Gilna, P.; Keller, M.; Langan, P.; Naskar, A.K.; Saddler, J.N.; Tschaplinski, T.J.; Tuskan, G.A.; Wyman, C.E. Lignin Valorization: Improving Lignin Processing in the Biorefinery. *Science* **2014**, *344* (6185), 1246843–1246843.

(3) Mansouri, N.-E. E.; Salvadó, J. Structural Characterization of Technical Lignins for the Production of Adhesives: Application to Lignosulfonate, Kraft, Soda-Anthraquinone, Organosolv and Ethanol Process Lignins. *Ind. Crops Prod.* **2006**, *24* (1), 8–16.

(4) Johansson, A.; Aaltonen, O.; Ylinen, P. Organosolv Pulping — Methods and Pulp Properties. *Biomass* **1987**, *13* (1), 45–65.

(5) Montane, D.; Tornefernandez, V.; Fierro, V. Activated Carbons from Lignin: Kinetic Modeling of the Pyrolysis of Kraft Lignin Activated with Phosphoric Acid. *Chem. Eng. J.* **2005**, *106* (1), 1–12.

(6) Browning, W. C. Lignosulfonate Stabilized Emulsions in Oil Well Drilling Fluids. *SPE-393-G* **1955**, *7* (06), 9–15.

(7) Yamaguchi, A.; Hiyoshi, N.; Sato, O.; Osada, M.; Shirai, M. Lignin Gasification over Supported Ruthenium Trivalent Salts in Supercritical Water. *Energy Fuels* **2008**, *22* (3), 1485–1492.

(8) Cho, J.; Chu, S.; Dauenhauer, P. J.; Huber, G. W. Kinetics and Reaction Chemistry for Slow Pyrolysis of Enzymatic Hydrolysislignin and Organosolv Extracted Lignin Derived from Maplewood. *Green Chem* **2012**, *14* (2), 428–439.

(9) Kubo, S.; Kadla, J. F. Lignin-Based Carbon Fibers: Effect of Synthetic Polymer Blending on Fiber Properties. *J. Polym. Environ.* **2005**, *13* (2), 97–105.

(10) Silva, E. A. B. da; Zabkova, M.; Araújo, J. D.; Cateto, C. A.; Barreiro, M. F.; Belgacem, M. N.; Rodrigues, A. E. An Integrated Process to Produce Vanillin and Lignin-Based Polyurethanes from Kraft Lignin. *Chem. Eng. Res. Des.* **2009**, *87* (9), 1276–1292.

(11) Hemberger, P.; Custodis, V. B. F.; Bodi, A.; Gerber, T.; van Bokhoven, J. A. Understanding the Mechanism of Catalytic Fast Pyrolysis by Unveiling Reactive Intermediates in Heterogeneous Catalysis. *Nat. Commun.* **2017**, *8*, 15946.

(12) Holladay, JE.; Bozell, JJ.; White, JF.; Johnson, D. *Top Value-Added Chemicals from Biomass*; PACIFIC NORTHWEST NATIONAL LABORATORY operated by BATTELLE for the UNITED STATES DEPARTMENT OF ENERGY, Vol. II: Results of Screening for Potential Candidates from Biorefinery Lignin, **2007**.

(13) Haveren, J. van; Scott, E. L.; Sanders, J. Bulk Chemicals from Biomass. *Biofuels Bioprod. Biorefining* **2008**, *2* (1), 41–57.

(14) Ahuja, K.; Deb, S. *Lignin Market Share - Industry Size, Growth Analysis Report 2017-2024*; GMI181; Global Market Insights, **2018**.

(15) Shabtai, J. S.; Zmierczak, W. W.; Chornet, E.; Johnson, D. Process for Converting Lignins into a High Octane Blending Component. Patent US20030115792, **2003**.

(16) de Wild, P.; Van der Laan, R.; Kloekhorst, A.; Heeres, E. Lignin Valorisation for Chemicals and (Transportation) Fuels via (Catalytic) Pyrolysis and Hydrodeoxygenation. *Environ. Prog. Sustain. Energy* **2009**, *28* (3), 461–469.

(17) Mullen, C. A.; Boateng, A. A. Catalytic Pyrolysis-GC/MS of Lignin from Several Sources. *Fuel Process. Technol.* **2010**, *91* (11), 1446–1458.

(18) Ma, Z.; Troussard, E.; van Bokhoven, J. A. Controlling the Selectivity to Chemicals from Lignin via Catalytic Fast Pyrolysis. *Appl. Catal. Gen.* **2012**, *423–424*, 130–136.

(19) Goheen, D. W. Hydrogenation of Lignin by the Noguchi Process. In *Lignin Structure and Reactions*; Marton, J., Ed.; AMERICAN CHEMICAL SOCIETY: WASHINGTON, D.C., **1966**, 59, 205–225.

(20) Parkhurst, H.; Huibers, D.; Jones, M. Production of Phenol from Lignin in:, Symposium on Alternate Feedstocks for Petrochemicals ACS San Francisco Meeting; Am. Chem. Soc., Div. Pet. Chem., Prepr.: San Francisco, CA, USA, **1980**, 25(3), 657–667.

(21) Shin, E.-J.; Keane, M. A. Gas-Phase Hydrogenation/Hydrogenolysis of Phenol over Supported Nickel Catalysts. *Ind. Eng. Chem. Res.* **2000**, *39* (4), 883–892.

(22) González-Borja, M. Á.; Resasco, D. E. Anisole and Guaiacol Hydrodeoxygenation over Monolithic Pt–Sn Catalysts. *Energy Fuels* **2011**, *25* (9), 4155–4162.

(23) Zhao, H. Y.; Li, D.; Bui, P.; Oyama, S. T. Hydrodeoxygenation of Guaiacol as Model Compound for Pyrolysis Oil on Transition Metal Phosphide Hydroprocessing Catalysts. *Appl. Catal. Gen.* **2011**, *391* (1–2), 305–310.

(24) Olcese, R. N.; Bettahar, M.; Petitjean, D.; Malaman, B.; Giovanella, F.; Dufour, A. Gas-Phase Hydrodeoxygenation of Guaiacol over Fe/SiO_2 Catalyst. *Appl. Catal. B Environ.* **2012**, *115–116*, 63.

(25) Olcese, R.; Bettahar, M. M.; Malaman, B.; Ghanbaja, J.; Tibavizco, L.; Petitjean, D.; Dufour, A. Gas-Phase Hydrodeoxygenation of Guaiacol over Iron-Based Catalysts. Effect of Gases Composition, Iron Load and Supports (Silica and Activated Carbon). *Appl. Catal. B Environ.* **2013**, *129*, 528–538.

(26) Pindoria, R. V.; Megaritis, A.; Herod, A. A.; Kandiyoti, R. A Two-Stage Fixed-Bed Reactor for Direct Hydrotreatment of Volatiles from the Hydropyrolysis of Biomass: Effect of Catalyst Temperature, Pressure and Catalyst Ageing Time on Product Characteristics. *Fuel* **1998**, *77* (15), 1715–1726.

(27) Grange, P.; Laurent, E.; Maggi, R.; Centeno, A.; Delmon, B. Hydrotreatment of Pyrolysis Oils from Biomass: Reactivity of the Various Categories of Oxygenated Compounds and Preliminary Techno-Economical Study. *Catal. Today* **1996**, *29* (1–4), 297–301.

(28) Saiz-Jimenez, C.; De Leeuw, J. W. Lignin Pyrolysis Products: Their Structures and Their Significance as Biomarkers. *Org. Geochem.* **1986**, *10* (4–6), 869–876.

(29) Bridgwater, A. V.; Peacocke, G. V. C. Fast Pyrolysis Processes for Biomass. *Renew. Sustain. Energy Rev.* **2000**, *4* (1), 1–73.

(30) Amen-Chen, C.; Pakdel, H.; Roy, C. Production of Monomeric Phenols by Thermochemical Conversion of Biomass: A Review. *Bioresour. Technol.* **2001**, *79* (3), 277–299.

(31) Kawamoto, H.; Horigoshi, S.; Saka, S. Pyrolysis Reactions of Various Lignin Model Dimers. *J. Wood Sci.* **2007**, *53* (2), 168–174.

(32) Jiang, G.; Nowakowski, D. J.; Bridgwater, A. V. A Systematic Study of the Kinetics of Lignin Pyrolysis. *Thermochim. Acta* **2010**, *498* (1–2), 61–66.

(33) Dickerson, T.; Soria, J. Catalytic Fast Pyrolysis: A Review. *Energies* **2013**, *6* (1), 514–538.

(34) Asadieraghi, M.; Ashri Wan Daud, W. M.; Abbas, H. F. Heterogeneous Catalysts for Advanced Bio-Fuel Production through Catalytic Biomass Pyrolysis Vapor Upgrading: A Review. *RSC Adv* **2015**, *5* (28), 22234–22255.

(35) Faix, O.; Meier, D.; Grobe, I. Studies on Isolated Lignins and Lignins in Woody Materials by Pyrolysis-Gas Chromatography-Mass Spectrometry and off-Line Pyrolysis-Gas Chromatography with Flame Ionization Detection. *J. Anal. Appl. Pyrolysis* **1987**, *11*, 403–416.

(36) Huber, G. W.; Iborra, S.; Corma, A. Synthesis of Transportation Fuels from Biomass: Chemistry, Catalysts, and Engineering. *Chem. Rev.* **2006**, *106* (9), 4044–4098.

(37) Czernik, S.; Bridgwater, A. V. Overview of Applications of Biomass Fast Pyrolysis Oil. *Energy Fuels* **2004**, *18* (2), 590–598.

(38) Wang, D.; Czernik, S.; Montané, D.; Mann, M.; Chornet, E. Biomass to Hydrogen via Fast Pyrolysis and Catalytic Steam Reforming of the Pyrolysis Oil or Its Fractions. *Ind. Eng. Chem. Res.* **1997**, *36* (5), 1507–1518.

(39) Wang, D.; Czernik, S.; Chornet, E. Production of Hydrogen from Biomass by Catalytic Steam Reforming of Fast Pyrolysis Oils. *Energy Fuels* **1998**, *12* (1), 19–24.

(40) Rioche, C.; Kulkarni, S.; Meunier, F. C.; Breen, J. P.; Burch, R. Steam Reforming of Model Compounds and Fast Pyrolysis Bio-Oil on Supported Noble Metal Catalysts. *Appl. Catal. B Environ.* **2005**, *61* (1–2), 130–139.

(41) Adjaye, J. D.; Bakhshi, N. N. Production of Hydrocarbons by Catalytic Upgrading of a Fast Pyrolysis Bio-Oil. Part I: Conversion over Various Catalysts. *Fuel Process. Technol.* **1995**, *45* (3), 161–183.

(42) Vitolo, S.; Seggiani, M.; Frediani, P.; Ambrosini, G.; Politi, L. Catalytic Upgrading of Pyrolytic Oils to Fuel over Different Zeolites. *Fuel* **1999**, *78* (10), 1147–1159.

(43) French, R.; Czernik, S. Catalytic Pyrolysis of Biomass for Biofuels Production. *Fuel Process. Technol.* **2010**, *91* (1), 25–32.

(44) Furimsky, E. Catalytic Hydrodeoxygenation. *Appl Catal A* **2000**, *199(2)*, 147–190.

(45) Elliott, D. C. Historical Developments in Hydroprocessing Bio-Oils. *Energy Fuels* **2007**, *21* (3), 1792.

(46) Choudhary, T. V.; Phillips, C. B. Renewable Fuels via Catalytic Hydrodeoxygenation. *Appl. Catal. Gen.* **2011**, *397* (1–2), 1–12.

(47) Bu, Q.; Lei, H.; Zacher, A. H.; Wang, L.; Ren, S.; Liang, J.; Wei, Y.; Liu, Y.; Tang, J.; Zhang, Q.; Ruan, R. A Review of Catalytic Hydrodeoxygenation of Lignin-Derived Phenols from Biomass Pyrolysis. *Bioresour. Technol.* **2012**, *124*, 470–477.

(48) He, Z.; Wang, X. Hydrodeoxygenation of Model Compounds and Catalytic Systems for Pyrolysis Bio-Oils Upgrading. *Catal. Sustain. Energy* **2012**, *1*.

(49) Saidi, M.; Samimi, F.; Karimipourfard, D.; Nimmanwudipong, T.; Gates, B. C.; Rahimpour, M. R. Upgrading of Lignin-Derived Bio-Oils by Catalytic Hydrodeoxygenation. *Energy Env. Sci* **2014**, *7* (1), 103–129.

(50) Shafaghat, H.; Rezaei, P. S.; Ashri Wan Daud, W. M. Effective Parameters on Selective Catalytic Hydrodeoxygenation of Phenolic Compounds of Pyrolysis Bio-Oil to High-Value Hydrocarbons. *RSC Adv* **2015**, *5* (126), 103999–104042.

(51) Olcese, R. N.; Lardier, G.; Bettahar, M.; Ghanbaja, J.; Fontana, S.; Carré, V.; Aubriet, F.; Petitjean, D.; Dufour, A. Aromatic Chemicals by Iron-Catalyzed Hydrotreatment of Lignin Pyrolysis Vapor. *ChemSusChem* **2013**, *6* (8), 1490–1499.

(52) Olcese, R. N.; Francois, J.; Bettahar, M. M.; Petitjean, D.; Dufour, A. Hydrodeoxygenation of Guaiacol, A Surrogate of Lignin Pyrolysis Vapors, Over Iron Based Catalysts: Kinetics and Modeling of the Lignin to Aromatics Integrated Process. *Energy Fuels* **2013**, *27* (2), 975–984.

(53) Badawi, M.; Cristol, S.; Paul, J.-F.; Payen, E. DFT Study of Furan Adsorption over Stable Molybdenum Sulfide Catalyst under HDO Conditions. *Comptes Rendus Chim.* **2009**, *12* (6–7), 754–761.

(54) Badawi, M.; Paul, J.-F.; Cristol, S.; Payen, E. Guaiacol Derivatives and Inhibiting Species Adsorption over MoS_2 and CoMoS Catalysts under HDO Conditions: A DFT Study. *Catal. Commun.* **2011**, *12* (10), 901–905.

(55) Verma, A. M.; Kishore, N. DFT Study on Gas-Phase Hydrodeoxygenation of Guaiacol by Various Reaction Schemes. *Mol. Simul.* **2017**, *43* (2), 141–153.

(56) Wang, W.; Yang, Y.; Luo, H.; Peng, H.; Wang, F. Effect of La on Ni–W–B Amorphous Catalysts in Hydrodeoxygenation of Phenol. *Ind. Eng. Chem. Res.* **2011**, *50* (19), 10936–10942.

(57) Hong, D.-Y.; Miller, S. J.; Agrawal, P. K.; Jones, C. W. Hydrodeoxygenation and Coupling of Aqueous Phenolics over Bifunctional Zeolite-Supported Metal Catalysts. *Chem Commun* **2010**, *46* (7), 1038.

(58) Yang, Y.; Luo, H.; Tong, G.; Smith, K. J.; Tye, C. T. Hydrodeoxygenation of Phenolic Model Compounds over MoS_2 Catalysts with Different Structures. *Chin. J. Chem. Eng.* **2008**, *16* (5), 733.

(59) Bui, V. N.; Toussaint, G.; Laurenti, D.; Mirodatos, C.; Geantet, C. Co-Processing of Pyrolisis Bio Oils and Gas Oil for New Generation of Bio-Fuels: Hydrodeoxygenation of Guaïacol and SRGO Mixed Feed. *Catal. Today* **2009**, *143* (1–2), 172–178.

(60) Bui, V. N.; Laurenti, D.; Afanasiev, P.; Geantet, C. Hydrodeoxygenation of Guaiacol with CoMo Catalysts. Part I: Promoting Effect of Cobalt on HDO Selectivity and Activity. *Appl. Catal. B Environ.* **2011**, *101* (3–4), 239–245.

(61) Bykova, M. V.; Ermakov, D. Yu.; Kaichev, V. V.; Bulavchenko, O. A.; Saraev, A. A.; Lebedev, M. Yu.; Yakovlev, V. A. Ni-Based Sol–Gel Catalysts as Promising Systems for Crude Bio-Oil Upgrading: Guaiacol Hydrodeoxygenation Study. *Appl. Catal. B Environ.* **2012**, *113–114*, 296–307.

(62) Peters, J. E.; Carpenter, J. R.; Dayton, D. C. Anisole and Guaiacol Hydrodeoxygenation Reaction Pathways over Selected Catalysts. *Energy Fuels* **2015**, *29* (2), 909–916.

(63) Zhu, X.; Lobban, L. L.; Mallinson, R. G.; Resasco, D. E. Bifunctional Transalkylation and Hydrodeoxygenation of Anisole over a Pt/HBeta Catalyst. *J. Catal.* **2011**, *281* (1), 21–29.

(64) Li, K.; Wang, R.; Chen, J. Hydrodeoxygenation of Anisole over Silica-Supported Ni_2P, MoP, and NiMoP Catalysts. *Energy Fuels* **2011**, *25* (3), 854–863.

(65) Jacobson, K.; Maheria, K. C.; Kumar Dalai, A. Bio-Oil Valorization: A Review. *Renew. Sustain. Energy Rev.* **2013**, *23*, 91–106.

(66) Ma, Z.; van Bokhoven, J. Chapter 8. Thermal Conversion of Biomass; Pyrolysis and Hydrotreating. In *Catalysis*; Spivey, J., Han, Y.-F., Dooley, K., Eds.; Royal Society of Chemistry: Cambridge, **2014**, 26, 249–272.

(67) Nimmanwudipong, T.; Runnebaum, R. C.; Block, D. E.; Gates, B. C. Catalytic Conversion of Guaiacol Catalyzed by Platinum Supported on Alumina: Reaction Network Including Hydrodeoxygenation Reactions. *Energy Fuels* **2011**, *25* (8), 3417–3427.

(68) Popov, A.; Kondratieva, E.; Goupil, J. M.; Mariey, L.; Bazin, P.; Gilson, J.-P.; Travert, A.; Maugé, F. Bio-Oils Hydrodeoxygenation: Adsorption of Phenolic Molecules on Oxidic Catalyst Supports. *J. Phys. Chem. C* **2010**, *114* (37), 15661–15670.

(69) Hong, Y.; Hensley, A.; McEwen, J.-S.; Wang, Y. Perspective on Catalytic Hydrodeoxygenation of Biomass Pyrolysis Oils: Essential Roles of Fe-Based Catalysts. *Catal. Lett.* **2016**, *146* (9), 1621–1633.

(70) Duan, J.; Han, J.; Sun, H.; Chen, P.; Lou, H.; Zheng, X. Diesel-like Hydrocarbons Obtained by Direct Hydrodeoxygenation of Sunflower Oil over Pd/Al-SBA-15 Catalysts. *Catal. Commun.* **2012**, *17*, 76.

(71) Corma, A. From Microporous to Mesoporous Molecular Sieve Materials and Their Use in Catalysis. *Chem. Rev.* **1997**, *97* (6), 2373–2420.

(72) Jasik, A.; Wojcieszak, R.; Monteverdi, S.; Ziolek, M.; Bettahar, M. M. Study of Nickel Catalysts Supported on Al_2O_3, SiO_2 or Nb_2O_5 Oxides. *J. Mol. Catal. Chem.* **2005**, *242* (1–2), 81–90.

(73) Sauer, J.; Hill, J.-R. The Acidity of Surface Silanol Groups. A Theoretical Estimate Based on Ab Initio Calculations on a Model Surface. *Chem. Phys. Lett.* **1994**, *218* (4), 333–337.

(74) Sulpizi, M.; Gaigeot, M.-P.; Sprik, M. The Silica–Water Interface: How the Silanols Determine the Surface Acidity and Modulate the Water Properties. *J. Chem. Theory Comput.* **2012**, *8* (3), 1037.

(75) Rosenholm, J. M.; Czuryszkiewicz, T.; Kleitz, F.; Rosenholm, J. B.; Lindén, M. On the Nature of the Brønsted Acidic Groups on Native and Functionalized Mesoporous Siliceous SBA-15 as Studied by Benzylamine Adsorption from Solution. *Langmuir* **2007**, *23* (8), 4315–4323.

(76) Dalstein, L.; Potapova, E.; Tyrode, E. The Elusive Silica/Water Interface: Isolated Silanols under Water as Revealed by Vibrational Sum Frequency Spectroscopy. *Phys. Chem. Chem. Phys.* **2017**, *19* (16), 10343–10349.

(77) Shetty, M.; Buesser, B.; Román-Leshkov, Y.; Green, W. H. Computational Investigation on Hydrodeoxygenation (HDO) of Acetone to Propylene on α-MoO_3 (010) Surface. *J. Phys. Chem. C* **2017**, *121* (33), 17848–17855.

(78) Prasomsri, T.; Nimmanwudipong, T.; Román-Leshkov, Y. Effective Hydrodeoxygenation of Biomass-Derived Oxygenates into Unsaturated Hydrocarbons by MoO_3 Using Low H_2 Pressures. *Energy Environ. Sci.* **2013**, *6* (6), 1732.

(79) Valencia, D.; García-Cruz, I.; Ramírez-Verduzco, L. F.; Aburto, J. Adsorption of Biomass-Derived Products on MoO_3: Hydrogen Bonding Interactions under the Spotlight. *ACS Omega* **2018**, *3* (10), 14165–14172.

(80) Moon, J.-S.; Kim, E.-G.; Lee, Y.-K. Active Sites of Ni_2P/SiO_2 Catalyst for Hydrodeoxygenation of Guaiacol: A Joint XAFS and DFT Study. *J. Catal.* **2014**, *311*, 144–152.

(81) Dupont, C.; Lemeur, R.; Daudin, A.; Raybaud, P. Hydrodeoxygenation Pathways Catalyzed by MoS_2 and NiMoS Active Phases: A DFT Study. *J. Catal.* **2011**, *279* (2), 276–286.

(82) Garcia-Pintos, D.; Voss, J.; Jensen, A. D.; Studt, F. Hydrodeoxygenation of Phenol to Benzene and Cyclohexane on Rh(111) and Rh(211) Surfaces: Insights from Density Functional Theory. *J. Phys. Chem. C* **2016**, *120* (33), 18529–18537.

(83) Chiu, C.; Genest, A.; Borgna, A.; Rösch, N. Hydrodeoxygenation of Guaiacol over Ru(0001): A DFT Study. *ACS Catal.* **2014**, *4* (11), 4178–4188.

(84) Zhang, J.; Fidalgo, B.; Shen, D.; Zhang, X.; Gu, S. Mechanism of Hydrodeoxygenation (HDO) in Anisole Decomposition over Metal Loaded Brønsted Acid Sites: Density Functional Theory (DFT) Study. *Mol. Catal.* **2018**, *454*, 30–37.

(85) Verma, A. M.; Kishore, N. DFT Analyses of Reaction Pathways and Temperature Effects on Various Guaiacol Conversion Reactions in Gas Phase Environment. *ChemistrySelect* **2016**, *1* (19), 6196.

(86) Banerjee, A.; Mushrif, S. H. Reaction Pathways for the Deoxygenation of Biomass-Pyrolysis-Derived Bio-Oil on Ru: A DFT Study Using Furfural as a Model Compound. *ChemCatChem* **2017**, *9* (14), 2828.

(87) Ren, H.; Yu, W.; Salciccioli, M.; Chen, Y.; Huang, Y.; Xiong, K.; Vlachos, D. G.; Chen, J. G. Selective Hydrodeoxygenation of Biomass-Derived Oxygenates to Unsaturated Hydrocarbons Using Molybdenum Carbide Catalysts. *ChemSusChem* **2013**, *6* (5), 798–801.

(88) Xiong, K.; Yu, W.; Vlachos, D. G.; Chen, J. G. Reaction Pathways of Biomass-Derived Oxygenates over Metals and Carbides: From Model Surfaces to Supported Catalysts. *ChemCatChem* **2015**, *7* (9), 1402–1421.

(89) Lin, Z.; Chen, R.; Qu, Z.; Chen, J. G. Hydrodeoxygenation of Biomass-Derived Oxygenates over Metal Carbides: From Model Surfaces to Powder Catalysts. *Green Chem.* **2018**, *20* (12), 2679–2696.

(90) Mian, S. A.; Saha, L. C.; Jang, J.; Wang, L.; Gao, X.; Nagase, S. Density Functional Theory Study of Catechol Adhesion on Silica Surfaces. *J. Phys. Chem. C* **2010**, *114* (48), 20793–20800.

(91) Mian, S. A.; Gao, X.; Nagase, S.; Jang, J. Adsorption of Catechol on a Wet Silica Surface: Density Functional Theory Study. *Theor. Chem. Acc.* **2011**, *130* (2–3), 333–339.

(92) Mian, S. A.; Yang, L.-M.; Saha, L. C.; Ahmed, E.; Ajmal, M.; Ganz, E. A Fundamental Understanding of Catechol and Water Adsorption on a Hydrophilic Silica Surface: Exploring the Underwater Adhesion Mechanism of Mussels on an Atomic Scale. *Langmuir* **2014**, *30* (23), 6906–6914.

(93) Badawi, M.; Paul, J.-F.; Payen, E.; Romero, Y.; Richard, F.; Brunet, S.; Popov, A.; Kondratieva, E.; Gilson, J.-P.; Mariey, L.; Travert, A.; Maugé, F. Hydrodeoxygenation of Phenolic Compounds by Sulfided $(Co)Mo/Al_2O_3$ Catalysts, a Combined Experimental and Theoretical Study. *Oil Gas Sci. Technol. – Rev. D'IFP Energ. Nouv.* **2013**, *68* (5), 829–840.

(94) Badawi, M.; Paul, J. F.; Cristol, S.; Payen, E.; Romero, Y.; Richard, F.; Brunet, S.; Lambert, D.; Portier, X.; Popov, A.; Kondratieva, E.; Goupil, J.M.; El Fallah, J.; Gilson, J.P.; Mariey, L.; Travert, A.; Maugé, F. Effect of Water on the Stability of Mo and CoMo Hydrodeoxygenation Catalysts: A Combined Experimental and DFT Study. *J. Catal.* **2011**, *282* (1), 155–164.

(95) Comas-Vives, A. Amorphous SiO_2 Surface Models: Energetics of the Dehydroxylation Process, Strain, Ab Initio Atomistic Thermodynamics and IR Spectroscopic Signatures. *Phys. Chem. Chem. Phys.* **2016**, *18* (10), 7475–7482.

(96) Rozanska, X.; Delbecq, F.; Sautet, P. Reconstruction and Stability of β-Cristobalite 001, 101, and 111 Surfaces during Dehydroxylation. *Phys. Chem. Chem. Phys.* **2010**, *12* (45), 14930.

(97) Goumans, T. P. M.; Wander, A.; Brown, W. A.; Catlow, C. R. A. Structure and Stability of the (001) α-Quartz Surface. *Phys Chem Chem Phys* **2007**, *9* (17), 2146–2152.

(98) Tielens, F.; Gervais, C.; Lambert, J. F.; Mauri, F.; Costa, D. Ab Initio Study of the Hydroxylated Surface of Amorphous Silica: A Representative Model. *Chem. Mater.* **2008**, *20* (10), 3336–3344.

(99) Iarlori, S.; Ceresoli, D.; Bernasconi, M.; Donadio, D.; Parrinello, M. Dehydroxylation and Silanization of the Surfaces of β-Cristobalite Silica: An Ab Initio Simulation. *J. Phys. Chem. B* **2001**, *105* (33), 8007–8013.

(100) Handzlik, J.; Ogonowski, J. Structure of Isolated Molybdenum(VI) and Molybdenum(IV) Oxide Species on Silica: Periodic and Cluster DFT Studies. *J. Phys. Chem. C* **2012**, *116* (9), 5571–5584.

(101) Abbasi, A.; Nadimi, E.; Plänitz, P.; Radehaus, C. Density Functional Study of the Adsorption of Aspirin on the Hydroxylated (001) α-Quartz Surface. *Surf. Sci.* **2009**, *603* (16), 2502–2506.

(102) Folliet, N.; Gervais, C.; Costa, D.; Laurent, G.; Babonneau, F.; Stievano, L.; Lambert, J.-F.; Tielens, F. A Molecular Picture of the Adsorption of Glycine in Mesoporous Silica through NMR Experiments Combined with DFT-D Calculations. *J. Phys. Chem. C* **2013**, *117* (8), 4104–4114.

(103) Tielens, F.; Folliet, N.; Bondaz, L.; Etemovic, S.; Babonneau, F.; Gervais, C.; Azaïs, T. Molecular Picture of the Adsorption of Ibuprofen and Benzoic Acid on Hydrated Amorphous Silica through DFT-D Calculations Combined with Solid-State NMR Experiments. *J. Phys. Chem. C* **2017**, *121* (32), 17339–17347.

(104) Rozanska, X.; Sautet, P.; Delbecq, F.; Lefebvre, F.; Borshch, S.; Chermette, H.; Basset, J.-M.; Grinenval, E. Polyoxometalate Grafting onto Silica: Stability Diagrams of $H_3PMo_{12}O_{40}$ on {001}, {101}, and {111} β-Cristobalite Surfaces Analyzed by DFT. *Phys. Chem. Chem. Phys.* **2011**, *13* (35), 15955.

(105) Sautet, P.; Delbecq, F. Catalysis and Surface Organometallic Chemistry: A View from Theory and Simulations. *Chem. Rev.* **2010**, *110* (3), 1788–1806.

(106) Kumar, K.; Kumar, A. Adsorptive Separation of Carbon Dioxide from Flue Gas Using Mesoporous MCM-41: A Molecular Simulation Study. *Korean J. Chem. Eng.* **2018**, *35* (2), 535–547.

(107) Shen, J.; Hill, J. M.; Watwe, R. M.; Spiewak, B. E.; Dumesic, J. A. Microcalorimetric, Infrared Spectroscopic, and DFT Studies of Ethylene Adsorption on Pt/SiO_2 and Pt−Sn/SiO_2 Catalysts. *J. Phys. Chem. B* **1999**, *103* (19), 3923–3934.

(108) Jiang, D.; Sumpter, B. G.; Dai, S. Olefin Adsorption on Silica-Supported Silver Salts − A DFT Study. *Langmuir* **2006**, *22* (13), 5716–5722.

(109) Handzlik, J.; Grybos, R.; Tielens, F. Structure of Monomeric Chromium(VI) Oxide Species Supported on Silica: Periodic and Cluster DFT Studies. *J. Phys. Chem. C* **2013**, *117*, 8138–8149.

(110) Guesmi, H.; Tielens, F. Chromium Oxide Species Supported on Silica: A Representative Periodic DFT Model. *J. Phys. Chem. C* **2012**, *116* (1), 994–1001.

(111) Guesmi, H.; Gryboś, R.; Handzlik, J.; Tielens, F. Characterization of Molybdenum Monomeric Oxide Species Supported on Hydroxylated Silica: A DFT Study. *Phys Chem Chem Phys* **2014**, *16* (34), 18253–18260.

(112) Islam, M. M.; Costa, D.; Calatayud, M.; Tielens, F. Characterization of Supported Vanadium Oxide Species on Silica: A Periodic DFT Investigation. *J. Phys. Chem. C* **2009**, *113* (24), 10740–10746.

(113) Sauer, J.; Hobza, P.; Zahradnik, R. Quantum Chemical Investigation of Interaction Sites in Zeolites and Silica. *J. Phys. Chem.* **1980**, *84* (24), 3318–3326.

(114) Somorjai, G. A.; Li, Y. Major Successes of Theory-and-Experiment-Combined Studies in Surface Chemistry and Heterogeneous Catalysis. *Top. Catal.* **2010**, *53* (5–6), 311–325.

(115) Rimola, A.; Fabbiani, M.; Sodupe, M.; Ugliengo, P.; Martra, G. How Does Silica Catalyze the Amide Bond Formation under Dry Conditions? Role of Specific Surface Silanol Pairs. *ACS Catal.* **2018**, *8* (5), 4558–4568.

(116) Tielens, F.; Gierada, M.; Handzlik, J.; Calatayud, M. Characterization of Amorphous Silica Based Catalysts Using DFT Computational Methods. *Catal. Today* **2019**.

(117) Douhal, A.; Anpo, M. *Chemistry of Silica and Zeolite-Based Materials: Synthesis, Characterization and Applications*, 1st edition.; Elsevier: Waltham, MA, **2019**.

(118) Gierada, M.; Petit, I.; Handzlik, J.; Tielens, F. Hydration in Silica Based Mesoporous Materials: A DFT Model. *Phys. Chem. Chem. Phys.* **2016**, *18* (48), 32962–32972.

(119) Pfeiffer-Laplaud, M.; Costa, D.; Tielens, F.; Gaigeot, M.-P.; Sulpizi, M. Bimodal Acidity at the Amorphous Silica/Water Interface. *J. Phys. Chem. C* **2015**, *119* (49), 27354–27362.

(120) Yang, J.; Meng, S.; Xu, L.; Wang, E. G. Water Adsorption on Hydroxylated Silica Surfaces Studied Using the Density Functional Theory. *Phys. Rev. B* **2005**, *71* (3).

(121) Yang, J.; Wang, E. G. Water Adsorption on Hydroxylated α -Quartz (0001) Surfaces: From Monomer to Flat Bilayer. *Phys. Rev. B* **2006**, *73* (3).

(122) Cimas, Á.; Tielens, F.; Sulpizi, M.; Gaigeot, M.-P.; Costa, D. The Amorphous Silica–Liquid Water Interface Studied by *Ab Initio* Molecular Dynamics (AIMD): Local Organization in Global Disorder. *J. Phys. Condens. Matter* **2014**, *26* (24), 244106.

(123) Bandura, A. V.; Kubicki, J. D.; Sofo, J. O. Periodic Density Functional Theory Study of Water Adsorption on the α-Quartz (101) Surface. *J. Phys. Chem. C* **2011**, *115* (13), 5756–5766.

(124) Lourenço, M. A. O.; Siquet, C.; Sardo, M.; Mafra, L.; Pires, J.; Jorge, M.; Pinto, M. L.; Ferreira, P.; Gomes, J. R. B. Interaction of CO_2 and CH_4 with Functionalized Periodic Mesoporous Phenylene–Silica: Periodic DFT Calculations and Gas Adsorption Measurements. *J. Phys. Chem. C* **2016**, *120* (7), 3863–3875.

(125) Martinez, U.; Pacchioni, G. Interaction of CO, CO_2 and CH_4 with Mesoporous Organosilica: Periodic DFT Calculations with Dispersion Corrections. *Microporous Mesoporous Mater.* **2010**, *129* (1–2), 62–67.

(126) Ustinov, E. A.; Do, D. D.; Jaroniec, M. Application of Density Functional Theory to Equilibrium Adsorption of Argon and Nitrogen on Amorphous Silica Surface. *Appl. Surf. Sci.* **2005**, *252* (3), 548.

(127) Natal-Santiago, M. A.; Dumesic, J. A. Microcalorimetric, FTIR, and DFT Studies of the Adsorption of Methanol, Ethanol, and 2,2,2-Trifluoroethanol on Silica. *J. Catal.* **1998**, *175* (2), 252–268.

(128) Natal-Santiago, M. A.; Hill, J. M.; Dumesic, J. A. Studies of the Adsorption of Acetaldehyde, Methyl Acetate, Ethyl Acetate, and Methyl Trifluoroacetate on Silica. *J. Mol. Catal. Chem.* **1999**, *140* (2), 199–214.

(129) Shen, J.; Muthukumar, K.; Jeschke, H. O.; Valentí, R. Physisorption of an Organometallic Platinum Complex on Silica: An *Ab Initio* Study. *New J. Phys.* **2012**, *14* (7), 073040.

(130) Fujiki, J.; Furuya, E. Density Functional Theory Study of Adsorption of Benzothiophene and Naphthalene on Silica Gel. *Fuel* **2016**, *164*, 180–185.

(131) Dubinin, M. M. The Potential Theory of Adsorption of Gases and Vapors for Adsorbents with Energetically Nonuniform Surfaces. *Chem. Rev.* **1960**, *60* (2), 235–241.

(132) Everett, D. H. Manual of Symbols and Terminology for Physicochemical Quantities and Units, Appendix II: Definitions, Terminology and Symbols in Colloid and Surface Chemistry. *Pure Appl. Chem.* **1972**, *31* (4), 577–638.

(133) Hamley, I. W. *Introduction to Soft Matter: Synthetic and Biological Self-Assembling Materials*, Rev. ed.; John Wiley & Sons: Chichester, England ; Hoboken, NJ, **2007**.

(134) Iler, R. K. *The Chemistry of Silica: Solubility, Polymerization, Colloid and Surface Properties, and Biochemistry*; Wiley: New York, **1979**.

(135) Domínguez-Gutiérrez, D.; Surtchev, M.; Eiser, E.; Elsevier, C. J. Ru(II)-Based Metallosurfactant Forming Inverted Aggregates. *Nano Lett.* **2006**, *6* (2), 145–147.

(136) Owen, T.; Butler, A. Metallosurfactants of Bioinorganic Interest: Coordination-Induced Self Assembly. *Coord. Chem. Rev.* **2011**, *255* (7–8), 678–687.

(137) Guerrero-Martínez, A.; Vida, Y.; Domínguez-Gutiérrez, D.; Albuquerque, R. Q.; De Cola, L. Tuning Emission Properties of Iridium and Ruthenium Metallosurfactants in Micellar Systems. *Inorg. Chem.* **2008**, *47* (20), 9131–9133.

(138) Domínguez-Gutiérrez, D.; De Paoli, G.; Guerrero-Martínez, A.; Ginocchietti, G.; Ebeling, D.; Eiser, E.; De Cola, L.; Elsevier, C. J. Inverted Aggregates of Luminescent Ruthenium Metallosurfactants. *J. Mater. Chem.* **2008**, *18* (24), 2762.

(139) Koutsantonis, G. A.; Nealon, G. L.; Buckley, C. E.; Paskevicius, M.; Douce, L.; Harrowfield, J. M.; McDowall, A. W. Wormlike Micelles from a Cage Amine Metallosurfactant. *Langmuir* **2007**, *23* (24), 11986–11990.

(140) Griffiths, P. C.; Fallis, I. A.; Chuenpratoom, T.; Watanesk, R. Metallosurfactants: Interfaces and Micelles. *Adv. Colloid Interface Sci.* **2006**, *122* (1–3), 107–117.

(141) de la Iglesia, P.; Jaeger, V. W.; Xi, Y.; Pfaendtner, J.; Pozzo, L. D. Structure Characterization and Properties of Metal–Surfactant Complexes Dispersed in Organic Solvents. *Langmuir* **2015**, *31* (33), 9006–9016.

(142) Kim, S.; Bellouard, C.; Eastoe, J.; Canilho, N.; Rogers, S. E.; Ihiawakrim, D.; Ersen, O.; Pasc, A. Spin State As a Probe of Vesicle Self-Assembly. *J. Am. Chem. Soc.* **2016**, *138* (8), 2552–2555.

(143) Danks, M. J.; Jervis, H. B.; Nowotny, M.; Zhou, W.; Maschmeyer, T. A.; Bruce, D. W. High-Activity Heterogeneous Catalysts Prepared in One Step from the Mesophases of Metallosurfactants. *Catal. Lett.* **2002**, *82* (1), 95–98.

(144) Lee, H. S.; Kim, W. H.; Lee, J. H.; Choi, D. J.; Jeong, Y.-K.; Chang, J. H. Transition Metal-Chelating Surfactant Micelle Templates for Facile Synthesis of Mesoporous Silica Nanoparticles. *J. Solid State Chem.* **2012**, *185*, 89–94.

(145) Liu, H.; Ma, D.; Blackley, R. A.; Zhou, W.; Bao, X. Highly Active Mesostructured Silica Hosted Silver Catalysts for CO Oxidation Using the One-Pot Synthesis Approach. *Chem. Commun.* **2008**, 23, 2677.

(146) Kim, S.; Bellouard, C.; Pasc, A.; Lamouroux, E.; Blin, J.-L.; Carteret, C.; Fort, Y.; Emo, M.; Durand, P.; Stébé, M.-J. Nanoparticle-Free Magnetic Mesoporous Silica with Magneto-Responsive Surfactants. *J. Mater. Chem. C* **2013**, *1* (42), 6930–6934.

(147) King, N. C.; Blackley, R. A.; Zhou, W.; Bruce, D. W. The Preparation by True Liquid Crystal Templating of Mesoporous Silicates Containing Nanoparticulate Metals. *Chem. Commun.* **2006**, No. 32, 3411.

(148) King, N. C.; Blackley, R. A.; Wears, M. L.; Newman, D. M.; Zhou, W.; Bruce, D. W. The Synthesis of Mesoporous Silicates Containing Bimetallic Nanoparticles and Magnetic Properties of PtCo Nanoparticles in Silica. *Chem. Commun.* **2006**, No. 32, 3414.

(149) Corma, A. Inorganic Solid Acids and Their Use in Acid-Catalyzed Hydrocarbon Reactions. *Chem. Rev.* **1995**, *95* (3), 559–614.

(150) Kresge, C. T.; Leonowicz, M. E.; Roth, W. J.; Vartuli, J. C.; Beck, J. S. Ordered Mesoporous Molecular Sieves Synthesized by a Liquid-Crystal Template Mechanism. *Nature* **1992**, *359* (6397), 710–712.

(151) Beck, J. S.; Vartuli, J. C.; Roth, W. J.; Leonowicz, M. E.; Kresge, C. T.; Schmitt, K. D.; Chu, C. T. W.; Olson, D. H.; Sheppard, E. W.; McCullen, S. B.; Higgins, J.B.; Schlenker, J.L. A New Family of Mesoporous Molecular Sieves Prepared with Liquid Crystal Templates. *J. Am. Chem. Soc.* **1992**, *114* (27), 10834–10843.

(152) Wan, Y.; Zhao. On the Controllable Soft-Templating Approach to Mesoporous Silicates. *Chem. Rev.* **2007**, *107* (7), 2821–2860.

(153) Grün, M.; Unger, K. K.; Matsumoto, A.; Tsutsumi, K. Novel Pathways for the Preparation of Mesoporous MCM-41 Materials: Control of Porosity and Morphology. *Microporous Mesoporous Mater.* **1999**, *27* (2–3), 207–216.

(154) Kosslick, H.; Lischke, G.; Landmesser, H.; Parlitz, B.; Storek, W.; Fricke, R. Acidity and Catalytic Behavior of Substituted MCM-48. *J. Catal.* **1998**, *176* (1), 102–114.

(155) Zhao, D. Triblock Copolymer Syntheses of Mesoporous Silica with Periodic 50 to 300 Angstrom Pores. *Science* **1998**, *279* (5350), 548–552.

(156) Zhao, D.; Huo, Q.; Feng, J.; Chmelka, B. F.; Stucky, G. D. Nonionic Triblock and Star Diblock Copolymer and Oligomeric Surfactant Syntheses of Highly Ordered, Hydrothermally Stable, Mesoporous Silica Structures. *J. Am. Chem. Soc.* **1998**, *120* (24), 6024–6036.

(157) Fulvio, P. F.; Pikus, S.; Jaroniec, M. Tailoring Properties of SBA-15 Materials by Controlling Conditions of Hydrothermal Synthesis. *J. Mater. Chem.* **2005**, *15* (47), 5049.

(158) Ebelmen. Ueber die Erzeugung von durchsichtigem Kiesel und von Hydrophan. *J. Fur Prakt. Chem.* **1846**, *37* (1), 58–59.

(159) Brinker, C. J. Hydrolysis and Condensation of Silicates: Effects on Structure. *J. Non-Cryst. Solids* **1988**, *100* (1–3), 31–50.

(160) Brinker, C. J.; Scherer, G. W. *Sol-Gel Science: The Physics and Chemistry of Sol-Gel Processing*; Academic Press: Boston, **1990**.

(161) Wright, J. D.; Sommerdijk, N. A. J. M. *Sol-Gel Materials: Chemistry and Applications*; Advanced chemistry texts; Gordon and Breach Science Publ: Amsterdam, **2001**.

(162) Ertan, A.; Kodumuri, P.; Talu, O.; Tewari, S. N. Effect of Synthesis Time and Treatment on Porosity of Mesoporous Silica Materials. *Adsorption* **2009**, *15* (1), 81–86.

(163) Rouquerol, J.; Avnir, D.; Fairbridge, C. W.; Everett, D. H.; Haynes, J. M.; Pernicone, N.; Ramsay, J. D. F.; Sing, K. S. W.; Unger, K. K. Recommendations for the Characterization of Porous Solids (Technical Report). *Pure Appl. Chem.* **1994**, *66* (8), 1739–1758.

(164) Huo, Q.; Margolese, D. I.; Ciesla, U.; Demuth, D. G.; Feng, P.; Gier, T. E.; Sieger, P.; Firouzi, A.; Chmelka, B. F. Organization of Organic Molecules with Inorganic Molecular Species into Nanocomposite Biphase Arrays. *Chem. Mater.* **1994**, *6* (8), 1176–1191.

(165) Narayan, R.; Nayak, U.; Raichur, A.; Garg, S. Mesoporous Silica Nanoparticles: A Comprehensive Review on Synthesis and Recent Advances. *Pharmaceutics* **2018**, *10* (3), 118.

Chapter 2

Theoretical and Experimental Methods

Chap. 2 Theoretical and Experimental Methods

Part 1. Density Functional Theory

Computational chemistry uses the theoretical laws of quantum chemistry[1] implemented as algorithms and codes in specific computer programs in order to predict the chemical and physical properties of systems (molecules, solids, atoms, surfaces...). The sought properties are the structure geometry, the interaction energies, multipolar moments, and vibrational frequencies, etc. The most represented area of the discipline is the processing of electronic configurations of systems. Numerical chemistry describes both the upstream (prediction and prospecting) and the downstream (explanation) sides of the experiment. The first calculation in chemistry were produced by Heitler and London in 1927.[2]

2.1.1 Before Density Functional Theory

The goal of all researchs concerning quantum chemistry is to determine the ground-state energy, which present the most stable state of the system. Therefore, to predict this energy, all studies focus on the resolution of the **Schrödinger equation**[3] showed in the equation *(1)*.

$$H\psi(r_1, r_2, \dots, r_N, R_1, R_2, \dots, R_M) = E\psi(r_1, r_2, \dots, r_N, R_1, R_2, \dots, R_M) \qquad (1)$$

Where ψ is the wave function, E is the total energy, H is the Hamiltonian describing both the kinetic and the potential energies, N is the number of electrons, and M is the number of nucleus (the spin is neglected in all equations for simplicity).

Born-Oppenheimer[4] assume that the electrons move in a field around fixed nucleus, taking into account the heavy mass of nucleus compared to electrons (1800 times). This permit to decompose the wave function of the system, therefore reducing the number of variables (4N + 3M) on which depend Schrödinger equation, and leading to the equation *(2)*.

$$H\psi(r_1, r_2, \dots, r_N) = E\psi(r_1, r_2, \dots, r_N) \qquad (2)$$

Where H is the sum of electrons kinetic energies (T_e), electron-nucleus attraction energies ($V_{N\text{-}e}$), and repulsion energies of electrons ($V_{e\text{-}e}$).

Despite this approximation, the exact resolution of the Schrödinger equation remains difficult for large systems, where it is necessary to solve 3N-interconnected equations. Different methods are developed, we distinguish two main families:

- The first aims to obtain an approximated solution of the wave function ψ, which depends on each electron coordinates. The most common method is the Hartree-Fock method.[5]
- The second approach is the Density Functional Theory (DFT),[6] based on the density of electrons (dependent only on three variables) instead of the wave function (3N variables).

The ground state variational principle states that the calculated energy for an assumed wave function ψ is a superior limit for the ground-state energy E_0.[7]

$$E_0 = \min(E[\psi]) = \min(<\psi(T + V_{N-e} + V_{e-e})\psi >) \qquad (3)$$

In Hartree approximation, the probability of the existence of each electron is independent from others, so two electrons can occupy the same position. However, electrons are fermions characterized by their spin. Therefore, an energy called exchange energy (E_X) is added to take into account that two electrons with same spin cannot get close from each other indefinitely. This energy is taken into consideration in the Pauli exclusion condition stating that the wave function must be antisymmetric, which is obtained by replacing the wave functions by a Slater determinant.[8,9] This method approximates the wave function as a product of non-interacted orbitals (Hartree product,[10,11] *equ. (4)*). The Hartree-Fock method enable the resolution of Schrödinger's equation in a self-coherent process to obtain the system with the lowest energy, by expressing the wave function as a Slater determinant,[12,13] and then minimize the energy by using orthonormal orbitals (Fock complement,[14] *equ. (5)*).

$$\psi\,(r_1, r_2, \dots, r_N) = \psi(r_1)\psi(r_2)\dots\psi(r_N) \qquad (4)$$

$$E_{HF} = \min\,(E[\psi_{HF}]) \quad where\ \psi_{HF} = \psi_0 = \psi_{ground\ state} \qquad (5)$$

However, only the exchange energy is properly described by this method, contrary to the correlation energy (E_C) that explains the overestimation of the energy ($E_{HF} > E_{exact}$). The Fock complement undertake the exchange hole concerning electrons with the same spin, but it does not correct the correlation hole described by electrons with opposite spins.[15]

$$E_{exact} = E_{HF} + E_C \qquad (6)$$

2.1.2 Early DFT Approximations

Density Functional Theory provides a compensation between the accuracy and the cost of the calculation, it transforms the 3N dimension problem (related to the wave function ψ) to a three-dimensional problem (related to the electron density ρ).[16–19] The critical key in DFT is defining the density of electrons as the probability of finding one of the N electrons in an elementary volume dr, as expressed below.

$$\rho(r) = \int[\psi^2(r)]dr = \sum_i \psi_i(r)^* \psi_i(r) \tag{7}$$

Where $N = \int \rho(r)dr$

The Thomas-Fermi model expresses the uniform electron gas energy as a function of its density. It consist of dividing the system into an infinite number of elementary volumes d^3r, where electrons are characterized by a uniform distribution of positive charge called Jellium. However, it does not take into consideration the exchange and correlation energies.[20,21]

$$T\big(\rho(r)\big) = {}^{3}/_{10} \int K_F(r)\rho(r)dr = A_S \int \rho^{5/3}(r)dr \tag{8}$$

Where $A_S = 2.871$ and $K_F = \left(3\pi^2\rho(r)\right)^{1/3}$ is the Fermi wave vector

While the Slater-Dirac model gives a simple definition of the exchange energy. However, it does not take into consideration the correlation energy.[22]

$$E_X[\rho(r)] = \int \epsilon_X[\rho(r)]\rho(r)dr = \left({}^{-9\alpha}/_{8}\right)\left({}^{3}/_{\pi}\right)^{1/3} \int \rho^{4/3}(r)dr \tag{9}$$

Where α=1 for Slater deviation, and α=2/3 for Dirac deviation.

2.1.3 Hohenberg-Kohn Theorem

2.1.3.a First theorem

The first theorem of Hohenberg-Kohn[23] states that the electron density only determines the Hamiltonian operator, and thus all the properties of the system. Therefore, the energy of the ground state is a function only dependent on electron density, as followed.

$$E = E[\rho(r)] = E_{N-e}[\rho] + T[\rho] + E_{e-e}[\rho] = \int \rho(r)V_{ext}(r)dr + F_{HK}[\rho(r)] \tag{10}$$

Where:

- $V_{ext}(r)$ is a unique functional of ρ(r).
- F_{HK} [ρ(r)] is a universal functional valid for any electron number and any external potential. It is the sum of kinetic (T [ρ(r)]) and the electron-electron interaction (E_{e-e} [ρ(r)]) energies.

The electron-electron interaction energy can be decomposed as the Coulomb energy J [ρ(r)] and the unconventional contribution E_{ncl} [ρ(r)] (describing the exchange, self-interacting correlation and Coulomb correlation).

$$E_{e-e}[\rho(r)] = J[\rho] + E_{ncl}[\rho] = {}^{1}/_{2} \iint [{}^{\rho(r_1)\rho(r_2)}/_{r_{12}}]dr_1dr_2 + E_{ncl}[\rho(r)] \tag{11}$$

2.1.3.b Second theorem

It states that for any ρ(r) associated with an external potential V_{ext} [ρ(r)], E [ρ(r)] is an upper limit of E_0. Therefore, the electron density that minimizes the total energy of the system is the electron density corresponding to the ground state.

$$E_0[\rho_0(r)] = \min\left(\int \rho(r)V_{ext}(r)dr + F_{HK}[\rho(r)]\right) \qquad (12)$$

2.1.4 Kohn-Sham Equations

The main remaining problematic for solving the system is the prediction of the kinetic energy T [ρ(r)] and the unconventional contribution E_{ncl} [ρ(r)]. Kohn-Sham[24] propose to solve a fictitious system of wave functions of a single non-interacting electron depending only on three spatial variables. This system is described by the following function.[24–26]

$$F_{HK}\,[\rho(r)] = T_S\,[\rho(r)] + J[\rho(r)] + E_{XC}\,[\rho(r)] \qquad (13)$$

Where T_S [ρ(r)] is the kinetic energy of the single electron non-interacting system and E_{XC} [ρ(r)] is the exchange-correlation energy.

$$T_S[\rho(r)] = \sum \psi_i^{\,*}(r)\frac{-h^2}{2m_e}\psi_i(r) \qquad (14)$$

$$E_{XC}[\rho] = (T[\rho] - T_S[\rho]) + (E_{e-e}[\rho] - J[\rho]) \qquad (15)$$

Applying the variational principle, the Schrodinger equation and the total ground state Kohn-Sham energy can be reformulated as follow.

$$H_{KS}\psi_i(\vec{r}) = \varepsilon_i\psi_i(\vec{r}) \qquad (16)$$

$$\left[{-h^2}/{2m_e}\,\nabla_i^{\,2} - V_{eff}\big(\rho(\vec{r})\big)\right]\psi_i(\vec{r}) = \varepsilon_i\psi_i(\vec{r}) \qquad (17)$$

Where $V_{eff}(\vec{r}) = V_{ext}(\vec{r}) + {\partial E_H(\rho(\vec{r}))}/{\partial\rho(\vec{r})} + {\partial E_{XC}(\rho(\vec{r}))}/{\partial\rho(\vec{r})}$ (18)

and $E_{KS}\,[\rho(r)] = T_S[\rho(r)] + \int(V_{ext} + V_H)\rho(r)dr + E_{XC}[\rho(r)]$ (19)

The resolution of this new system of equations implies finding new approximations for the determination of the exchange-correlation energy. Thereby, different functionals have been developed in order to obtain an expression of this term.[27]

2.1.5 Exchange-Correlation Functionals

Different approximations describing the exchange-correlation functional are developed in order to perform more accurate calculations.[28–30] They are divided according to Jacob ladder into five categories, however choosing the appropriate approximation is depending on the system studied, the properties researched, and the time-cost of the calculation (**Table 2.1.1**).

Table 2.1.1 *Jacob ladder presenting different examples of various exchange-correlation functionals.*

<table>
<tr><th colspan="3">Jacob ladder - Accuracy</th></tr>
<tr><th>Scale</th><th>Method</th><th>Example</th></tr>
<tr><td>Fifth Scale</td><td>Totally non-local</td><td>-</td></tr>
<tr><td rowspan="2">Fourth Scale</td><td>Hybrid Meta GGA</td><td>M06 suite[31]</td></tr>
<tr><td>Hybrid GGA</td><td>B3LYP[32,33], TPSSh[34]</td></tr>
<tr><td>Third Scale</td><td>Meta GGA</td><td>TPSS[35]</td></tr>
<tr><td>Second Scale</td><td>GGA</td><td>PW91[36], BLYP[37,38], PBE[39]</td></tr>
<tr><td>First Scale</td><td>LDA</td><td>VWN[40]</td></tr>
<tr><td colspan="3">Ground</td></tr>
</table>

2.1.5.a Local density approximation (LDA)

This approximation develops the idea of a "uniform electron gas" system where the electrons move such that the total set is neutral, which means that it does not take the electron density variation into consideration.[25]

$$E_{XC}^{LDA}[\rho(r)] = \int \epsilon_{XC}[\rho(r)]\rho(r)dr \quad where \ \epsilon_{XC}[\rho(r)] = \epsilon_X[\rho(r)] + \epsilon_C[\rho(r)] \qquad (20)$$

The exchange part $\epsilon_X[\rho(r)]$ can be determined using the Slater-Dirac model, while the correlation part $\epsilon_C[\rho(r)]$ is deduced by the Monte Carlo simulations according to the effective radius $r_s(r)$.

The LDA can be easily expanded to the Local Spin Density Approximation LSDA for magnetic spin-polarized systems by simply considering the spin-polarized electron density instead of the electron density ρ[r].

$$E_{XC}^{LSDA}[\rho(r)] = \int [\rho_{\uparrow}(r) + \rho_{\downarrow}(r)]\epsilon_{XC}[\rho_{\uparrow}(r), \rho_{\downarrow}(r)]dr \qquad (21)$$

2.1.5.b Generalized gradient approximation (GGA)

For systems with large fluctuations in density, the gradient of the density makes it possible to correct the local approach. It takes into consideration the non-homogeneity of the electron density $\nabla\boldsymbol{\rho}(r)$. The GGA approximation shows significant improvements comparing to the LDA, especially in the estimation of the total energy, atomization energies, and energy barriers.[28] The exchange-correlation energy is therefore expressed as function of both the density of electrons and its gradient.

$$E_{XC}[\rho(r)] = fct\ (\rho(r), \nabla\boldsymbol{\rho}(r)) \qquad (22)$$

2.1.5.c Meta-GGA and hybrid functionals

Meta-GGA functional are dependent on the density, its gradient and Laplacian. The exchange-correlation energy E_{XC} depends on the electron density kinetic τ. These functional predict more accurately than the previous GGA methods some properties such as the atomizing energy.[41]
More recently, new functional hybrids have been used to better describe the exchange contributions. They are based on a combination of a certain percentage (determined empirically) of the exact exchange offered by the Hartree-Fock method, with the GGA exchange-correlation functional. This variant describe better the electronic structures of molecules. The functional Hybrid-Meta GGA (HM-GGA) are currently the subject of many developments, they involve the Hartree-Fock exchange, the electron density, its gradient, and Laplacian.

2.1.6 Applying DFT for Periodic Systems

The resolution of the Schrödinger equation for a crystal implies, in the Kohn-Sham method, the determination of an infinity number of mono-electronic wave functions; such a calculation is impossible. The plane wave expansion of KS wave functions is thus useful, since it takes the advantage of the crystal periodicity.

In the real space, the structure is characterized by a density function that determines how much matter exist at a given point. While in the reciprocal space, the structure is defined in a function F(k) that tell us what components of wave $e^{i\vec{k}\vec{r}}$ of periodicity k are required to produce the same arrangement of atoms. Therefore, using Bloch theorem,[42] each electron wave function $\psi_{i,k}(\vec{r})$ is written as the product of a plane wave $e^{i\vec{k}\vec{r}}$ of vector $\vec{k}$ (in the first Brillouin zone BZ) and a periodic function f having the same periodicity as the crystal.

$$\psi_{i,k}(\vec{r}) = \mathrm{f} * e^{i\vec{k}\vec{r}} = \sum_{\vec{G}} c_{i,\vec{k},\vec{G}} * \ e^{i(\vec{k}+\vec{G})\vec{r}} \qquad (23)$$

Where $\vec{G}$ are reciprocal lattice vectors and $c_{i,\vec{k},\vec{G}}$ are coefficients for a chosen basis set.

The problem then returns to calculating a finite number of wave functions for an infinite number of $\vec{k}$. However, applying Bloch theorem, the calculation can be solved in a finite number of points

$\vec{k}$ represented by the first Brillouin zone. Thus, the convergence of the energy must be verified for the chosen $\vec{k}$ points. On the other hand, it appears that the coefficients $c_{i,\vec{k},\vec{G}}$ associated with the plane waves of great kinetic energy are markedly lower than those associated with plane waves of lower kinetic energy. This justifies the introduction of a cut in the base to a certain energy called cut-off energy $E_{cut-off}$. In practice, it is also important to test the convergence of the system energy with the cut-off energy.[43]

The properties of solids generally depend much more on valence electrons than on those of the heart. It thus seems more judicious to represent the electrons of the heart by an effective potential called pseudo-potential, instead of explicitly dealing with them. The notion of pseudo-potential makes it possible to modify the potential near the cores, so as to be affected by the core electrons while retaining the influence (by screen effect) of valence electrons.[44] For periodic calculations, the pseudo-potentials US-PP method[45] and the Projected Augmented Wave (PAW) approach developed by Blöchl[46] are commonly used. PAW method consists in linking by a linear transformation the function of all electrons (electrons of valence + core) to a pseudo-function of valence.[47] This method has yielded a good accuracy to calculation time ratio for various systems.

Kohn-Sham equations are solved using a coherent automated process (SCF for Self-Consistent Field) using the electronic minimization algorithm RMM-DIIS (Residual Minimization Scheme) until the energy difference between each SCF cycle reach a chosen convergence criteria, as showed in **Figure 2.1.1**.[48] The forces acting on the different atoms are calculated according to this equation.

$$F_i = -\partial E(r_1 \ldots . r_n)/\partial r_i \tag{24}$$

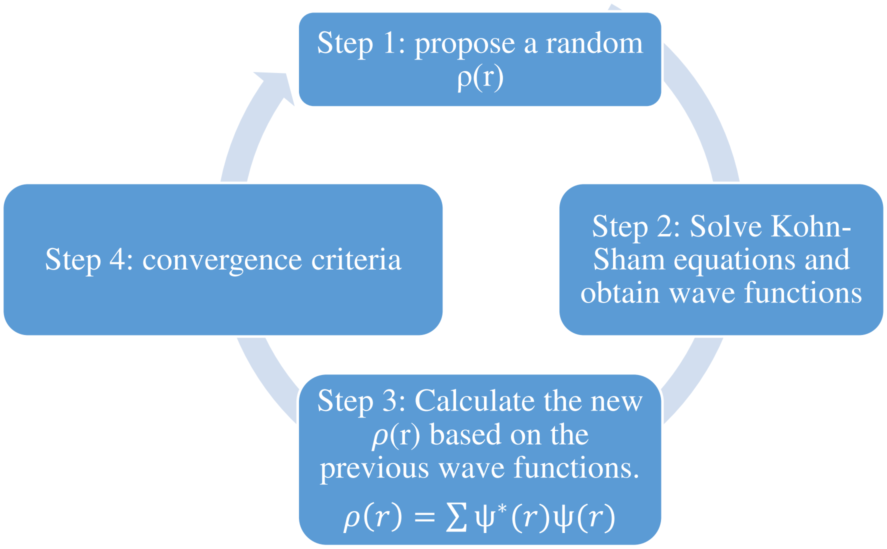

Figure 2.1.1 *Self-Consistent Field SCF calculations used to solve the DFT KS equations.*

The Hellman-Feynman theorem[49] states that the electron density can be maintained constant when the forces applying to the different nuclei are evaluated. This property allow us to calculate the forces acting on the ions. Once determined, the atoms are then relaxed to obtain a new geometry and the Kohn-Sham equations are again resolved. This pattern is repeated until the corresponding geometry is obtained to a minimum energy. Different configurations studied is usually optimized until the forces exerted on each atom are less than 0.03 eV / Å.

2.1.7 Dispersion Correction Methods

Van der Waals vdW interactions affect importantly the physical and chemical properties of most studied systems. However, the local and semi-local DFT approximations fail to describe those non-local forces. Therefore, new dispersion-correction methods have been developed in order to fulfill the gap. One approach considers using specific non-local correlation functionals but is very costly,[50–52] and the second approach incorporate additive correction schemes to the existing functionals. Following this approach, we used D2 method developed by Grimme et *al.*[53–55]

Part 2. Silica-Supported Catalysts

Supported catalysts have been used extensively for heterogeneous catalysis reactions; Munnik[56] reviewed the development in their synthesis methods. Due to its distinct structure, it was claimed that SBA-15 would provide a good catalyst support. While mesopores act as channels for the reactants and products diffusion, micropores in the wall act as active sites for reactions.[57] The SBA-15 silica surface can be easily functionalized, enabling their use as catalyst supports in various applications.[58,59] In this context, the synthesis and functionalization of SBA-15 have been reported for catalytic applications as hydrodesulphurization,[60] esterification,[61] oxidation,[62,63] hydrogenation,[64] C-C coupling,[65] hydrodeoxygenation reactions,[66,67] catalytic reforming,[68] biorefinery production,[69] and biodiesel production.[66,70] Recently, various studies reviewed the use of metals and metal oxides for heterogeneous catalysis applications.[71–75] The deposition of metals and metal oxides on mesoporous silica support, in addition to the metal-silica interactions and the effect of the silica structural properties have been discussed, in order to improve their catalytic performance.[76–83] SBA-15-supported metallic materials have been synthesized using various methods and tested as catalysts.[84–91]

2.2.1 Synthesis of SBA-15 Silica Material

The silica material SBA-15 is prepared by hydrothermal sol-gel synthesis following the soft templating strategy corporative self-assembly (CSA) mechanism using the non-ionic pluronic® P123 as directing agent (template).[92] The P123 is a polyethylene (PEO)/polypropylene (PPO) block copolymer, PEO-PPO-PEO, where the PEO blocks are hydrophilic and PPO blocks are hydrophobic. Thus, the PEO-PPO-PEO surfactant self-assembles spontaneously in spherical micelles above its critical micellar concentration (CMC). During the cooperative formation mechanism of the hybrid sol-gel, the silica precursors condensation occurs driving the self-assembly of the micelles into micellar cylinders hexagonally packed which is like a liquid crystal phase. The silica precursor polymerization takes place around those micelles. A mesoporous silica material with a hexagonally packed pore channels is obtained by removing the P123 template. Some microporosity is also generated by PEO segments.[93,94] The **Figure 2.2.1** is a summary of the most common procedure and conditions used to synthesize a SBA-15 material.[95–99]

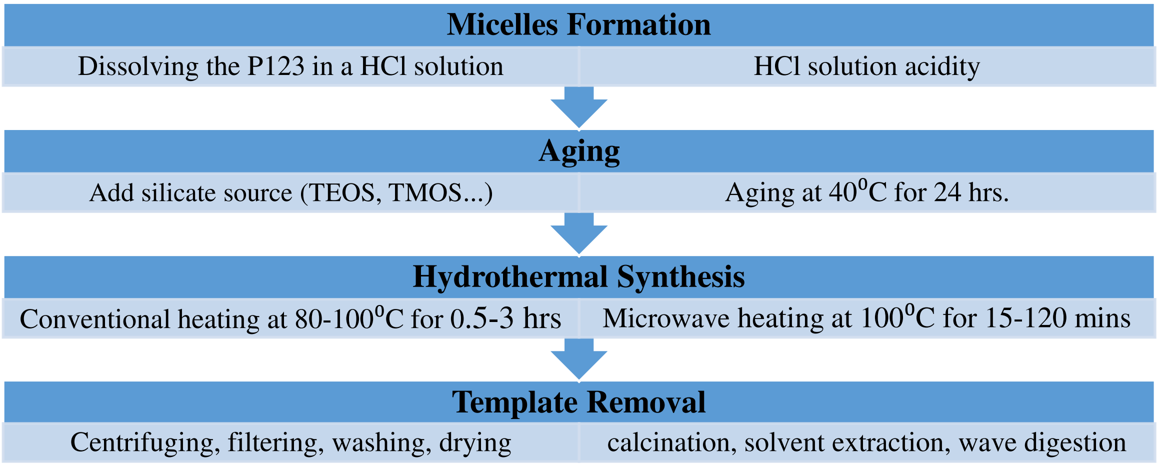

Figure 2.2.1 *Synthesis procedure of SBA-15 silica under various conditions.*

2.2.2 Synthesis of Supported Metal Catalysts

2.2.2.a Chemical impregnation

This traditional method consists on wetting a post-synthesized solid support in a solution containing the metal precursor. Firstly, the metal salt precursor is dissolved in the minimum amount of solvent, and then the salt solution is kneaded with the silica support forming a thick paste. The solvent is removed using a rotary evaporator and the solid is dried, calcined and reduced giving the catalyst.[100] The synthesis of magnetic Fe-SBA-15 mesoporous silica molecular sieves using this method have been investigated by Huang *et al.*[101] in 2010.

2.2.2.b Co-precipitation

This method consist on the precipitation of the metal precursor during the synthesis of the silica support enabling the deposition of metal nanoparticles on the mesoporous silica structure.[100,102] Following this method, Liu *et al.*[103] proved that silver nanoparticles (of 3.5 nm) are relatively well dispersed on the silica surface, which improve their catalytic performance, compared to larger nanoparticles (15-18 nm) unevenly dispersed prepared by the impregnation method. A highly ordered Fe-SBA-15 mesoporous material have been elaborated via the direct hydrothermal synthesis following the co-precipitation method by Li *et al.*[104]

2.2.2.c Deposition-precipitation

Haruta *et al.*[105] reported a method that involves the adjustment of the pH of the dissolved metal precursor, in order to reach complete deposition of the metal hydroxide on the support surface. The metal hydroxide is then calcined and reduced to give the metal nanoparticles.[106] This method suffers from particles agglomeration, which lead to the formation of a wide size range of non-dispersed nanoparticles.[107] Recently, Shi *et al.*[108] applied this method using urea as solvent to adjust the pH over the heating, in order to synthetize bimetallic Fe-Ni nanoparticle catalysts supported on silica surface.

2.2.2.d Microemulsions

The solid support is impregnated with a microemulsion containing a dissolved metal salt precursor in the water phase. This strategy enables to obtain a more controllable distribution of metal nanoparticles due to the restricted location of a limited amount of metal ions that interact with the support in the aqueous phase.[109,110]

2.2.2.e Other methods

Researchers reported other chemical methods for the synthesis of supported metal nanoparticle catalysts as the photochemical deposition, the chemical vapor deposition, the electrochemical deposition, and the ion-exchange reduction that involves the adsorption of metal ions on the support surface followed by the reduction of those ions into metal nanoparticles. In addition to those methods, various physical and physicochemical routes have been investigated as the sonochemical deposition via ultrasonic radiation, microwave irradiation deposition, the vaporization and deposition via pulsed laser ablation, the plasma deposition, the sonoelectrochemical deposition that combines the use of ultrasound waves and electrochemistry, and the flame spray pyrolysis.[102]

2.2.3 Synthesis of Single Atom Catalysts (SACs) using Metallosurfactants Templates

2.2.3.a Reminders on SACs

The modern synthesis methods of single atom catalysts opened the frontiers for designing new catalysts with higher activities, selectivities, and stabilities.[111] Isolated single metal atom catalysts anchored on supports maximize the usage efficiency of metal atoms as catalytic active sites.[112] Different methods have been reported for the synthesis of SACs such as the wet impregnation method for the synthesis of FeO_x-supported platinum catalysts for CO oxidation reaction,[113] the atomic layer deposition for the synthesis of graphene-supported platinum catalysts for methanol oxidation reaction,[114] the photochemical impregnation method for the synthesis of TiO_2-supported palladium catalysts for the hydrogenation of benzaldehyde,[115] the high temperature atom trapping method for the synthesis of Nb/graphene for the cathodic oxygen reduction reaction,[116] and the modular synthetic approach for the synthesis of Co/MOF for the photocatalytic CO_2 reduction.[117] **Figure 2.2.2** presents the catalyst activity with respect to metal size showing that as the metal size decreases, the highest activity is therefore obtained for supported metallic single atoms.[118]

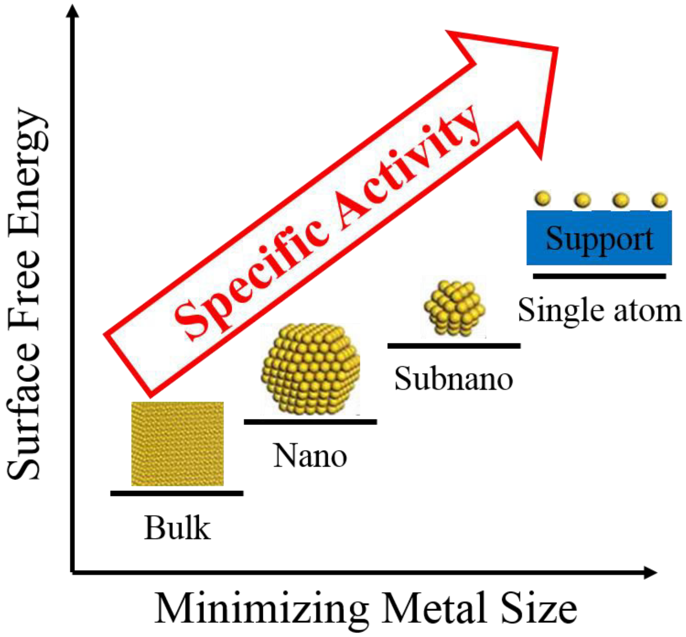

Figure 2.2.2 *The catalyst activity with respect to the size of metal particles.*

2.2.3.b SACs using metallosurfactant templates

Few researches treated the synthesis of metallic silica-supported catalysts using metallosurfactants as templates for the structuration of the silica framework.[119–121] Using this method, studies proved the ability to obtain uniformly sized well-dispersed metal nanoparticles on silica support providing a better activity than those prepared using conventional impregnation methods.[103,120,121] King *et al.*[120,121] prepared mesoporous silicates containing metallic and bimetallic nanoparticles (Fe, Co, Cr, PtCo) having magnetic properties. They prepared the catalyst by the sol-gel synthesis through the liquid crystal templating using the $C_{12}EO_8$ surfactant as templates. Following this synthesis strategy too, Liu *et al.*[103] elaborated a mesoporous silica with isolated silver nanoparticles anchored in the framework. This catalyst gave 100% conversion for CO oxidation reaction, which is higher than that obtained using noble metal catalysts. The average size of silver nanoparticles is around 4 nm, four times smaller than that obtained for catalysts synthesized by the simple impregnation method (17 nm), which gives a better catalytic performance. However, none of the previous studies was able to obtain catalysts having isolated metal atoms following the templating method.

Part 3. Hydrodeoxygenation Process

Different studies treated the lignocellulosic biomass valorization through the hydrodeoxygenation reaction of the lignin-derived bio-oils. **Figure 2.3.1** describes the process scheme followed to achieve this purpose starting from lignin extraction followed by the pyrolysis process and ending with the HDO reaction and products recuperation. In this section, we describe the HDO system and the characterization techniques used in catalytic conversion tests.

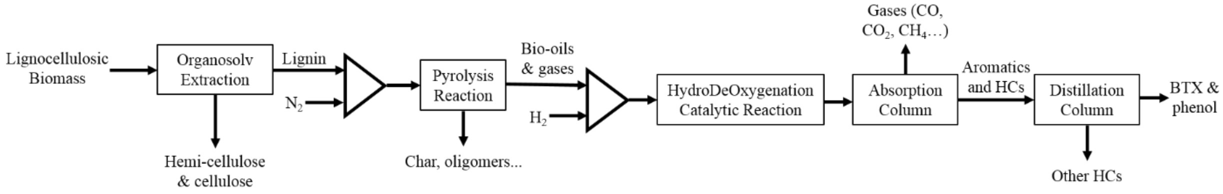

Figure 2.3.1 *Process scheme of the valorization of lignocellulosic biomass into aromatics.*

2.3.1 Introduction

The HDO system, used for guaiacol (as a model molecule of bio-oils)[122] catalytic conversion in order to test the catalytic performance of the synthetized materials, is presented in **Figure 2.3.2**. This system and experimental conditions applied are similar to those used by Olcese *et al.*[123] for Fe@SiO$_2$ catalysts. As the system was re-installed completely, a detailed description of the work done, installations, and equipment calibration will be given in **Chapter 5**. The main advantage of our system comparing to that used by Olcese *et al.*[123] is the installation of an online mass spectrometer on the outgoing flow of the reactor, which allow following qualitatively the products with respect to time, and predicting the possible mechanisms and catalyst deactivation time.

Principally, the gas-phase HDO reaction was performed in a fixed-bed U-type reactor, where liquid guaiacol was injected by syringe through a septum into the gas flow line (argon or nitrogen). The injection and the total flow rate were fixed in order to obtain a guaiacol vol% of 0.5%. This low percentage inhibit the guaiacol condensation in the flow line, which heated at 220 °C. The reactor was heated by a rounded oven, symmetrically placed and well isolated to reduce temperature loss between them. The flow going out from the reactor was also heated at 220 °C to prevent condensation of remaining unreacted guaiacol or heavy molecules. A small portion of the outgoing flow (< 1%) was injected through an online mass spectrometer in order to follow the reaction qualitatively with time, while the remaining quantity is passed through impingers (bullers) to condensate large molecules. Those molecules are later quantified by a gas chromatography mass spectrometer GCMS using an internal etalon. The outgoing flow from impingers, containing small non-condensed molecules, is then injected through an online gas chromatography µGC to analyze and quantify them.

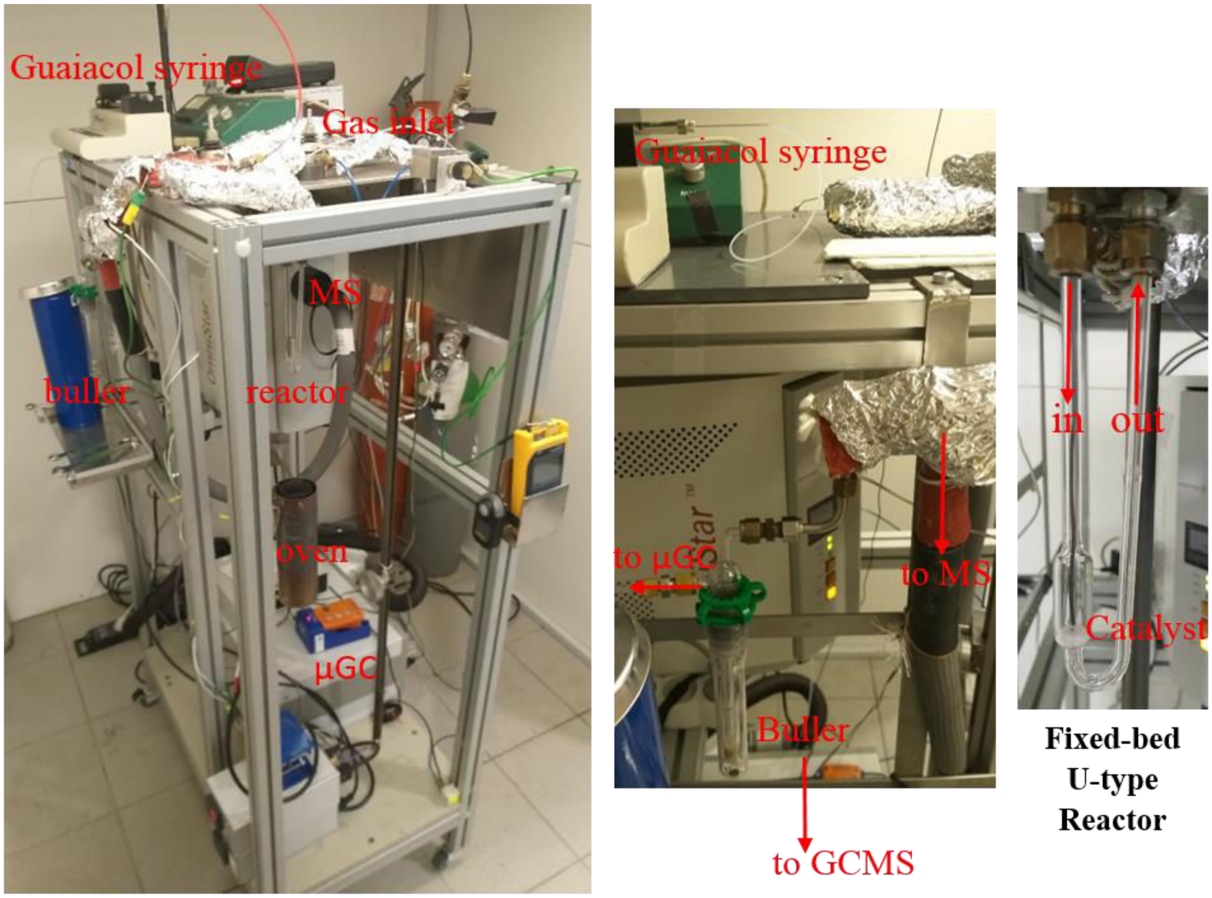

Figure 2.3.2 *Representation of the HDO system and the fixed-bed U-type reactor.*

2.3.2 Characterization Techniques

2.3.2.a Gas chromatography µGC

The outlet flux from the reactor was connected to two impingers filled with methanol; the first is cooled with glass (273 K) and then second with a liquid nitrogen/2-isopropanol solution (233 K) in order to protect the µGC from condensable heavy products. A µGC-Varian 490, with four modules, was installed on the output of the impingers in order to analyze online quantitatively the concentration of incondensable gases (methane, ethane, CO, CO_2...). It aims also to quantify the quantity of hydrogen consumed during temperature programmed reduction (TPR) measurements. Gas Injection was performed every 293 seconds. The four modules were composed of two molecular sieves 5A, a PoraPlot U and CP–Wax 52CB columns. The signal was calibrated using various standard calibration bottles from Air Liquide. In order to calculate the molar quantities of gases, data were integrated over the time integral of each injection and added overall the reaction duration. BTX molecules signal was not detected, which ensure their condensation in impingers.

2.3.2.b Mass spectrometer MS

A small amount (< 1mL/min) of the gas flux going out from the reactor, containing unconverted guaiacol and produced products, was injected in an online mass spectrometer (MS, electron impact 70eV) before arriving to the impingers. The mass spectra of different molecules was recorded with respect to time during the HDO reaction (one point every 17 sec), aiming to follow the kinetics of the reaction and to predict the deactivation of the catalyst with time. We followed the signal of the ion current of the m/z values of 94, 81, 78 (and 77), 44, 32, 28, and 18 corresponding to phenol, guaiacol, benzene, CO_2, O_2, CO (and N_2), and water respectively.

2.3.2.c Gas chromatography mass spectrometry GCMS

Impingers, containing each 10 ml of methanol, allow the condensation and recuperation of condensable vapors in order to quantify them. Once the catalysis was finished, both impingers were disconnected and washed with methanol, and then 10 µL of 1-tetradecene was added to the solution as internal standard for the GCMS. The collected compounds of both impinger were analyzed together with an Agilent 7890 Gas Chromatography coupled to an Agilent 5975C MS analyzer. One µL of the solution (containing products and internal standard) were injected with a split ratio of 20 into an Agilent HP-5MS (30m*250µm*0.25µm) column (0.93 Nml/min of He) connected with a heart-cutting system to an Agilent DB-Wax123 (30m*320µm*0.25µm) column (3.44 Nml/min of He; $R.T._{heart\text{-}cutting}$: 26-27.3 min). The temperature of the oven was programmed as follows: hold for 10 mins at 313K, and then increased at to 473K with a rate of 5 K/min and hold at this temperature for 21 min. The exit of HP-5MS column was connected simultaneously to a Flame Ionization Detector (FID) and to a Mass Spectrometer (MS). The exit of DB-Wax123 column was connected to a separate FID.

The relative response factor (RRF) of the three main compounds (guaiacol, phenol, and benzene) were determined experimentally with various standard solutions. For other compounds (toluene, cresol, xylene…), the response factors on FID were predicted using the Saint Laumer method.[124] Different solutions containing benzene, phenol, and guaiacol were prepared at various concentrations and analyzed by GCMS in order to determine experimentally the RFF values of those components. The n_i/n_{etalon} (experimental mole number of component i / experimental mole number of 1-tetradecene etalon) ratio is plotted with respect to A_i/A_{etalon} (corrected area of component i / corrected area of 1-tetraadecene) ratio as showed in **Figure 2.3.3**, where i is benzene, phenol, or guaiacol. The slop of those curves correspond to the RRF value of each component. Therefore, the relative response factor RRF for benzene is 2.76, that of phenol is 3.75, and that of guaiacol is 3.15.

Those RRF values will be used to quantify the number of mole of products analyzed as they correlate the molar ratio to the area (obtained from GCMS-FID) ratio as follow.

$$n_i = RFF_i * n_{etalon} * {}^{A_i}/_{A_{etalon}}$$

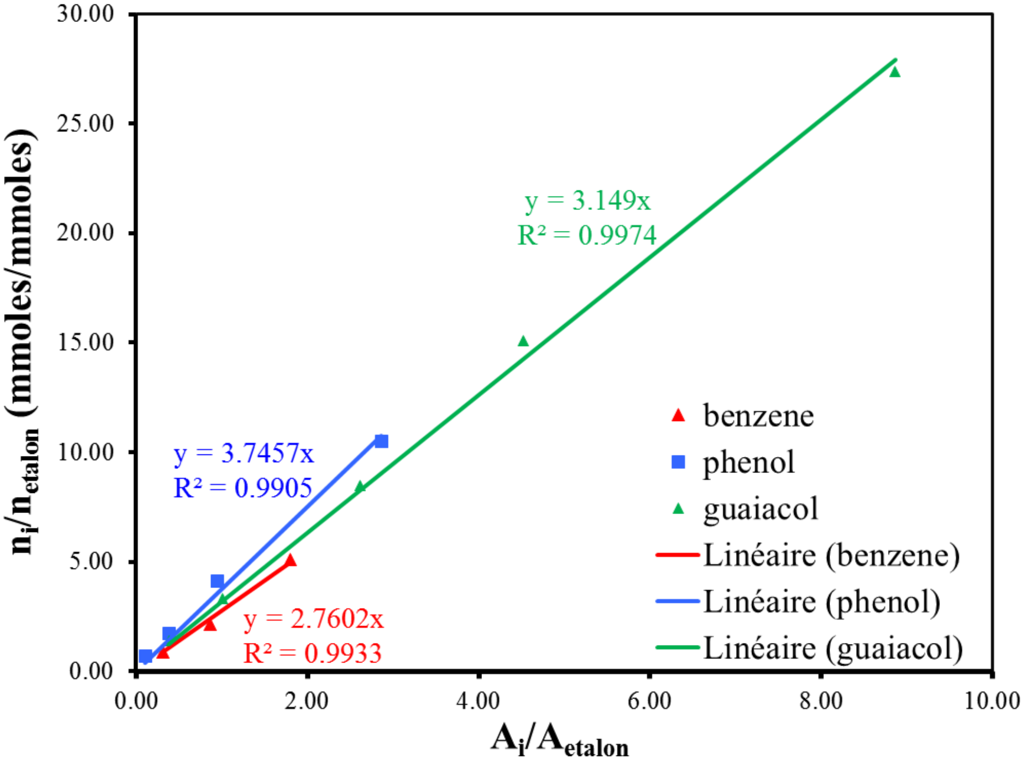

Figure 2.3.3 *Experimental molar ratio (component i / 1-tetradecene etalon) plotted with respect to the corrected area ratio (component i / etalon), and the corresponding relative response factor (RRF) values.*

References

(1) Heisenberg, W. About quantum theoretical reinterpretation of kinematic and mechanical relations. In *Original Scientific Papers Wissenschaftliche Originalarbeiten*; Blum, W., Rechenberg, H., Dürr, H.-P., Eds.; Springer Berlin, Heidelberg, 1985, 382–396.
(2) Heitler, W.; London, F. Interaction of neutral atoms and homopolar bonding according to quantum mechanics. *Z. Fur Phys.* **1927**, *44* (6–7), 455–472.
(3) Schrödinger, E. An Undulatory Theory of the Mechanics of Atoms and Molecules. *Phys Rev* **1926**, *28* (6), 1049–1070.
(4) Born, M.; Oppenheimer, R. The quantum theory of molecules. *Ann. Phys.* **1927**, *389* (20), 457–484.
(5) Slater, J. C. A Simplification of the Hartree-Fock Method. *Phys. Rev.* **1951**, *81* (3), 385–390.
(6) Jones, R. O.; Gunnarsson, O. The Density Functional Formalism, Its Applications and Prospects. *Rev. Mod. Phys.* **1989**, *61* (3), 689–746.
(7) Epstein, S. *The Variation Method in Quantum Chemistry*; Elsevier Science: Saint Louis, **2014**.
(8) Fleming, G. N. The Evolution of Pauli's Exclusion Principle. *Stud. Hist. Philos. Sci. Part B Stud. Hist. Philos. Mod. Phys.* **2007**, *38* (1), 202–208.
(9) Szabo, A.; Ostlund, N. S. *Modern Quantum Chemistry: Introduction to Advanced Electronic Structure Theory*; Dover Publications: Mineola, N.Y, **1996**.
(10) Hartree, D. R. The Wave Mechanics of an Atom with a Non-Coulomb Central Field. Part I. Theory and Methods. *Math. Proc. Camb. Philos. Soc.* **1928**, *24* (01), 89.
(11) Slater, J. C. Note on Hartree's Method. *Phys. Rev.* **1930**, *35* (2), 210–211.
(12) Pople, J. A. Nobel Lecture: Quantum Chemical Models. *Rev. Mod. Phys.* **1999**, *71* (5), 1267–1274.
(13) Nesbet, R. K. *Variational Principles and Methods in Theoretical Physics and Chemistry*; Cambridge University Press: New York, **2003**.
(14) Fock, V. Approximation method for solving the quantum mechanical multibody problem. *Z. Fur Phys.* **1930**, *61* (1–2), 126–148.
(15) Bartlett, R. J.; Stanton, J. F. Applications of Post-Hartree-Fock Methods: A Tutorial. In *Reviews in Computational Chemistry*; Lipkowitz, K. B., Boyd, D. B., Eds.; John Wiley & Sons, Inc.: Hoboken, NJ, USA, **2007**, 65–169.
(16) Dreizler, R. M.; Gross, E. K. U. *Density Functional Theory: An Approach to the Quantum Many-Body Problem*; Springer Berlin Heidelberg: Berlin, Heidelberg, **1990**.
(17) Parr, R. G.; Yang, W. *Density-Functional Theory of Atoms and Molecules*, International series of monographs on chemistry; Oxford Univ. Press [u.a.]: New York, NY, **1994**.
(18) Koch, W.; Holthausen, M. C. *A Chemist's Guide to Density Functional Theory*; Wiley-VCH Verlag GmbH: Weinheim, FRG, **2001**.
(19) Burke, K. *The ABC of DFT*; Department of Chemistry, University of California, Irvine, CA 92697, **2007**.
(20) Thomas, L. H. The Calculation of Atomic Fields. *Math. Proc. Camb. Philos. Soc.* **1927**, *23* (05), 542.
(21) Csavinszky, P. Complementary Variational Principles in the Thomas-Fermi Theory. *Phys. Rev. A* **1972**, *5* (5), 2198–2204.
(22) Rosen, A.; Ellis, D. E. Relativistic Molecular Calculations in the Dirac–Slater Model. *J. Chem. Phys.* **1975**, *62* (8), 3039–3049.
(23) Hohenberg, P.; Kohn, W. Inhomogeneous Electron Gas. *Phys. Rev.* **1964**, *136* (3B), B864–B871.
(24) Kohn, W.; Sham, L. J. Quantum Density Oscillations in an Inhomogeneous Electron Gas. *Phys. Rev.* **1965**, *137* (6A), A1697–A1705.
(25) Kohn, W.; Sham, L. J. Self-Consistent Equations Including Exchange and Correlation Effects. *Phys. Rev.* **1965**, *140* (4A), A1133–A1138.
(26) Kohn, W. Nobel Lecture: Electronic Structure of Matter—Wave Functions and Density Functionals. *Rev. Mod. Phys.* **1999**, *71* (5), 1253–1266.

(27) Cramer, C. J. *Essentials of Computational Chemistry: Theories and Models*, 2nd ed.; Wiley: Chichester, West Sussex, England, Hoboken, NJ, **2004**.

(28) Johnson, B. G.; Gill, P. M. W.; Pople, J. A. The Performance of a Family of Density Functional Methods. *J. Chem. Phys.* **1993**, *98* (7), 5612–5626.

(29) Burke, K. Perspective on Density Functional Theory. *J. Chem. Phys.* **2012**, *136* (15), 150901.

(30) Jensen, F. *Introduction to Computational Chemistry*, 2nd ed.; John Wiley & Sons: Chichester, England, Hoboken, NJ, **2007**.

(31) Zhao, Y.; Truhlar, D. G. The M06 Suite of Density Functionals for Main Group Thermochemistry, Thermochemical Kinetics, Noncovalent Interactions, Excited States, and Transition Elements: Two New Functionals and Systematic Testing of Four M06-Class Functionals and 12 Other Functionals. *Theor. Chem. Acc.* **2008**, *120* (1–3), 215–241.

(32) Becke, A. D. Density-functional Thermochemistry. III. The Role of Exact Exchange. *J. Chem. Phys.* **1993**, *98* (7), 5648–5652.

(33) Stephens, P. J.; Devlin, F. J.; Chabalowski, C. F.; Frisch, M. J. Ab Initio Calculation of Vibrational Absorption and Circular Dichroism Spectra Using Density Functional Force Fields. *J. Phys. Chem.* **1994**, *98* (45), 11623–11627.

(34) Staroverov, V. N.; Scuseria, G. E.; Tao, J.; Perdew, J. P. Comparative Assessment of a New Nonempirical Density Functional: Molecules and Hydrogen-Bonded Complexes. *J. Chem. Phys.* **2003**, *119* (23), 12129–12137.

(35) Tao, J.; Perdew, J. P.; Staroverov, V. N.; Scuseria, G. E. Climbing the Density Functional Ladder: Nonempirical Meta–Generalized Gradient Approximation Designed for Molecules and Solids. *Phys. Rev. Lett.* **2003**, *91* (14).

(36) Perdew, J. P.; Chevary, J. A.; Vosko, S. H.; Jackson, K. A.; Pederson, M. R.; Singh, D. J.; Fiolhais, C. Atoms, Molecules, Solids, and Surfaces: Applications of the Generalized Gradient Approximation for Exchange and Correlation. *Phys. Rev. B* **1992**, *46* (11), 6671–6687.

(37) Becke, A. D. Density-Functional Exchange-Energy Approximation with Correct Asymptotic Behavior. *Phys. Rev. A* **1988**, *38* (6), 3098–3100.

(38) Lee, C.; Yang, W.; Parr, R. G. Development of the Colle-Salvetti Correlation-Energy Formula into a Functional of the Electron Density. *Phys. Rev. B* **1988**, *37* (2), 785–789.

(39) Perdew, J. P.; Burke, K.; Ernzerhof, M. Generalized Gradient Approximation Made Simple. *Phys. Rev. Lett.* **1996**, *77* (18), 3865–3868.

(40) Vosko, S. H.; Wilk, L.; Nusair, M. Accurate Spin-Dependent Electron Liquid Correlation Energies for Local Spin Density Calculations: A Critical Analysis. *Can. J. Phys.* **1980**, *58* (8), 1200–1211.

(41) Sousa, S. F.; Fernandes, P. A.; Ramos, M. J. General Performance of Density Functionals. *J. Phys. Chem. A* **2007**, *111* (42), 10439–10452.

(42) Kittel, C. *Physique de l'état solide*; Dunod: Paris, **1990**.

(43) Singh, D. J.; Nordström, L. *Planewaves, Pseudopotentials, and the LAPW Method*, 2nd ed.; Springer: New York, NY, **2006**.

(44) *Modern methods and algorithms of quantum chemistry: Winterschool, Forschungszentrum Jülich, Germany. Proceedings*; Grotendorst, J., Ed.; NIC series, **2000**.

(45) Vanderbilt, D. Soft Self-Consistent Pseudopotentials in a Generalized Eigenvalue Formalism. *Phys. Rev. B* **1990**, *41* (11), 7892–7895.

(46) Blöchl, P. E. Projector Augmented-Wave Method. *Phys. Rev. B* **1994**, *50* (24), 17953–17979.

(47) Kresse, G.; Joubert, D. From Ultrasoft Pseudopotentials to the Projector Augmented-Wave Method. *Phys. Rev. B* **1999**, *59* (3), 1758–1775.

(48) Kresse, G.; Furthmüller, J. Efficient Iterative Schemes for *Ab Initio* Total-Energy Calculations Using a Plane-Wave Basis Set. *Phys. Rev. B* **1996**, *54* (16), 11169–11186.

(49) Pauling, L. *The Nature of the Chemical Bond and the Structure of Molecules and Crystals: An Introduction to Modern Structural Chemistry*, 3. ed., 17. print.; Cornell Univ. Press: Ithaca, New York, **2000**.

(50) Dion, M.; Rydberg, H.; Schröder, E.; Langreth, D. C.; Lundqvist, B. I. Van Der Waals Density Functional for General Geometries. *Phys. Rev. Lett.* **2004**, *92* (24), 246401.

(51) Lee, K.; Murray, É. D.; Kong, L.; Lundqvist, B. I.; Langreth, D. C. Higher-Accuracy van Der Waals Density Functional. *Phys. Rev. B* **2010**, *82* (8).

(52) Klimeš, J.; Bowler, D. R.; Michaelides, A. Van Der Waals Density Functionals Applied to Solids. *Phys. Rev. B* **2011**, *83* (19).

(53) Grimme, S. Accurate Description of van Der Waals Complexes by Density Functional Theory Including Empirical Corrections. *J. Comput. Chem.* **2004**, *25* (12), 1463–1473.

(54) Grimme, S. Semiempirical GGA-Type Density Functional Constructed with a Long-Range Dispersion Correction. *J. Comput. Chem.* **2006**, *27* (15), 1787–1799.

(55) Bučko, T.; Hafner, J.; Lebègue, S.; Ángyán, J. G. Improved Description of the Structure of Molecular and Layered Crystals: Ab Initio DFT Calculations with van Der Waals Corrections. *J. Phys. Chem. A* **2010**, *114* (43), 11814–11824.

(56) Munnik, P.; de Jongh, P. E.; de Jong, K. P. Recent Developments in the Synthesis of Supported Catalysts. *Chem. Rev.* **2015**, *115* (14), 6687–6718.

(57) Reichhardt, N. V. Towards a Responsive Functional Material: Modification of Porosity and Grafting of Poly(N-Isopropylacrylamide) in Mesoporous Silica SBA-15, Physical Chemistry, Center of Chemistry and Chemical Engineering, Lund University, Lund, **2011**.

(58) ALOthman, Z. A Review: Fundamental Aspects of Silicate Mesoporous Materials. *Materials* **2012**, *5* (12), 2874–2902.

(59) Yu Lai, Dr. C. Mesoporous Silica Nanomaterials Applications in Catalysis. *J. Thermodyn. Catal.* **2014**, *05* (01).

(60) Huirache-Acuña, R.; Nava, R.; Peza-Ledesma, C.; Lara-Romero, J.; Alonso-Núez, G.; Pawelec, B.; Rivera-Muñoz, E. SBA-15 Mesoporous Silica as Catalytic Support for Hydrodesulfurization Catalysts—Review. *Materials* **2013**, *6* (9), 4139–4167.

(61) Karimi, B.; Vafaeezadeh, M. SBA-15-Functionalized Sulfonic Acid Confined Acidic Ionic Liquid: A Powerful and Water-Tolerant Catalyst for Solvent-Free Esterifications. *Chem. Commun.* **2012**, *48* (27), 3327.

(62) Karimi, B.; Abedi, S.; Clark, J. H.; Budarin, V. Highly Efficient Aerobic Oxidation of Alcohols Using a Recoverable Catalyst: The Role of Mesoporous Channels of SBA-15 in Stabilizing Palladium Nanoparticles. *Angew. Chem. Int. Ed.* **2006**, *45* (29), 4776–4779.

(63) Chaudhary, V.; Sharma, S. An Overview of Ordered Mesoporous Material SBA-15: Synthesis, Functionalization and Application in Oxidation Reactions. *J. Porous Mater.* **2017**, *24* (3), 741–749.

(64) Luo, G.; Yan, S.; Qiao, M.; Fan, K. RuB/Sn-SBA-15 Catalysts: Preparation, Characterization, and Catalytic Performance in Ethyl Lactate Hydrogenation. *Appl. Catal. Gen.* **2007**, *332* (1), 79–88.

(65) Mohammadi Ziarani, G.; Rohani, S.; Ziarati, A.; Badiei, A. Applications of SBA-15 Supported Pd Metal Catalysts as Nanoreactors in C–C Coupling Reactions. *RSC Adv.* **2018**, *8* (71), 41048–41100.

(66) Li, X.; Zhang, J.; Liu, B.; Liu, J.; Wang, C.; Chen, G. Hydrodeoxygenation of Lignin-Derived Phenols to Produce Hydrocarbons over Ni/Al-SBA-15 Prepared with Different Impregnants. *Fuel* **2019**, *243*, 314–321.

(67) Chen, S.; Zhou, G.; Miao, C. Green and Renewable Bio-Diesel Produce from Oil Hydrodeoxygenation: Strategies for Catalyst Development and Mechanism. *Renew. Sustain. Energy Rev.* **2019**, *101*, 568–589.

(68) Singh, S.; Kumar, R.; Setiabudi, H. D.; Nanda, S.; Vo, D.-V. N. Advanced Synthesis Strategies of Mesoporous SBA-15 Supported Catalysts for Catalytic Reforming Applications: A State-of-the-Art Review. *Appl. Catal. Gen.* **2018**, *559*, 57–74.

(69) Rahmat. A Review: Mesoporous Santa Barbara Amorphous-15, Types, Synthesis and Its Applications towards Biorefinery Production. *Am. J. Appl. Sci.* **2010**, *7* (12), 1579–1586.

(70) Zuo, D.; Lane, J.; Culy, D.; Schultz, M.; Pullar, A.; Waxman, M. Sulfonic Acid Functionalized Mesoporous SBA-15 Catalysts for Biodiesel Production. *Appl. Catal. B Environ.* **2013**, *129*, 342–350.

(71) Védrine, J. Heterogeneous Catalysis on Metal Oxides. *Catalysts* **2017**, *7* (11), 341.

(72) Pan, Y.; Shen, X.; Yao, L.; Bentalib, A.; Peng, Z. Active Sites in Heterogeneous Catalytic Reaction on Metal and Metal Oxide: Theory and Practice. *Catalysts* **2018**, *8* (10), 478.

(73) Liu, L.; Corma, A. Metal Catalysts for Heterogeneous Catalysis: From Single Atoms to Nanoclusters and Nanoparticles. *Chem. Rev.* **2018**, *118* (10), 4981–5079.

(74) Védrine, J. C. Metal Oxides in Heterogeneous Oxidation Catalysis: State of the Art and Challenges for a More Sustainable World. *ChemSusChem* **2019**, *12* (3), 577–588.

(75) Huang, A.; He, Y.; Zhou, Y.; Zhou, Y.; Yang, Y.; Zhang, J.; Luo, L.; Mao, Q.; Hou, D.; Yang, J. A Review of Recent Applications of Porous Metals and Metal Oxide in Energy Storage, Sensing and Catalysis. *J. Mater. Sci.* **2019**, *54* (2), 949–973.

(76) González-Arellano, C.; Corma, A.; Iglesias, M.; Sánchez, F. Improved Palladium and Nickel Catalysts Heterogenised on Oxidic Supports (Silica, MCM-41, ITQ-2, ITQ-6). *Adv. Synth. Catal.* **2004**, *346* (11), 1316–1328.

(77) Saib, A. M.; Claeys, M.; van Steen, E. Silica Supported Cobalt Fischer–Tropsch Catalysts: Effect of Pore Diameter of Support. *Catal. Today* **2002**, *71* (3–4), 395–402.

(78) Katrib, A.; Petit, C.; Légaré, P.; Hilaire, L.; Maire, G. An Investigation of Metal-Support Interaction in Bimetallic Pt-Mo Catalysts Deposited on Silica and Alumina. *Surf. Sci.* **1987**, *189–190*, 886–893.

(79) van de Loosdrecht, J.; van der Kraan, A. M.; van Dillen, A. J.; Geus, J. W. Metal-Support Interaction: Titania-Supported and Silica-Supported Nickel Catalysts. *J. Catal.* **1997**, *170* (2), 217–226.

(80) Coulter, K. E.; Sault, A. G. Effects of Activation on the Surface Properties of Silica-Supported Cobalt Catalysts. *J. Catal.* **1995**, *154* (1), 56–64.

(81) Boudart, M. Catalysis by Supported Metals. In *Advances in Catalysis*; Elsevier, **1969**, 20, 153–166.

(82) Min, B. K.; Santra, A. K.; Goodman, D. W. Understanding Silica-Supported Metal Catalysts: Pd/Silica as a Case Study. *Catal. Today* **2003**, *85* (2–4), 113–124.

(83) Zhang, Y.; Hanayama, K.; Tsubaki, N. The Surface Modification Effects of Silica Support by Organic Solvents for Fischer–Tropsch Synthesis Catalysts. *Catal. Commun.* **2006**, *7* (5), 251–254.

(84) Pudukudy, M.; Yaakob, Z.; Akmal, Z. S. Direct Decomposition of Methane over SBA-15 Supported Ni, Co and Fe Based Bimetallic Catalysts. *Appl. Surf. Sci.* **2015**, *330*, 418–430.

(85) Rioux, R. M.; Song, H.; Hoefelmeyer, J. D.; Yang, P.; Somorjai, G. A. High-Surface-Area Catalyst Design: Synthesis, Characterization, and Reaction Studies of Platinum Nanoparticles in Mesoporous SBA-15 Silica. *J. Phys. Chem. B* **2005**, *109* (6), 2192–2202.

(86) Bonelli, R.; Lucarelli, C.; Pasini, T.; Liotta, L. F.; Zacchini, S.; Albonetti, S. Total Oxidation of Volatile Organic Compounds on Au/FeO_x Catalysts Supported on Mesoporous SBA-15 Silica. *Appl. Catal. Gen.* **2011**, *400* (1–2), 54–60.

(87) Khodakov, A. Y.; Bechara, R.; Griboval-Constant, A. Fischer–Tropsch Synthesis over Silica Supported Cobalt Catalysts: Mesoporous Structure versus Cobalt Surface Density. *Appl. Catal. Gen.* **2003**, *254* (2), 273–288.

(88) Yang, Y.; Ochoa-Hernández, C.; de la Peña O'Shea, V. A.; Pizarro, P.; Coronado, J. M.; Serrano, D. P. Effect of Metal–Support Interaction on the Selective Hydrodeoxygenation of Anisole to Aromatics over Ni-Based Catalysts. *Appl. Catal. B Environ.* **2014**, *145*, 91–100.

(89) Yang, C.; Kalwei, M.; Schüth, F.; Chao, K. Gold Nanoparticles in SBA-15 Showing Catalytic Activity in CO Oxidation. *Appl. Catal. Gen.* **2003**, *254* (2), 289–296.

(90) Carrero, A.; Calles, J. A.; Vizcaíno, A. J. Hydrogen Production by Ethanol Steam Reforming over Cu-Ni/SBA-15 Supported Catalysts Prepared by Direct Synthesis and Impregnation. *Appl. Catal. Gen.* **2007**, *327* (1), 82–94.

(91) Yang, C.-M.; Lin, H.-A.; Zibrowius, B.; Spliethoff, B.; Schüth, F.; Liou, S.-C.; Chu, M.-W.; Chen, C.-H. Selective Surface Functionalization and Metal Deposition in the Micropores of Mesoporous Silica SBA-15. *Chem. Mater.* **2007**, *19* (13), 3205–3211.

(92) Zhao, D. Triblock Copolymer Syntheses of Mesoporous Silica with Periodic 50 to 300 Angstrom Pores. *Science* **1998**, *279* (5350), 548–552.

(93) Impéror-Clerc, M.; Davidson, P.; Davidson, A. Existence of a Microporous Corona around the Mesopores of Silica-Based SBA-15 Materials Templated by Triblock Copolymers. *J. Am. Chem. Soc.* **2000**, *122* (48), 11925–11933.

(94) Vradman, L.; Titelman, L.; Herskowitz, M. Size Effect on SBA-15 Microporosity. *Microporous Mesoporous Mater.* **2006**, *93* (1–3), 313–317.

(95) Thielemann, J. P.; Girgsdies, F.; Schlögl, R.; Hess, C. Pore Structure and Surface Area of Silica SBA-15: Influence of Washing and Scale-Up. *Beilstein J. Nanotechnol.* **2011**, *2*, 110–118.

(96) Benamor, T.; Vidal, L.; Lebeau, B.; Marichal, C. Influence of Synthesis Parameters on the Physico-Chemical Characteristics of SBA-15 Type Ordered Mesoporous Silica. *Microporous Mesoporous Mater.* **2012**, *153*, 100–114.

(97) Ojeda-López, R.; Pérez-Hermosillo, I. J.; Marcos Esparza-Schulz, J.; Cervantes-Uribe, A.; Domínguez-Ortiz, A. SBA-15 Materials: Calcination Temperature Influence on Textural Properties and Total Silanol Ratio. *Adsorption* **2015**, *21* (8), 659–669.

(98) Ertan, A.; Kodumuri, P.; Talu, O.; Tewari, S. N. Effect of Synthesis Time and Treatment on Porosity of Mesoporous Silica Materials. *Adsorption* **2009**, *15* (1), 81–86.

(99) Zhao, D.; Sun, J.; Li, Q.; Stucky, G. D. Morphological Control of Highly Ordered Mesoporous Silica SBA-15. *Chem. Mater.* **2000**, *12* (2), 275–279.

(100) Barau, A.; Budarin, V.; Caragheorgheopol, A.; Luque, R.; Macquarrie, D. J.; Prelle, A.; Teodorescu, V. S.; Zaharescu, M. A Simple and Efficient Route to Active and Dispersed Silica Supported Palladium Nanoparticles. *Catal. Lett.* **2008**, *124* (3–4), 204–214.

(101) Huang, H.; Ji, Y.; Qiao, Z.; Zhao, C.; He, J.; Zhang, H. Preparation, Characterization, and Application of Magnetic Fe-SBA-15 Mesoporous Silica Molecular Sieves. *J. Autom. Methods Manag. Chem.* **2010**, *2010*, 1–7.

(102) Campelo, J. M.; Luna, D.; Luque, R.; Marinas, J. M.; Romero, A. A. Sustainable Preparation of Supported Metal Nanoparticles and Their Applications in Catalysis. *ChemSusChem* **2009**, *2* (1), 18.

(103) Liu, H.; Ma, D.; Blackley, R. A.; Zhou, W.; Bao, X. Highly Active Mesostructured Silica Hosted Silver Catalysts for CO Oxidation Using the One-Pot Synthesis Approach. *Chem. Commun.* **2008**, 23, 2677.

(104) Li, Y.; Feng, Z.; Lian, Y.; Sun, K.; Zhang, L.; Jia, G.; Yang, Q.; Li, C. Direct Synthesis of Highly Ordered Fe-SBA-15 Mesoporous Materials under Weak Acidic Conditions. *Microporous Mesoporous Mater.* **2005**, *84* (1–3), 41–49.

(105) Haruta, M.; Tsubota, S.; Kobayashi, T.; Kageyama, H.; Genet, M. J.; Delmon, B. Low-Temperature Oxidation of CO over Gold Supported on TiO_2, α-Fe_2O_3, and Co_3O_4. *J. Catal.* **1993**, *144* (1), 175.

(106) Daté, M.; Okumura, M.; Tsubota, S.; Haruta, M. Vital Role of Moisture in the Catalytic Activity of Supported Gold Nanoparticles. *Angew. Chem.* **2004**, *116* (16), 2181–2184.

(107) Cushing, B. L.; Kolesnichenko, V. L.; O'Connor, C. J. Recent Advances in the Liquid-Phase Syntheses of Inorganic Nanoparticles. *Chem. Rev.* **2004**, *104* (9), 3893–3946.

(108) Shi, D.; Yang, Q.; Peterson, C.; Lamic-Humblot, A.-F.; Girardon, J.-S.; Griboval-Constant, A.; Stievano, L.; Sougrati, M. T.; Briois, V.; Bagot, P. A. J.; Wojcieszak, R.; Paul, S.; Marceau, E. Bimetallic

Fe-Ni/SiO_2 Catalysts for Furfural Hydrogenation: Identification of the Interplay between Fe and Ni during Deposition-Precipitation and Thermal Treatments. *Catal. Today* **2018**.

(109) Eriksson, S. Preparation of Catalysts from Microemulsions and Their Applications in Heterogeneous Catalysis. *Appl. Catal. Gen.* **2004**, *265* (2), 207–219.

(110) Ruta, M.; Semagina, N.; Kiwi-Minsker, L. Monodispersed Pd Nanoparticles for Acetylene Selective Hydrogenation: Particle Size and Support Effects. *J. Phys. Chem. C* **2008**, *112* (35), 13635–13641.

(111) Wang, A.; Li, J.; Zhang, T. Heterogeneous Single-Atom Catalysis. *Nat. Rev. Chem.* **2018**, *2* (6), 65.

(112) Zhang, H.; Liu, G.; Shi, L.; Ye, J. Single-Atom Catalysts: Emerging Multifunctional Materials in Heterogeneous Catalysis. *Adv. Energy Mater.* **2018**, *8* (1), 1701343.

(113) Qiao, B.; Wang, A.; Yang, X.; Allard, L. F.; Jiang, Z.; Cui, Y.; Liu, J.; Li, J.; Zhang, T. Single-Atom Catalysis of CO Oxidation Using Pt_1/FeO_x. *Nat. Chem.* **2011**, *3* (8), 634–641.

(114) Sun, S.; Zhang, G.; Gauquelin, N.; Chen, N.; Zhou, J.; Yang, S.; Chen, W.; Meng, X.; Geng, D.; Banis, M. N.; Li, R.; Ye, S.; Knights, S.; Botton, G.; Sham, T.-K.; Sun, X. Single-Atom Catalysis Using Pt/Graphene Achieved through Atomic Layer Deposition. *Sci. Rep.* **2013**, *3* (1).

(115) Liu, P.; Zhao, Y.; Qin, R.; Mo, S.; Chen, G.; Gu, L.; Chevrier, D. M.; Zhang, P.; Guo, Q.; Zang, D.; Wu, B.; Fu, G.; Zheng, N. Photochemical Route for Synthesizing Atomically Dispersed Palladium Catalysts. *Science* **2016**, *352* (6287), 797–800.

(116) Zhang, X.; Guo, J.; Guan, P.; Liu, C.; Huang, H.; Xue, F.; Dong, X.; Pennycook, S. J.; Chisholm, M. F. Catalytically Active Single-Atom Niobium in Graphitic Layers. *Nat. Commun.* **2013**, *4* (1).

(117) Zhang, H.; Wei, J.; Dong, J.; Liu, G.; Shi, L.; An, P.; Zhao, G.; Kong, J.; Wang, X.; Meng, X.; Zhang, J.; Ye, J. Efficient Visible-Light-Driven Carbon Dioxide Reduction by a Single-Atom Implanted Metal-Organic Framework. *Angew. Chem. Int. Ed.* **2016**, *55* (46), 14310–14314.

(118) Yang, X.-F.; Wang, A.; Qiao, B.; Li, J.; Liu, J.; Zhang, T. Single-Atom Catalysts: A New Frontier in Heterogeneous Catalysis. *Acc. Chem. Res.* **2013**, *46* (8), 1740–1748.

(119) Lee, H. S.; Kim, W. H.; Lee, J. H.; Choi, D. J.; Jeong, Y.-K.; Chang, J. H. Transition Metal-Chelating Surfactant Micelle Templates for Facile Synthesis of Mesoporous Silica Nanoparticles. *J. Solid State Chem.* **2012**, *185*, 89–94.

(120) King, N. C.; Blackley, R. A.; Zhou, W.; Bruce, D. W. The Preparation by True Liquid Crystal Templating of Mesoporous Silicates Containing Nanoparticulate Metals. *Chem. Commun.* **2006**, 32, 3411.

(121) King, N. C.; Blackley, R. A.; Wears, M. L.; Newman, D. M.; Zhou, W.; Bruce, D. W. The Synthesis of Mesoporous Silicates Containing Bimetallic Nanoparticles and Magnetic Properties of PtCo Nanoparticles in Silica. *Chem. Commun.* **2006**, 32, 3414.

(122) Zhao, H. Y.; Li, D.; Bui, P.; Oyama, S. T. Hydrodeoxygenation of Guaiacol as Model Compound for Pyrolysis Oil on Transition Metal Phosphide Hydroprocessing Catalysts. *Appl. Catal. Gen.* **2011**, *391* (1–2), 305–310.

(123) Olcese, R. N.; Bettahar, M.; Petitjean, D.; Malaman, B.; Giovanella, F.; Dufour, A. Gas-Phase Hydrodeoxygenation of Guaiacol over Fe/SiO_2 Catalyst. *Appl. Catal. B Environ.* **2012**, *115–116*, 63.

(124) de Saint Laumer, J.-Y.; Cicchetti, E.; Merle, P.; Egger, J.; Chaintreau, A. Quantification in Gas Chromatography: Prediction of Flame Ionization Detector Response Factors from Combustion Enthalpies and Molecular Structures. *Anal. Chem.* **2010**, *82* (15), 6457–6462.

Chapter 3

Atomistic Description of Phenol, CO and H_2O Adsorption over Crystalline and Amorphous Silica Surfaces for Hydrodeoxygenation Applications

Chap. 3 Atomistic Description of Phenol, CO and H_2O Adsorption over Crystalline and Amorphous Silica Surfaces for Hydrodeoxygenation Applications

The content of this chapter is published in the journal of Applied Surface Science (ELSEVIER) devoted for the better understanding of the chemistry and properties of surfaces and interfaces using analytical techniques and/or computational methods.

Berro, Y.; Gueddida, S.; Lebègue, S.; Pasc, A.; Canilho, N.; Kassir, M.; El Haj Hassan, F.; Badawi, M., *Appl. Surf. Sci.*, **2019**, 494, 721-730.

Abstract

The upgrading of lignin-derived bio-oils involves a HydroDeOxygenation (HDO) reaction through either the Hydrogenation (Hyd) or the Direct DeOxygenation (DDO) route, the latter limiting hydrogen consumption. Herein, dispersion-corrected DFT has been used to evaluate the adsorption behavior of phenol (as a representative model of bio-oils) and two by-products (water and CO) over various crystalline and amorphous silica surfaces to evaluate their potential selectivity (DDO/ Hyd) and efficiency (low inhibiting effect) for HDO processing. Phenol can adsorb through three modes, flat π-interaction, flat O-interaction or perpendicular O-interaction. All crystalline surfaces show a preference for the flat π-interaction, which is expected to promote the Hyd route. Over amorphous surfaces the flat O-interaction dominates, and a very specific and strong interaction (around -120 kJ/mol) was found on SiO2-3.3 and SiO2-2.0 surfaces where the phenol molecule loses its aromaticity, which is very promising for its degradation under catalytic conditions. In addition, this makes those surfaces very efficient to adsorb selectively phenol in presence of water and CO. Remarkably, on all silica surfaces, the interaction energy of CO is nearly negligible, which makes them more attractive for HDO process compared to sulfide catalysts with respect to the inhibiting effect criteria.

3.1 Introduction

Hydrocarbons derived from lignocellulosic biomass have gathered an increasing interest for fuel production as they are respectful of environmental norms on CO_2 emissions.[1–3] Lignin consists of aryl ether units connected by ether and alkyl bonds, and the cleavage of those bonds yields to monomeric phenols and methoxyphenols.[4] Thus, bio-oils obtained by the pyrolysis of lignin contain a large number of phenolic compounds, up to 30% of the total oxygenated compounds, which represent 45 wt.% of the fraction. The other oxygenates present multiple functions such as aromatics, aldehydes, ketones, esters, acids, and alcohols.

A high oxygen content leads to deleterious properties such as thermal and chemical instability, high viscosity and poor engine efficiency.[5–8] Those bio-oils can be upgraded by HydroDeOxygenation (HDO), a thermal catalytic reaction under hydrogen pressure, to obtain oxygen-free molecules (aromatics or/and cycloalkanes) and water as the main by-product. It appears that phenolic compounds like guaiacol and alkylphenols are the most refractory compounds to the HDO process.[9] Therefore, in addition to studies devoted to the HDO of real feeds,[10–13] the majority of research efforts are dedicated to the catalytic conversion of phenolic model molecules[14] such guaiacol and its derivates.[15–19] Beside experimental studies, Density Functional Theory (DFT) calculations were used also to study the adsorption of oxygenated compounds and the competition of inhibiting molecules on catalytic sites present under HDO conditions.[20–25]

These experimental and theoretical studies have shown that phenolic compounds follow two main deoxygenation routes: (i) the hydrogenation route (Hyd), which consists of the hydrogenation of the benzene ring into cyclohexyl before C-O bond cleavage or (ii) the direct deoxygenation (DDO) route where the C-O bond is directly broken, which limits the consumption of hydrogen.[14–16,26,27] Excessive hydrogen consumption during the HDO reaction via the Hyd route increases the operating costs. Those costs are due to the use of large H_2 storage and pressurizing equipment, in addition to high H_2 and electricity consumption.[13] Therefore, the development of catalysts that enhance the DDO pathway is actively sought. Besides being selective towards the DDO pathway, a suitable HDO catalyst must meet other criteria such as a high activity, a good stability (*i.e.* no or limited deactivation), resistance to the inhibiting effect of the by-products, H_2O[28,29] and CO,[26,30] and sustainability for environmental purposes.

Several catalysts and supports have been investigated extensively experimentally and theoretically in this field, including sulfides and metals.[11–14,19,27–33] Conventional sulfides CoMo and NiMo catalysts show promising performances following the DDO route.[5,16,27] However, their main drawback is the necessity to add H_2S in the feed to prevent catalyst oxidation.[21,34,35] In addition, H_2S can poison the active sites leading to a strong deactivation of the catalysts.[26,28,35] Sulfide catalysts are also sensitive to water[29] and carbon monoxide[26,30] under HDO conditions. Noble metals showed a high activity but are expensive and have a low selectivity toward aromatics.[13,19,33] Olcese *et al.*[18,36,37] studied the competition between DDO and Hyd routes using non-noble metals (Fe and Co) and showed that Fe/SiO_2 presents an interesting selectivity toward the DDO pathway. They proposed that the metallic reduced iron particles promote the dissociation of H_2, and then the H atoms react with the phenolic molecules adsorbed on the silanol groups of the silica surface.[36] The adsorption mechanisms of phenolic bio-oil molecules on different supports were studied by Popov *et al.*,[38] showing that silica is more suitable for this purpose compared to alumina and silica-alumina supports.

Several DFT and combined DFT/experimental studies were done by Badawi *et al.*[20–22,30] in order to study the adsorption of oxygenated bio-oils and inhibiting competitive molecules (H_2S, water, and CO) over MoS_2 and CoMoS catalysts under HDO conditions. Those studies enlightened the main reason of the deficiency and deactivation of sulfided catalysts which is the very high competitive adsorption of water and CO. Using Density Functional Theory at finite temperature, Mian *et al.*[39] investigated the adsorption of catechol on the hydrophilic (001) cristobalite silica surface, having geminal silanol sites, in presence of competitive water molecules, and they concluded that catechol molecules displace preadsorbed water molecules and adsorb on the surface with a binding energy of -96 kJ/mol. Simonetti *et al.*[40] admitted the nomination of “parallel” and “perpendicular” when examining the adsorption modes of 5-fluorouracil on β-cristobalite surface. They identified the H-bonding interactions between the molecule and the surface silanols, and proved their effect on stabilizing the molecule on the silica surface. They also discussed the occurrence of π-interaction (between the aromatic ring and the silanol group) in the “parallel” adsorption,[40,41] in accordance with Rimola *et al.*[42] results on benzene-silanol interactions. Other molecules have been studied showing the importance of the H-bonding interactions, induced by the existence of silanols on the silica surface, in controlling drug delivery.[43,44] Inspired by those previous works in HDO field as well as by similar studies on the adsorption modes during the HydroDeSulfurization HDS of thiophene[45–47] we investigated herein two main adsorption modes: (1) perpendicular O-interaction of phenol (perp O-int) *vs* (2) flat π-interaction (flat π-int) on silica surface. The phenol perp O-int adsorption mode is expected to favor the DDO route and to produce benzene as a major product, while the phenol flat π-int adsorption mode is expected to favor the Hyd route and to produce cyclohexanol that deoxygenate to give cyclohexane as a major product **(see Figure 3.1)**.

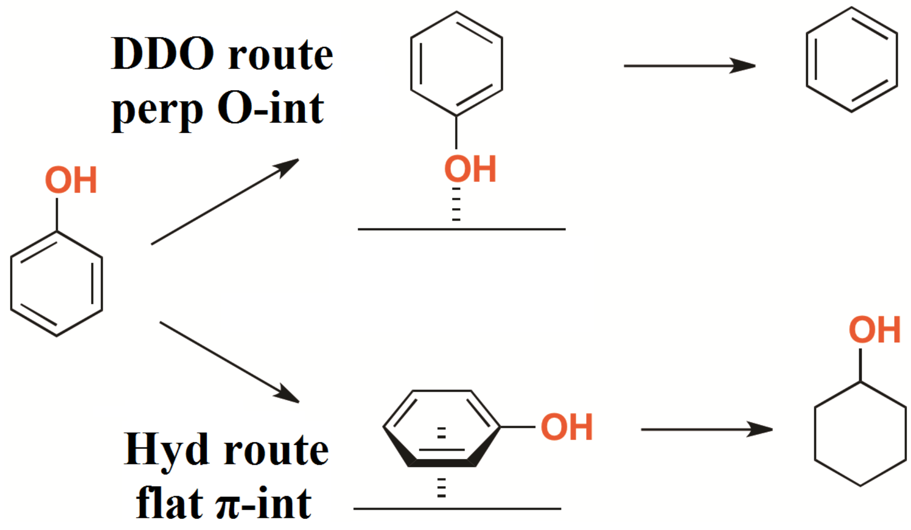

Figure 3.1 *Phenol adsorption mechanisms over silica surface: perpendicular O-interaction (perp O-int) promoting the DDO route vs flat π-interaction (flat π-int) promoting the Hyd route.*

Despite the fact that previous studies showed promising performance of silica-supported catalysts in HDO processing,[13,18,19,37,38] the adsorption mechanisms and energies of phenolic molecules and by-products such as H_2O and CO over different sites of various possibly used silica surfaces for the HDO application have not been studied yet. Here, the adsorption energies of phenol (as a representative model of bio-oil vapors) and the by-products (water and CO) are computed by DFT calculations over different crystalline and amorphous silica structures in order to identify the most efficient surface that favors perp O-int (therefore expected to promote the DDO route) and bears the lowest inhibiting effect of the by-products. The present study is organized as follows: first, we will present the silica models used in this work, including crystalline surfaces ((111), (101), (001) β-cristobalite, and (001) α-quartz) and amorphous surfaces[48] (with a silanols density ranging from 1.1 to 7.2 OH/nm^2). Then, the DFT methods and parameters, and the calculation method of the adsorption energies are described. After, we will present the results of the phenol adsorption following different modes and the potential promotion of the DDO or the Hyd routes attached to each mode. Then, the inhibiting effect of water and CO on the adsorption of phenol over all silica surfaces is interpreted. From those results and experimental conditions, a conclusion is deducted on the most appropriate surface that would promote the DDO route with less competition of inhibiting molecules.

3.2 Materials and Methods

3.2.1 Models of Silica Surfaces

3.2.1.a β-cristobalite surfaces

In order to build our models, we used the bulk geometry of SiO_2 that was previously relaxed in the tetragonal $I\bar{4}2d$ space group.[49,50] Surfaces are modeled by slabs, constructed by cutting the bulk crystal along the (111), (101) and (001) crystallographic planes. The surfaces are terminated by oxygen atoms which are saturated with hydrogen, hence forming hydroxyl-group-covered surfaces (–OH), which are representative of the energetically most stable SiO_2 surfaces.[50]

Three layers of [111], [101] and [001] silica surfaces having isolated silanols with a density of 4.29 OH/nm^2, 5.24 vicinal sites per nm^2 and 7.42 geminal sites per nm^2, respectively, were constructed. The two bottom layers are frozen in the geometry of the bulk and the top layer is free to relax. The [111] surface unit cell **(Figure 3.2.a)** is composed of 96 Si, 208 O, and 32 H atoms with a = 20.26, b = 20.57, c = 31.54 Å (including 15 Å of vacuum). The [101] surface **(Figure 3.2.b)** unit cell is composed of 80 Si, 176 O, and 32 H atoms, while the [001] surface **(Figure 3.2.c)** is composed of 64 Si, 144 O, and 32 H atoms.

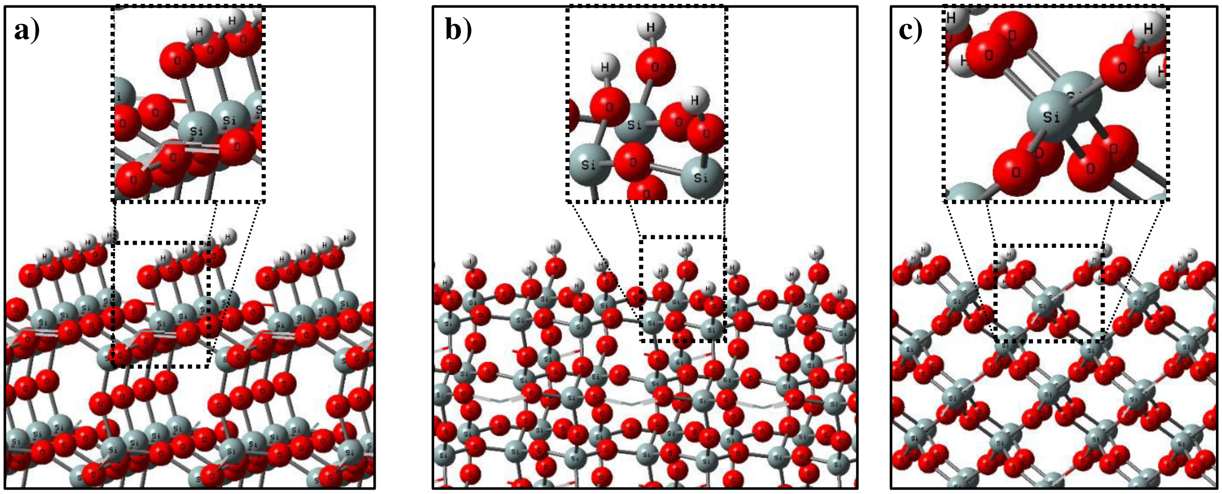

Figure 3.2 a) *[111] β-cristobalite unit cell with isolated silanols (4.29 OH/nm^2),* ***b)*** *[101] β-cristobalite unit cell with vicinal silanols (5.24 OH/nm^2), and* ***c)*** *[001] β-cristobalite unit cell with geminal silanols (7.42 OH/nm^2).*

3.2.1.b [001] α-quartz surface

Periodic DFT studies of the cleaved, reconstructed and fully hydroxylated [001] α-quartz surfaces at various thickness have been performed by Goumans *et al.*[51] The surface investigated herein is the fully hydroxylated one used also by Abbasi *et al.*[52] with 8.28 OH/nm^2 of geminal, H-bonded to each other's, silanols. The studied surface, shown in **Figure 3.3**, is constructed using a SiO_2 slab in a tetragonal supercell 14.74*14.74*25 Å^3 (including 10 Å of vacuum) and composed of 36 H, 126 O, and 54 Si atoms.

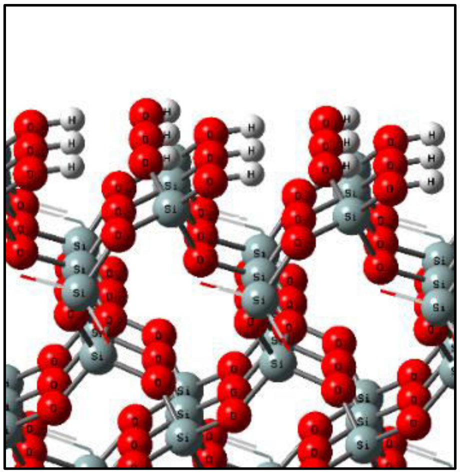

***Figure 3.3** Fully hydroxylated [001] α-quartz silica surface with 8.28 geminal OH/nm^2.*

3.2.1.c Amorphous surfaces

Amorphous surfaces are notoriously difficult to handle with periodic calculations. Here, we use some of the geometries constructed by Comas-Vives[48] via the dehydroxylation of a fully hydroxylated surface. The amorphous silica structures having a silanols density of 7.2, 5.9, 4.6, 3.3, 2, and 1.1 OH/nm^2 were chosen as a representative sample, and labelled SiO_2-7.2, SiO_2-5.9, SiO_2-4.6, SiO_2-3.3, SiO_2-2, and SiO_2-1.1 respectively. **Figure 3.4** shows the fully hydroxylated SiO_2-7.2 **(Figure 3.4.a)** and fully dehydroxylated SiO_2-1.1 **(Figure 3.4.b)** amorphous surfaces. Five silanol group types (isolated, vicinal, geminal, nest-1, and nest-2) are present on the SiO_2-7.2 fully hydroxylated surface, while only isolated silanols are present on the SiO_2-1.1 fully dehydroxylated surface.

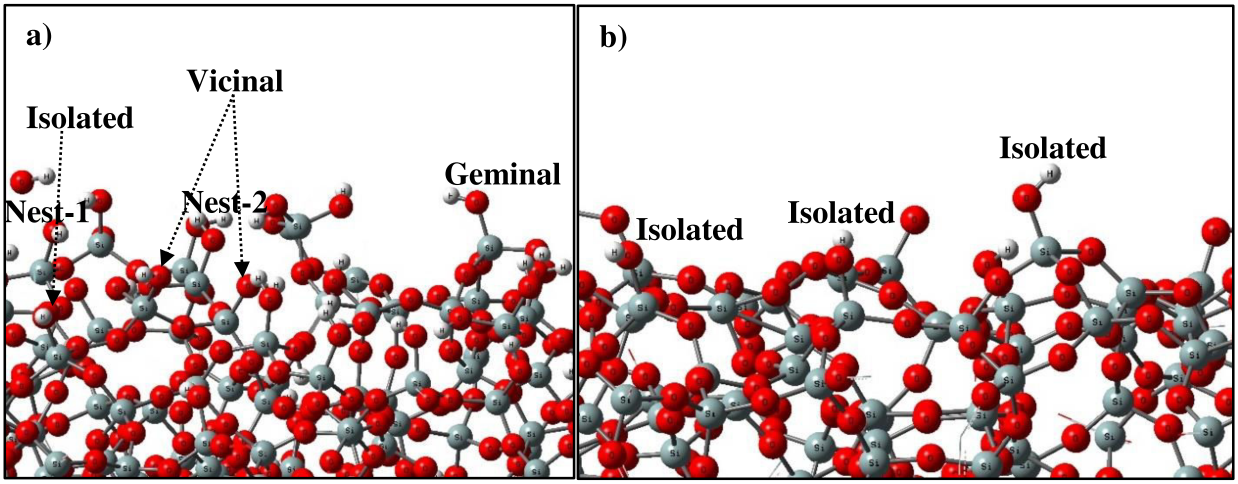

Figure 3.4 a) *Amorphous SiO_2-7.2 (7.2 OH/nm^2) surface with various silanol groups,* ***b)*** *Amorphous SiO_2-1.1 (1.1 OH/nm^2) surface with only isolated silanol groups.*

3.2.2 Computational Methods

Periodic DFT calculations[53,54] have been performed using the Vienna Ab initio Simulation Package (VASP),[55,56] where the electronic wave functions have been expanded into plane waves up to a 450 eV cut-off energy. The semi-local Perdew−Burke−Ernzerhof (PBE) exchange-correlation functional in the generalized gradient approximation (GGA) proposed by Perdew *et al.*[57] was chosen. The projector augmented wave (PAW) method[58,59] was used to describe the electron-ion interactions and the Kohn-Sham equations were solved self-consistently until the energy difference between cycles decreases below 10^{-6} eV. A Gaussian smearing of $\sigma = 0.1$ eV was applied to band occupations in order to improve the total energy convergence. The atomic positions have been relaxed until all forces were smaller than 0.03 eV/ Å per atom. The Γ-point was used for the Brillouin zone integration.

The importance of dispersion forces on DFT calculations for similar adsorption applications where adsorbates are very close to the surface was highlighted by Sun *et al.*[60] Therefore, Van der Waals (vdW) interactions have been taken into account[61–65] to describe the long-range electron correlation that contributes significantly to the adsorption process. A computationally affordable approach consist in adding a pairwise interatomic C_6R^{-6} term to the DFT energy[66–71]. Here, the semi-empirical D2 approach of Grimme[68,69] is adopted. In **Annex 1**, we will present the effect of dispersion (vdW) forces on the adsorption energies of studied molecules over crystalline surfaces, in order to highlight the importance of taking into account those interactions.

Several sets of DFT calculations have been conducted, the first considers the relaxation of the first layer of the silica structure (with the bottom fixed) and enable us to obtain the energy of pure silica surface $\mathrm{E_{Sil,DFT}}$. The second set enables determining the energies of isolated molecules water, CO, and phenol in the gaseous phase $\mathrm{E_{X,DFT}}$ (where all atoms are relaxed). The third is a geometrical optimization of the interaction of those molecules on the silica surface, giving $\mathrm{E_{Sil-X,DFT}}$ (the molecules and the first silica layer are relaxed). From those energies, we calculate the adsorption energies $\mathrm{E_{ads,DFT}}$ between molecules and the silica surface as follow.

$$\mathrm{E_{ads,DFT}} = \mathrm{E_{Sil-X,DFT}} - \mathrm{E_{Sil,DFT}} - \mathrm{E_{X,DFT}}$$

3.3 Results and Discussions

3.3.1 Phenol Adsorption Modes on Silica Surfaces

The type and the number of interacting silanol groups with the phenol molecule affect the adsorption mode. On one hand, the perp O-int adsorption mode, that is expected to promote the DDO route, includes usually the interaction of the oxygen atom of phenol with the hydrogen atom of the silanol group (H-bond acceptor, Ph**O**H·····**H**O-Si) and/or the interaction of the hydrogen atom of phenol with the oxygen atom of the silanol group (H-bond donor, PhO**H**·····H**O**-Si). On the other hand, the flat π-int adsorption mode, that would favor the Hyd route, is induced principally by the interaction of the phenol ring with the OH of the silanol group (π-interaction, HO-**Ph(π)**·····**HO**-Si), but it may include the H-bond donor and H-bond acceptor interactions types. The third adsorption mode, flat O-int, is found over amorphous surfaces where the phenol molecule interacts with the surface through its hydroxyl group (H-bond donor or/and acceptor), which would be to the advantage of the DDO route. However, the aromatic ring is parallel to the surface and would be close enough to promote also the Hyd route **(Figure 3.5)**.

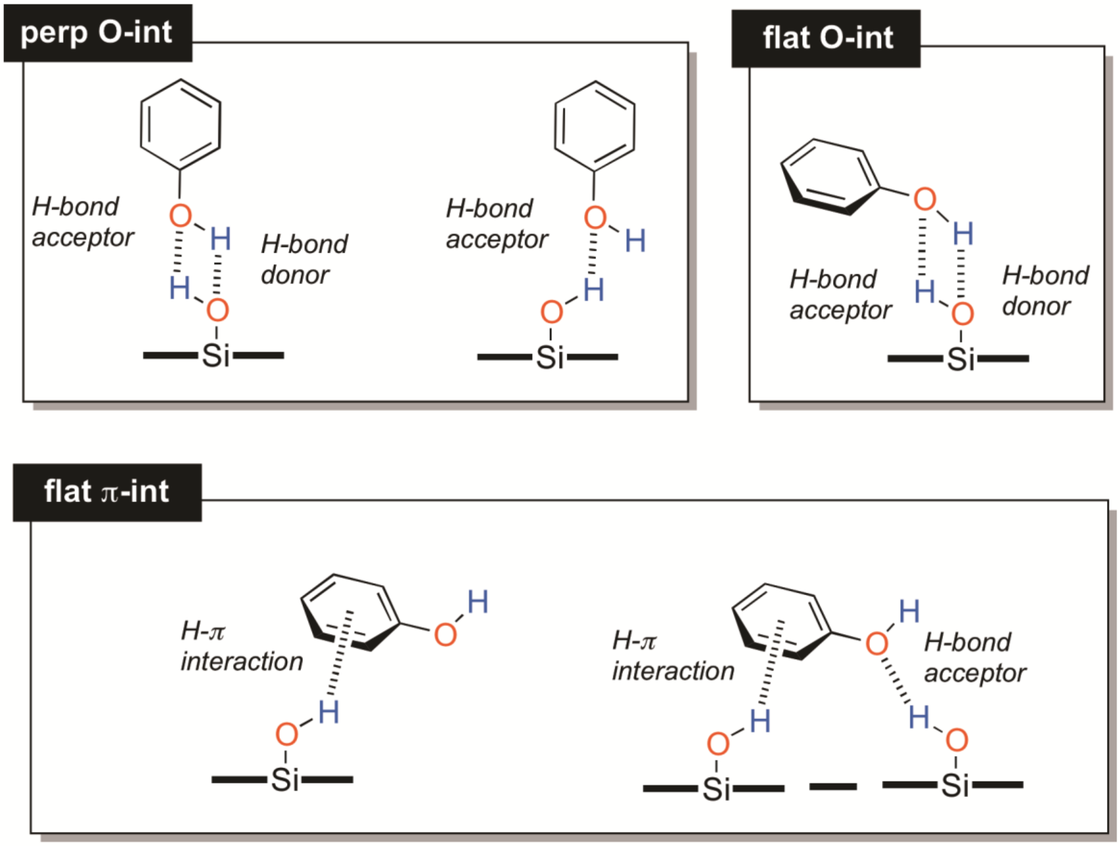

Figure 3.5 The possible types of interaction (H-bond donor, H-bond acceptor, and π-interaction) occuring during the adsorption of phenol via the three modes perp O-int, flat π-int, and flat O-int over silica surfaces.

3.3.1.a Crystalline silica surfaces

Two possible phenol adsorption mechanisms (perp O-int and flat π-int) have been identified over the [001], [101], [001] β-cristobalite surfaces, and [001] α-quartz surfaces (**Figure 3.6**). The adsorption energies of phenol in both modes over the various crystalline surfaces are compared in **Figure 3.7**. Results show that the [101] β-cristobalite surface, having vicinal silanols, favors equally the perp O-int and the flat π-int modes in comparison to other crystalline surfaces where the flat π-int mode dominates.

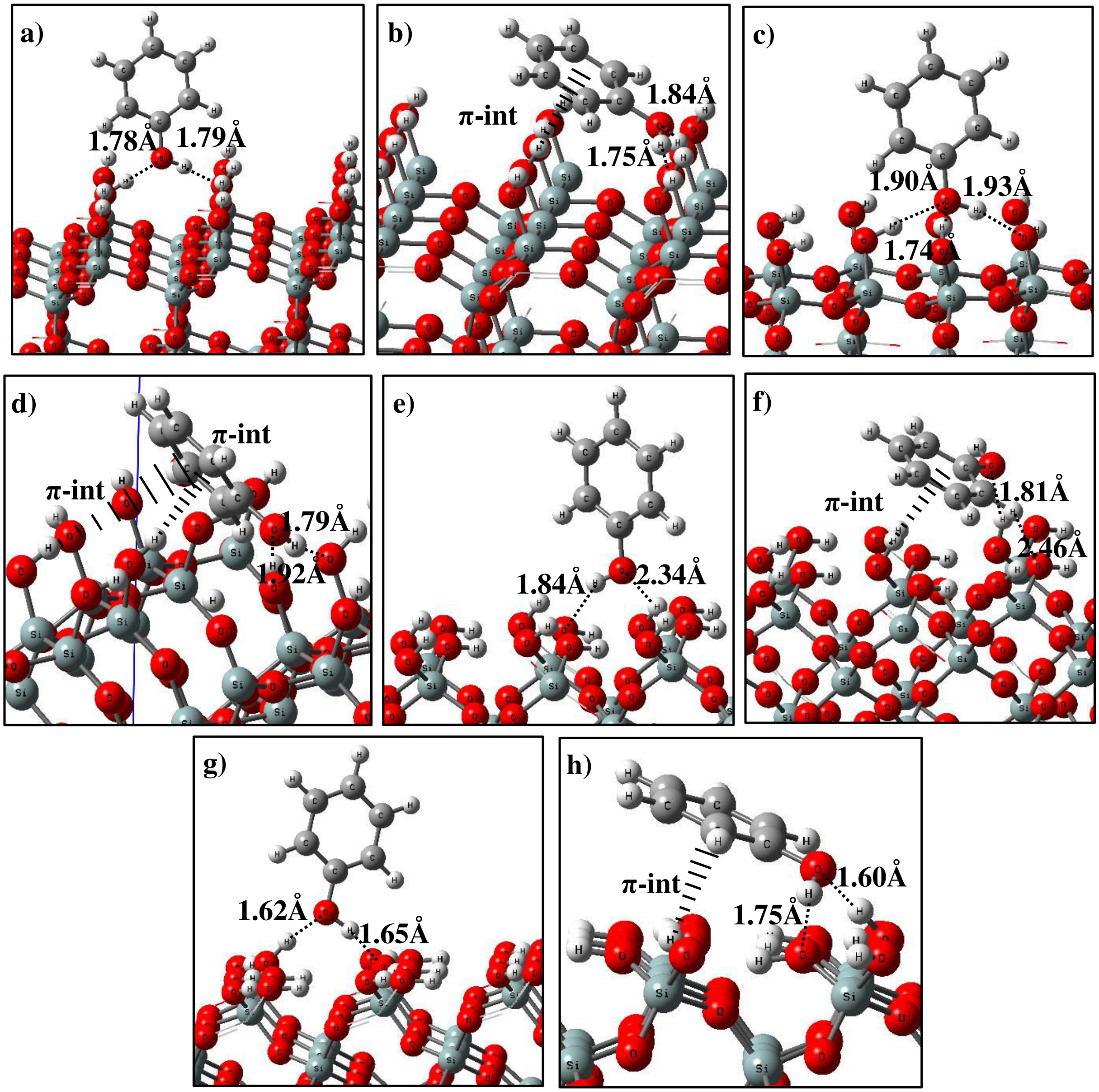

***Figure 3.6** Phenol adsorption configuration modes over crystalline silica surfaces: **a)** perp O-int over [111] β-cristobalite, **b)** flat π-int over [111] β-cristobalite, **c)** perp O-int over [101] β-cristobalite, **d)** flat π-int over [101] β-cristobalite, **e)** perp O-int over [001] β-cristobalite, **f)** flat π-int over [001] β-cristobalite, **g)** perp O-int over [001] α-quartz, **h)** flat π-int over [001] α-quartz.*

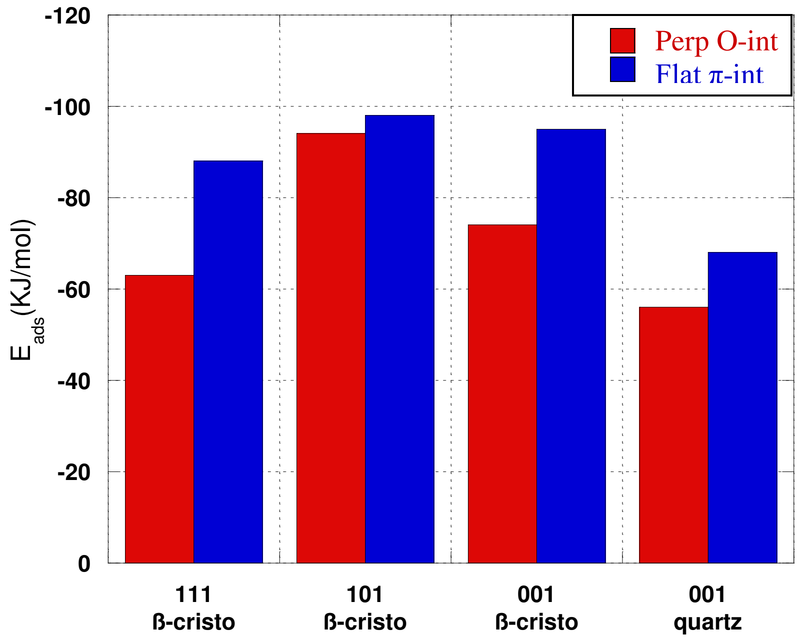

Figure 3.7 *Adsorption energies of phenol (perp O-int vs flat π-int) over crystalline surfaces.*

The interaction types and lengths between phenol molecule and silanol groups of different surfaces are presented in **Table 3.1**. The length of the interaction between the OH group of the phenol and the silanols varies from 1.60 to 2.05 Å depending on the silica surface (density and type of silanols). When comparing the phenol perp O-int with the flat π-int over the [101] β-cristobalite; it appears that the H-bond donor and acceptor interaction types present similar bonding lengths resulting in similar interactions. Another important geometrical parameter is the length of the C-O bond of the phenol molecule, the initial C-O bond length before interaction with silica surfaces being of approximately 1.40 Å. This length decreases to an average of 1.38 Å with no large variation depending on the adsorption mechanism and the silica surface. It is obvious that high adsorption energies correspond to phenol adsorption over silica surfaces having three interactions, while those having two interactions show an energy around -65 kJ/mol, and those with only one-interaction show lower energy values.

Table 3.1 *Interaction types and distances between phenol and crystalline surfaces.*

	perp O-int	**flat π-int**
[111] β-cristobalite	Ph**O**H·····**H**O-Si: 1.82 Å	Ph**O**H·····**H**O-Si: 2.05 Å
	PhO**H**·····H**O**-Si: 1.79 Å	PhO**H**·····H**O**-Si: 1.76 Å
	-	HO-**Ph(π)**·····**HO**-Si
[101] β-cristobalite	Ph**O**H·····**H**O-Si: 1.92 Å	Ph**O**H·····**H**O-Si: 1.92 Å
	Ph**O**H·····**H**O-Si: 2.05 Å	PhO**H**·····H**O**-Si: 1.79 Å
	PhO**H**·····H**O**-Si: 1.82 Å	HO-**Ph(π)**·····**HO**-Si
[001] β-cristobalite	Ph**O**H·····**H**O-Si: 1.71 Å	Ph**O**H·····**H**O-Si: 2.00 Å
	PhO**H**·····H**O**-Si: 1.70 Å	PhO**H**·····H**O**-Si: 1.74 Å
	-	HO-**Ph(π)**·····**HO**-Si
[001] α-quartz	Ph**O**H·····**H**O-Si: 1.60 Å	Ph**O**H·····**H**O-Si: 1.60 Å
	-	PhO**H**·····H**O**-Si: 1.75 Å
	-	HO-**Ph(π)**·····**HO**-Si

3.3.1.b Amorphous silica surfaces

Figure 3.8 shows the adsorption modes of phenol on various amorphous silica surfaces as a function of the silanol type and densities. Adsorption energies of phenol corresponding to various interaction modes (perp O-int, flat π-int, and flat O-int) over all considered sites of silica surfaces are compared in **Table 3.2**.

Based on the models of Comas-Vives,[48] five types of silanols (isolated, nest-1, vicinal, nest-2, geminal) are present on the most saturated surfaces for 3.3 OH/nm^2 and higher. Nest 1 site is composed of a vicinal silanol and an isolated silanol while nest 2 is composed of a geminal silanol associated to one OH group of a neighbor vicinal silanol. For SiO_2-2.0, one can observe the disappearance of nest-2 and geminal sites. For the most unsaturated surface SiO_2-1.1, only isolated sites are present. If we compare the strength of adsorption sites per sites, the interaction of phenol with the silanols globally increase in the following order: isolated and vicinal (from -19 to 55 kJ/mol) < geminal (from -22 to -76 kJ/mol) < nest-2 (from -31 to -77 kJ/mol) < nest-1 (from -33 to -120 kJ/mol).

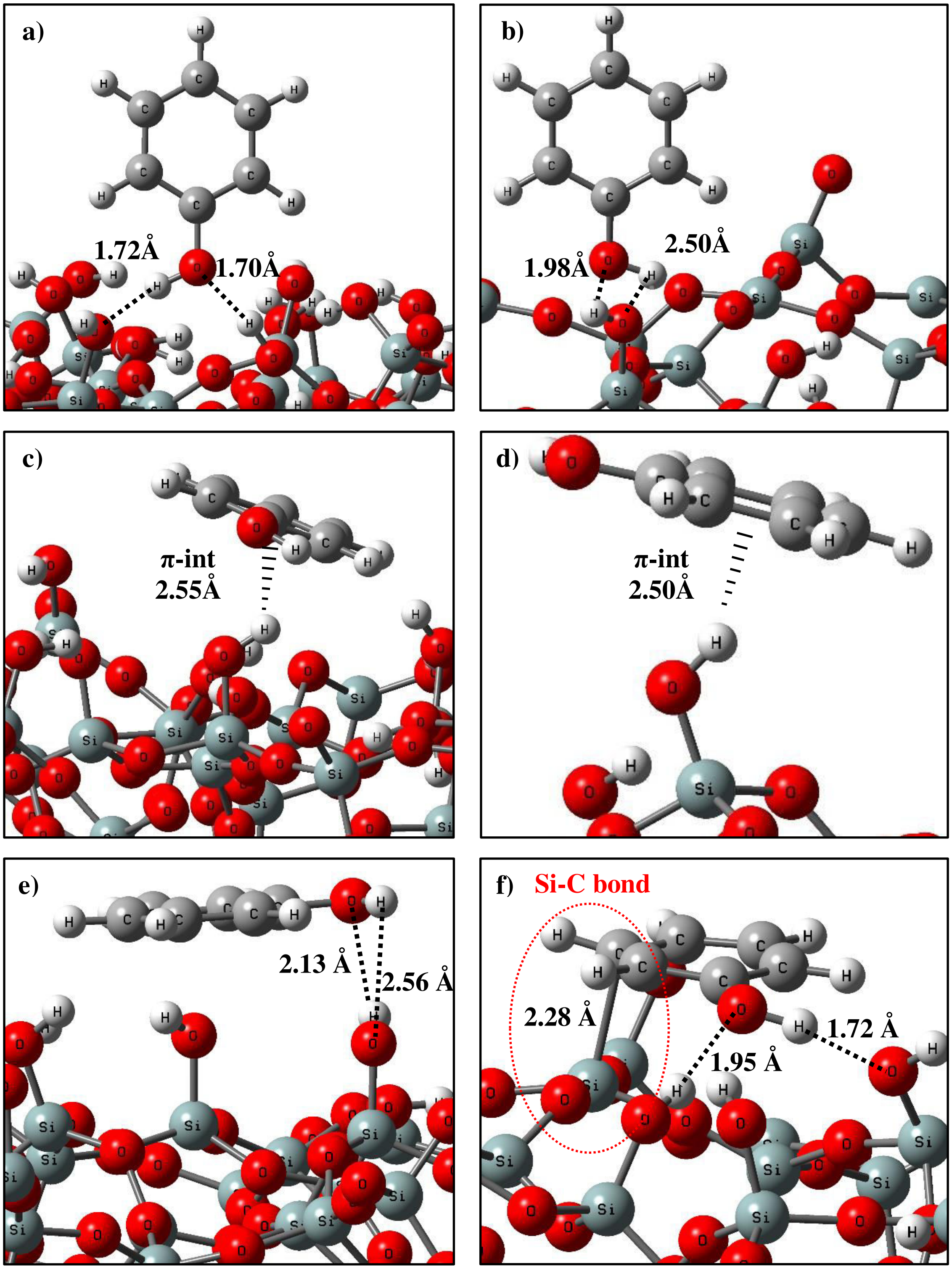

***Figure 3.8** Adsorption mechanisms of phenol over different sites of various amorphous silica surfaces: **a)** perp O-int over nest-2 site of SiO_2-7.2, **b)** perp O-int over vicinal site of SiO_2-2, **c)** flat π-int over vicinal site of SiO_2-5.9, **d)** flat π-int over isolated site of SiO_2-1.1, **e)** flat O-int over nest-2 site of SiO_2-3.3. f) flat O-int over nest-1 site of SiO_2-2.0.*

Table 3.2 *Phenol adsorption energies (kJ/mol) over different sites of amorphous surfaces with various silanol densities and types. The most favorable configuration for phenol adsorption is indicated in bold for each silanols density.*

Silanols Site		Isolated	Nest-1	Vicinal	Nest-2	Geminal
SiO_2-7.2	**perp O-int**	-33	-54	-30	-65	-46
	flat π-int	-34	-59	-26	-45	-29
	flat O-int	-31	-34	-55	**-70**	-51
SiO_2-5.9	**perp O-int**	-26	-50	-29	-51	-27
	flat π-int	-22	-46	-29	-31	-27
	flat O-int	-26	**-52**	-30	-35	-24
SiO_2-4.6	**perp O-int**	-19	-69	-23	-62	-76
	flat π-int	-42	**-82**	-33	-65	-43
	flat O-int	-27	-80	-19	-44	-58
SiO_2-3.3	**perp O-int**	-34	-54	-20	-73	-23
	flat π-int	-29	-33	-18	-42	-22
	flat O-int	-31	**-117**	-35	-77	-24
SiO_2-2.0	**perp O-int**	-19	-53	-21	*	*
	flat π-int	-22	-35	-17	*	*
	flat O-int	-30	**-120**	-38	*	*
SiO_2-1.1	**perp O-int**	-22	*	*	*	*
	flat π-int	-24	*	*	*	*
	flat O-int	**-26**	*	*	*	*

For the SiO_2-7.2 surface which presents the highest silanol density, the most favorable configuration for phenol adsorption is a flat O-int on the nest 2 (-70 kJ/mol), followed by a flat π-int on the nest 1 (-59 kJ/mol). For silanol density ranging from 2 to 5.9 OH/nm^2, the phenol always prefers to accommodate on the nest 1, via a flat O-int mode, except for SiO_2-4.6 where the flat O-int and flat π-int modes coexist (adsorption energy around -80 kJ/mol). In addition for this silanol density, phenol can adsorb quite strongly (-76 kJ/mol) on the geminal site through a perp O-int mode, which could favor the DDO route in HDO reaction.

For SiO_2-2 and SiO_2-3.3 surfaces, very high interaction energies (around -120 kJ/mol) are observed for nest 1, due to an optimal accommodation of the phenol molecule on the surface. For this configuration (see **Figure 3.8.f**), two hydrogen bonds are formed, one between the H atom of the hydroxyl group of phenol and the O atom of an isolated silanol (1.72 Å), the other between the O atom of phenol and the H atom of a vicinal silanol (1.95 Å). In addition, a deformation of the phenol structure (loss of its planarity corresponding to a destabilization around 20 kJ/mol compared to the molecule alone), is observed leading to a specific interaction between the aromatic ring and a Si atom of the surface (distance between this Si atom and the carbon γ of 2.28 Å). Similar adsorption configurations have been found in the literature for furan[20] and thiophene[45] on MoS_2 surfaces, which chemically activate the molecules. The interaction energy of phenol with the nest 1 progressively decreases when the silanol density increases, as the presence of additional silanol group(s) hinder or limit the interaction(s) described above. Finally, the SiO_2-1.1 weakly adsorb phenol (around -25 kJ/mol) without favoring any adsorption mode.

Phenol can be more adsorbed on amorphous silica surfaces than crystalline surfaces in general because of the presence of silanol nests on the amorphous surfaces which allows the phenol to interact though several hydrogen bonds, π-ring interaction and Si-C bonds at the same time. However, when comparing similar sites of both types of surface (namely geminal, vicinal and isolated silanols), we observe higher phenol adsorption energies over crystalline surfaces, due to the surrounding environment of the site and the morphology of the structure. For example, the adsorption energy of phenol on the isolated site for all the amorphous surfaces is around -30 kJ/mol, which is much smaller than the one found (-88 kJ/mol) over the [111] β-cristobalite surface (having only isolated silanols). This high value is due to the surrounding isolated silanols over the crystalline surface where the phenol molecule interacts with several isolated silanols, while over the amorphous surface the isolated site is really far from any other silanol.

Regarding the potential consequences on the reactivity of phenol upon HDO conditions, it is hard to conclude on the DDO or HYD selectivity as the flat O-int is the most favorable configuration for almost all amorphous silica surfaces. Only the SiO_2-4.6 shows a potential good HDO selectivity as it could favor the DDO route if phenol adsorbs on geminal sites. Further investigations such as the calculation of reaction mechanisms are needed to provide better conclusions, but they are beyond the scope of the present work. Nonetheless, one important feature of materials to be used in HDO processes is their ability to prevent inhibiting effect of by products on the adsorption of reactants, which will be developed in the next section.

3.3.2 Competitive Adsorption of Inhibiting Molecules

The competitive adsorption of inhibiting molecules (water and CO) is one of the main parameters that affect the hydrodeoxygenation process. A comparative histogram of adsorption energy of water, CO, and phenol onto crystalline silica surfaces is presented in **Figure 3.9**. The interaction energy of CO is low (around -20 kJ/mol) whatever the crystalline surface. As the energy of phenol adsorption is around -90 kJ/mol, the inhibition effect of CO is expected to be negligible. Those results suggest that silica-based materials are particularly promising for the HDO process comparing to conventional MoS_2 and CoMoS catalysts which suffer from a strong competitive adsorption of CO (CO interaction energy over CoMoS 50% M-edge is four times higher than that of phenol, with a value of -160 kJ/mol), in addition to the poisoning effect of H_2S.[30]

Our computed water adsorption energies are similar to those calculated by Yang *et al.*[72] for [111] β-cristobalite (-77 kJ/mol compared to -74 kJ/mol) and [001] β-cristobalite (-42 kJ/mol compared to -43 kJ/mol). As well, similar adsorption energy is found over the [001] α-quartz as that reported by Yang *et al.*[73] (-58 kJ/mol compared to -53 kJ/mol). The competition between water and phenol cannot be considered minor, with an adsorption energy difference of about -10 kJ/mol, except on the [001] β-cristobalite surface. The water adsorption energy of those surfaces is much higher than the water liquefaction heat (-44 kJ/mol) that is usually used to define the hydrophobicity of the surface.[74,75] Therefore, the [111] β-cristobalite, [101] β-cristobalite and [001] α-quartz surfaces can be considered as hydrophilic, unlike the [001] β-cristobalite surface where the adsorption energy of water is around -42 kJ/mol.

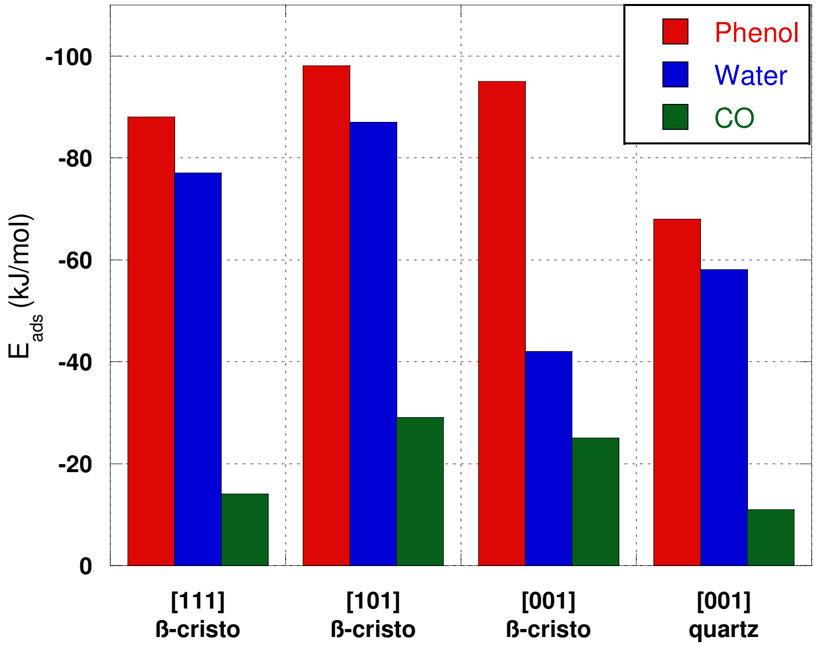

Figure 3.9 *Adsorption energies of phenol and inhibiting molecules over crystalline surfaces.*

The adsorption energies of phenol and inhibiting molecules on various sites of amorphous surfaces are gathered in **Table 3.3**. As for crystalline surfaces, CO is weakly adsorbed compared to phenol.

Indeed, the CO adsorption energy over the more hydroxylated surface (SiO_2-7.2) is around -20 kJ/mol, and it is much smaller over other surfaces. The inhibiting effect of water on the adsorption of phenol is expected to be important for the most hydroxylated surfaces (SiO_2-7.2 and SiO_2-5.9) as the adsorption energy of water can exceed the one of phenol by 50 kJ/mol on some sites (as the isolated silanol). However, the effect of water becomes more and more limited when decreasing the silanol density, in line with the fact that amorphous surfaces having a silanol density larger than 5 OH/nm^2 can be considered hydrophilic (E_{ads} > heat of liquefaction). Over SiO_2-4.6, the adsorption energies of water and phenol are similar for every sites except the isolated one where phenol is more adsorbed than water by 22 kJ/mol. Remarkably, the adsorption of phenol is expected to be not impacted by the presence of water on the SiO_2-3.3 and SiO_2-2.0 surfaces as their nest-1 site can strongly interact with phenol (around -120 kJ/mol), which is much larger than water on the same site (around -50 kJ/mol) or other sites (between -20 and -30 kJ/mol).

Table 3.3 *Inhibiting molecules competition: Adsorption energies (kJ/mol) of water, CO, and phenol over different sites of amorphous surfaces.*

Silanol Sites		**Isolated**	**Nest-1**	**Vicinal**	**Nest-2**	**Geminal**
SiO_2-7.2	**Phenol**	-34	-59	-55	-70	-51
	H_2O	-85	-67	-26	-74	-30
	CO	-18	-21	-18	-21	-19
SiO_2-5.9	**Phenol**	-26	-52	-30	-51	-27
	H_2O	-76	-55	-39	-58	-24
	CO	-8	-9	-14	-14	-11
SiO_2-4.6	**Phenol**	-42	-82	-33	-65	-76
	H_2O	-20	-81	-32	-63	-67
	CO	-10	-13	-12	-21	-13
SiO_2-3.3	**Phenol**	-34	-117	-35	-77	-24
	H_2O	-34	-51	-24	-70	-19
	CO	-11	-11	-11	-12	-7
SiO_2-2.0	**Phenol**	-30	-120	-38	*	*
	H_2O	-31	-55	-24	*	*
	CO	-14	-13	-11	*	*
SiO_2-1.1	**Phenol**	-26	*	*	*	*
	H_2O	-33	*	*	*	*
	CO	-13	*	*	*	*

3.4 Conclusions

The HydroDeOxygenation (HDO) reaction is a key step in the upgrading of lignin and occurs through either the Hydrogenation (Hyd) or the Direct DeOxygenation (DDO) route, the latter being highly desirable because it limits the hydrogen consumption. The selectivity (DDO route promotion) and the efficiency (low inhibiting effect of by-products) of the HDO reaction are strongly depending on the surface properties of the catalyst. Knowing that the adsorption is the first step of the catalytic mechanism, this study focuses on the adsorption properties of different crystalline and amorphous silica surfaces. The adsorption energies of phenol via three interaction modes (perpendicular O-interaction, flat π-interaction, and flat O-interaction), and inhibitor molecules (water and CO) over silica surfaces are investigated and compared using dispersion-corrected DFT calculations. The flat π-interaction, where the phenol is parallel to the surface and interacts with it through its aromatic ring, dominates over all crystalline surfaces, which would favor the Hyd route. Over amorphous surfaces the flat O-interaction dominates, and a very specific and strong interaction (around -120 kJ/mol) was found on SiO_2-3.3 and SiO_2-2.0 surfaces where the phenol molecule loses its aromaticity, which is very promising for its degradation under catalytic conditions.

Furthermore, the competitive effect of inhibiting molecules (water and CO) is interpreted. We have shown that CO competition is negligible over all silica surfaces, which make them more attractive than conventional sulfide catalysts in respect with this criterion. The inhibiting effect of water on the adsorption of phenol is expected to be important for the amorphous surfaces having a silanol density higher than 5 OH/ nm^2. However, the SiO_2-3.3 and SiO_2-2.0 surfaces exhibit a very weak adsorption of water (and CO) compared to phenol. Our results should motivate the synthesis of amorphous silica having between 2 and 4 OH/nm^2 and further catalytic tests for HDO applications as they could present a highly selective adsorption of phenolic molecules towards by-products H_2O and CO.

References

(1) The Promotion of the Use of Biofuels or Related Other Renewable Fuels for Transport. EU Directive 2001/0256(COD), **2003**.

(2) Holladay, JE.; Bozell, JJ.; White, JF.; Johnson, D. *Top Value-Added Chemicals from Biomass*; PACIFIC NORTHWEST NATIONAL LABORATORY operated by BATTELLE for the UNITED STATES DEPARTMENT OF ENERGY, **2007**; Vol. II: Results of Screening for Potential Candidates from Biorefinery Lignin.

(3) Haveren, J. van; Scott, E. L.; Sanders, J. Bulk Chemicals from Biomass. *Biofuels Bioprod. Biorefining* **2008**, *2* (1), 41–57.

(4) Binder, J. B.; Gray, M. J.; White, J. F.; Zhang, Z. C.; Holladay, J. E. Reactions of Lignin Model Compounds in Ionic Liquids. *Biomass Bioenergy* **2009**, *33* (9), 1122–1130.

(5) Furimsky, E. Catalytic Hydrodeoxygenation. *Appl Catal A* **2000**, *199(2)*, 147–190.

(6) Czernik, S.; Bridgwater, A. V. Overview of Applications of Biomass Fast Pyrolysis Oil. *Energy Fuels* **2004**, *18* (2), 590–598.

(7) Bridgwater, A. V.; Peacocke, G. V. C. Fast Pyrolysis Processes for Biomass. *Renew. Sustain. Energy Rev.* **2000**, *4* (1), 1–73.

(8) Huber, G. W.; Iborra, S.; Corma, A. Synthesis of Transportation Fuels from Biomass: Chemistry, Catalysts, and Engineering. *Chem. Rev.* **2006**, *106* (9), 4044–4098.

(9) Marsman, J. H.; Wildschut, J.; Evers, P.; de Koning, S.; Heeres, H. J. Identification and Classification of Components in Flash Pyrolysis Oil and Hydrodeoxygenated Oils by Two-Dimensional Gas Chromatography and Time-of-Flight Mass Spectrometry. *J. Chromatogr. A* **2008**, *1188* (1), 17–25.

(10) Elliott, D. C. Historical Developments in Hydroprocessing Bio-Oils. *Energy Fuels* **2007**, *21* (3), 1792.

(11) Choudhary, T. V.; Phillips, C. B. Renewable Fuels via Catalytic Hydrodeoxygenation. *Appl. Catal. Gen.* **2011**, *397* (1–2), 1–12.

(12) He, Z.; Wang, X. Hydrodeoxygenation of Model Compounds and Catalytic Systems for Pyrolysis Bio-Oils Upgrading. *Catal. Sustain. Energy* **2012**, *1*.

(13) Saidi, M.; Samimi, F.; Karimipourfard, D.; Nimmanwudipong, T.; Gates, B. C.; Rahimpour, M. R. Upgrading of Lignin-Derived Bio-Oils by Catalytic Hydrodeoxygenation. *Energy Env. Sci* **2014**, *7* (1), 103–129.

(14) Bu, Q.; Lei, H.; Zacher, A. H.; Wang, L.; Ren, S.; Liang, J.; Wei, Y.; Liu, Y.; Tang, J.; Zhang, Q.; Ruan, R. A Review of Catalytic Hydrodeoxygenation of Lignin-Derived Phenols from Biomass Pyrolysis. *Bioresour. Technol.* **2012**, *124*, 470–477.

(15) Romero, Y.; Richard, F.; Brunet, S. Hydrodeoxygenation of 2-Ethylphenol as a Model Compound of Bio-Crude over Sulfided Mo-Based Catalysts: Promoting Effect and Reaction Mechanism. *Appl. Catal. B Environ.* **2010**, *98* (3–4), 213–223.

(16) Bui, V. N.; Laurenti, D.; Afanasiev, P.; Geantet, C. Hydrodeoxygenation of Guaiacol with CoMo Catalysts. Part I: Promoting Effect of Cobalt on HDO Selectivity and Activity. *Appl. Catal. B Environ.* **2011**, *101* (3–4), 239–245.

(17) Loricera, C. V.; Pawelec, B.; Infantes-Molina, A.; Álvarez-Galván, M. C.; Huirache-Acuña, R.; Nava, R.; Fierro, J. L. G. Hydrogenolysis of Anisole over Mesoporous Sulfided CoMoW/SBA-15(16) Catalysts. *Catal. Today* **2011**, *172* (1), 103–110.

(18) Olcese, R. N.; Bettahar, M.; Petitjean, D.; Malaman, B.; Giovanella, F.; Dufour, A. Gas-Phase Hydrodeoxygenation of Guaiacol over Fe/SiO_2 Catalyst. *Appl. Catal. B Environ.* **2012**, *115–116*, 63.

(19) Zhao, H. Y.; Li, D.; Bui, P.; Oyama, S. T. Hydrodeoxygenation of Guaiacol as Model Compound for Pyrolysis Oil on Transition Metal Phosphide Hydroprocessing Catalysts. *Appl. Catal. Gen.* **2011**, *391* (1–2), 305–310.

(20) Badawi, M.; Cristol, S.; Paul, J.-F.; Payen, E. DFT Study of Furan Adsorption over Stable Molybdenum Sulfide Catalyst under HDO Conditions. *Comptes Rendus Chim.* **2009**, *12* (6–7), 754–761.

(21) Badawi, M.; Paul, J. F.; Cristol, S.; Payen, E.; Romero, Y.; Richard, F.; Brunet, S.; Lambert, D.; Portier, X.; Popov, A.; Kondratieva, E.; Goupil, J.M.; El Fallah, J.; Gilson, J.P.; Mariey, L.; Travert, A.; Maugé, F. Effect of Water on the Stability of Mo and CoMo Hydrodeoxygenation Catalysts: A Combined Experimental and DFT Study. *J. Catal.* **2011**, *282* (1), 155–164.

(22) Badawi, M.; Paul, J.-F.; Payen, E.; Romero, Y.; Richard, F.; Brunet, S.; Popov, A.; Kondratieva, E.; Gilson, J.-P.; Mariey, L.; Travert, A.; Maugé, F. Hydrodeoxygenation of Phenolic Compounds by Sulfided (Co)Mo/Al_2O_3 Catalysts, a Combined Experimental and Theoretical Study. *Oil Gas Sci. Technol. – Rev. D'IFP Energ. Nouv.* **2013**, *68* (5), 829–840.

(23) Moon, J.-S.; Kim, E.-G.; Lee, Y.-K. Active Sites of Ni_2P/SiO_2 Catalyst for Hydrodeoxygenation of Guaiacol: A Joint XAFS and DFT Study. *J. Catal.* **2014**, *311*, 144–152.

(24) Garcia-Pintos, D.; Voss, J.; Jensen, A. D.; Studt, F. Hydrodeoxygenation of Phenol to Benzene and Cyclohexane on Rh(111) and Rh(211) Surfaces: Insights from Density Functional Theory. *J. Phys. Chem. C* **2016**, *120* (33), 18529–18537.

(25) Verma, A. M.; Kishore, N. DFT Study on Gas-Phase Hydrodeoxygenation of Guaiacol by Various Reaction Schemes. *Mol. Simul.* **2017**, *43* (2), 141–153.

(26) Bouvier, C.; Romero, Y.; Richard, F.; Brunet, S. Effect of H_2S and CO on the Transformation of 2-Ethylphenol as a Model Compound of Bio-Crude over Sulfided Mo-Based Catalysts: Propositions of Promoted Active Sites for Deoxygenation Pathways Based on an Experimental Study. *Green Chem.* **2011**, *13* (9), 2441.

(27) Weigold, H. Behaviour of Co-Mo-Al_2O_3 Catalysts in the Hydrodeoxygenation of Phenols. *Fuel* **1982**, *61* (10), 1021–1026.

(28) Laurent, E.; Delmon, B. Study of the Hydrodeoxygenation of Carbonyl, Carboxylic and Guaiacyl Groups over Sulfided CoMo/γ-Al_2O_3 and NiMo/γ-Al_2O_3 Catalyst. *Appl. Catal. Gen.* **1994**, *109* (1), 97.

(29) Laurent, E.; Delmon, B. Influence of Water in the Deactivation of a Sulfided NiMo/γ-Al_2O_3 Catalyst during Hydrodeoxygenation. *J. Catal.* **1994**, *146* (1), 281–291.

(30) Badawi, M.; Paul, J.-F.; Cristol, S.; Payen, E. Guaiacol Derivatives and Inhibiting Species Adsorption over MoS_2 and CoMoS Catalysts under HDO Conditions: A DFT Study. *Catal. Commun.* **2011**, *12* (10), 901–905.

(31) Asadieraghi, M.; Ashri Wan Daud, W. M.; Abbas, H. F. Heterogeneous Catalysts for Advanced Bio-Fuel Production through Catalytic Biomass Pyrolysis Vapor Upgrading: A Review. *RSC Adv* **2015**, *5* (28), 22234–22255.

(32) De, S.; Saha, B.; Luque, R. Hydrodeoxygenation Processes: Advances on Catalytic Transformations of Biomass-Derived Platform Chemicals into Hydrocarbon Fuels. *Bioresour. Technol.* **2015**, *178*, 108–118.

(33) Wildschut, J.; Mahfud, F. H.; Venderbosch, R. H.; Heeres, H. J. Hydrotreatment of Fast Pyrolysis Oil Using Heterogeneous Noble-Metal Catalysts. *Ind. Eng. Chem. Res.* **2009**, *48* (23), 10324–10334.

(34) Ferrari, M.; Maggi, R.; Delmon, B.; Grange, P. Influences of the Hydrogen Sulfide Partial Pressure and of a Nitrogen Compound on the Hydrodeoxygenation Activity of a CoMo/Carbon Catalyst. *J. Catal.* **2001**, *198* (1), 47–55.

(35) Şenol, O. I.; Ryymin, E.-M.; Viljava, T.-R.; Krause, A. O. I. Effect of Hydrogen Sulphide on the Hydrodeoxygenation of Aromatic and Aliphatic Oxygenates on Sulphided Catalysts. *J. Mol. Catal. Chem.* **2007**, *277* (1–2), 107–112.

(36) Olcese, R. N. Valorisation Des Vapeurs de Pyrolyse de Lignine Par Hydrodéoxygénation Directe Catalysées Par Le Fer. PhD Thesis, Université de Lorraine: Nancy, **2012**.

(37) Olcese, R.; Bettahar, M. M.; Malaman, B.; Ghanbaja, J.; Tibavizco, L.; Petitjean, D.; Dufour, A. Gas-Phase Hydrodeoxygenation of Guaiacol over Iron-Based Catalysts. Effect of Gases Composition, Iron Load and Supports (Silica and Activated Carbon). *Appl. Catal. B Environ.* **2013**, *129*, 528–538.

(38) Popov, A.; Kondratieva, E.; Goupil, J. M.; Mariey, L.; Bazin, P.; Gilson, J.-P.; Travert, A.; Maugé, F. Bio-Oils Hydrodeoxygenation: Adsorption of Phenolic Molecules on Oxidic Catalyst Supports. *J. Phys. Chem. C* **2010**, *114* (37), 15661–15670.

(39) Mian, S. A.; Yang, L.-M.; Saha, L. C.; Ahmed, E.; Ajmal, M.; Ganz, E. A Fundamental Understanding of Catechol and Water Adsorption on a Hydrophilic Silica Surface: Exploring the Underwater Adhesion Mechanism of Mussels on an Atomic Scale. *Langmuir* **2014**, *30* (23), 6906–6914.

(40) Simonetti, S.; Compañy, A. D.; Pronsato, E.; Juan, A.; Brizuela, G.; Lam, A. Density Functional Theory Based-Study of 5-Fluorouracil Adsorption on β-Cristobalite (111) Hydroxylated Surface: The Importance of H-Bonding Interactions. *Appl. Surf. Sci.* **2015**, *359*, 474–479.

(41) Compañy, A. D.; Juan, A.; Brizuela, G.; Simonetti, S. 5-Fluorouracil Adsorption on Hydrated Silica: Density Functional Theory Based-Study. *Adsorption* **2017**, *23* (2–3), 321–325.

(42) Rimola, A.; Civalleri, B.; Ugliengo, P. Physisorption of Aromatic Organic Contaminants at the Surface of Hydrophobic/Hydrophilic Silica Geosorbents: A B3LYP-D Modeling Study. *Phys. Chem. Chem. Phys.* **2010**, *12* (24), 6357.

(43) Simonetti, S.; Compañy, A. D.; Brizuela, G.; Juan, A. β-Cristobalite (001) Surface as 4-Formaminoantipyrine Adsorbent: First Principle Study of the Effect on Adsorption of Surface Modification. *Colloids Surf. B Biointerfaces* **2016**, *148*, 287–292.

(44) Grau, E. N.; Román, G.; Compañy, A. D.; Brizuela, G.; Juan, A.; Simonetti, S. Surface Modification vs Sorption Strength: Study of Nedaplatin Drug Supported on Silica. *Appl. Surf. Sci.* **2019**, *465*, 693.

(45) Cristol, S.; Paul, J.; Schovsbo, C.; Veilly, E.; Payen, E. DFT Study of Thiophene Adsorption on Molybdenum Sulfide. *J. Catal.* **2006**, *239* (1), 145–153.

(46) Moses, P. G.; Hinnemann, B.; Topsøe, H.; Nørskov, J. K. The Effect of Co-Promotion on MoS_2 Catalysts for Hydrodesulfurization of Thiophene: A Density Functional Study. *J. Catal.* **2009**, *268* (2), 201–208.

(47) Pelardy, F.; Daudin, A.; Devers, E.; Dupont, C.; Raybaud, P.; Brunet, S. Deep HDS of FCC Gasoline over Alumina Supported CoMoS Catalyst: Inhibiting Effects of Carbon Monoxide and Water. *Appl. Catal. B Environ.* **2016**, *183*, 317–327.

(48) Comas-Vives, A. Amorphous SiO_2 Surface Models: Energetics of the Dehydroxylation Process, Strain, Ab Initio Atomistic Thermodynamics and IR Spectroscopic Signatures. *Phys. Chem. Chem. Phys.* **2016**, *18* (10), 7475–7482.

(49) Handzlik, J.; Ogonowski, J. Structure of Isolated Molybdenum(VI) and Molybdenum(IV) Oxide Species on Silica: Periodic and Cluster DFT Studies. *J. Phys. Chem. C* **2012**, *116* (9), 5571–5584.

(50) Rozanska, X.; Delbecq, F.; Sautet, P. Reconstruction and Stability of β-Cristobalite 001, 101, and 111 Surfaces during Dehydroxylation. *Phys. Chem. Chem. Phys.* **2010**, *12* (45), 14930.

(51) Goumans, T. P. M.; Wander, A.; Brown, W. A.; Catlow, C. R. A. Structure and Stability of the (001) α-Quartz Surface. *Phys Chem Chem Phys* **2007**, *9* (17), 2146–2152.

(52) Abbasi, A.; Nadimi, E.; Plänitz, P.; Radehaus, C. Density Functional Study of the Adsorption of Aspirin on the Hydroxylated (001) α-Quartz Surface. *Surf. Sci.* **2009**, *603* (16), 2502–2506.

(53) Hohenberg, P.; Kohn, W. Inhomogeneous Electron Gas. *Phys. Rev.* **1964**, *136* (3B), B864–B871.

(54) Kohn, W.; Sham, L. J. Quantum Density Oscillations in an Inhomogeneous Electron Gas. *Phys. Rev.* **1965**, *137* (6A), A1697–A1705.

(55) Kresse, G.; Hafner, J. *Ab Initio* Molecular Dynamics for Liquid Metals. *Phys. Rev. B* **1993**, *47* (1), 558.

(56) Kresse, G.; Hafner, J. *Ab Initio* Molecular-Dynamics Simulation of the Liquid-Metal–Amorphous-Semiconductor Transition in Germanium. *Phys. Rev. B* **1994**, *49* (20), 14251–14269.

(57) Perdew, J. P.; Burke, K.; Ernzerhof, M. Generalized Gradient Approximation Made Simple. *Phys. Rev. Lett.* **1996**, *77* (18), 3865–3868.

(58) Kresse, G.; Furthmüller, J. Efficient Iterative Schemes for *Ab Initio* Total-Energy Calculations Using a Plane-Wave Basis Set. *Phys. Rev. B* **1996**, *54* (16), 11169–11186.

(59) Kresse, G.; Joubert, D. From Ultrasoft Pseudopotentials to the Projector Augmented-Wave Method. *Phys. Rev. B* **1999**, *59* (3), 1758–1775.

(60) Sun, T.; Wang, Y.; Zhang, H.; Liu, P.; Zhao, H. Adsorption and Oxidation of Oxalic Acid on Anatase TiO_2 (001) Surface: A Density Functional Theory Study. *J. Colloid Interface Sci.* **2015**, *454*, 180–186.

(61) Tkatchenko, A.; Scheffler, M. Accurate Molecular Van Der Waals Interactions from Ground-State Electron Density and Free-Atom Reference Data. *Phys. Rev. Lett.* **2009**, *102* (7), 073005.

(62) Bučko, T.; Hafner, J.; Lebègue, S.; Ángyán, J. G. Improved Description of the Structure of Molecular and Layered Crystals: Ab Initio DFT Calculations with van Der Waals Corrections. *J. Phys. Chem. A* **2010**, *114* (43), 11814–11824.

(63) Göltl, F.; Grüneis, A.; Bučko, T.; Hafner, J. Van Der Waals Interactions between Hydrocarbon Molecules and Zeolites: Periodic Calculations at Different Levels of Theory, from Density Functional Theory to the Random Phase Approximation and Møller-Plesset Perturbation Theory. *J. Chem. Phys.* **2012**, *137* (11), 114111.

(64) Bučko, T.; Lebègue, S.; Hafner, J.; Ángyán, J. G. Improved Density Dependent Correction for the Description of London Dispersion Forces. *J. Chem. Theory Comput.* **2013**, *9* (10), 4293–4299.

(65) Bučko, T.; Lebègue, S.; Ángyán, J. G.; Hafner, J. Extending the Applicability of the Tkatchenko-Scheffler Dispersion Correction via Iterative Hirshfeld Partitioning. *J. Chem. Phys.* **2014**, *141* (3), 034114.

(66) Zimmerli, U.; Parrinello, M.; Koumoutsakos, P. Dispersion Corrections to Density Functionals for Water Aromatic Interactions. *J. Chem. Phys.* **2004**, *120* (6), 2693–2699.

(67) Dion, M.; Rydberg, H.; Schröder, E.; Langreth, D. C.; Lundqvist, B. I. Van Der Waals Density Functional for General Geometries. *Phys. Rev. Lett.* **2004**, *92* (24), 246401.

(68) Grimme, S. Accurate Description of van Der Waals Complexes by Density Functional Theory Including Empirical Corrections. *J. Comput. Chem.* **2004**, *25* (12), 1463–1473.

(69) Grimme, S. Semiempirical GGA-Type Density Functional Constructed with a Long-Range Dispersion Correction. *J. Comput. Chem.* **2006**, *27* (15), 1787–1799.

(70) Grimme, S.; Antony, J.; Ehrlich, S.; Krieg, H. A Consistent and Accurate Ab Initio Parametrization of Density Functional Dispersion Correction (DFT-D) for the 94 Elements H-Pu. *J. Chem. Phys.* **2010**, *132* (15), 154104.

(71) Grimme, S.; Ehrlich, S.; Goerigk, L. Effect of the Damping Function in Dispersion Corrected Density Functional Theory. *J. Comput. Chem.* **2011**, *32* (7), 1456–1465.

(72) Yang, J.; Meng, S.; Xu, L.; Wang, E. G. Water Adsorption on Hydroxylated Silica Surfaces Studied Using the Density Functional Theory. *Phys. Rev. B* **2005**, *71* (3).

(73) Yang, J.; Wang, E. G. Water Adsorption on Hydroxylated α -Quartz (0001) Surfaces: From Monomer to Flat Bilayer. *Phys. Rev. B* **2006**, *73* (3).

(74) Bakaev, V. A.; Steele, W. A. On the Computer Simulation of a Hydrophobic Vitreous Silica Surface. *J. Chem. Phys.* **1999**, *111* (21), 9803–9812.

(75) Leed, E. A.; Pantano, C. G. Computer Modeling of Water Adsorption on Silica and Silicate Glass Fracture Surfaces. *J. Non-Cryst. Solids* **2003**, *325* (1–3), 48–60.

Chapter 4

Synthesis of Metal@silica Catalysts

Chap. 4 Synthesis of Metal@silica Catalysts

Part 1. Conventional Synthesis of Catalysts

The silica supported metal catalyst are conventionally prepared by the impregnation of a pre-synthesized porous silica material in a metal salt solution, under various conditions of metal source, temperature and pH. The variation of physical and chemical conditions aims to control the interactions between metal atoms and the silica surface in order to control the iron imprinting on the support. Thus, to achieve a good impregnation for interesting catalytic properties two methods were tested: (i) the simple impregnation at room temperature, and (ii) the co-precipitation pH-controlled by the decomposition of urea (DPU) under heating. The catalyst properties are determined mostly by the iron loading and distribution at the silica surface, the morphological state of Fe (atomic or nanoparticles) and the iron oxidation state. In fact, obtaining Fe(II) species, instead of Fe(III), will facilitate the reduction step into metallic iron Fe(0) and therefore reduce the size of metallic nanoparticles formed during this step, which enable to obtain more catalytic active sites.

4.1.1 SBA-15-like Silica Support

The synthesis of the silica support is performed by hydrothermal sol-gel method (see **Chap 2.2.1**) under similar conditions of those used for the synthesis of the SBA-15 silica.[1,2] Firstly, a micellar solution is prepared in a round-bottom flask by dissolving 2.5% of Pluronic polymer P123® surfactant in 100mL of acidic HCl (1M) solution. The solution is then degassed and defoamed in an ultrasonic bath to remove air bubbles. An amount of 3.75 mL of tetramethyl orthosilicate, TMOS, corresponding to the molar ratio n_{P123}/n_{TMOS} of 0.017, is mixed with the solution at room temperature for 30 minutes. The solution is then transferred into a Teflon bottle of a metallic autoclave and putted in the oven for 24 hours at 40°C then for 48 hours at 100°C. In order to remove the surfactant to release the porosity in the final silica framework, different ways have been applied resulting in three sort of materials surfactant-free (SBA-15-1SC, SBA-15-3S, and SBA-15-3SC) having some different structural properties.

- **SBA-15-1SC**: The first way is similar to the standard procedure used for SBA-15 silica. It consists of washing over one day the recovered sol-gel in a Soxhlet extractor with a mixture of 50/50% ethanol/methanol solvent. After the washing and drying, the powder is calcined under airflow. The calcination procedure is as follow: (step 1) the powder is heated from room temperature (T_R) to 373K with a rate of 2°/min and held for one hour, (step2) heating from 373K to 623K (2°/min) and held for one hour, (step 3) heating from 623K to 823K (2°/min) and held for three hours, (step 4) cooling overnight to T_R.

- **SBA-15-3S**: This way differs from the first one by time and repetition of the Soxhlet washing. The gel is washed over three successive days instead of one day (the washing solution is renewed every 24 hours) without further calcination step. Then the wet silica material was dried at room temperature under air overnight. This method allow conserving the silanols (OH groups) on the silica surface.
- **SBA-15-3SC**: The third way is similar to the second one, but the silica powder is furthermore calcined. It is applied to remove any remaining surfactant traces and to obtain a comparable material to the first SBA-15-1SC (both calcined) as we observed a modification in the porosity distribution for the SBA-15-3S.

The structural properties of the three synthesized SBA-15-like materials are essential for their use as supports for catalysis applications. Small angle X-ray scattering (SAXS) patterns proved that the meso-porosity of the three silica materials is hexagonally structured (**Figure 4.1.1A**). In fact, three reflection peaks corresponding to the (100), (110) and (200) orientations planes of an hexagonal structure characterized by a spacing ratio of 1:$\sqrt{3}$:2 according to the Bragg law[3], are visible :

$$n\lambda = 2d_{hkl}sin\theta \qquad where\ n = 1\ and\ \lambda = 1.54\ nm \qquad (1)$$

The interlayer distance (d_{100}) and the unit cell dimension (a_0), which can be determined by applying the following relation corresponding to a hexagonal structure, are collected in **Table 4.1.1**.

$$d_{hkl} = \frac{a_0}{\sqrt{\frac{4}{3}(h^2+k^2+hk)}} \qquad (2)$$

The pore size distribution of those hexagonally structured mesopores are determined form N_2 adsorption/desorption isotherms, which allow to investigate the wall thickness by simply subtracting the pore diameter ($Ø_{BET}$) from the unit cell dimension (a_0). Both calcined materials (SBA-15-1SC and SBA-15-3SC) exhibit a type IV isotherm with one hysteresis loop, while the SBA-15-3S exhibits a type II isotherm with two desorption branches indicating the coexistence of mesopores with different sizes. Furthermore, for all materials, the first inflection point appears for p/p_0 of 0.45, which suggests a small pore size (around 5 nm) according to Kelvin's equation. However, both 3-times washed materials (SBA-15-3S and SBA-15-3SC) showed a high adsorption for p/p_0 between 0.45 and 0.60, which indicates the coexistence of 5 nm pores with larger pores corresponding to higher p/p_0 ($0.60 < p/p_0 < 0.80$). While for the SBA-15-1SC, the isotherms for p/p_0 between 0.45 and 0.60 are almost negligible which indicates the existence of large pores only (> 5 nm). All those observations are consistent with the pore size distribution determined by the BJH method and showed in **Figure 4.1.1C**. For SBA-15-1SC silica, a dV/dp value of 0.55 $cm^3 \cdot g^{-1} \cdot nm^{-1}$ was obtained for large pores of 7.5 nm, while a negligible value (around 0.08 $cm^3 \cdot g^{-1} \cdot nm^{-1}$) is obtained for smaller pores (5 nm). For the 3-times washed materials, both small (5 nm) and large (7-8 nm) coexistent with the same percentage. Those materials also showed a lower surface-active area and pore volume than the SBA-15-1SC silica (**Table 4.1.1**). The silanols density $\rho_{Si\text{-}OH}$ was determined by combining thermo-gravimetric analysis (TGA) results with S_{BET} values showing that the non-calcined material have around 9 OH/nm^2 while calcined ones have 2-3 OH/nm^2.[4]

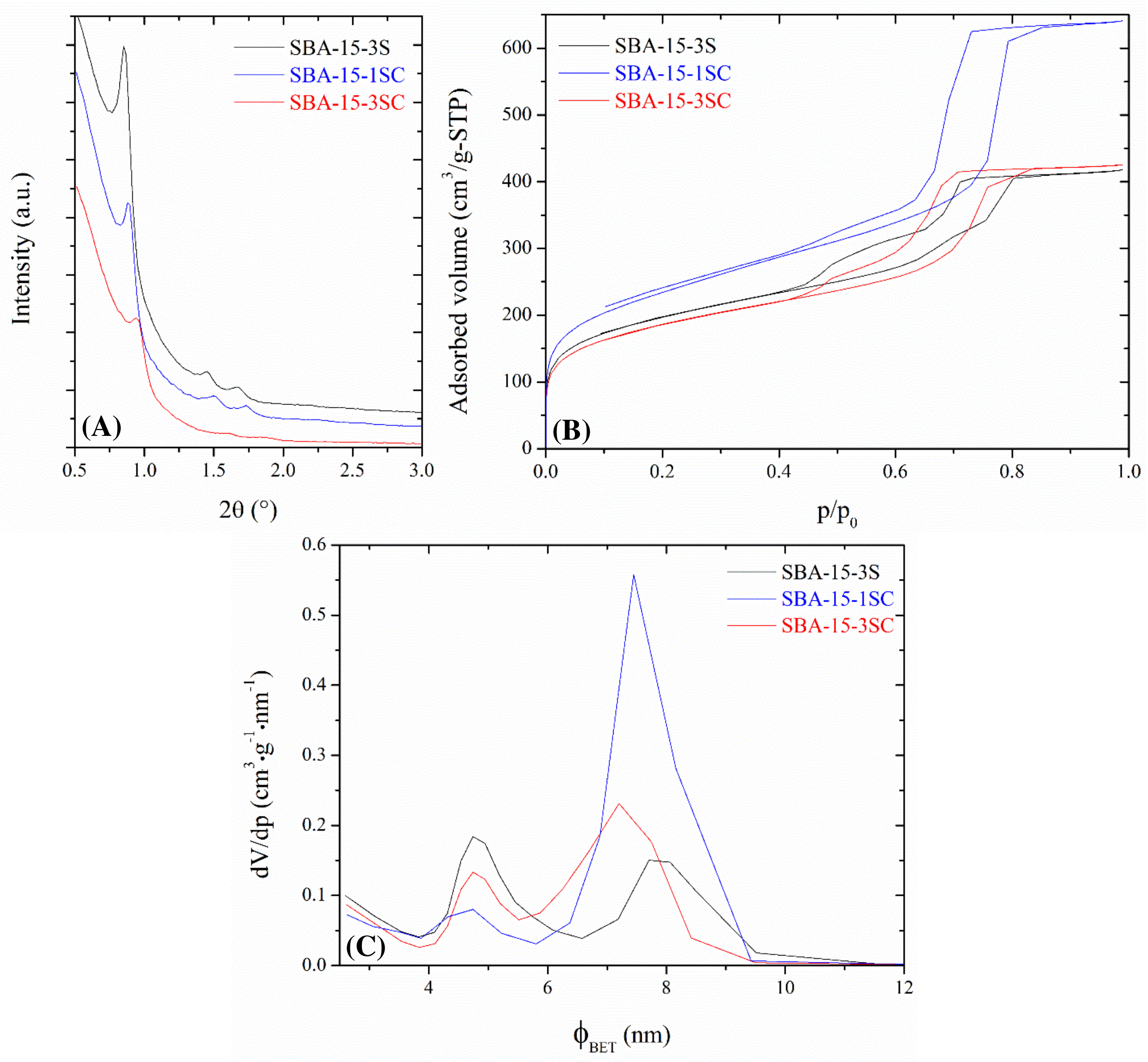

***Figure 4.1.1** Textural characteristics of the three silica materials: **(A)** SAXS patterns, **(B)** N_2 adsorption/desorption isotherms, **(C)** pore size distribution.*

Table 4.1.1 *Textural characteristics of silica materials: the interlayer distance/unit cell dimension for hexagonal networks* d_{Bragg}/a_0, *the pore diameter* $\emptyset_{BET}$, *the wall thickness* ε, *the surface area* S_{BET} *and* S_{NLDFT}, *the mesopores volume* $V_{0.97}$, *and the silanols density* $\rho_{Si\text{-}OH}$.

	d_{Bragg}/a_0 (nm)	$\emptyset_{BET}$ (nm)	ε (nm)	S_{BET} ($m^2 \cdot g^{-1}$)	S_{NLDFT} ($m^2 \cdot g^{-1}$)	$V_{0.97}$ ($cm^3 \cdot g^{-1}$)	$\rho_{Si\text{-}OH}$ (OH/nm^2)
SBA-15-3S	10.4/12.0	4.7/8.0	4.0	714	788	0.661	8.9
SBA-15-3SC	9.3/10.7	4.7/7.3	3.4	674	754	0.642	1.8
SBA-15-1SC	10.1/11.7	7.5	4.2	746	843	0.803	2.7

All synthesized silica materials have hexagonally structured mesopores with thick walls ($\varepsilon \simeq 4$ nm), high surface area S_{BET} (around 700 m^2/g), and large pore volume $V_{0.97}$. Remarkable, three-times washed materials showed a bit lower pore volume than the SBA-15-1SC (0.15 cm^3/g less).

Concluding, the calcined (SBA-15-1SC and SBA-15-3SC) silica materials differ from the non-calcined one (SBA-15-3S) by the silanols density, which can affect the interaction between the iron species and the silica surface during the impregnation step, and therefore the following steps. The SBA-15-3SC differ from the SBA-15-1SC by its porosity diameter distribution, as it shows two peaks at 5 and 8 nm, which can cause pore blocking during the catalysis.

4.1.2 Synthesis of Fe, Cu and Fe-Cu@silica Catalysts by the Impregnation Method

The three Silica supported metal catalysts, Fe@silica, Cu@silica and Fe-Cu@silica, were prepared following the highly used impregnation method by incipient wettness.[5,6] Usually, a pre-synthesized silica material is immersed in a concentrated solution of metal salt. Thus, in a typical procedure for getting Fe@silica catalysts here studied, each of the three sort of dry silica powder previously described is mixed with a concentrated aqueous solution of iron nitrate nonanhydrate (0.44 g/mL). Then the pasty blend was put under vacuum at room temperature for 3 h, and finally dried for 24 h at 373K in the oven. In order to vary the impregnation conditions each silica support (SBA-15-3S, SBA-15-3SC, and SBA-15-1SC), have been treated with four different *silica/iron nitrate* mass ratio of *0.60, 0.77, 0.85*. The final iron loading compare to silica was determined by elemental analysis using an Inductively Coupled Plasma Atomic Emission Spectroscopy (ICP-AES). Using those experimental data, three catalysts with 15% iron load (theoretical calculation of the *silica/iron nitrate* ratio depending on the impregnation efficiency for each silica support, bold values in **Table 4.1.2**) are prepared and labelled 15%Fe/SAB-15-1SC, 15%Fe/SBA-15-3S, and 15%Fe/SBA-15-3SC.

A copper catalyst Cu@SBA-15-3SC, containing also 15 wt% of Cu was prepared following the same preparation procedure as for Fe@silica catalysts using the silica support SBA-15-3SC as reference. Thus, 0.92 g of SBA-15-3SC silica were mixed with 0.79 g of copper chloride dissolved in 1.80 mL of deionized water. While a third type of catalyst supporting both Fe and Cu (Fe-Cu@SBA-15-3SC) has been elaborated at a weight loading of 15 and 2.5 wt%, respectively. In that case, the catalyst was obtained by mixing 1.08 g of silica with 0.93 g of iron nitrate and 0.13 g of copper chloride dissolved in 2.40 mL of deionized water.

Finally, before performing the catalytic tests, the three types of catalysts resulting M@SiO$_2$ (where M is Fe, Cu, or Fe-Cu) were grounded and sieved (150–250 µm), and then calcined in the HDO reactor at 773K under nitrogen flow (50 ml/min) for 1 h. Before starting the HDO reaction, the calcinated catalyst was reduced in situ using pure H$_2$ (50 ml/min) by increasing the temperature from T$_R$ to 773K (10K/min), and hold it at this temperature for 30 mins.

Table 4.1.2 *Data concerning the impregnation procedure and the corresponding iron loading (%) for different silica/(iron nitrate) mass ratio.*

Silica	**$m_{silica}/m_{iron\ nitrate}$**	**$m_{iron\ nitrate}$ (mg)**	**m_{silica} (mg)**	**$V_{ionized\ water}$ (µL)**	**Iron loading (% Fe)**
SBA-15-3S	0.60	57.7	34.6	131.7	29
	0.77	56.0	43.5	127.0	22
	0.85	56.4	47.9	128.8	22
	1.33	**56.5**	**75.1**	**129.0**	**15**
SBA-15-3SC	0.60	61.0	36.6	138.6	25
	0.77	56.0	43.5	127.0	20
	0.85	62.0	52.7	141.0	20
	1.16	**57.2**	**66.4**	**130.0**	**15**
SBA-15-1SC	0.60	73.0	43.8	166.0	23
	0.77	62.0	48.2	140.6	18
	0.85	74.7	63.5	170.0	18
	1.05	**65.0**	**68.3**	**148.1**	**15**

4.1.3 Synthesis of Fe@SiO_2 Following the Co-precipitation with Decomposition of Urea (DPU)

The synthesis of metallic supported catalysts through a co-precipitation method has been also developed. This way of synthesis involved the thermal decomposition of urea (DPU) in order to control the oxidation state of metallic species and therefore facilitate the reduction step to increase the amount of metal active sites.[7–11] Recently, Shi *et al.*[12] applied this method to synthesize silica-supported bimetallic Fe-Ni catalysts for furfural hydrogenation. This method consists of slow decomposition of urea by heating along the reaction time, which increase the pH of the solution and favor the decomposition-precipitation of the metallic compounds onto the silica support. They studied the effect of the reactants on the oxidation state of the produced metal catalyst, and proved that Fe(II) sulfate source must be selected instead of Fe(III) nitrate source to facilitate the reduction into metallic iron. They also showed that using nickel nitrate as precursor and nitric acid as acidifier will lead to the oxygenation of Fe(II) to Fe(III) upon heating, while using Ni(II) sulfate hexahydrate and sulfuric acid will give a green product indicating the Fe(II) oxidation state.[12]

Based on this previous works, SBA-15-3SC has been chosen to elaborate a metal catalyst by the precipitation method. Thus, 0.7 g of dried SBA-15-3SC silica material and 7.57 g of urea (0.84 mol/L) were dissolved with 0.02 mol/L of sulfuric acid (0.16 mL) in a three-necked flask containing 150 mL of deionized water. The mixture is stirred and degased by argon flow bubbling for 2 h to ensure an oxygen-free medium. Then, 3.24 g of iron(II) sulfate heptahydrate (0.14 mol/L) are injected and the suspension is slowly heated to 353K and kept at this temperature for 22 h. This allow the decomposition of urea, which increase the pH of the solution to 5.5 and allow the deposition of Fe(II) species on the silica support. After cooling the solution to room temperature, the solid is recovered by centrifugation, washed with distilled water, and dried under argon flow at T_R to prevent the oxidation of Fe(II) species. The resulted green powder, characteristic of Fe(II) content, is stored under argon to preserve the iron catalyst from the undesirable oxidation reaction of Fe(II) in Fe(III). This product, labelled Fe/SBA-15-3SC-DPU, is grounded and sieved (150-250 µm), and then reduced directly in situ without intermediate calcination step. The reduction is done under pure H_2 flow (50 ml/min) by increasing the temperature from T_R to 773K (10K/min), and hold it at this temperature for 30 mins.

Part 2. *via* Mixed Micelles

The work presented in this section is particularly focused on the physico-chemical characterization of mixed micelle solutions of CTAF and P123. The later solutions were used as templates in the hydrothermal synthesis of porous silica materials. This strategy was investigated to elaborate in a 'one pot' sol-gel synthesis an iron catalyst supported on porous silica. Thus, in this part of the work, we aim to understand the micellar self-assembly between the two surfactants CTAF/P123 according the mixing ratio for interpreting the textural properties of the silica framework and the iron rate.

4.2.1 Physico-Chemical Characterization of Mixed Micelles Solutions

The metallo-surfactant CTAF for cetyltrimethylammoniumtrichloromonobromoferrate was first synthesized from cetyltrimethylammonium bromide (CTAB) as described by Kim *et al.*[13] by dissolving equivalent molar amount of iron (III) chloride and CTAB in methanol. Then, the solution was heated to reflux overnight. The solvent was then evaporated and the surfactant was dried in vacuum at 60°C for 4 h.

Then various micellar aqueous solutions mixing CTAF and P123 surfactants are prepared by simply dissolving them together in the appropriate molar ratio (r = CTAF/P123 = 0.1, 0.2, 0.5, 1, 2, 5, and 10) in distilled water under magnetic stirring. Regarding the molar ratios chosen, the approach was to favor the progressive dilution of the CTAF chains in P123 micelles to get a majority of mixed micelles. In order to figure out the effective formation of mixed micelles, several physico-chemical characterizations of routine have been done on the solutions prepared at specific r, such as surface tension measurements to determine the critical micellar concentration (CMC), dynamic light scattering and Zeta potential analysis to distinguish the size of the micelles and their surface potential according to CATF/P123 ratio.

Surface tension – Critical Micellar Concentration

The CMC is determined with a tensiometer able to measure the surface tension (σ in mN/m) of a liquid by immersing slowly a dimensionally well define platinum (Pt) plate, in the solution to be analyzed. As shown in **Figure 4.2.1**, the Pt plate is dipped in the liquid over 0.5 cm, and then the recipient containing the solution is gradually lowered until the pullout of the plate. The pullout force value (F) is instantaneously saved to calculate the corresponding surface tension, σ, by the mathematic formulation mentioned in **Figure 4.2.1**. In fact, it is essentially the surface tension force that retains the Pt plate in the liquid during the lowering motion.

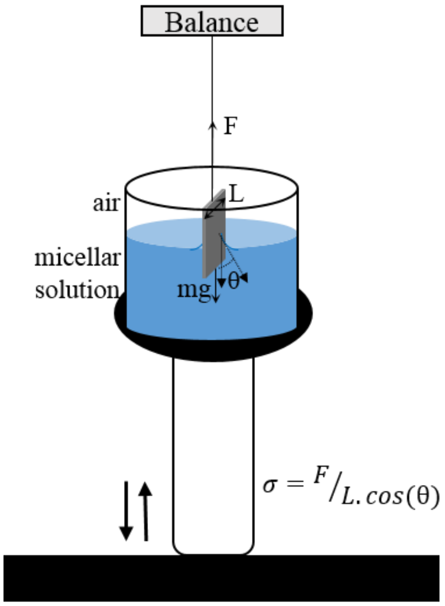

Figure 4.2.1 *Superficial tension resulting from immersing a platinum plate in the micellar solution.*

The micellar solutions of pure P123, pure CTAF and the mixed CATF/P123 prepared at the defined molar ratio have been measured at controlled temperature of 27°C and measured in the same day. To do so, the prepared surfactant stock solutions were diluted progressively several times to reach extremely low surfactant concentrations where σ should be close to water (72 mN/m). Then, the surface tension of each dilutions has been measured in order to determine the respective CMC according to mixing molar ratios.[14,15] Thus, the surface tension values recorded are plotted with respect to the total concentration of surfactant $C_{\text{CTAF+P123}}$ (**Figure 4.2.2**). Therefore, the CMC values were deduced from the point of intersection between the tangents as shown by the dashed lines on **Figures 4.2.2** and summarized on **Table 4.2.1**.

Table 4.2.1 *Critical micellar concentrations values obtained for P123, CTAF, and r=CTAF/P123 micellar solutions.*

	P123	**r = 0.1**	**r = 0.2**	**r = 0.5**	**r = 1**	**r = 2**	**r = 5**	**r = 10**	**CTAF**
$\text{CMC}_{\text{CTAF+P123}}$ (mol/L)	$2*e^{-5}$	$5*e^{-4}$	$2*e^{-4}$	$3*e^{-5}$	$4*e^{-4}$	$4*e^{-5}$	$2*e^{-4}$	$2*e^{-4}$	e^{-3}
CMC_{P123} (mol/L)	$2*e^{-5}$	$4.5*e^{-4}$	$1.7*e^{-4}$	$2*e^{-5}$	$2*e^{-4}$	$1.3*e^{-5}$	$0.3*e^{-4}$	$0.2*e^{-4}$	*
CMC_{CTAF} (mol/L)	*	$0.5*e^{-4}$	$0.3*e^{-4}$	$1*e^{-5}$	$2*e^{-4}$	$2.7*e^{-5}$	$1.7*e^{-4}$	$1.8*e^{-4}$	e^{-3}

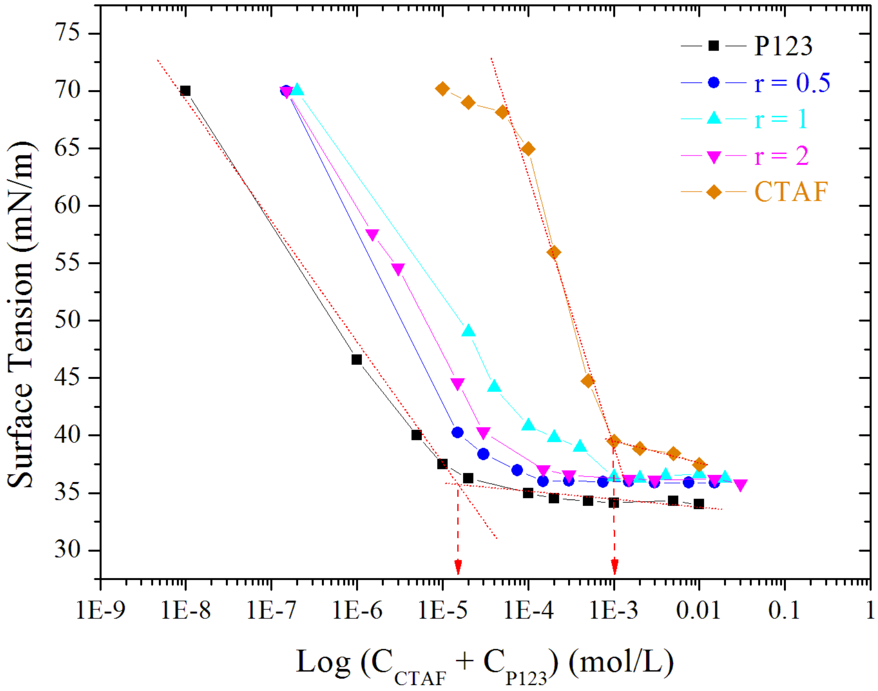

Figure 4.2.2 *Variation of the surface tension with respect to the total concentration of surfactant (CTAF+P123) for pure and mixed micellar solutions for r=0.5, 1 and 2.*

Hydrodynamic Diameter – Zeta Potential

The hydrodynamic diameters (D_H) and the Zeta potential of the micelles formed in the solutions prepared at the different CTAF/P123 ratios were both determined by dynamic light scattering DLS using a Malvern Zetasizer ZS90, at a detection angle of 90°. These data are shown in **Figure 4.2.3** and **Figure 4.2.4**, respectively. As expected from literature, the D_H of pure P123 micelles is centered at 18 ± 2.5nm when taken at full width at half maximum (FWHM) of the size distribution curve. Concerning pure CTAF micelles, the diameter value taken also at FWHM is of 5.5 ±1.5 nm which is relatively close of the CTAB micelle size known to be 3 nm.[16] The iron counter ion present in the hydrophilic head of the CTAF chain is giving a positive polarity without disturbing the micelle self-assembly compare to CTAB since D_H values of both ionic surfactants remained close. In between this two extreme sizes, the micellar diameter of mixed non-ionic/metallo micelles, the size distribution is rather narrow according and the D_H is of 12 ±1.5 nm for low CTAF/P123 ratio (r = 0.1, 0.2, and 0.5). For equimolar amount of CTAF/P123 (r = 1), the micelles size slightly increase to 13 ±3 nm. Then as the ratio increases (r = 2, 5 and 10), the micellar diameter decreases progressively from 13 to 8.5 ±2 nm for the CTAF/P123 ratio of 10. According to these results mixing CTAF with P123 decreased dramatically the proportion of pure P123 micelles since the characteristic size peak has disappeared in favor to smaller micelles resulting from the self-assembly of CTAF and P123 chains. It can be also noticed that the coexistence between mixed and pure CTAF micelles is not distinguee since the size shift to smaller diameter is progressive when CTAF/P123 ratio increases. This means that CTAF chains are mostly participating to the mixed micelles formation.

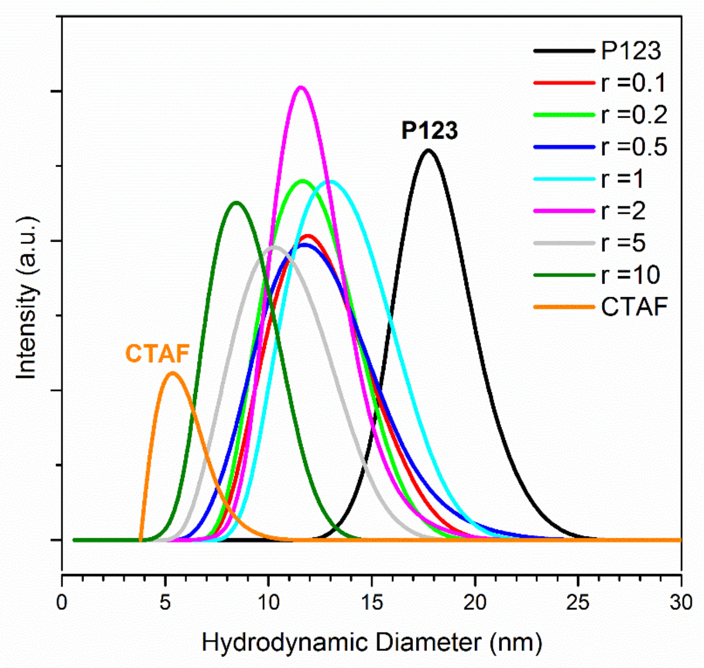

Figure 4.2.3 *Micelles size distribution: hydrodynamic diameter recorded for pure P123, pure CTAF and mixed CTAF/P123 (variable r) solutions.*

The Zeta potential (ZP) is describing the potential difference between the stationary layer of the dispersion medium attached to the dispersed colloidal particle and the mobile dispersion medium.[17] It is therefore a function of the surface charge of the particle, any adsorbed layer at the interface, and the nature and composition of the surrounding suspension medium.[18] The zeta potential is determined by measuring the electrophoretic particle velocity in an electrical field. During the particle movement the diffuse layer (**Figure 4.2.5**) is shorn off, hence the particle obtains a charge due to the loss of the counter ions in the diffuse layer this potential at the plane of shear is called the zeta potential.[19] In the case of micelles, the Zeta potential is directly induced by the electric charges spread at water interface due to the orientation of the ionic head of the surfactant to the aqueous phase. The **Figure 4.2.4** shows the Zeta potential variation recorded when the CTAF/P123 molar ratio (r) has been increased. As except for non-ionic surfactants, the pure P123 micelles have a ZP value of zero. But, as soon as CTAF is introduce the ZP became positive and the value raised progressively to 40 mV by increasing of the ratio r up to 10, which is close to the native value of CTAF micelles (42 mV). The increase in the ZP value is coherent with the addition of metallosurfactant.

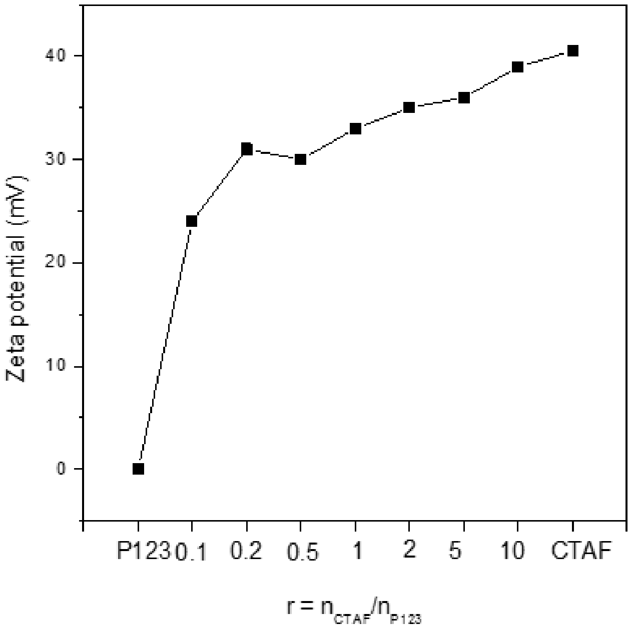

Figure 4.2.4 *Zeta potential variation with respect to the CTAF/P123 molar ratio.*

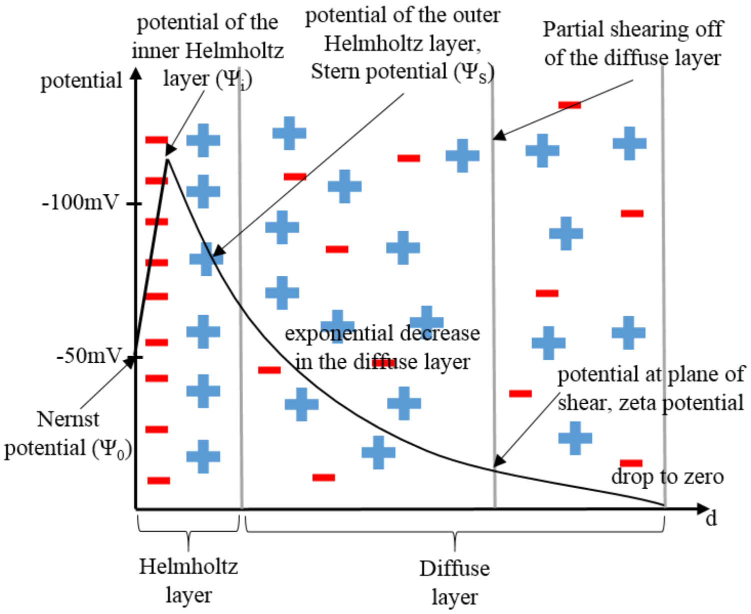

Figure 4.2.5 *Schematic presentation explaining the zeta potential (ZP).*

These preliminary characterizations tend to demonstrate that self-assembly between the cationic CTAF and the non-ionic copolymer P123 lead to new mixed micelles in the all range of molar ratio chose. The as formed mixed micelles have their specific CMC, DH and Zeta potential ranging mainly in between the values of the respective pure surfactant micelles.

4.2.2 Small Angle Neutron Scattering (SANS) Experiments

Small angle neutron scattering experiments consist of sending a beam of neutrons through the sample, where those neutron are elastically scattered by nuclear interaction with the nuclei or magnetic momentum interaction with unpaired electrons.[20,21] This method enable to investigate the structure at the nanoscale (1-1000nm) with a high sensitivity, possibility of isotopes labelling, and strong scattering by magnetic moments.[22] Being a nuclear property, the nuclear scattering amplitude can be considerably different between isotopes of some chemical species. Therefore, due to the large difference between the neutron scattering lengths of hydrogen and deuterium, the latter can be used as a phase contrast for hydrogen-containing materials.[23] Different researchers used this technique to investigate the structure of micellar solutions in order to determine the size and shapes of micelles and the interaction between them.[24–27] SANS experiments have been performed on a variety of surfactant types as conventional,[28] mixed,[29] block co-polymers,[30] Gemini,[31] and multi-headed.[32] Inspired by a previous SANS study on metallosurfactant vesicles,[33] we performed SANS experiments using the ISIS neutron source at STFC Rutherford Appleton laboratory in order to probe the structural properties of the mixed of CTAF/P123. For this purpose, micellar solutions at the specific *r* where prepared in three different concentrations in D_2O as a solvent. An identical series of solutions have also been prepared by mixing CTAB and P123 at the molar ratio r previously defined, for comparison. The solutions where analyzed in banjo type quartz cuvettes with a light path of 1 mm or 2 mm depending on the concentration. Moreover, solutions of mixed micelles prepared from head-deuterated metallosurfactants CTAFd (9 Deuterium atoms by polar head) and P123 were also analyzed, which aim to understand the structuration of the micelles. The features of the self-assemblies (structure, shape, size) are expected to affect the properties of the textural properties of Fe@silica materials and therefore understanding the influence of iron content on the properties of the micelles are of paramount importance for the design of the porous ferrisilicate catalysts. **Table 4.2.2** summarizes the measured samples (137 scattering data collected out of the cell and solvent references), where pure (P123, CTAB, CTAF, CTAFd) and mixed (P123/CTAB, P123/CTAF, P123/CTAFd) micellar solutions are measured in successive dilutions to determine the form factor scattering signal from the diluted regime.

***Table 4.2.2** Summary of the micellar samples, concentrations and operating conditions applied during the SANS experiments.*

r	**Surfactant molar ratio**		**Concentrations (mol/L)**				**Labelling**	**Temperature & solvent**
	CTAB, CTAF, or CTAFd	P123	P123 (P)	CTAB (B)	CTAF (F)	CTAFd (Fd)		
-	0	1	$5e^{-3}$ to $2e^{-4}$	*			P	25 or 40 °C H$_2$O, D2O, or H$_2$O-D$_2$O (75-25%)
0.1	1	10	e^{-2} $5e^{-3}$ e^{-3}	e^{-3} $5e^{-4}$ *	e^{-3} $5e^{-4}$ e^{-4}		P10:B1 P10:F1 P10:Fd1	
0.2	1	5	e^{-2} $5e^{-3}$ e^{-3}	$2e^{-3}$ e^{-3} *	$2e^{-3}$ e^{-3} $2e^{-4}$		P5:B1 P5:F1 P5:Fd1	
0.5	1	2	$2e^{-3}$ e^{-3} $2e^{-4}$	e^{-3} $5e^{-4}$ *	e^{-3} $5e^{-4}$ e^{-4}		P2:B1 P2:F1 P2:Fd1	
1	1	1	e^{-2} $5e^{-3}$ e^{-3}	e^{-2} $5e^{-3}$ *	e^{-2} $5e^{-3}$ e^{-3}		P1:B1 P1:F1 P1:Fd1	
2	2	1	$2e^{-3}$ e^{-3} $2e^{-4}$	$4e^{-3}$ $2e^{-3}$ *	$4e^{-3}$ $2e^{-3}$ $4e^{-4}$		P1:B2 P1:F2 P1:Fd2	
5	5	1	$2e^{-3}$ e^{-3} $2e^{-4}$	e^{-2} $5e^{-3}$ *	e^{-2} $5e^{-3}$ e^{-3}		P1:B5 P1:F5 P1:Fd5	
10	10	1	e^{-3} $5e^{-4}$ e^{-4}	e^{-2} $5e^{-3}$ *	e^{-2} $5e^{-3}$ e^{-3}		P1:B10 P1:F10 P1:Fd10	
-	1	0	*	$5e^{-3}$ to $2e^{-4}$			B, F, or Fd	

The standard Guinier plot[34] (ln(I(Q)) vs Q^2) have been applied to the scattering signal of pure surfactants (P123 (P), CTAB (B), and CTAF (F)) and mixed micellar solutions (P123/CTAB (P$_x$:B$_x$) and P123:CTAF (P$_x$:F$_x$)) recorded in D$_2$O medium at 25°C in order to obtain the gyration diameter D$_g$ (or gyration radius R$_g$). The D$_g$ values for pure micelles are around 12.5 nm for P123, and 4.5 nm for CTAB and CTAF as shown in **Figure 4.2.6**. When comparing the respective R$_g$ values of CTAF and CTAB, it can be deduced that the iron does not induce any significant change in the micelle gyration diameters. Concerning mixed P123/CTAF micelles, it is noticeable that the D$_g$ are higher by 2 to 3 nm (for samples P10:F1 to P1F5) compared to P123/CTAB micelles size. However, the D$_g$ values for both series follow a decrease when the molar amount of CTAF increases, except for the micellar solution P1F2 associated to the molar ratio *r* of 0.5.

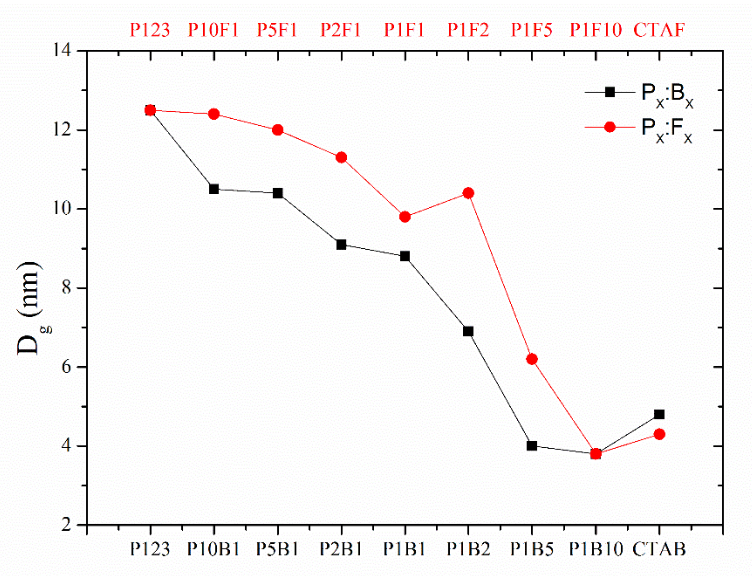

Figure 4.2.6 *Comparison of the gyration diameter values (D_g) determined from a Guinier plot representation of the scattering data for P123/CTAB and P123/CTAF samples at 25 °C.*

Figure 4.2.7 shows a comparison of the D_g values for the P123/CTAF (P_x:F_x) and P123/CTAFd (P_x:Fd_x), as well of the hydrodynamic radius values (D_h) measured by dynamic light scattering (DLS) of P123/CTAF micelles. The D_g and D_h values follow globally the same decreasing trend as the molar amount of CTAF (or CTAFd) is rising. It can be observed that the deuteration did not induce any alteration on the physico-chemistry behavior of the metallosurfactant, since the D_h values determine for both CTAF/P123 and CTAFd/P123 mixed micellar solutions are strongly close event for the sample P1F2 meaning that the micelle formation could undergoes a transition in the arrangement around the molar ratio *r* of 0.5.

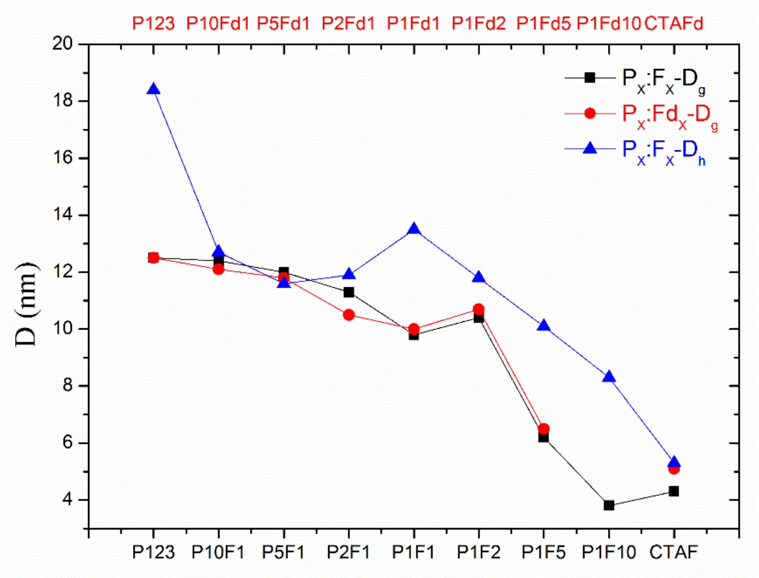

Figure 4.2.7 *Comparison of the D_g of P123/CTAF and P123/CTAFd samples, and the hydrodynamic diameter D_h determined by DLS of P123/CTAF samples.*

According to literature, a spherical form factor leads to an R_g/R_h ratio of 0,775. However, one can notice from **Figure 4.2.8** that the R_g/R_h calculated for the sample set P123/CTAF varies from 0.65 for pure P123 micelles to a maximum of around 1.0 and then the ratio drops dramatically to 0.43 before rising again to the value of 0.785 for the solution of pure CTAF micelles. An increase of the R_g/R_h ratio value could mean that the micelles are becoming elongated when molecular amount of P123 is decreasing.

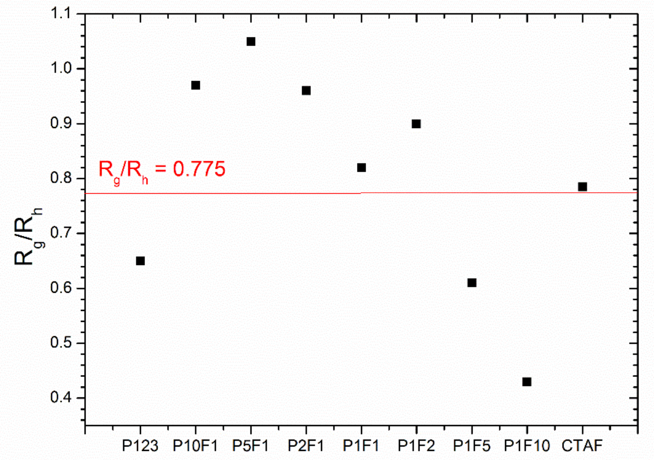

Figure 4.2.8 *Rg/Rh (gyration/hydrodynamic) ratio determined for P123/CTAF samples.*

From the **Figure 4.2.6,** one can notice also that the sample P1F2 is a kind of a pivot point as the D_g value is slightly above the trend curve that mainly drops to the D_g value of pure CTAF micelles. This specific transition is also present for the sample prepared with deuterated CTAF (P1Fd2). However, it disappears when analyzed at 40°C (see **Figure 4.2.9**). The molar ratio *r*, between 1 and 0.5 seems to be a self-assembly transition at room temperature and this is being interpreted out of the data fitting results that are under interpretation.

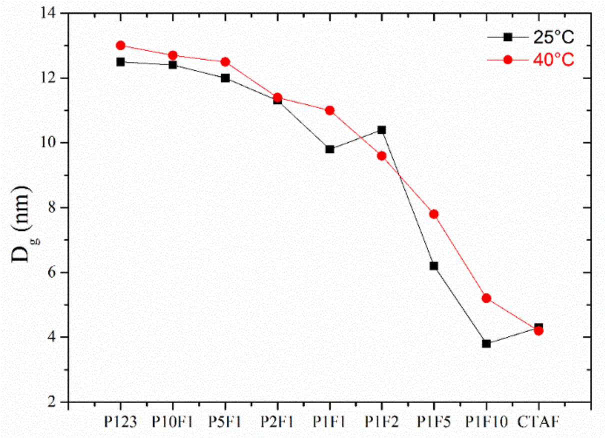

Figure 4.2.9 *Comparison of the D_g values of P123/CTAF samples at 25°C and 40°C.*

These preliminary results seem to indicate that the mixed micelles shape varies with the CTAF/P123 molar ratio, but this has to be refined by the fitting shape modeling.

4.2.3 Magnetic Studies

The magnetic properties of micellar solutions (in D_2O) were performed using a PPMS-9T (Physical Property Measurements System) from Quantum Design. Samples are measured at a field dependence of magnetization of 5 kOe with a range of temperature decreased from 70K to 2K, and the contribution of D_2O solvent was excluded.

The **Figure 4.2.10** shows the field dependence of magnetization for mixed micellar solutions (P10-F1, P5F1, P2F1, P1F1, P1F2, P1F5, and P1F10) in function of the temperature. Those measurements can be fitted by the sum of two Brillouin functions as follow:

$$M(H,T) = c^{5/2} {M_s}^{5/2}\, \mathcal{B}^{5/2}\left(\frac{H}{T-\theta}\right) + (1-c){M_s}^{1/2}\, \mathcal{B}^{1/2}\left(\frac{H}{T}\right) + d$$

Where "$c^{5/2}$" represent the proportion of the high spin $S = 5/2$, $M_S^{5/2}$ and $M_S^{1/2}$ are the saturation magnetization of Fe^{3+} in the high spin and low spin states, respectively ($M_S^{5/2} = 500\ emu/gFe$ and $M_S^{1/2} = 100\ emu/gFe$), $B^S(H,T)$ are the corresponding Brillouin functions ($S = 5/2\ or\ 1/2$), θ present the interactions between high spin Fe^{3+}, and d is a residual contribution.

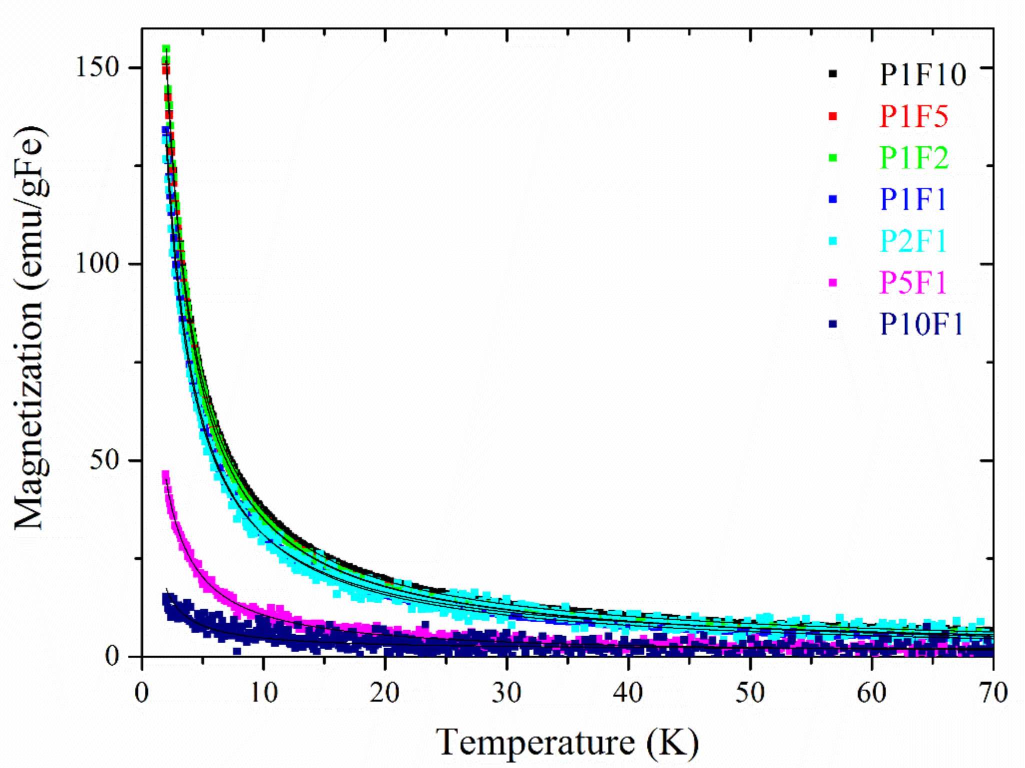

Figure 4.2.10 *Field dependence behavior of the magnetization of mixed micellar solutions (P123/CTAF) as function of the temperature.*

The **Figure 4.2.11A** is the plot of the percentage of $c^{5/2}$ high spin parameter determined by the Brillouin fitting applied to the magnetization signal obtained for the pure CTAF and all mixed micelles (except P5F1 and P10F1). It can be seen that the percentage of $c^{5/2}$ is higher than 80% which means that iron species are involved in the micelles. A sudden decrease of $c^{5/2}$ from 0.8 to 0.2 is observed for P5F1 micelles, while $c^{5/2}$ proportion is zero for P10F1. This indicates that for P10F1 micelles are similar to P123 micelles, and that the metallosurfactant did not incorporate in the micellar structure but probably the surfactant chains are dispersed in water.

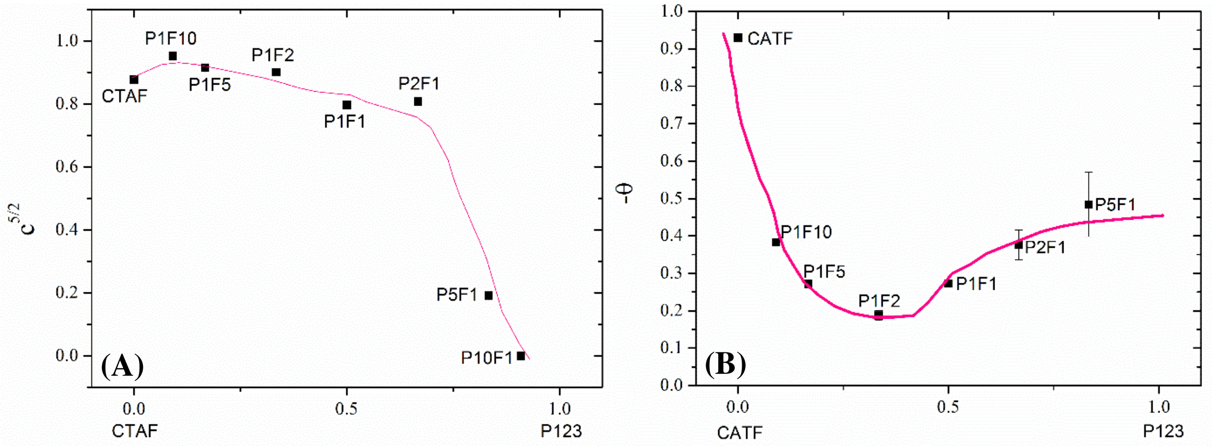

Figure 4.2.11 Dependence with respect to the CTAF/P123 molar ratio (r) of the ***(A)*** *proportion of high spin $c^{5/2}$, and* ***(B)*** *interactions between high spin Fe(III).*

The absolute value of *θ* also determined from the Brillouin function fitting, represents the interactions between high spin Fe species. The θ values have been also plotted according to the CTAF/P123 molar ratio as shown on **Figure 4.2.11B**. The data reveal that the interaction between the high spin decreases as the amount P123 increases in the micelles. This observation can be explained by the fact that the number of first CTAF neighbors are gradually distant by P123 chains as the mixed micelles are being formed. However, the value of θ never reach zero, which means that the CTAF is not dispersed completely as individual chains in the mixed micelles but probably more as aggregated chains. The minimum absolute value of *θ* is obtained for P1F2 micelles, therefore suggesting the best dispersion and interaction between non-ionic P123 and metallic CTAF surfactants for those micelles.

4.2.4 Conclusions

The characterization of mixed non-ionic/metallo (P123/CTAF) micellar solutions are performed in order to understand the structuration of those micelles. This allow determining their effect, as templates for the sol-gel process, on the structural properties of the framework of the silica-supported iron catalysts. Routine characterization enable to determine the critical micellar concentration (CMC), the hydrodynamic diameter (D_h) and the zeta potential (ZP) of those micelles that confirms the structural dependence as function of the CTAF added, where the D_h decreases and the ZP increases as the CTAF/P123 molar ratio increases. Small angle neutron scattering (SANS) measurements confirm that the shape of the mixed micelles deviate from spherical shape found for pure P123 and CTAF micelles, however additional fitting shape modeling is required in order to determine their exact shape. Preliminary models show that the spherical shape become ellipsoidal as we add CTAF until an extent where it return spherical when we approach from pure CTAF micelles. Magnetic measurements allow to determine the percentage of high spin Fe^{3+} species and the interactions between them, which can help to locate them in the micelles and therefore determine their dispersion on the silica mesopores.

Part 3. Imprinting Isolated Single Iron Atoms onto Mesoporous Silica by Templating with Metallosurfactants

The content of this chapter is submitted to the journal "Chemistry of materials (ACS)" devoted for chemical engineering and materials science researches. It is specialized for studies focusing on the development of materials with useful optical, electrical, mechanical, magnetic and catalytic properties from design and synthesis to applications.

Berro, Y.; Gueddida, S.; Bouizi, Y.; Bellouard, C.; Bendeif, El-E.; Ganzmuller, A.; Celzard, A.; Fierro, V.; Ihiawakrim, D.; Ersen, O.; Kassir, M.; El Haj Hassan, F.; Lebègue, S.; Badawi, M.; Canilho, N. & Pasc, A.

Abstract

One of the main drawbacks of metal-supported materials, traditionally prepared by the impregnation of metal salts onto pre-synthesized porous supports, is the formation of large and unevenly dispersed particles. Generally, the larger are the particles, the smaller is the number of catalytic sites. Maximum atom exposure can be reached within single-atom materials, which appear therefore as the next generation of porous catalysts. Herein, we designed single iron atom-supported silica materials through the sol-gel hydrothermal treatment using mixtures of a non-ionic (pluronic P123) and a metallosurfactant (cetyltrimethylammoniumtrichloromonobromoferrate, CTAF) as porogens. The ratio between the Pluronic P123 and the CTAF enables the control the silica structural and textural properties. More important, CTAF acts as an iron source, which amount could be simply tuned by varying the non-ionic/metallo surfactants molar ratio. The fine distribution of iron atoms onto the silica mesopores results from the iron distribution within the mixed micelles, which are serving as templates for the polymerization of silica matrix. Several characterization methods were used to determine the structural and textural properties of the silica material (XRD, N_2 sorption isotherms and TEM) and the homogeneous distribution and lack of clustering of iron atoms in the resulting materials (elemental analysis, Squid, PDF, Mas-NMR and TEM mapping). The oxidation state of single-iron atoms determined experimentally were confirmed by DFT calculations. This strategy might found straightforward applications in preparing versatile single atom catalysts, with improved efficiency compared to nanosized ones.

4.3.1 Introduction

Increasing the number of active sites of a material in order to enhance its catalytic activity is a continuous challenge.[35–37]. This is commonly addressed by increasing the surface of catalytic particles and thus by decreasing their size. The most promising catalysts with the lowest size limit and thus, the highest atom efficiency are considered isolated single atom catalysts (SACs).[38–44]. Several studies already demonstrated the efficiency of SACs compared to nanosized catalysts. For instance, in the water gas shift reaction[45] catalyzed by Ir_1/FeO_x, single atoms promoted more than 70% of the catalytic activity, while subnano clusters and nanoparticles accounted for less than 30%. Pt-based SAC also proved to have high activity for the CO oxidation reaction.[46,47] This was correlated with the existence of vacant 5d orbitals of Pt ion atoms, which reduce both the CO adsorption energy and the reaction activation barriers.[47,48] Also Au-based SAC dispersed on FeO_x nanocrystallites showed higher stability and sintering resistance compared to conventional gold nanostructures.[49,50] Liu *et al.*[51] succeeded to synthetize Pd/TiO2 SACs, having nine times higher activity for C=C bond hydrogenation reaction than commercial Pd catalysts.

The main advancement of the SAC strategy was to reach similar or better catalytic activity with non-precious metal catalysts compared to expensive noble metals.[52–56] Thus, Pt catalysts could be replaced with Co[52] or Fe[53]-based SACs in the oxygen reduction reaction (ORR). The latest actually outperformed all ORR’s reported catalysts to date, including commercial Pt/C.

Despite the recent progress in this topic, one important challenge remains the preparation of SACs, with a tuned porosity and a controlled metal loading, while preventing agglomeration and migration of isolated atoms.[51,57] Herein, we show for the first time that micelles of ferrosurfactants can act as both porogen of the silica framework and as fine imprinters of iron atoms at the surface of mesopores, leading thus to the formation of mesoporous silica-supported isolated single iron atom catalysts (Fe/SiO_2 SACs). The interest in such catalysts come from their wide applications as bifunctional metal-acidic catalysts for biomass upgrading,[6] syngas production,[58] Fisher-Tropsch synthesis,[59–61] Friedel-Craft alkylation,[62] or oxidation reactions.[63–66]

Common synthesis methods of $Fe@SiO_2$ involve either the salt impregnation of a pre-synthetized silica support with an iron salt solution[5] or the co-precipitation method.[67] But, those routes suffer from the formation of large nanoparticles aggregates and the interference of metal precursors during the polycondensation of the silica framework. Campelo *et al.*[68] compared different synthesis methods and showed that the co-precipitation of silica and metal precursors directed by the hydrothermal sol-gel synthesis gives a better dispersion of metal species on the silica surface than the salt impregnation of a pre-synthetized silica support. However, the metal precursors interfere with the polycondensation of the silica framework, resulting to undesirable altered structural morphology.[69] Improvement of nanoparticles distribution in a mesoporous silica matrix could be reached by using self-assembled surfactants phases, such as micelles or liquid crystal.[70–72] Among them, our group reported ferrosurfactants able to form either micelles,[13] vesicles[33] or to stabilize solid lipid nanoparticles. The latest, dispersed in a micellar solution of a non-ionic surfactant, P123, could lead to highly dispersed iron oxide nanoparticles within a mesoporous-macroporous silica matrix. The ferrosurfactant acted as the only source of iron and thus triggered the formation of nanoparticles within the macropores.[73] More recently, Yang *et al.*[54] also proposed a non-ionic surfactant (F127®)-assisted method for single iron atoms catalyst synthesis enabling the dispersion of iron species and therefore exhibiting a higher catalytic activity for ORR application.

Motivated by these pioneer works, the present study aims to elaborate mesoporous silica materials with supported isolated single iron atoms, Fe@silica SACs, through the sol-gel self-assembling mechanism from mixed micelles of non-ionic and metallo-surfactants. The non-ionic surfactant template (here the Pluronic P123®) was chosen to control the structural and textural properties of the silica framework (high surface-active area, pore volume, pore size) as it was demonstrated by XRD and N_2 sorption isotherms. More important, the metallosurfactant allows controlling the iron loading and the homogeneous distribution of iron atoms and lack of clustering as it was demonstrated by elemental analysis, STEM mapping, Pair Distribution Function (PDF) analysis, Mas-NMR and Squid measurements.

4.3.2 Materials and Methods

4.3.2.1 Chemicals

Tetramethylorthosilicate (TMOS), Pluronic® P123, and hexadecyltrimethylammonium bromide (CTAB) were purchased from Sigma-Aldrich. Iron-(III) chloride ($FeCl_3$) was purchased from Alfa Aesar. All reagents were used without further purification. Cetylrimethylammoniumtrichloromonobromoferrate (CTAF, $C_{16}H_{33}N(CH_3)^{3+}$, $FeCl_3Br^-$) was synthesized as previously reported.[13,33,73]

4.3.2.2 Preparation of Silica Materials

Silica materials were prepared by sol-gel process, through the cooperative templating mechanism, from micellar solutions of P123 ($M_w = 5800$ g·mol^{-1}) and CTAF ($M_w = 465.55$ g·mol^{-1}), and TMOS ($M_w = 152.22$ g·mol^{-1}) as inorganic precursor. The micellar solutions were prepared by adding 200 mg of P123 and an appropriate amount of CTAF (18, 36, 90, 181 mg) in 10 mL of 1M HCl, to reach the CTAF/P123 molar ratio r of 1, 2, 5 and 10, respectively. In a typical procedure, 310 mg of TMOS were added into those micellar solutions to obtain a P123/TMOS molar ratio of 0.017.

The mixture was stirred at room temperature for 30 min before being transferred into a Teflon bottle and placed in a stainless-steel autoclave at 373 K for 48 h. The resulting hybrid product is then filtered through a paper filter on a funnel, and dried in the air for 24 h. The surfactant can be removed by Soxhlet extraction with ethanol to afford pristine silica (P@SiO_2(r)) or by calcination, to remove the organic part and to afford ferrisilicates (Fe@SiO_2(r)). The programming of the calcination procedure was set as follow: (step 1) increasing temperature from room temperature (RT) to 373 K (2°·min^{-1}) and held for 1 h, (step 2) heating ramp from the 373 K to 623 K (2°·min^{-1}) and held for 1 h, and (step 3) heating ramp from 623 K to 823 K (2°·min^{-1}) and held for 3 h. The yield of the sol-gel process was of 80% while the one of the iron loading yield in ferrisilicates was evaluated to 25%, except for Fe@SiO_2(10), of only 7%.

4.3.2.3 Characterization Methods

a) Nitrogen sorption measurements

The textural properties of the synthesized materials after calcination are determined from the nitrogen adsorption/desorption isotherms obtained at 77 K (p/p_0 increasing from 0 to 0.99 and decreasing from 0.99 to 0.10) using an automatic Micromeritics ASAP 2020 instrument. The specific surface was determined using two methods, the BET method[74] and the 2D-NLDFT method.[75] The total pore volume is determined from the nitrogen adsorption at a relative pressure of 0.97, while the meso-pore volume V_{meso} is calculated by the difference between the total pore volume and the micro-pore volume calculated using the 2D-NLDFT method and the Dubinin Radushkevich DR method.[76] The pores size distributions are computed using the corrected BJH-KJS method.[77]

b) X-ray diffraction

The measurements were performed using a Panalytical X’Pert Pro diffractometer equipped with a Cu tube, a Ge (111) incident-beam monochromator (λ=1.5406Å) and an X’Celerator detector. Small-angle X-ray scattering (SAXS) measurements were collected using 0.02 rad Soller slits, 1/16° fixed divergence and anti-scatter slits. The X’Celerator detector was used as “scanning line detector (1D)” with 0.518° active length. Data collection was carried out in the scattering angle range 0.8–12° with a 0.0167° step over 60 min.

c) Elemental analysis

Si and Fe chemical analysis were performed using an Inductively Coupled Plasma Atomic Emission Spectroscopy (ICP-AES) at the Petrographic and Geochemical Research Center - CRPG UMR 7358 CNRS-UL, 54500 Vandoeuvre-lès-Nancy, France.

d) Spectroscopic measurements (ATR and UV-Vis)

ATR-IR spectra were collected using a Lambda 1050 UV/vis/NIR spectrophotometer (UltraViolet/VISible/Near InfraRed PerkinElmer device) with a diamond ATR crystal. The software used for collecting and viewing spectra was the PerkinElmer UV WinLab. Each absorbance spectrum was obtained by accumulation of 32 scans at 4.0 cm^{-1} resolution using a clean ATR crystal exposed to the ambient atmosphere as a background. The spectra were collected for powdered samples with background corrections, and were plotted without further corrections.

Diffuse reflectance spectra of powder samples were recorded at room temperature in the 200–650 nm range using a UV-visible-NIR spectrometer (Varian Cary 5000) equipped with an integrating sphere attachment.

e) Transmission electron microscopy and elemental cartography

Transmission electron microscopy (TEM) analyses were performed using a JEOL 2100 F electron microscope operating at 200 kV equipped with a probe Cs corrector. The “HAADF-STEM” images were acquired in scanning TEM (STEM) using a high angle annular dark field detector (HAADF). The elemental maps were acquired by Energy Dispersive X-Ray (EDX) Spectroscopy in STEM mode using a JEOL Silicon Drift Detector (DrySD60GV: sensor size 60 mm^2) with a solid angle of approximately 0.5 sr.

f) Total scattering X-ray measurements and PDF analysis

The total scattering X-ray measurements were performed at the High energy Beamline for Buried-interface Structures and Materials Processing ID31 of the European Synchrotron Radiation Facility (ESRF). The data-sets were collected using a large area, high energy single-photon counting detector, Pilatus3 2M CdTe and a high energy monochromatic beam (68.5 keV, $\lambda = 0.18099$ Å). Sample powder was loaded into a 1 mm diameter kapton capillary. The raw two-dimensional data sets were azimuthally integrated and converted to one-dimensional intensity versus 2θ using PyFAI software package.[78] We note here that the total scattering measurements have been conducted under the same experimental conditions for all the studied samples (Fe@SiO_2(1), Fe@SiO_2(2), Fe@SiO_2(5) and Fe@SiO_2(10)). The collected data were then corrected for experimental effects (absorption, multiple scattering, polarization, Compton scattering and Laue diffuse scattering) and the scattering signal from the air and the experimental set up was measured independently under the exact same conditions as the samples and subtracted as a background in the data reduction procedure. The data were truncated at a finite maximum value of Q_{max}=18 $Å^{-1}$ beyond which the signal-to-noise ratio became unfavorable. All the differential experimental atomic pair distribution functions (d-PDF) were obtained by using the PDFgetX3 program[79] and following the procedure we reported earlier.[80,81]

g) Solid-state nuclear magnetic resonance

Solid-State NMR spectra were acquired on a DSX 500 Bruker spectrometer with a magnetic field of 11.7 T at 600 MHz. Bruker Magic Angle Spinner MAS probes of 4 and 2.5 mm rotor diameter were used for the experiment. ^{29}Si and ^{1}H spectra are recorded at 300K using High Power Decoupling HPDec pulse program with MAS frequencies of 12.5 kHz.

h) Magnetic measurements

Magnetic measurements were performed with a SQUID-VSM magnetometer (from Quantum Design) used in the dc-mode, which allows measuring magnetic moments up to 10^{-8} emu. Samples are introduced in a gelatin capsule placed in a plastic straw and studied at both temperatures (2 and 300 K) and both field (0 and 7 T) dependences of magnetization.

i) Density functional theory calculations

Periodic spin polarized density functional theory (DFT) calculations were performed using the VASP package[82] by means of the projector augmented wave (PAW) method.[83] The GGA+U[84–86] method was used for the exchange and correlation potential, in order to take into account the strong electron-electron interaction due to the iron localized open d shell. The values of the parameters U and J were set to 3 eV and 0.9 eV, respectively.[87] Dispersion effects were considered by means of the DFT-D2 correction by Grimme *et al.*,[88] as implemented in VASP.[89]

In this work, we investigated the interaction between a single iron atom and amorphous silica-surfaces, considering three different silanol densities: 7.2, 4.6 and 3.3 OH/nm^2.[90,91] The fully hydroxylated surface (SiO_2-7.2) was represented by a supercell containing 402 atoms, and for SiO_2-4.6 and SiO_2-3.3, 384 and 375 atoms, respectively. In all the cases, the periodically repeated slabs were separated by more than 20 Å of vacuum in the z direction. A plane-wave basis set with a kinetic energy cutoff of 450 eV was used to ensure the convergence of our calculations. Due to the large size of the supercell, only the Γ point was used to sample the Brillouin zone. The total energy converged to within 10^{-6} eV. For the atomic relaxation, the single iron atom and the atoms of the first layer of the silica-surface were relaxed by nullifying the forces on the atoms with a precision of 0.03 eV/Å and the other layers were kept fixed.

4.3.3 Results and Discussions

4.3.3.1 Synthesis of Silica Materials

Silica materials were prepared through the self-assembling mechanism (**Figure 4.3.1**) by adding a silica precursor (tetramethoxylsilane, TMOS) to a mixed micellar solution of a non-ionic surfactant, the Pluronic P123, and a metallosurfactant, CTAF, at various molar ratio, r (of 1, 2, 5, 10 where $r = n_{CTAF}/n_{P123}$).

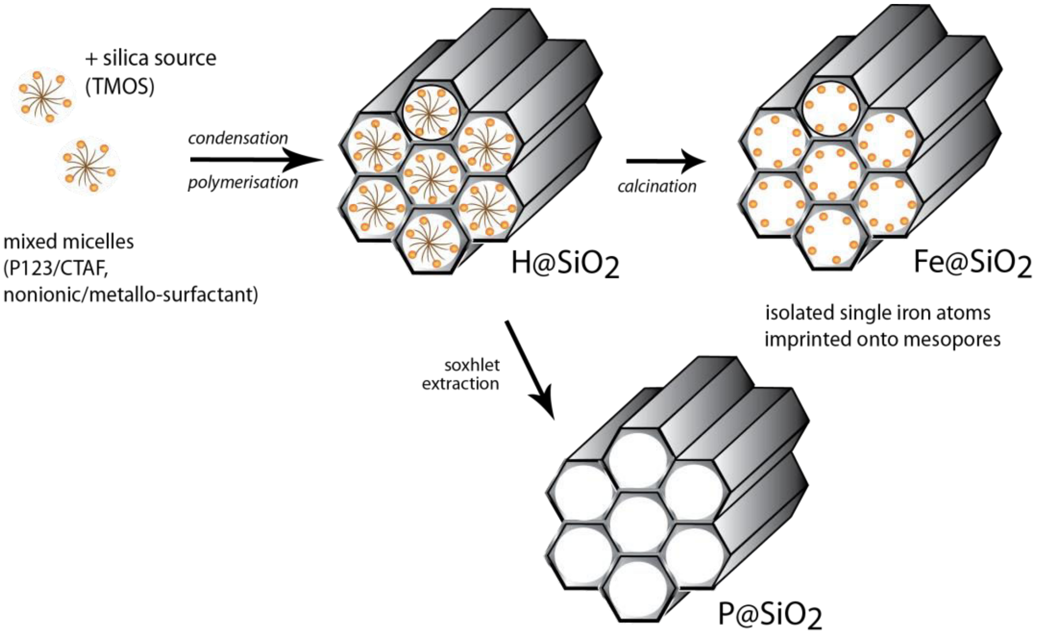

Figure 4.3.1 *Schematic representation of the sol-gel synthesis of silica materials through the self-assembling mechanism based on mixed micelles of metallo-surfactant CTAF and P123.*

The hydrothermal reaction conditions are similar to the one used communally for the synthesis of SBA-15 (hydrothermal treatment under acidic catalysis, 1M HCl, for 48 h at 373 K).[1,2] Indeed, under these reaction conditions and in the absence of CTAF, the pristine material exhibit hexagonally ordered mesopores of around 8 nm diameter and a surface area and pore volume of 846 $m^2 \cdot g^{-1}$ and of 0.984 $cm^3 \cdot g^{-1}$, respectively, as it was determined from XRD and N_2 adsorption measurements (**Annex 2**). These values are in agreement with a typical SBA-15 silica material.[2] By adding CTAF, mixed micelles are formed which affect both the mesostructure and the textural properties of the resulting materials, as reported in **Table 4.3.1**.

Table 4.3.1 *Textural properties of the Fe@SiO$_2$(r) materials (r=1, 2, 5, 10): the interlayer distance/unit cell dimension for hexagonal networks d_{Bragg}/a_0, the pore diameter $Ø_{BET}$, the wall thickness ε, the surface area S_{BET} and S_{NLDFT}, the mesopores volume $V_{0.97}$, and the silanols density $\rho_{Si\text{-}OH}$.*

	d_{Bragg}/a_0 (nm)	$Ø_{BET}$ (nm)	ε (nm)	S_{BET} (m^2/g)	S_{NLDFT} (m^2/g)	$V_{0.97}$ (cm^3/g)	$\rho_{Si\text{-}OH}$ (OH/nm^2)
Fe@SiO$_2$(1)	9.4/10.9	4.8/7.3/12.4	3.6	731	809	1.34	-
Fe@SiO$_2$(2)	8.2/9.5	5.0/6.6/12.3	2.9	750	819	1.41	5.5
Fe@SiO$_2$(5)	7.8/-	4.9	2.9	957	974	1.43	3.8
Fe@SiO$_2$(10)	6.6/-	5.5	1.1	993	1013	1.34	4.0

4.3.3.2 Structural and Textural Characterization of Fe@SiO_2(r) Materials

From the XRD data (**Figure 4.3.2A**), it can be first seen that the mesopore ordering of the materials is decreasing with the increase of CTAF content. At low r values (r= 1 and 2), the materials exhibit three reflection peaks located respectively at 9.4, 5.5 and 4.7 nm for Fe@SiO_2(1) and at 8.2, 4.9, and 4.4 nm for Fe@SiO_2(2). Their relative positions are 1, $\sqrt{3}$ and 2, which can be attributed to the (100), (110) and (200) reflections of a hexagonal structure. According to Bragg's law, the unit cell dimension (a_0) can be calculated and was found to be equal to 10.9 nm for Fe@SiO_2(1) and 9.5 nm for Fe@SiO_2(2). This decrease of the cell unit could be due to the silica wall thickness and/or pore diameter. The hexagonal structuring of the pores was further confirmed by transmission electron microscopy (TEM) micrographs showing honeycomb like arrangements (*i.e.* Fe@SiO_2(1) in **Figure 4.3.3**). In addition to those hexagonally organized mesopores of about 8 nm of diameter and 3 nm of wall thickness, the micrographs also show the coexistence with larger, unorganized pores, of about 12 nm of diameter.

At higher r values (r= 5 and 10), the materials exhibit a broad peak located respectively at 7.8 nm for Fe@SiO_2(5) and at 6.6 nm for Fe@SiO_2(10). This indicates the formation of wormhole-like structures. The loss of structuring might be due to the increase of the total surfactant $n_{P123+CTAF}/n_{TMOS}$ molar ratio (R) with the increase of r values. As a matter of fact, in order to control the iron/silica ratio, only the P123/TMOS molar ratio was maintained constant, without adjusting R ($n_{P123+CTAF}/n_{TMOS}$) as a function of r (n_{CTAF}/n_{P123}). Or, it is communally accepted that the parameter R is paramount in getting well-defined architectures and it is strongly depending on the nature of the surfactant. For instance, hexagonally ordered materials could be obtained with solely P123 at R=0.017 and with solely CTAF at R=0.17.

Another important parameter influencing the morphology and the pore size of the resulting material is the size and nature of the micelles used as template. The iron ions from CTAF might induce the complexation of ethylene oxide units of P123 and thus the shrinking of the mixed micelles and the reduction of the silica/surfactant interaction. Obviously, when increasing the CTAF content, the repetition distance decreases, indicating a decrease of the pore size and/or of silica wall thickness.

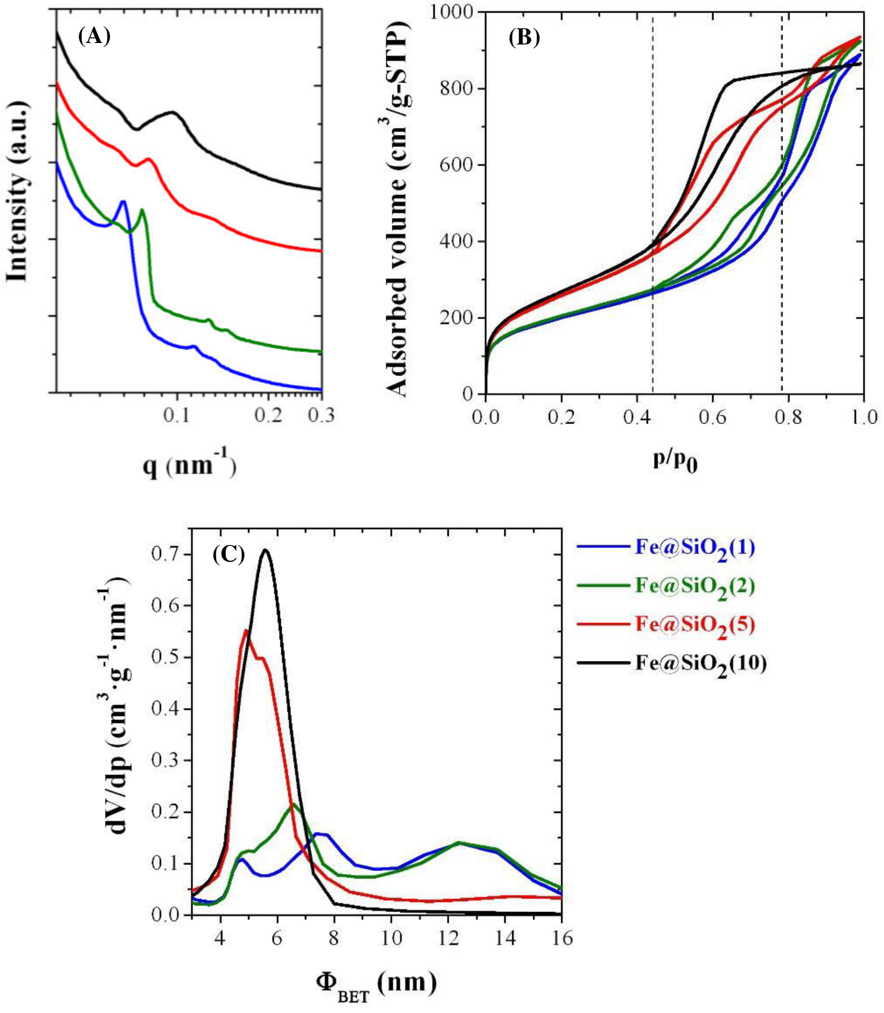

Figure 4.3.2 *Textural properties of Fe@SiO$_2$(r) materials (r = n_{CTAF}/n_{P123} = 1, 2, 5, 10):* ***(A)*** *XRD patterns,* ***(B)*** *N_2 adsorption-desorption isotherms and* ***(C)*** *pore size distribution.*

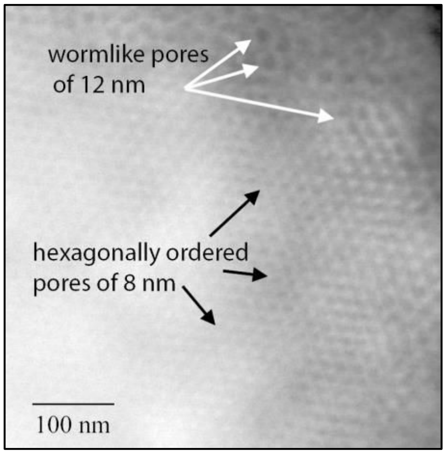

Figure 4.3.3 *Transmission electron micrograph of Fe@SiO$_2$(1).*

Further insights on the pore size distribution were reached from nitrogen adsorption/desorption isotherms. Except Fe@SiO$_2$(10) which exhibits a type IV isotherm with one hysteresis loop, characteristic of mesoporous materials, all materials exhibit rather a type II isotherms with two main steps desorption branch indicating the coexistence of mesopores of different sizes (**Figure 4.3.2B**). On all isotherms, it can be observed that the value of the relative pressure, at which the first capillary condensation occurs is almost the same, between 0.4 and 0.5. Since the p/p_0 position of the inflection point is related to the pore diameter, according to Kelvin's equation, this observation suggests that all materials have mesopores of about 5 nm diameter. As a matter of fact, Fe@SiO$_2$(10) has a monomodal distribution of mesopores centered on 5 nm, as shown on the pore diameter distribution obtained by the BJH method (**Figure 4.3.2C**). The second inflection point appears for the other materials at a p/p_0 value comprised between 0.7 and 0.8, suggesting those larger pores. For Fe@SiO$_2$(1) and Fe@SiO$_2$(2), three zones of N_2 isotherms can be identified, the first for p/p_0 between 0.50 and 0.75, the second between 0.75 and 0.80, and the third for p/p_0 between 0.80 and 0.99 which indicate the existence of three population of porosity size. For the Fe@SiO$_2$(5) material, one can observe two zones of N_2 isotherms, the first for p/p_0 between 0.50 and 0.80 corresponding the porosity peak around 5 nm and the second corresponding to bigger pores ($8 < D < 16$ nm) where $dV.dD^{-1}$ is around 0.05 $cm^3 \cdot g^{-1} \cdot nm^{-1}$. While the Fe@SiO$_2$(10) sample shows one N_2 adsorption zone ($0.50 < p/p_0 < 0.80$) corresponding to the 5 nm pore diameter peak, with no adsorption for p/p_0 above 0.80. The pore sizes of all materials are higher than the one obtained by using only CTAF as template, without adding the non-ionic P123 surfactant (of 2.4 nm).[13] So is the wall thickness, ε, as it was calculated by the subtraction of the pore size (ϕ_{BET}) from the interlayer distance (d_{Bragg}) for the wormlike materials and from the cell unit for the hexagonal ordered ones. The surface areas are similar for the hexagonally ordered materials Fe@SiO$_2$(1) and Fe@SiO$_2$(2) on one side, and for the wormlike materials Fe@SiO$_2$(5) and Fe@SiO$_2$(10) on the other side. A sharp increase, of almost 200 $m^2 \cdot g^{-1}$, can be noticed between the two series of materials, with the decrease of the pore diameter. All materials have high surface area, S_{BET} and S_{NLDFT}, and the total pore volume $V_{0.97}$ (**Table 4.3.1**), and are therefore considered attractive for catalytic applications, as they might prevent coke blocking in hydrodeoxygenation reactions for example.

4.3.3.3 Chemical Characterization of Fe@SiO$_2$(r) Materials

The attenuated total reflectance infrared ATR-IR spectra of Fe@SiO$_2$(r) materials confirms the formation of the silica framework upon the sol-gel process and the removal of the organic part of the surfactant after calcination. Characteristic peaks of the stretching and bending vibration of Si-O-Si, Si-O and Si-OH bonds are present in the 900-1100 cm^{-1} region, while no peaks of CH_2 moieties appear in between 2800 and 2900 cm^{-1} (**Figure 4.3.4left**). The ATR spectra also show the presence of OH groups at 1633 cm^{-1} and at 3200-3700 cm^{-1} that were assigned to silanol groups and physisorbed water, respectively. Quantitative assessment of silanol densities on the surface of those materials was obtained from BET and TGA analysis (**Table 4.3.1** and **Annex 3** for the calculation method).

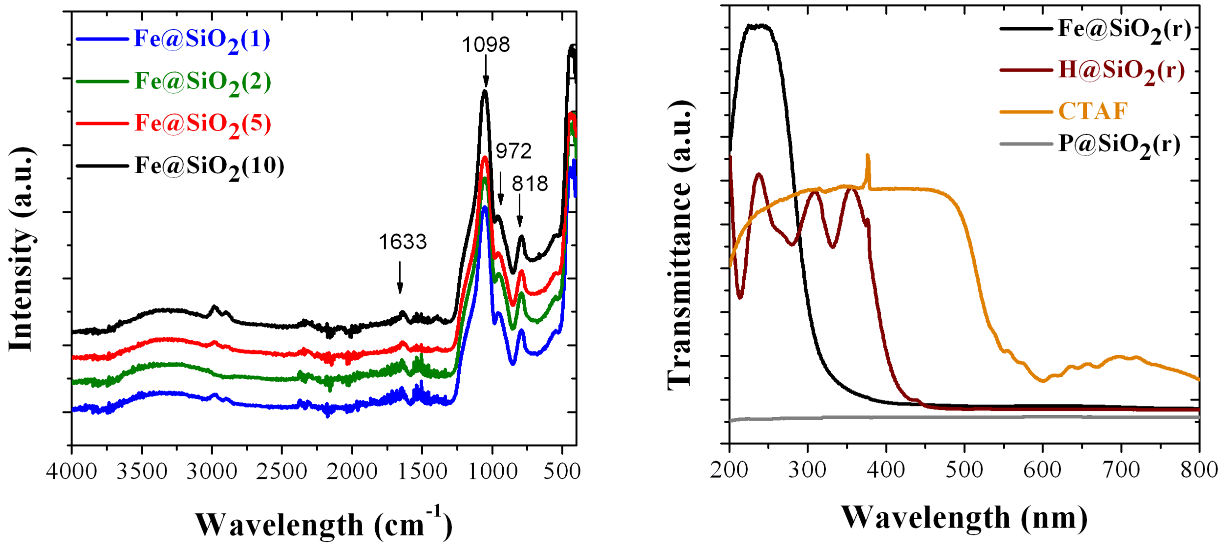

Figure 4.3.4 (left) *Infrared Attenuated Total Reflectance IR-ATR peaks of Fe@SiO$_2$(r) materials and* ***(right)*** *UV-Vis diffuse reflectance spectra of pristine and iron loaded materials.*

All materials exhibit silanols density values slightly higher than for the similarly synthesized SBA-15-like silica, with no CTAF (around 2.50 OH/nm^2). This may be due to the existence of iron atoms that obstruct silica crosslinking during the polymerization, which may indicate the formation of Si-O(H)…Fe bonds instead of Si-O-Si bonds.

The condensation degree of silica is assessed from ^{29}Si solid-state NMR. Relative proportion of Q_2 (geminal $SiO_2(OH)_2$ silanols), Q_3 (isolated and vicinal $SiO_3(OH)$ silanols), and Q_4 (SiO_4 bonds) units were determined after deconvolution of the peaks at -91, -99 and -110 ppm, respectively. All materials exhibit the same condensation degree Q_2:Q_3:Q_3 of 1:24:75 and relative surface of OH-OH sites, around 60%. In addition, NMR results show that the Chemical Shift Anisotropy CSA for ^{29}Si (in Q_2, Q_3, and Q_4 states) and ^{1}H (in O-H and OH-OH states) increases as the CTAF content increases and the relaxation time decreases (**Figure 4.3.5**). The study of the ^{29}Si relaxation time shows the existence of two characteristic relaxation time populations, τ_1 of the order of milliseconds (ms, short time) and τ_2 of the order of seconds (s, long time). The percentage of component with the short relaxation time increases from 29% for Fe@SiO$_2$(1), to 50% for Fe@SiO$_2$(2), before reaching a maximum of 65% for Fe@SiO$_2$(5) and Fe@SiO$_2$(10).

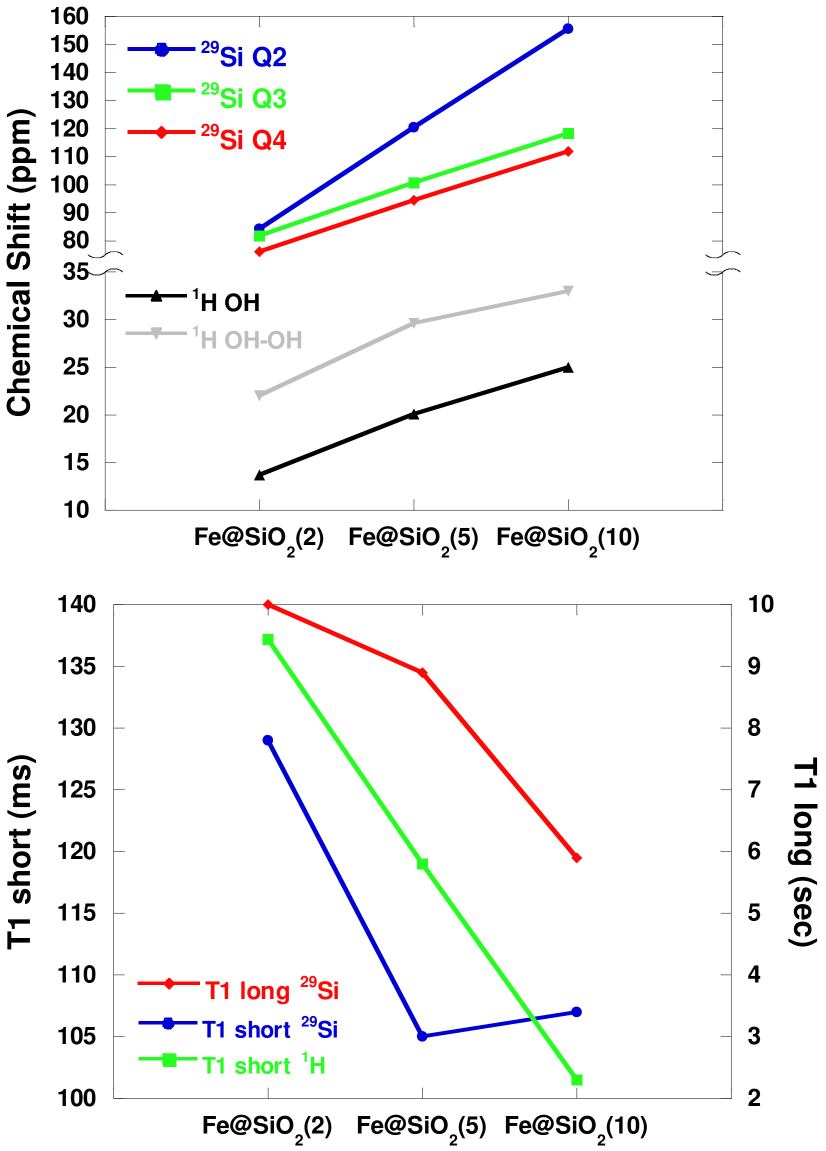

Figure 4.3.5 ***(top)*** *Chemical Shift of* ^{29}Si Q_2, ^{29}Si Q_3, ^{29}Si Q_4, ^{1}H *OH*, ^{1}H *OH-OH, and* ***(down)*** *Relaxation times of* ^{29}Si *(short and long) and* ^{1}H *(short) for Fe@SiO*$_2$*(r) materials (r=2, 5, 10).*

4.3.3.4 Characterization of Single Atom Fe@SiO$_2$(r) Materials

First quantitative assessment of the iron loading was obtained from both ICP-AES elementary analysis is found to be around 0.56, 0.98, 2.31, and 2.64 wt.% for Fe@SiO$_2$(1), Fe@SiO$_2$(2), Fe@SiO$_2$(5), and Fe@SiO$_2$(10), respectively, as compared to Si (see **Table 4.3.2** for the iron loading values compared to SiO$_2$). Those results were further confirmed by the elemental analysis maps obtained in the scanning transmission electron microscopy (STEM). The Fe content in these materials, as compared to the Si one, is found to be around 0.8, 1.1, 2.5, and 2.7 wt.% for Fe@SiO_2(1), Fe@SiO_2(2), Fe@SiO_2(5), and Fe@SiO_2(10), respectively. Moreover, as it can be seen in **Figure 4.3.6**, the micrographs show a homogeneous dispersion of iron atoms within the silica matrix, without formation of any agglomerates.

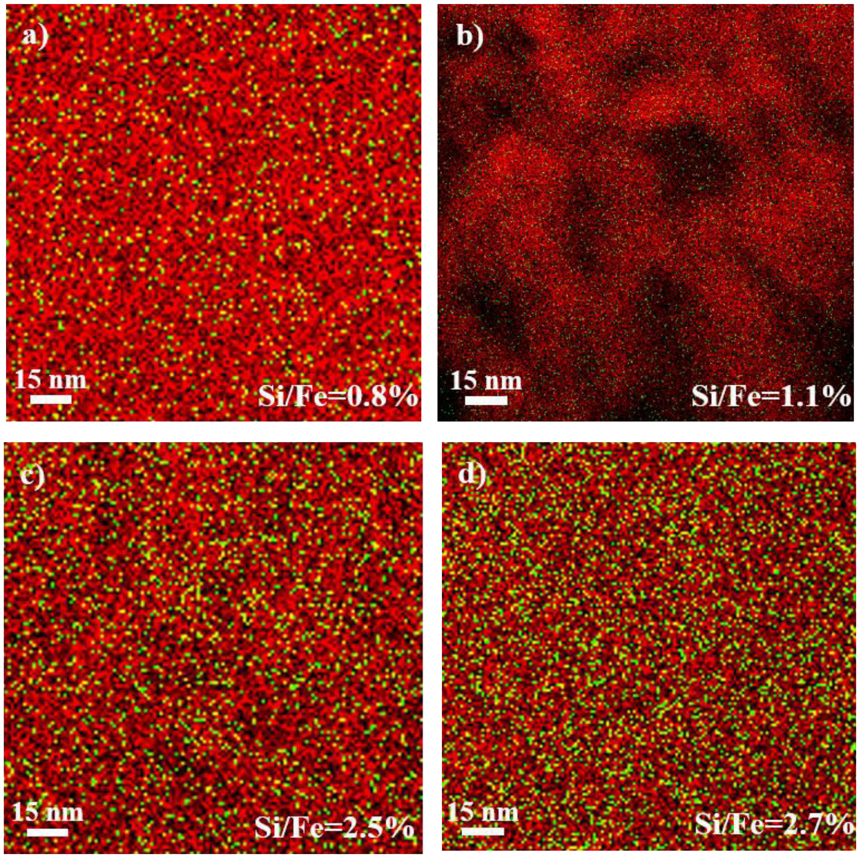

Figure 4.3.6 *Relative elemental maps of Fe and Si obtained by EDX in the scanning TEM mode for* ***(A)*** *Fe@SiO_2(1),* ***(B)*** *Fe@SiO_2(2),* ***(C)*** *Fe@SiO_2(5),* ***(D)*** *Fe@SiO_2(10) (iron in green and silica in red) with the corresponding Si/Fe mass ratio for each sample.*

UV-Vis diffuse reflectance spectra (**Figure 4.3.4right**) allowed us to determine the coordination of iron in the materials. The adsorption band at 235 nm, which can be assigned to the charge transfer of pπ–dπ transition between oxygen and iron in the ferrisilicate material, suggest tetrahedral iron atoms, insulated from each other. In addition, the absence of any absorbance band above 350 nm in the spectrum reveals the absence of octahedral iron ions, and consequently the absence of iron oxide nanoparticles in the Fe@SiO_2 materials.[92]

The absence of nanoparticles was also confirmed by the analysis of the experimental pair distribution function derived from the corresponding total scattering measurements of the materials (**Figure 4.3.7**).

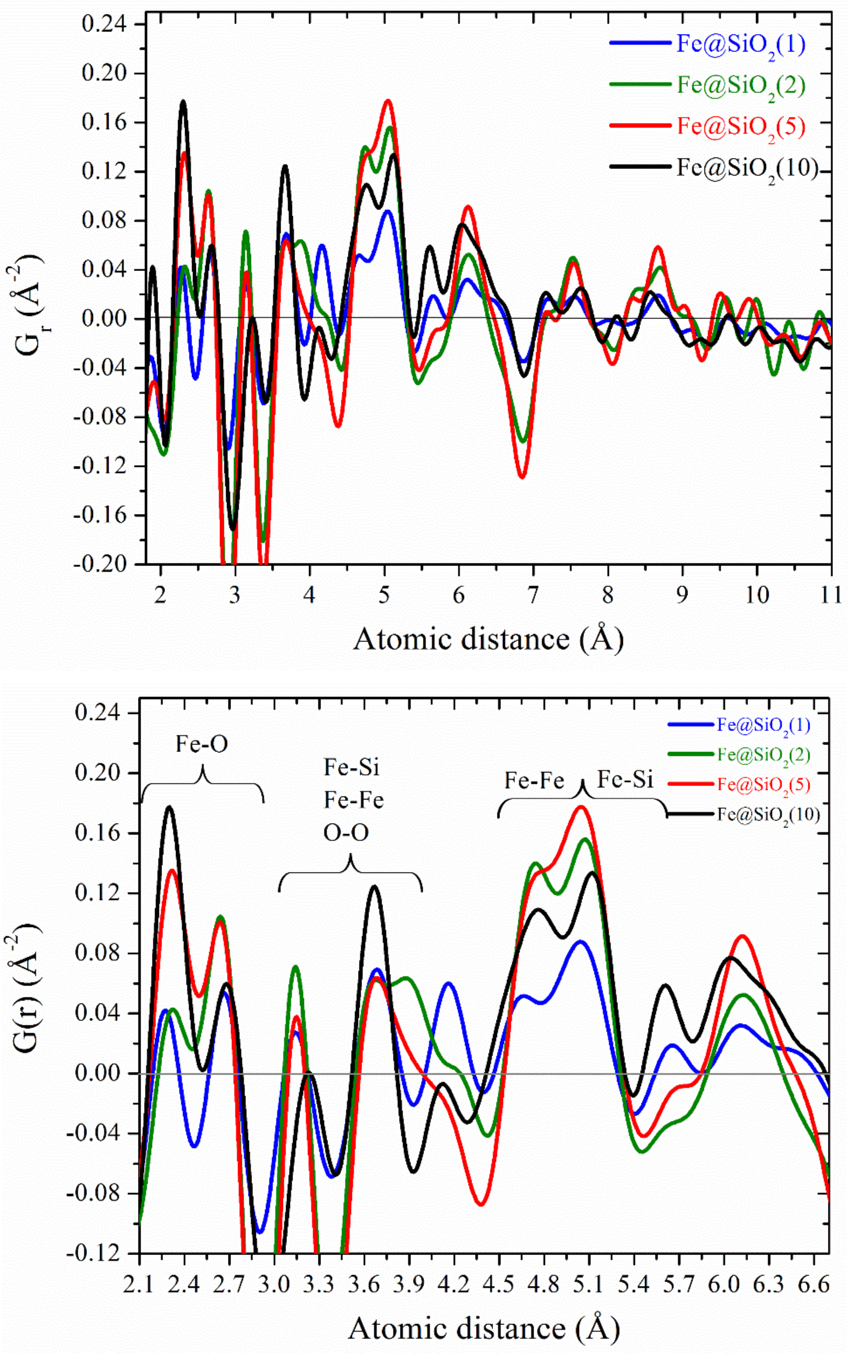

***Figure 4.3.7 (top)** Comparison of experimental atomic pair distribution functions (PDFs) in real space, G(r), for Fe@SiO2(r) materials **(down)** Allocation of the main interatomic distances in the range 2 – 7 Å.*

From the PDF diagrams, we can clearly observe well-defined features up to about 10 Å. The rapid damping of PDF oscillations beyond r~ 10 Å even for materials with higher metal content indicates that the isolated subnanometer iron systems of maximum dimensions ~10 Å are formed and are uniformly distributed throughout the samples without any agglomeration. **Figure 4.3.7** shows the main atomic pairs contributing to the PDF peaks. It is obvious that the intensities of the PDF peaks corresponding to the contributions of the Fe atoms increase as the CTAF surfactant content increases. The first two PDF peaks located in the r range of 1.9-2.6 Å are characteristic of Fe-O distances. The distribution of these bond lengths clearly indicate that the Fe center environment corresponds to a mixture of two spin states as was also determined from magnetic and NMR measurements and predicted from the theoretical calculations. It is noteworthy that the presence of the double peak between 1.9 and 2.6 Å indicates that two related Fe environments are seen in the confined. This structural organization is most likely correlated with the interatomic interactions. The interactions of the iron atoms with the silica pore walls result in the PDF peaks located at ~ 3 and 3.6 Å and thus indicate their confinement within the pores of the host silica matrices. Indeed, the formation of clusters or nanoparticles on the outer surface of the silica matrices will promote the growth of larger nanoparticles that eventually agglomerate. This effect will result in the PDF diagram by a spatial extent of atomic correlations.

WAXS analysis were also performed and results did not show any diffraction of iron nanoparticles, which is consistent with the homogeneous distribution of Fe atoms (**Figure 4.3.8**).

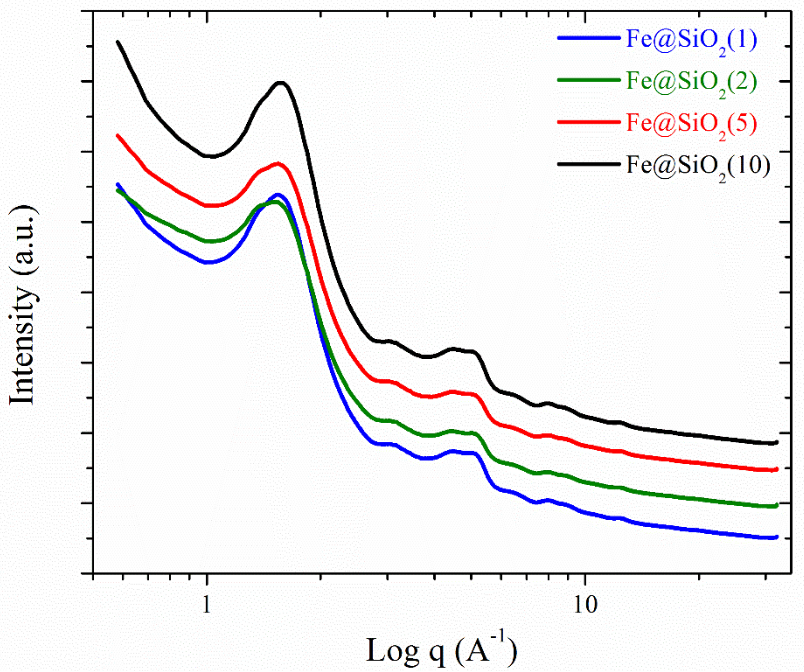

Figure 4.3.8 *Wide angle X-ray scattering WAXS measurements for Fe@SiO2(r) materials.*

Magnetic measurements have been performed in order to check the presence of paramagnetic Fe. **Figure 4.3.9** shows the field dependence of the Fe@SiO$_2$(r) measured at 10K after a first cooling at 15 K.min^{-1}. These measurements have been subtracted from the diamagnetic contribution of sample holder and pristine P@SiO$_2$(r) silica (described in **Annex 4.1**), and have been scaled with respect to Fe content using the elemental analysis results They can be fitted by a sum of two Brillouin functions as follow:

$$M(H,T) = xM_s^{5/2}B_{5/2}(H,T) + (1-x)M_s^{1/2}B_{1/2}(H,T)$$

where x is the only fitted parameter giving the proportion of the high spin S=5/2, $M_s^{5/2}$ and $M_s^{1/2}$ are the saturation magnetization of Fe^{3+} in the high spin and low spin states, respectively ($M_s^{5/2} = 500\, emu/gFe$ and $M_s^{1/2} = 100\, emu/gFe$), and $B_s(H,T)$ are the corresponding Brillouin functions (S=5/2, 1/2).

$$B_s(\alpha) = \frac{2S+1}{2S}\coth\frac{(2S+1)\alpha}{2S} - \frac{1}{2S}\coth\frac{\alpha}{2S}$$

where $\alpha = \dfrac{\mu_B H}{k_B T}$.

The fit with $M(H,T)$ equation has been performed for samples exhibiting a Curie temperature dependence under 1 kOe above 10K (see **Annex 4.1**).

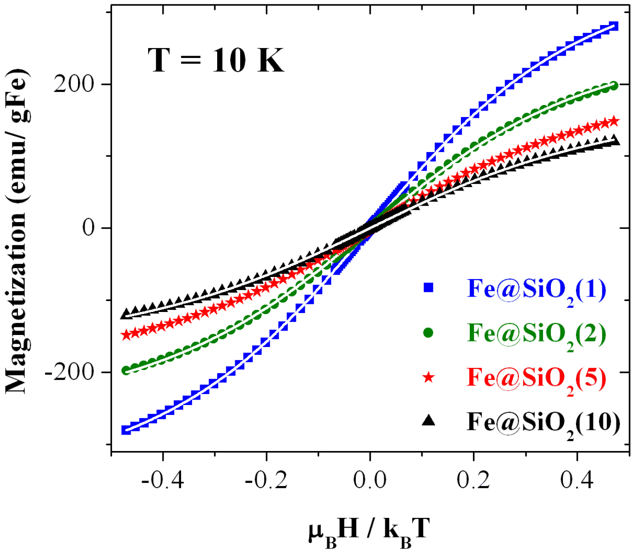

Figure 4.3.9 *Field dependence behavior of the magnetization measured at 10K and corrected from the diamagnetic signal for Fe@SiO$_2$(r) (r = 1, 2, 5, 10) samples. It is plotted as a function of the dimensionless parameter $\mu_B H/k_B T$ where μ_B is the Bohr magneton and k_B the Boltzmann constant. The straight lines are fits by the sum of the two Brillouin functions corresponding to S = 5/2 and 1/2.*

Despite only one parameter is fitted, a very good agreement is obtained between the simple model and the measurements. No ferromagnetic contribution is detectable at this scale. The high spin fraction deduced from the fit is reported in **Table 4.3.2**. They are in good agreement to those deduced from the Curie constant (see **Annex 4.1**). No fit with equation has been performed for the Fe@SiO_2(5) sample as the temperature dependence of the magnetization deviates from the Curie law below 15 K. This deviation is attributed to spin crossover towards low spin with decreasing temperature, which occurs below 10 K for other samples (**Annex 4.2**). Nevertheless, the high spin fraction reported in **Table 4.3.2** is stable with temperature above 10 K (or 15 K for Fe@SiO_2(5)) and is then a relevant parameter characterizing the Fe sites in the silica pores. It decreases as the Fe content increases, concomitantly with the decreasing size of the pores. This fraction reflects the ratio of two distinct relaxation time populations (short and long) observed by NMR for ^{29}Si. Beyond the sharing of Fe spin state according to Si sites or pore sizes, the consistent quantitative analysis in terms of Curie or Brillouin laws without interaction between Fe spins (no Curie-Weiss temperature) supports the assumption of isolated Fe atomic centers well dispersed within the materials.

Table 4.3.2 *Fe content (wt.%) with respect to the total samples mass used to scale the magnetization. Fraction of Fe(III) spins in the high spin state (5/2) deduced from the temperature dependence of magnetization (Curie law) or field dependence of magnetization measured at 10 K.*

	Fe loading (wt.%)	$x_{5/2}^{Curie}$	$x_{5/2}^{Brillouin}$
Fe@SiO_2(1)	0.23	0.72	0.71
Fe@SiO_2(2)	0.41	0.49	0.47
Fe@SiO_2(5)	0.97	0.31*	-
Fe@SiO_2(10)	1.08	0.25	0.24

*No fit with Brillouin functions has been performed for Fe@SiO_2(5) as it deviates from the Curie low below 15K. For this sample, the fit with the Curie law has been performed in the 15-30 K.

4.3.3.5 DFT Calculations

To find the most stable configurations of the Fe/SiO_2 system, several structural optimizations were started from reasonable estimations at various adsorption positions (top, bridge) on surfaces with various silanol densities (SiO_2-7.2, SiO_2-4.6 and SiO_2-3.3).[61,62] For each configuration, two sets of calculations were performed for the Low-Spin (LS) and High-Spin (HS) states of iron.

The Fe atom is adsorbed on the silica surface through its oxygen atoms by removing the corresponding hydrogen atoms. **Figure 4.3.10** shows the single iron atom adsorbed on the typical silica surface with a silanol coverage equal to 4.6 OH per nm^2 at top (left panel) and bridge (down panel) positions. From the values of the total energy determined for Fe/SiO_2 (**Table 4.3.3**), one can deduce that the adsorption of the single iron atom on various amorphous silica-surface at different adsorption positions stabilizes the HS state. For the top positions, the HS state magnetic moment of iron is 4.97 μB (S =5/2) while the one of the LS state is 1.00 μB (S =1/2), which correspond to Fe^{3+}. The equilibrium distance between the iron atom and the substrate is found to be 1.81 Å in HS and 1.78 Å in LS. However, the HS and LS state magnetic moments of the iron in the bridge positions are found to be 4.00 μB (S = 2) and 0.00 μB (S = 0), respectively, which are the HS and LS states of Fe^{2+}. For the HS state, the iron-surface distances were found to be 1.99 and 1.85 Å for both oxygen atoms, whereas for the LS state, these distances became 1.85 and 1.81 Å, respectively. For various silica surfaces, the calculations show that the adsorption of the iron atom at top positions had the lowest total energy.

Table 4.3.3 *Total energies (in eV) for the adsorbed iron atom in its HS and LS states on* SiO_2*-7.2,* SiO_2*-4.6 and* SiO_2*-3.3 surfaces at different adsorption positions.*

Surface	**Position**	**E_{tot} (eV)**	**Mag (μ_B)**	**Ion**	**Spin State**
SiO_2-7.2	Top	-2889.3588	4.97	Fe^{3+}	HS
		-2888.6689	-1.00	Fe^{3+}	LS
	Bridge	-2886.4333	4.00	Fe^{2+}	HS
		-2885.4143	0.00	Fe^{2+}	LS
SiO_2-4.6	Top	-2795.1569	4.99	Fe^{3+}	HS
		-2794.4990	1.00	Fe^{3+}	LS
	Bridge	-2793.3893	4.00	Fe^{2+}	HS
		-2792.6772	0.00	Fe^{2+}	LS
SiO_2-3.3	Top	-2745.5974	4.99	Fe^{3+}	HS
		-2745.3764	1.00	Fe^{3+}	LS
	Bridge	-2743.4778	4.00	Fe^{2+}	HS
		-2742.7219	1.00	Fe^{2+}	LS

This means that the density of the silanols at the surface of the material does not affect significantly the properties of the iron atom, for which the Fe^{3+} ion is predominantly in the HS state. This result is in agreement with the experimental findings for Fe@SiO_2(1) where the density of the iron atoms per nm^2 of silica is very low, of only 0.03, and not expected to undergo any spin transition under geometrical constrains. This means that the density of silanols at the surface of the oxide does not affect significantly the properties of the iron atom for which the Fe^{3+} ion is, according to our calculations, expected to be predominant, in agreement with the experimental results.

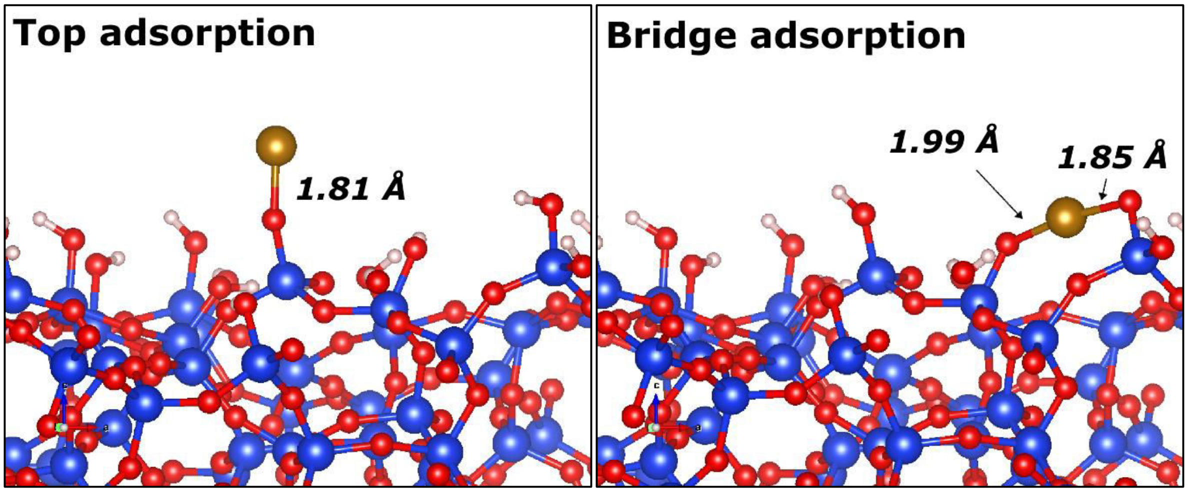

Figure 4.3.10 *Panels showing the single iron atom adsorbed on amorphous silica surface with a silanol density of 4.6 OH/nm^2 at top (left) and bridge (right) positions, respectively.*

4.3.4 Conclusions

In this study, we demonstrated that single iron atoms supported materials (Fe/SiO$_2$) could be prepared through the hydrothermal synthesis using mixed non-ionic/metallosurfactants as templates. The non-ionic pluronic P123 surfactant allows controlling the structural and textural properties of the silica framework while the ferrosurfactant acts as a metal donor, in addition to its role of porogen. The iron loading in the final materials depends on the molar ratio of surfactants and can be accurately tuned, up to 1wt% (0.15 Fe atoms/nm^2). Pair distribution function analysis, STEM mapping and magnetic measurements demonstrated the absence of any particles or clusters. DFT calculations showed that the atoms are predominated Fe^{3+}, in agreement with the experimental data. Those materials proved a good distribution of iron atoms on the silica surface, with increased number of active sites, which might find straightforward applications in catalysis.

References

(1) Zhao, D. Triblock Copolymer Syntheses of Mesoporous Silica with Periodic 50 to 300 Angstrom Pores. *Science* **1998**, *279* (5350), 548–552.

(2) Zhao, D.; Sun, J.; Li, Q.; Stucky, G. D. Morphological Control of Highly Ordered Mesoporous Silica SBA-15. *Chem. Mater.* **2000**, *12* (2), 275–279.

(3) Bragg, W. H.; Bragg, W. L. The Reflection of X-Rays by Crystals. *Proc. R. Soc. Math. Phys. Eng. Sci.* **1913**, *88* (605), 428–438.

(4) Blin, J. L.; Carteret, C. Investigation of the Silanols Groups of Mesostructured Silica Prepared Using a Fluorinated Surfactant: Influence of the Hydrothermal Temperature. *J. Phys. Chem. C* **2007**, *111* (39), 14380–14388.

(5) Huang, H.; Ji, Y.; Qiao, Z.; Zhao, C.; He, J.; Zhang, H. Preparation, Characterization, and Application of Magnetic Fe-SBA-15 Mesoporous Silica Molecular Sieves. *J. Autom. Methods Manag. Chem.* **2010**, *2010*, 1–7.

(6) Olcese, R. N.; Bettahar, M.; Petitjean, D.; Malaman, B.; Giovanella, F.; Dufour, A. Gas-Phase Hydrodeoxygenation of Guaiacol over Fe/SiO_2 Catalyst. *Appl. Catal. B Environ.* **2012**, *115–116*, 63.

(7) Burattin, P.; Che, M.; Louis, C. Characterization of the Ni(II) Phase Formed on Silica Upon Deposition−Precipitation. *J. Phys. Chem. B* **1997**, *101* (36), 7060–7074.

(8) Burattin, P.; Che, M.; Louis, C. Molecular Approach to the Mechanism of Deposition−Precipitation of the Ni(II) Phase on Silica. *J. Phys. Chem. B* **1998**, *102* (15), 2722–2732.

(9) Burattin, P.; Che, M.; Louis, C. Metal Particle Size in Ni/SiO_2 Materials Prepared by Deposition−Precipitation: Influence of the Nature of the Ni(II) Phase and of Its Interaction with the Support. *J. Phys. Chem. B* **1999**, *103* (30), 6171–6178.

(10) Burattin, P.; Che, M.; Louis, C. Ni/SiO_2 Materials Prepared by Deposition−Precipitation: Influence of the Reduction Conditions and Mechanism of Formation of Metal Particles. *J. Phys. Chem. B* **2000**, *104* (45), 10482–10489.

(11) Mutz, B.; Belimov, M.; Wang, W.; Sprenger, P.; Serrer, M.-A.; Wang, D.; Pfeifer, P.; Kleist, W.; Grunwaldt, J.-D. Potential of an Alumina-Supported Ni_3Fe Catalyst in the Methanation of CO_2: Impact of Alloy Formation on Activity and Stability. *ACS Catal.* **2017**, *7* (10), 6802–6814.

(12) Shi, D.; Yang, Q.; Peterson, C.; Lamic-Humblot, A.-F.; Girardon, J.-S.; Griboval-Constant, A.; Stievano, L.; Sougrati, M. T.; Briois, V.; Bagot, P. A. J.; Wojcieszak, R.; Paul, S.; Marceau, E. Bimetallic Fe-Ni/SiO_2 Catalysts for Furfural Hydrogenation: Identification of the Interplay between Fe and Ni during Deposition-Precipitation and Thermal Treatments. *Catal. Today* **2019**, *334*, 162–172.

(13) Kim, S.; Bellouard, C.; Pasc, A.; Lamouroux, E.; Blin, J.-L.; Carteret, C.; Fort, Y.; Emo, M.; Durand, P.; Stébé, M.-J. Nanoparticle-Free Magnetic Mesoporous Silica with Magneto-Responsive Surfactants. *J. Mater. Chem. C* **2013**, *1* (42), 6930–6934.

(14) Muller, P. Glossary of Terms Used in Physical Organic Chemistry (IUPAC Recommendations 1994). *Pure Appl. Chem.* **1994**, *66* (5), 1077–1184.

(15) Moroi, Y. *Micelles: Theoretical and Applied Aspects*; The Language of science; Plenum Press: New York, **1992**.

(16) Patel, V.; Dharaiya, N.; Ray, D.; Aswal, V. K.; Bahadur, P. PH Controlled Size/Shape in CTAB Micelles with Solubilized Polar Additives: A Viscometry, Scattering and Spectral Evaluation. *Colloids Surf. Physicochem. Eng. Asp.* **2014**, *455*, 67–75.

(17) Electrokinetic Potential, ζ. In *IUPAC Compendium of Chemical Terminology*; Nič, M., Jirát, J., Košata, B., Jenkins, A., McNaught, A., Eds.; IUPAC: Research Triagle Park, NC, **2009**.

(18) Uragami, T. *Science and Technology of Separation Membranes*; John Wiley & Sons, Ltd: Chichester, UK, **2017**.

(19) Keck, C. M. Cyclosporine Nanosuspensions. Freie Universität Berlin **2006**.

(20) Hannon, A. C. Neutron Diffraction, Theory. In *Encyclopedia of Spectroscopy and Spectrometry*; Elsevier, **1999**, 1493–1503.

(21) *Small Angle Neutron Scattering*; TECDOC Series; INTERNATIONAL ATOMIC ENERGY AGENCY: Vienna, **2006**.

(22) Svergun, D. I.; Feĭgin, L. A.; Taylor, G. W. *Structure Analysis by Small-Angle x-Ray and Neutron Scattering*, **2016**.

(23) Dragolici, C. A. Experimental Methods in the Study of Neutron Scattering at Small Angles. In *Neutron Scattering*; Monteiro, W. A., Ed.; InTech, **2016**.

(24) Chen, S. H. Small Angle Neutron Scattering Studies of the Structure and Interaction in Micellar and Microemulsion Systems. *Annu. Rev. Phys. Chem.* **1986**, *37* (1), 351–399.

(25) Windsor, C. G. An Introduction to Small-Angle Neutron Scattering. *J. Appl. Crystallogr.* **1988**, *21* (6), 582–588.

(26) Chen, S. H.; Sheu, E. Y.; Kalus, J.; Hoffman, H. Small-Angle Neutron Scattering Investigation of Correlations in Charged Macromolecular and Supramolecular Solutions. *J. Appl. Crystallogr.* **1988**, *21* (6), 751–769.

(27) Caponetti, E.; Triolo, R. Application of Small Angle Neutron Scattering to Micellar Fluids. *Adv. Colloid Interface Sci.* **1990**, *32* (2–3), 235–270.

(28) Aswal, V. K.; Goyal, P. S.; Menon, S. V. G.; Dasannacharya, B. A. Role of Inter-Micellar Interaction on Micellar Growth. *Phys. B Condens. Matter* **1995**, *213–214*, 607–609.

(29) De, S.; Aswal, V. K.; Goyal, P. S.; Bhattacharya, S. Small-Angle Neutron Scattering Studies of Different Mixed Micelles Composed of Dimeric and Monomeric Cationic Surfactants. *J. Phys. Chem. B* **1997**, *101* (29), 5639–5645.

(30) Jain, N. J.; Aswal, V. K.; Goyal, P. S.; Bahadur, P. Salt Induced Micellization and Micelle Structures of' PEO/PPO/PEO Block Copolymers in Aqueous Solution. *Colloids Surf. Physicochem. Eng. Asp.* **2000**, *173* (1–3), 85–94.

(31) Aswal, V. K.; Haldar, J.; De, S.; Goyal, P. S.; Bhattacharya, S. Characterization of Vesicles from Ion-Paired Gemini Surfactants by Small Angle Neutron Scattering. *Phys. Chem. Chem. Phys.* **2003**, *5* (5), 907–910.

(32) Haldar, J.; Aswal, V. K.; Goyal, P. S.; Bhattacharya, S. Molecular Modulation of Surfactant Aggregation in Water: Effect of the Incorporation of Multiple Headgroups on Micellar Properties. *Angew. Chem. Int. Ed.* **2001**, *40* (7), 1228–1232.

(33) Kim, S.; Bellouard, C.; Eastoe, J.; Canilho, N.; Rogers, S. E.; Ihiawakrim, D.; Ersen, O.; Pasc, A. Spin State As a Probe of Vesicle Self-Assembly. *J. Am. Chem. Soc.* **2016**, *138* (8), 2552–2555.

(34) Guinier Plot. In *IUPAC Compendium of Chemical Terminology*; Nič, M., Jirát, J., Košata, B., Jenkins, A., McNaught, A., Eds.; IUPAC: Research Triagle Park, NC, **2009**.

(35) Li, M.; Zhao, Z.; Cheng, T.; Fortunelli, A.; Chen, C.-Y.; Yu, R.; Zhang, Q.; Gu, L.; Merinov, B. V.; Lin, Z.; Zhu, E.; Yu, T.; Jia, Q.; Guo, J.; Zhang, L.; Goddard III, W.; Huang, Y.; Duan, X. Ultrafine Jagged Platinum Nanowires Enable Ultrahigh Mass Activity for the Oxygen Reduction Reaction. *Science* **2016**, *354* (6318), 1414–1419.

(36) Chen, P.; Zhou, T.; Xing, L.; Xu, K.; Tong, Y.; Xie, H.; Zhang, L.; Yan, W.; Chu, W.; Wu, C.; Xie, Y. Atomically Dispersed Iron-Nitrogen Species as Electrocatalysts for Bifunctional Oxygen Evolution and Reduction Reactions. *Angew. Chem.* **2017**, *129* (2), 625–629.

(37) Thomas, J. M.; Raja, R. The Advantages and Future Potential of Single-Site Heterogeneous Catalysts. *Top. Catal.* **2006**, *40* (1–4), 3–17.

(38) Yang, X.-F.; Wang, A.; Qiao, B.; Li, J.; Liu, J.; Zhang, T. Single-Atom Catalysts: A New Frontier in Heterogeneous Catalysis. *Acc. Chem. Res.* **2013**, *46* (8), 1740–1748.

(39) Wang, A.; Li, J.; Zhang, T. Heterogeneous Single-Atom Catalysis. *Nat. Rev. Chem.* **2018**, *2* (6), 65.

(40) Zhang, H.; Liu, G.; Shi, L.; Ye, J. Single-Atom Catalysts: Emerging Multifunctional Materials in Heterogeneous Catalysis. *Adv. Energy Mater.* **2018**, *8* (1), 1701343.

(41) Chen, Y.; Ji, S.; Chen, C.; Peng, Q.; Wang, D.; Li, Y. Single-Atom Catalysts: Synthetic Strategies and Electrochemical Applications. *Joule* **2018**, *2* (7), 1242–1264.

(42) Jones, J.; Xiong, H.; DeLaRiva, A. T.; Peterson, E. J.; Pham, H.; Challa, S. R.; Qi, G.; Oh, S.; Wiebenga, M. H.; Pereira Hernandez, X. I.; Wang, Y.; Datye, A.K. Thermally Stable Single-Atom Platinum-on-Ceria Catalysts via Atom Trapping. *Science* **2016**, *353* (6295), 150–154.

(43) Sun, S.; Zhang, G.; Gauquelin, N.; Chen, N.; Zhou, J.; Yang, S.; Chen, W.; Meng, X.; Geng, D.; Banis, M. N.; Li, R.; Ye, S.; Knights, S.; Botton, G.A.; Sham, T.-K.; Sun, X. Single-Atom Catalysis Using Pt/Graphene Achieved through Atomic Layer Deposition. *Sci. Rep.* **2013**, *3* (1).

(44) Yan, H.; Cheng, H.; Yi, H.; Lin, Y.; Yao, T.; Wang, C.; Li, J.; Wei, S.; Lu, J. Single-Atom Pd_1/Graphene Catalyst Achieved by Atomic Layer Deposition: Remarkable Performance in Selective Hydrogenation of 1,3-Butadiene. *J. Am. Chem. Soc.* **2015**, *137* (33), 10484–10487.

(45) Lin, J.; Wang, A.; Qiao, B.; Liu, X.; Yang, X.; Wang, X.; Liang, J.; Li, J.; Liu, J.; Zhang, T. Remarkable Performance of Ir_1/FeO_x Single-Atom Catalyst in Water Gas Shift Reaction. *J. Am. Chem. Soc.* **2013**, *135* (41), 15314–15317.

(46) Qiao, B.; Liu, L.; Zhang, J.; Deng, Y. Preparation of Highly Effective Ferric Hydroxide Supported Noble Metal Catalysts for CO Oxidations: From Gold to Palladium. *J. Catal.* **2009**, *261* (2), 241–244.

(47) Qiao, B.; Wang, A.; Yang, X.; Allard, L. F.; Jiang, Z.; Cui, Y.; Liu, J.; Li, J.; Zhang, T. Single-Atom Catalysis of CO Oxidation Using Pt_1/FeO_x. *Nat. Chem.* **2011**, *3* (8), 634–641.

(48) Li, F.; Li, Y.; Zeng, X. C.; Chen, Z. Exploration of High-Performance Single-Atom Catalysts on Support M_1/FeO_x for CO Oxidation via Computational Study. *ACS Catal.* **2015**, *5* (2), 544–552.

(49) Qiao, B.; Liang, J.-X.; Wang, A.; Xu, C.-Q.; Li, J.; Zhang, T.; Liu, J. J. Ultrastable Single-Atom Gold Catalysts with Strong Covalent Metal-Support Interaction (CMSI). *Nano Res.* **2015**, *8* (9), 2913.

(50) Qiao, B.; Liu, J.; Wang, Y.-G.; Lin, Q.; Liu, X.; Wang, A.; Li, J.; Zhang, T.; Liu, J. (Jimmy). Highly Efficient Catalysis of Preferential Oxidation of CO in H_2-Rich Stream by Gold Single-Atom Catalysts. *ACS Catal.* **2015**, *5* (11), 6249–6254.

(51) Liu, P.; Zhao, Y.; Qin, R.; Mo, S.; Chen, G.; Gu, L.; Chevrier, D. M.; Zhang, P.; Guo, Q.; Zang, D.; Wu, B.; Fu, G.; Zheng, N. Photochemical Route for Synthesizing Atomically Dispersed Palladium Catalysts. *Science* **2016**, *352* (6287), 797–800.

(52) Yin, P.; Yao, T.; Wu, Y.; Zheng, L.; Lin, Y.; Liu, W.; Ju, H.; Zhu, J.; Hong, X.; Deng, Z.; Zhou, G.; Wei, S.; Li, Y. Single Cobalt Atoms with Precise N-Coordination as Superior Oxygen Reduction Reaction Catalysts. *Angew. Chem.* **2016**, *128* (36), 10958–10963.

(53) Chen, Y.; Ji, S.; Wang, Y.; Dong, J.; Chen, W.; Li, Z.; Shen, R.; Zheng, L.; Zhuang, Z.; Wang, D.; Li, Y. Isolated Single Iron Atoms Anchored on N-Doped Porous Carbon as an Efficient Electrocatalyst for the Oxygen Reduction Reaction. *Angew. Chem.* **2017**, *129* (24), 7041–7045.

(54) Yang, L.; Cheng, D.; Xu, H.; Zeng, X.; Wan, X.; Shui, J.; Xiang, Z.; Cao, D. Unveiling the High-Activity Origin of Single-Atom Iron Catalysts for Oxygen Reduction Reaction. *Proc. Natl. Acad. Sci.* **2018**, *115* (26), 6626–6631.

(55) Fei, H.; Dong, J.; Feng, Y.; Allen, C. S.; Wan, C.; Volosskiy, B.; Li, M.; Zhao, Z.; Wang, Y.; Sun, H.; An, P.; Chen, W.; Guo, Z.; Lee, C.; Chen, D.; Shakir, I.; Liu, M.; Hu, T.; Li, Y.; Kirkland, A.I.; Duan, X.; Huang, Y. General Synthesis and Definitive Structural Identification of MN_4C_4 Single-Atom Catalysts with Tunable Electrocatalytic Activities. *Nat. Catal.* **2018**, *1* (1), 63–72.

(56) Back, S.; Lim, J.; Kim, N.-Y.; Kim, Y.-H.; Jung, Y. Single-Atom Catalysts for CO_2 Electroreduction with Significant Activity and Selectivity Improvements. *Chem. Sci.* **2017**, *8* (2), 1090–1096.

(57) Flytzani-Stephanopoulos, M.; Gates, B. C. Atomically Dispersed Supported Metal Catalysts. *Annu. Rev. Chem. Biomol. Eng.* **2012**, *3* (1), 545–574.

(58) Wang, N.; Chu, W.; Zhang, T.; Zhao, X. S. Synthesis, Characterization and Catalytic Performances of Ce-SBA-15 Supported Nickel Catalysts for Methane Dry Reforming to Hydrogen and Syngas. *Int. J. Hydrog. Energy* **2012**, *37* (1), 19–30.

(59) Kim, D. J.; Dunn, B. C.; Huggins, F.; Huffman, G. P.; Kang, M.; Yie, J. E.; Eyring, E. M. SBA-15-Supported Iron Catalysts for Fischer−Tropsch Production of Diesel Fuel. *Energy Fuels* **2006**, *20* (6), 2608–2611.

(60) Prieto, G.; Martínez, A.; Murciano, R.; Arribas, M. A. Cobalt Supported on Morphologically Tailored SBA-15 Mesostructures: The Impact of Pore Length on Metal Dispersion and Catalytic Activity in the Fischer–Tropsch Synthesis. *Appl. Catal. Gen.* **2009**, *367* (1–2), 146–156.

(61) Cano, L. A.; Cagnoli, M. V.; Bengoa, J. F.; Alvarez, A. M.; Marchetti, S. G. Effect of the Activation Atmosphere on the Activity of Fe Catalysts Supported on SBA-15 in the Fischer–Tropsch Synthesis. *J. Catal.* **2011**, *278* (2), 310–320.

(62) Sun, Y.; Walspurger, S.; Tessonnier, J.-P.; Louis, B.; Sommer, J. Highly Dispersed Iron Oxide Nanoclusters Supported on Ordered Mesoporous SBA-15: A Very Active Catalyst for Friedel–Crafts Alkylations. *Appl. Catal. Gen.* **2006**, *300* (1), 1–7.

(63) Nozaki, C.; Lugmair, C. G.; Bell, A. T.; Tilley, T. D. Synthesis, Characterization, and Catalytic Performance of Single-Site Iron(III) Centers on the Surface of SBA-15 Silica. *J. Am. Chem. Soc.* **2002**, *124* (44), 13194–13203.

(64) Karimi, B.; Abedi, S.; Clark, J. H.; Budarin, V. Highly Efficient Aerobic Oxidation of Alcohols Using a Recoverable Catalyst: The Role of Mesoporous Channels of SBA-15 in Stabilizing Palladium Nanoparticles. *Angew. Chem. Int. Ed.* **2006**, *45* (29), 4776–4779.

(65) Liu, X.; Wang, A.; Wang, X.; Mou, C.-Y.; Zhang, T. Au–Cu Alloy Nanoparticles Confined in SBA-15 as a Highly Efficient Catalyst for CO Oxidation. *Chem. Commun.* **2008**, No. 27, 3187.

(66) Rajabi, F.; Naserian, S.; Primo, A.; Luque, R. Efficient and Highly Selective Aqueous Oxidation of Sulfides to Sulfoxides at Room Temperature Catalysed by Supported Iron Oxide Nanoparticles on SBA-15. *Adv. Synth. Catal.* **2011**, *353* (11–12), 2060–2066.

(67) Li, Y.; Feng, Z.; Lian, Y.; Sun, K.; Zhang, L.; Jia, G.; Yang, Q.; Li, C. Direct Synthesis of Highly Ordered Fe-SBA-15 Mesoporous Materials under Weak Acidic Conditions. *Microporous Mesoporous Mater.* **2005**, *84* (1–3), 41–49.

(68) Campelo, J. M.; Luna, D.; Luque, R.; Marinas, J. M.; Romero, A. A. Sustainable Preparation of Supported Metal Nanoparticles and Their Applications in Catalysis. *ChemSusChem* **2009**, *2* (1), 18.

(69) Barau, A.; Budarin, V.; Caragheorgheopol, A.; Luque, R.; Macquarrie, D. J.; Prelle, A.; Teodorescu, V. S.; Zaharescu, M. A Simple and Efficient Route to Active and Dispersed Silica Supported Palladium Nanoparticles. *Catal. Lett.* **2008**, *124* (3–4), 204–214.

(70) King, N. C.; Blackley, R. A.; Zhou, W.; Bruce, D. W. The Preparation by True Liquid Crystal Templating of Mesoporous Silicates Containing Nanoparticulate Metals. *Chem. Commun.* **2006**, No. 32, 3411.

(71) King, N. C.; Blackley, R. A.; Wears, M. L.; Newman, D. M.; Zhou, W.; Bruce, D. W. The Synthesis of Mesoporous Silicates Containing Bimetallic Nanoparticles and Magnetic Properties of PtCo Nanoparticles in Silica. *Chem. Commun.* **2006**, No. 32, 3414.

(72) Liu, H.; Ma, D.; Blackley, R. A.; Zhou, W.; Bao, X. Highly Active Mesostructured Silica Hosted Silver Catalysts for CO Oxidation Using the One-Pot Synthesis Approach. *Chem. Commun.* **2008**, 23, 2677.

(73) Kim, S.; Durand, P.; Roques-Carmes, T.; Eastoe, J.; Pasc, A. Metallo-Solid Lipid Nanoparticles as Colloidal Tools for Meso–Macroporous Supported Catalysts. *Langmuir* **2015**, *31* (5), 1842–1849.

(74) Fagerlund, G. Determination of Specific Surface by the BET Method. *Matér. Constr.* **1973**, *6* (3), 239–245.

(75) Landers, J.; Gor, G. Yu.; Neimark, A. V. Density Functional Theory Methods for Characterization of Porous Materials. *Colloids Surf. Physicochem. Eng. Asp.* **2013**, *437*, 3–32.

(76) Fierro, V.; Torné-Fernández, V.; Montané, D.; Celzard, A. Adsorption of Phenol onto Activated Carbons Having Different Textural and Surface Properties. *Microporous Mesoporous Mater.* **2008**, *111* (1–3), 276–284.

(77) Luisa Ojeda, M.; Marcos Esparza, J.; Campero, A.; Cordero, S.; Kornhauser, I.; Rojas, F. On Comparing BJH and NLDFT Pore-Size Distributions Determined from N_2 Sorption on SBA-15 Substrata. *Phys. Chem. Chem. Phys.* **2003**, *5* (9), 1859.

(78) Kieffer, J.; Karkoulis, D. PyFAI, a Versatile Library for Azimuthal Regrouping. *J. Phys. Conf. Ser.* **2013**, *425* (20), 202012.

(79) Juhás, P.; Davis, T.; Farrow, C. L.; Billinge, S. J. L. *PDFgetX3* : A Rapid and Highly Automatable Program for Processing Powder Diffraction Data into Total Scattering Pair Distribution Functions. *J. Appl. Crystallogr.* **2013**, *46* (2), 560–566.

(80) Hsieh, K.-Y.; Bendeif, E.-E.; Gansmuller, A.; Pillet, S.; Woike, T.; Schaniel, D. Structure and Dynamics of Guest Molecules Confined in a Mesoporous Silica Matrix: Complementary NMR and PDF Characterisation. *RSC Adv.* **2013**, *3* (48), 26132.

(81) Bendeif, E.-E.; Gansmuller, A.; Hsieh, K.-Y.; Pillet, S.; Woike, Th.; Zobel, M.; Neder, R. B.; Bouazaoui, M.; El Hamzaoui, H.; Schaniel, D. Structure Determination of Molecular Nanocomposites by Combining Pair Distribution Function Analysis and Solid-State NMR. *RSC Adv.* **2015**, *5* (12), 8895.

(82) Kresse, G.; Furthmüller, J. Efficient Iterative Schemes for *Ab Initio* Total-Energy Calculations Using a Plane-Wave Basis Set. *Phys. Rev. B* **1996**, *54* (16), 11169–11186.

(83) Blöchl, P. E. Projector Augmented-Wave Method. *Phys. Rev. B* **1994**, *50* (24), 17953–17979.

(84) Perdew, J. P.; Burke, K.; Ernzerhof, M. Generalized Gradient Approximation Made Simple. *Phys. Rev. Lett.* **1996**, *77* (18), 3865–3868.

(85) Anisimov, V. I.; Aryasetiawan, F.; Lichtenstein, A. I. First-Principles Calculations of the Electronic Structure and Spectra of Strongly Correlated Systems: The **LDA**+*U* Method. *J. Phys. Condens. Matter* **1997**, *9* (4), 767–808.

(86) Bengone, O.; Alouani, M.; Blöchl, P.; Hugel, J. Implementation of the Projector Augmented-Wave LDA+U Method: Application to the Electronic Structure of NiO. *Phys. Rev. B* **2000**, *62* (24), 16392.

(87) Gueddida, S.; Alouani, M. Calculated Impact of Ferromagnetic Substrate on the Spin Crossover in a Fe(1,10 − Phenanthroline $)_2$(NCS$)_2$ Molecule. *Phys. Rev. B* **2016**, *93* (18).

(88) Grimme, S. Semiempirical GGA-Type Density Functional Constructed with a Long-Range Dispersion Correction. *J. Comput. Chem.* **2006**, *27* (15), 1787–1799.

(89) Bučko, T.; Hafner, J.; Lebègue, S.; Ángyán, J. G. Improved Description of the Structure of Molecular and Layered Crystals: Ab Initio DFT Calculations with van Der Waals Corrections. *J. Phys. Chem. A* **2010**, *114* (43), 11814–11824.

(90) Comas-Vives, A. Amorphous SiO_2 Surface Models: Energetics of the Dehydroxylation Process, Strain, Ab Initio Atomistic Thermodynamics and IR Spectroscopic Signatures. *Phys. Chem. Chem. Phys.* **2016**, *18* (10), 7475–7482.

(91) Berro, Y.; Gueddida, S.; Lebègue, S.; Pasc, A.; Canilho, N.; Kassir, M.; El HajHassan, F.; Badawi, M. Atomistic Description of Phenol, CO and H_2O Adsorption over Crystalline and Amorphous Silica Surfaces for Hydrodeoxygenation Applications. *Appl. Surf. Sci.* **2019**, *494*, 721–730.

(92) Li, B.; Xu, J.; Liu, J.; Zuo, S.; Pan, Z.; Wu, Z. Preparation of Mesoporous Ferrisilicate with High Content of Framework Iron by PH-Modification Method and Its Catalytic Performance. *J. Colloid Interface Sci.* **2012**, *366* (1), 114–119.

Chapter 5

Hydrodeoxygenation Catalytic Tests

Chap. 5 Hydrodeoxygenation Catalytic Tests

In this Chapter, we present the HDO catalytic tests for guaiacol conversion in order to determine the catalytic performance of synthesized materials. Those experiments enable us to understand the effect of the silica support textural properties (pore size and silanols density), copper incorporation, and synthesis method (impregnation, co-precipitation, sol-gel using metallosurfactants).

5.1 Introduction

5.1.1 Catalytic Materials

Among single iron atom catalysts (SACs) described in **Chap 4. Part. 3**, only the Fe@SiO_2(10) having the higher percentage of iron (around 1wt.%) have been tested for guaiacol conversion due to the unsatisfactory results obtained.

Silica supported metal (15%Fe@SBA-15-1SC, 15%Fe@SBA-15-3S, 15%Fe@SBA-15-3SC, and 15%Cu@SBA-15-3SC) and bimetallic (15%Fe3%Cu@SBA-15-3SC) catalysts, synthesized by the simple impregnation, were all tested. The 15%Fe@SBA-15-3SC-DPU, synthesized through the co-precipitation with decomposition of urea (DPU), is tested in order to determine the effect of the reduction step on the catalytic performance (see **Chap 4. Part. 1**).

Table 5.1 presents the catalysts used and the main characteristics of each one. Results obtained from catalytic tests allow investigating the effect of the silica support structural properties. SBA-15-1SC silica was washed for one day and calcined, SBA-15-3S silica was washed for three days, while SBA-15-3SC silica was washed for three days and calcined. The synthesis method (sol-gel using metallosurfactant, impregnation, and co-precipitation with decomposition of urea DPU), and copper incorporation (Fe-Cu vs. Fe) are also studied.

***Table 5.1** Materials tested for the HDO catalytic conversion of guaiacol, and their characteristics.*

Catalyst	Synthesis Method	Metal	Silica Pore Size (nm)	Silica silanols density (OH/nm^2)
Fe@SiO_2(10)	sol-gel (CTAF/P123)	1%Fe	5.5	4.0
15%Fe@SBA-15-1SC	Impregnation by incipient wetness	Fe	7.5	2.7
15%Fe@SBA-15-3S	Impregnation	Fe	4.7 / 8.0	8.9
15%Fe@SBA-15-3SC	Impregnation	Fe	4.7 / 7.3	1.8
15%Cu@SBA-15-3SC	Impregnation	Cu	4.7 / 7.3	1.8
15%Fe3%Cu@SBA-15-3SC	Impregnation	Fe-Cu	4.7 / 7.3	1.8
15%Fe@SBA-15-3SC-DPU	Co-precipitation DPU	Fe	4.7 / 7.3	1.8

5.1.2 Reaction Conditions

The gas-phase HDO conversion of guaiacol was performed in a catalytic fixed-bed U-shape tubular quartz reactor as presented in **Figure 5.1**, where guaiacol is considered as a model molecule representing the bio-oils vapors obtained from lignin pyrolysis.[1] All catalytic tests were done under experimental conditions similar to those used by Olcese *et al.*[2] for Fe@SiO_2 catalyst. The H_2 partial pressure and the total gas flow (carrier gas Argon) are controlled by mass flow controllers. Liquid guaiacol is injected using a syringe pump through a septum in a heated gas line at a precise speed in order to control the percentage volume of guaiacol in the gas flow. The inlet and outlet of the reactor are heated at 220°C in order to prevent the condensation of the guaiacol and products. The real mass of injected guaiacol is determined by the difference of the syringe mass before and after the experiment. Pressure is controlled by an electronic pressure sensor. The 4-ways valves allow performing the temperature-programmed reduction TPR measurements (using a 500-ppm H_2 in Ar gas flow) and the catalyst passivation (using 1000-ppm O_2 in Ar gas flow). Moreover, they are very advantageous for the calibration of the analysis equipment and carrying out blank measurements. The oven temperature is controlled using a temperature regulator, whereas the real reaction temperature is measured in the catalyst fixed bed through a thermocouple introduced inside the reactor. Catalysts are granulated into particles of 150-250 µm and supported on the fritted of the reactor.

The online mass spectrometer allows analyzing qualitatively the outgoing gas of the reactor in real time (every 17 sec), thus giving information about the evolution of the reaction products upon time on stream. Products are collected by condensation in a methanol solution using two impingers; the first one is cooled with ice (0°C) while the second one is cooled with a liquid nitrogen/iso-propanol solution at -40°C. Small non-condensed molecules are quantified online using a µ-gas chromatography (µGC) installed at the outlet of those impingers. An internal standard (10 µL of 1-tetradecene) is then injected in the overall volume of the methanol solution of the 2 impingers. The solution is then analyzed by GC-MS-FID system that combines the detection feature of the mass spectrometer for structure assignment of products (by comparison with NIST database) and a flame ionization detector to quantify the products. Calibration of the µGC for low percentage of CO, CO_2, CH_4 and other small molecules (C_2H_4, C_2H_6…) is done before experiments using calibration gas bottles. A blank test is performed with an empty reactor (no catalyst) in order to determine the corresponding MS peak intensities of guaiacol and impurities (N_2, O_2, and water) and to confirm the effectiveness of the condensation method and the accuracy of the GC-MS-FID analyzer.

The set-up has been improved during this Ph-D. All tubing lines, as well valves, were twisted with a resistance wire (heated at 220°C) and well isolated to prevent cold points that cause the condensation of guaiacol. CS Teflon coated silicon Septa (for guaiacol injection) and graphite joints (quartz reactor - metal tube) were used to support high temperatures. PID temperature regulators West 6100+ were used and calibrated in order to control the oven and resistance wire temperatures. The chassis of the system was modified in order to support the online µGC and the online MS with less wiring and tubing.

In a typical test, 100 mg of Fe@SiO_2 catalysts are firstly reduced under pure hydrogen flow of 50mL/min with a temperature rate of 10 K.min^{-1} until 550°C, then held at that temperature for 30 min. The temperature is then decreased under Ar flow to the reaction temperature of 400°C, and the total gas flow of 80 mL/min is set in order to obtain an H_2 partial pressure of 0.9 (72 mL/min H_2 + 7.5 mL/min Ar). After a stabilization time of 15 min, we inject guaiacol at a rate of 120µL/h (corresponding to 0.5 vol.%) for 30 min, the reaction period. This time of stream have been selected in order to screen the selectivity of the catalysts. Longer time on stream experiments are in progress. Then guaiacol injection was stopped and the catalyst bed was purged under pure argon flow (no H2). The space velocity, calculated as the catalyst mass (g_{cat}) divided by the injected guaiacol flow ($g_{gua.inj}$/h), is around 0.6 h^{-1}.

In order to identify the reduction effectiveness and the type of iron species present (by Mössbauer measurements), catalysts have been reduced as previously, and cooled to room temperature under argon flow. Then, passivation is performed at room temperature with 50 mL/min of 1000-ppm O_2 in Ar in order to prevent the fast oxidation of the catalyst caused by very active metal sites when exposed to air.

Temperature-programmed reduction (TPR) measurements are performed under 50 mL/min of 500-ppm H_2 in Ar with a temperature rate of 10 K.min^{-1} until 800°C.[3–5] The hydrogen consumption is detected and quantified with time by the online MS and µGC, therefore indicating different peaks corresponding at various temperatures and possible reduction reactions.

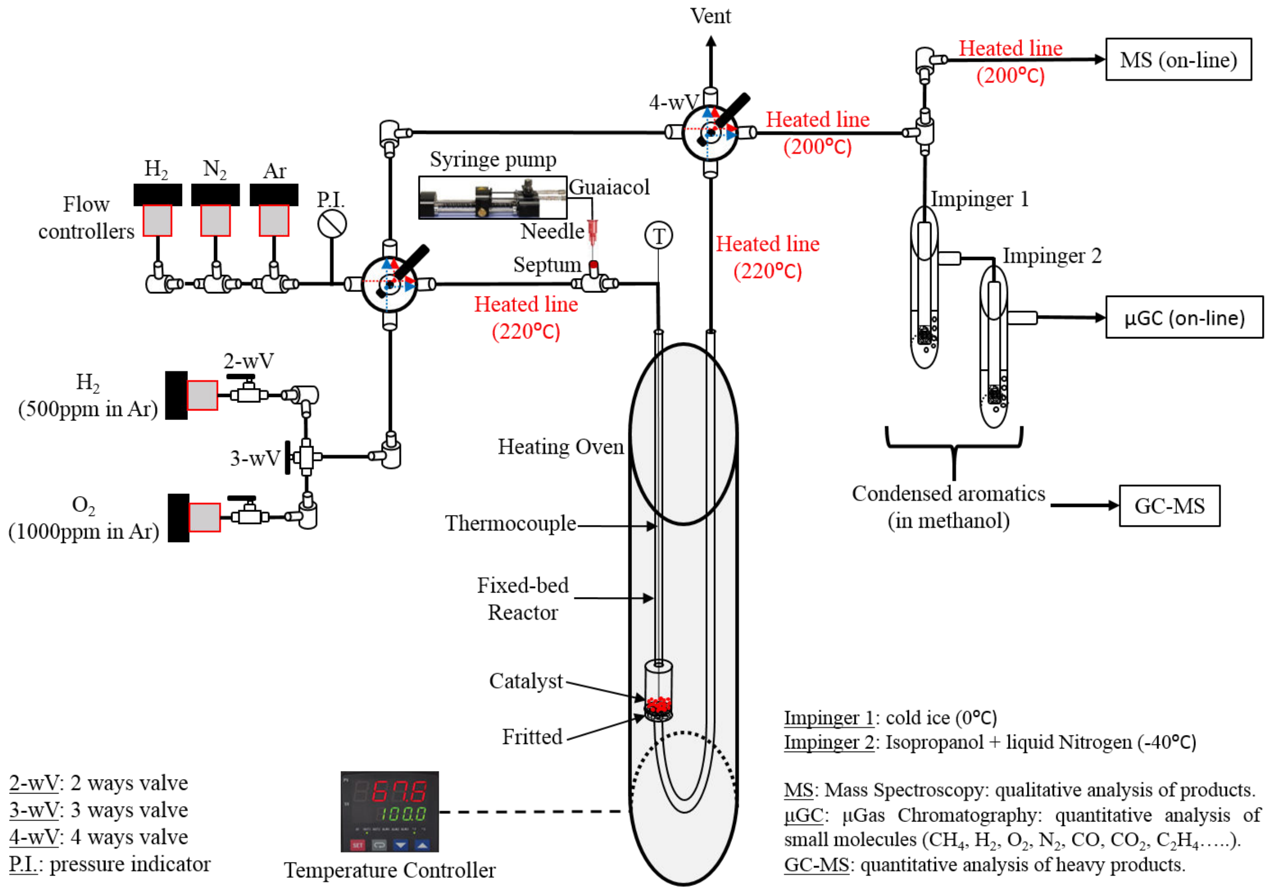

***Figure 5.1** Schematic presentation of our system for guaiacol HDO conversion process (Fixed-bed U-type reactor) and products analysis equipment.*

5.1.3 Conversion, Activity, Aromatics Selectivity, Carbon Yield, and Carbon Selectivity

In order to interpret the catalytic performance of the synthesized materials for the HDO of guaiacol, different terms are defined and computed. The conversion percentage of guaiacol (X_{gua} %), determined at the end of the reaction (during 30 min time on stream), is calculated as the percentage of converted guaiacol quantity (during 30 min, based on GC/MS-FID quantification) with respect to the initial quantity injected as follow:

$$X_{gua}\,(\%) = 100 * {(n_{gua.inj} - n_{gua.out})}/{n_{gua.inj}} \qquad (1)$$

The deoxygenation degree X_{HDO} (%) is a function of the mol number of condensed products (n_i) (except for unreacted guaiacol), and the number of oxygen atoms in the product i (a_i) as follow:

$$X_{HDO}\,(\%) = 100 * (1 - {100 \sum_i n_i a_i}/{2X_{gua} n_{gua.inj}}) \qquad (2)$$

Those definitions for guaiacol conversion (X_{gua}) and deoxygenation degree (HDO) have been proposed by Olcese *et al.*[2] in agreement with Bykova *et al.*[6] previously. However, as we aim to produce aromatics under less hydrogen consumption, those parameters do not give a clear idea about the catalyst selectivity with respect to desired aromatic products (partially or totally deoxygenated) including phenol, benzene, toluene, cresol, and xylenes. The yield of each product can be calculated as the quantity produced divided by the injected quantity of guaiacol; the following equation shows the calculation of the phenol yield.

$$Y_{phenol}\,(\%) = 100 * {}^{n_{phenol.produced}}\!/_{n_{gua.inj}} \qquad (3)$$

Therefore, the percentage selectivity of phenol (S_{phenol}) can be calculated by dividing its yield on the guaiacol conversion as follows:

$$S_{phenol}\,(\%) = 100 * {}^{Y_{phenol}}\!/_{X_{gua}} \qquad (4)$$

Similarly, the yield and selectivity of HDO desired aromatic products (phenol, cresol, BTX) are calculated as follow:

$$Y_{HDO}\,(\%) = 100 * {}^{\sum n_{desired\ products}}\!/_{n_{gua.inj}} \qquad (5)$$

$$S_{HDO}\,(\%) = 100 * {}^{Y_{HDO}}\!/_{X_{gua}} \qquad (6)$$

The HDO catalytic activity ($A_{HDO}\ mol.h^{-1}.g_{cat}^{-1}$) is calculated from the molar flow rate of injected guaiacol, the mass of the catalyst and the yield of HDO desired aromatics (phenol, BTX, cresol):

$$A_{HDO} = {}^{n_{gua.inj}}\!/_{g_{cat}} * {}^{Y_{HDO}}\!/_{100} \qquad (7)$$

An elemental molar balance (C, O, and H) is performed taking into consideration the condensed products analyzed by GCMS, as well small molecules (CO, CO_2, CH_4…) quantified by the µGC. The HDO carbon yield ($Y_{C.HDO}$) can be calculated as the sum of moles of carbon of all desired aromatic products (phenol, BTX, cresol) divided by the number of moles of carbon of the injected guaiacol as follows:

$$Y_{C.HDO}\,(\%) = 100 * {}^{(\sum n_{C.desired\ products})}\!/_{7n_{gua.inj}} \qquad (8)$$

Equation *(9)* is used to compute the HDO carbon selectivity ($S_{C.HDO}$).

$$S_{C.HDO}\,(\%) = 100 * {}^{Y_{C.HDO}}\!/_{X_{gua}} \qquad (9)$$

5.1.4 Blank Test (empty reactor)

An experimental blank test was performed under the same conditions of a catalytic test (673 K, H_2 partial pressure of 0.9, 80 mL/min total flow), where 0.5 vol.% of guaiacol was injected into the empty reactor (no catalyst) for 30 min residence time at 120 µL/h, and then collected in the impingers and analyzed by GCMS. This test was performed for several purposes:

- Confirm the heating of the system and the non-condensation of guaiacol in any part.
- Confirm the collecting of products by the impingers.
- Obtaining the ion current peak for guaiacol by online MS, as reference.
- Confirming the RRF value obtained by the direct calibration using prepared solutions. An RRF value of 3.1 was found confirming previously found result.

5.2 Catalytic Performance of Fe@SiO_2(10) Single Atom Catalysts (SACs)

Among previously synthetized single atom catalyst (SAC), the Fe@SiO_2(10) having the highest iron loading (around 1%) was tested for the guaiacol HDO conversion at first. As discussed in **Chap. 4 Part.3**, the Fe@SiO_2(10) catalyst was characterized by having single isolated iron atoms well dispersed on the silica mesopores, which supposed to increase the number of active sites. The Fe@SiO_2(10) material, previously calcined, was reduced in the reactor under pure H_2 up to 500°C for 30 min. Then the temperature was decreased to 400°C, the flow was regulated and the catalytic reaction start under the conditions mentioned before. During the reaction, that last for 30 min, a small part of the output flow exiting the reactor was analyzed in time by a mass spectrometer as described before. **Figure 5.2** shows qualitatively the evolution of chemical products with time during the reaction. At time zero, as guaiacol is injected, the guaiacol peak disappears suddenly and a high peak of water is observed indicating the high conversion of guaiacol. However, the water peak decreases very rapidly (after around 5 min) while the guaiacol peak reappears and both stabilize at constant values, which indicate the quick deactivation of the catalyst. Furthermore, no benzene or phenol production were detected.

After analyzing the products collected in the impingers by GCMS, only guaiacol was found with zero traces of produced aromatics (phenol, cresol, BTX…) confirming the online qualitative MS results. The remaining quantity of guaiacol was quantified and the conversion (X_{gua} %) calculated at t= 30 min was around 23%. Integrating the µGC results along the reaction period, a methane yield of 2.2% and CO_2 yield of 0.1 % were calculated. As no aromatics were found by GCMS, the selectivity ($S_{aromatics}$) was null, which make this catalyst unattractive.

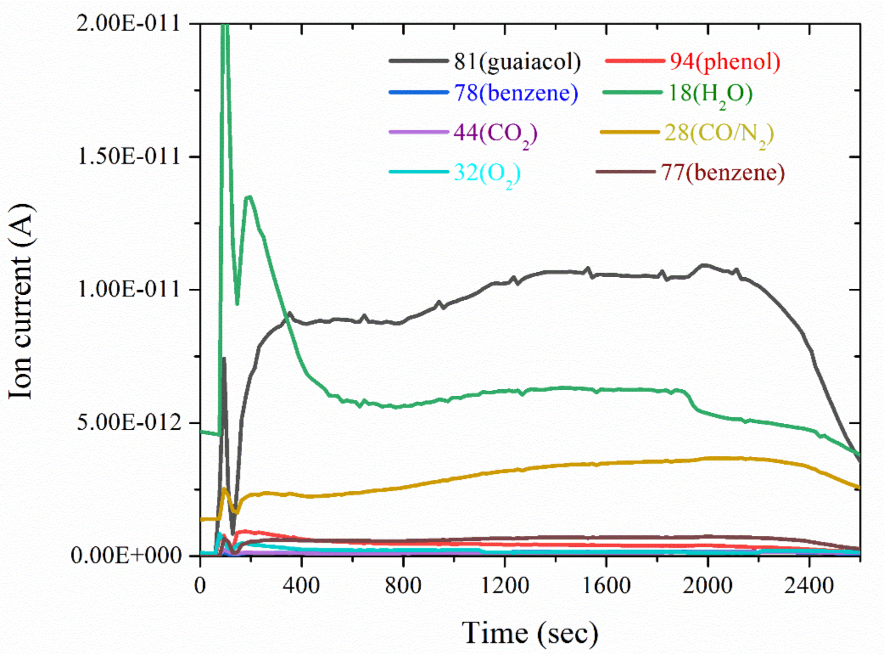

***Figure 5.2** Spectra of products evolution with time detected by the online mass spectrometer using Fe@SiO$_2$(10) catalyst.*

In order to interpret those unsatisfactory results obtained for the Fe@SiO$_2$(10) single atom catalysts (SACs), the first that come to mind is to check the speciation of the catalytic sites. Thus, we have to verify the oxidation state of iron species and to confirm the existence or not of metal iron through the reduction step. X-ray powder analysis (X'PERT Pro CuK$_\alpha$) was performed; however, iron species were not detected due their atomic behavior. Therefore, ^{57}Fe Mössbauer measurements were performed by Prof. Malaman (IJL, Université de Lorraine) using a constant-acceleration spectrometer in standard transmission geometry with a ^{57}CoRh source at 300 K.[7] **Figure 5.3** shows the Mössbauer spectra of the Fe@SiO$_2$(10) before reduction, after reduction at 500°C (with passivation), after reduction at 500°C with catalysis, and after temperature programmed reduction TPR analysis at 800°C. None of those spectra present any trace of metal iron. However, the catalytic activity of metal catalysts is dependent on the quantity of metal nanoparticles and their size. Thus, unsatisfactory catalysis results can be related to the non-formation of metal iron due to the difficulty of reduction of Fe(III) which exhibits strong chemical interactions with the silica framework.

In order to understand more properly the reduction step, TPR measurements were performed. **Figure 5.4** compares the hydrogen consumption, with respect to time and temperature, for single atom catalyst Fe@SiO$_2$(10) and conventionally-synthetized catalyst 15%Fe@SBA-15-1SC. Comparing TPR data for the two catalysts proves that the Fe(III) reduction into metallic iron is nearly negligible for the SAC Fe@SiO$_2$(10) even at high temperature, which can be due to the strong interactions with the silica surface.

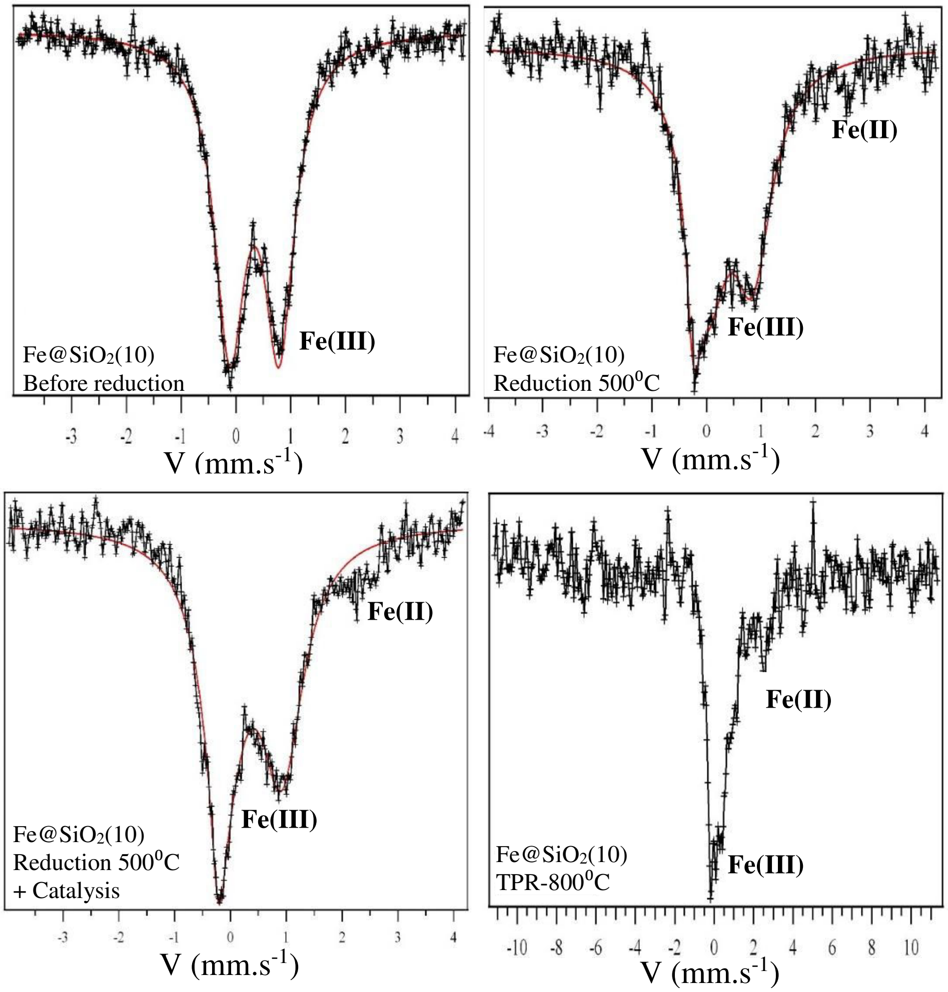

Figure 5.3 *Mössbauer spectra of Fe@SiO_2(10) catalyst: (i) before reduction, (ii) after reduction (at 500 °C), (iii) after reduction (at 500 °C) and catalysis (guaiacol + H_2 during 30 min), and (iv) after temperature programmed reduction (TPR at 800 °C).*

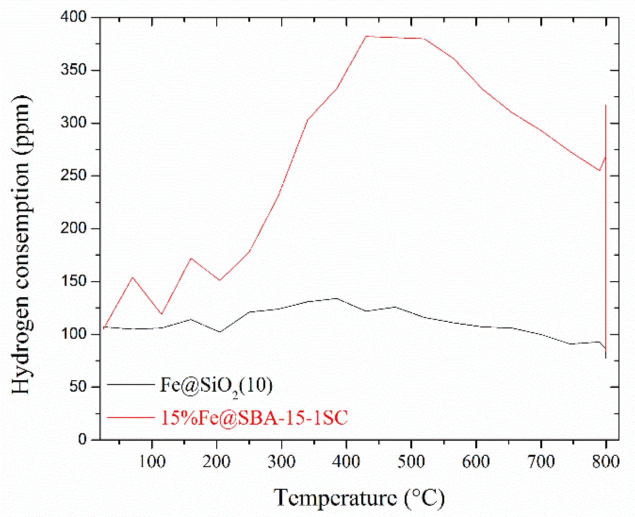

Figure 5.4 *Temperature programmed reduction (TPR) analysis: Hydrogen consumption with respect to temperature for Fe@SiO_2(10) and 15%Fe@SBA-15-1SC catalysts.*

Those results indicates that guaiacol, which is converted of 23%, mainly react on the Fe(III) atom sites during the beginning of the reaction, as observed from the online mass spectrometer. However, those sites deactivate very quickly (after 5 min) and do not have any selectivity towards aromatics. The catalyst weight increases of around 16 mg, which is almost equal to 20% of the injected guaiacol quantity. This allow to suggest that guaiacol conversion on those Fe(III) sites is mainly into heavy aromatics deposited as coke on the catalyst. In this case, Fe(III) atom sites could act as Lewis acid catalysts,[8] leading to the condensation of guaiacol under the form of (-benzene-O-CH_2-$)_n$.

Thus, different ideas were proposed in order to facilitate the reduction of iron species into metal iron that is more selective than Fe(III) sites. These ideas were the following:

1) using iron(II) sulfate as iron source instead of iron(III) chloride to elaborate the metallosurfactant,
2) replacing the calcination step by a pyrolysis step, allow obtaining Fe(II) species (that can be reduced more easily than Fe(III)) and inhibition of their oxidation during calcination.
3) elaborating copper metallosurfactant (CTACu) and adding them to the CTAF during the sol-gel silica polymerization which allow obtaining bimetallic Fe-Cu single atom catalyst, which can facilitate the reduction of iron as copper is a reduction catalyst.[9–11]

5.3 Catalytic Performance of Catalysts Produced by Impregnation of Silica Support

Metallic (15%Fe@SBA-15-1SC, 15% Fe@SBA-15-3S, 15%Fe@SBA-15-3SC, and 15% Cu@SBA-15-3SC) and bi-metallic (15%Fe3%Cu@SBA-15-3SC) catalysts synthetized by conventional impregnation method are tested catalytically for guaiacol conversion. As previously explained, 1SC refers to silica washed for one day then calcined, 3S refers to silica washed for three days, and 3SC refers to silica washed for three days then calcined. The main different between them is the pore size distribution and the silanols density before impregnation (as presented in **Table 5.1**). The effect of incorporating copper (in order to promote the reduction of iron oxides) to obtain bimetallic Fe-Cu catalyst is interpreted.

Comparing the performance of 15%Fe@SBA-15-3SC-DPU catalyst (synthetized by co-precipitation with decomposition of urea), having a green color confirming the existence of more-easily reduced Fe(II) species, with the 15%Fe@SBA-15-3SC catalyst (synthetized by the impregnation in iron (III) nitrate solution) allow to understand the effect of the iron oxidation state and its reducibility behavior.

The catalytic reaction was followed upon time on stream the mass spectrometer. **Figure 5.5** shows the molecules evolution (guaiacol reactant consumption and products formation) using the

15%Fe@SBA-15-1SC catalyst. **Figure 5.5**, shows that the ion intensity of the m/z 81 (that may be attributed to guaiacol) is about three times lower than that of guaiacol without conversion (blank test: around $3*10^{-12}$ A) during the first 15 min of the reaction ($< 1*10^{-12}$ A). Water (m/z=18) production was huge during this duration ($t < 1000$ s). Upon time on stream the m/z 81 (guaiacol) increases showing a decrease in the activity of the catalyst for guaiacol conversion. m/z 94 (may be assigned to phenol and related species) production is nearly stable all over the reaction duration. A small benzene peak was observed at the beginning of the reaction and quickly disappeared, which indicates the small formation of benzene. This was also confirmed after GCMS analysis of impingers where only small traces of benzene and toluene were quantified.

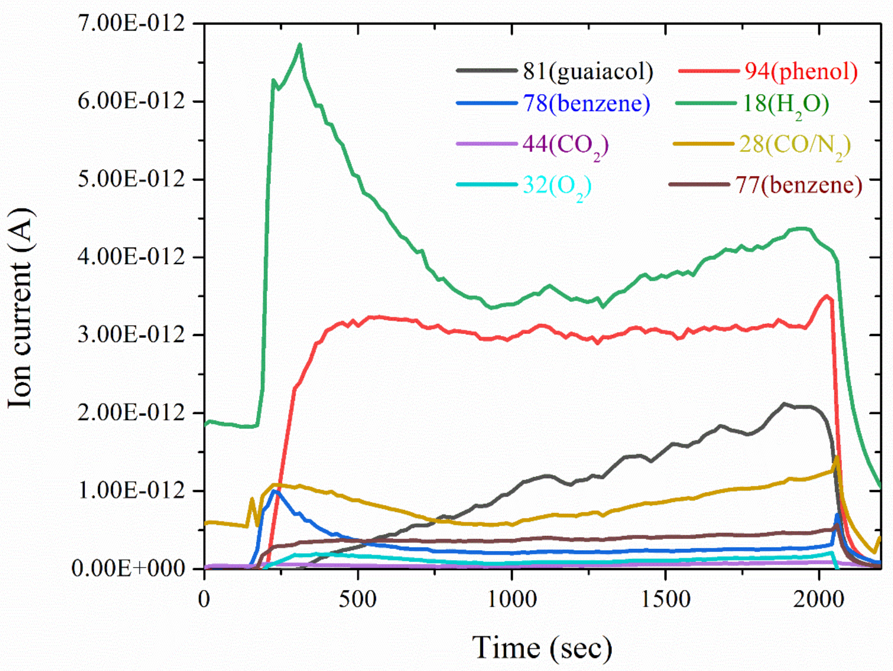

***Figure 5.5** Spectra of products evolution with time detected by the online mass spectrometer using 15%Fe@SBA-15-1SC catalyst.*

Further, a quantitative analysis of the products collected by µGC and by GCMS was performed. **Table 5.2** shows the permanent gas production with respect to the reaction time, and their total amount integrated along the reaction period (30 min). **Figure 5.6** shows the cumulative yield percentage of small products (CO_2, CH_4, & C_2H_4) with respect to time, where the weighted amount of guaiacol injected during the reaction period (30min) is 77 mg (0.62 mmol). Remarkably, no CO production is observed, which is important, as CO is a toxic molecule. In fact, CO have an inhibiting effect on conventional sulfided catalysts,[12] and a strong negative effect on the initial reaction rate due the carburization of iron and formation of coke.[13] This makes our catalyst more attractive, with respect to this criteria, comparing to Fe@silica studied by Olcese *et al.*[2,13]

Guaiacol can be converted to phenol through two ways: by producing CH_4 and H_2O (consuming two H_2 molecules) or by producing methanol (consuming only one H_2 molecule).[2] Methanol can be cracked into CO and H_2 (with coke), or transformed into ethylene (C_2H_4) through the methanol to olefins (MTO) reaction.[14] As well, CO can be converted into CO_2 and H_2 through water gas shift reaction (WGSR).[15] Olcese *et al.*[13] studied the conversion of CO under HDO conditions and proved that a considerable amount of carbon deposit is formed on the catalyst and CO_2 is produced from CO dismutation.

***Table 5.2** Quantitative analysis of products detected by μGC, and their total amount over the reaction period (30 min).*

	Products Quantity (μmol/min)					Cumulative Products Quantity (μmol)			
Time (min)	CO	CO_2	CH_4	C_2H_4	Δt (min)	CO	CO_2	CH_4	C_2H_4
0.33	0	0.05436	0	0	0.33	0	0.01812	0	0
5.22	0	0.05436	6.47996	0	5.22	0	0.28359	31.64382	0
10.10	0	0.05436	5.25863	0	10.10	0	0.54906	57.32345	0
14.98	0	0.05799	4.62078	0.05799	14.98	0	0.83223	79.88825	0.28317
19.87	0	0.05799	4.30548	0.05074	19.87	0	1.1154	100.91334	0.53094
24.75	0	0.06161	4.05179	0.05799	24.75	0	1.41626	120.69957	0.81411
29.63	0	0.05436	3.70025	0.05074	29.63	0	1.68173	138.76911	1.06187
					Total (mol)	0	0.00168	0.13877	0.00106

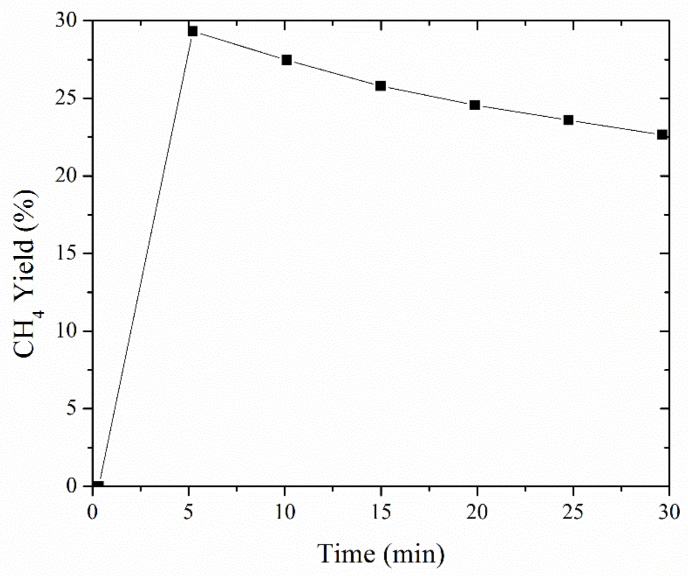

***Figure 5.6** Yield percentage of CH_4 in function of time.*

Table 5.3 shows the products observed by GCMS, their corresponding retention time and area. Using RRF values (see **Chapter 2**), those products were quantified. The elemental molar balance (of C, O, and H), and the corresponding carbon yield of formed product (CO, CO_2, CH_4, benzene, phenol….) after 30 min are presented in **Table 5.4**. The total carbon recovered and the total carbon yield are calculated and presented as well.

Table 5.3 *Quantitative quantity of products found by GCMS calculated from their corresponding areas and RRFs values with respect to the 1-tetradecene internal standard.*

Retention time R.T. (min)	Molecule	Molar mass (g/mol)	Area A_i	Relative response factor RRF	Molar quantity (mmol)	Mass (mg)
6.36	Benzene	78	259999	2.76	0.016	1.283
9.15	Toluene	92	96627	2.02	0.004	0.412
17.22	Phenol	94	2845747	3.75	0.244	22.953
20.05	Cresol	108	391527	2.15	0.019	2.085
21.47	Guaiacol	124	1571852	3.15	0.113	14.061
31.06	1-tetradecene (internal standard)	196	1725497	*	0.040	7.750

Table 5.4 *Elemental (C, O, and H) molar balance, and the corresponding carbon yield for each product.*

Molar Balance	Quantity (mmol)	C (mmol)	O (mmol)	H (mmol)	$C_{out/in}$ (%)
Guaiacol (In)	0.620	4.342	1.241	4.962	*
Output products					
CO	0	0	0	0	0
CO_2	0.002	0.002	0.003	0	0.04
CH_4	0.139	0.139	0	0.555	3.2
C_2H_4	0.001	0.002	0	0.004	0.05
Benzene	0.016	0.099	0	0.099	2.27
Toluene	0.004	0.031	0	0.036	0.72
Phenol	0.244	1.465	0.244	1.465	33.74
Cresol	0.019	0.135	0.019	0.154	3.11
Guaiacol	0.113	0.794	0.227	0.907	18.28
Total	0.539	2.667	0.494	3.216	61.42

From the data presented in previous tables (**Table 5.2**, **Table 5.3**, and **Table 5.4**) and using the equations showed in **section 5.1.3**, the performance of the 15%Fe@SBA-15-1SC was evaluated by calculating the guaiacol conversion (X_{gua}), the deoxygenation degree (X_{HDO}), the HDO selectivity (S_{HDO}), the HDO catalytic activity (A_{HDO}), the HDO carbon yield ($Y_{C.HDO}$), and the HDO carbon selectivity ($S_{C.HDO}$) at the end of the reaction (after 30 min). This catalyst showed a high conversion (82%) with a good selectivity to aromatic molecules (56%) with an activity of 5.61 $mmol. h^{-1}. g_{cat}^{-1}$.

Similarly, for all catalytic materials, data were collected from µGC (small molecules quantification) and from GCMS (large molecules quantification), then elemental molar balance and calculations were performed, giving the results showed in **Table 5.5** and **Table 5.6**. Those results enable to assess the performance of catalysts and to understand the effect of different parameters. Remarkably, the catalyst synthesized by the impregnation of the non-calcined silica material (SBA-15-3S) having 8 OH/nm^2 in the iron nitrate solution have a null selectivity to aromatics (phenol, BTX, cresol). This is consistent with the theoretical results found by DFT calculations that showed that amorphous silica surfaces with high silanols density suffer from water inhibition effect.[16] Comparing catalysts having different pore size distribution due to the washing step (15%Fe@SBA-15-3SC vs 15%Fe@SBA-15-1SC) showed that creating small pores may reduce the selectivity. This may be due to the pore blocking caused by large molecules (coke precursors) and iron nanoparticles. Copper catalyst (15%Cu@SBA-15-3SC) proved the best aromatics selectivity of 80% and the best aromatics carbon selectivity of around 70%; however, the guaiacol conversion (70%) after 30 min is smaller than that of bimetallic Fe-Cu catalyst (around 90%). This high conversion of bimetallic Fe-Cu catalyst, accompanied with the high selectivity (72%), made this catalyst very attractive for long catalysis time. Comparing bimetallic Fe-Cu catalyst with the metallic one (15%Fe@SBA-15-3SC), we observed the effect of incorporating copper. Thus, further tests must be performed aiming to increase furthermore the selectivity in order to achieve a similar aromatics carbon selectivity as that of copper catalyst with high conversion percentage. 15%Fe@SBA-15-3SC-DPU having Fe(II) species before reduction showed better results than 15%Fe@SBA-15-3SC having Fe(III) species before reduction step (73% conversion and 52% aromatics selectivity comparing to 52 and 26 % respectively). Thus, the effect of the oxidation state of iron before reduction is crucial as Fe(II) are reduced more easily than Fe(III). The effect of the oxidation state of iron species and their reduction are studied in the next section using X-ray powder and Mössbauer measurements in order to understand the effect of the studied parameters (silica textural properties, copper incorporation, and synthesis method) on the iron reduction and to control the reduction conditions.

Table 5.5 *Catalysts performance at 400 °C by mean of the guaiacol conversion (X_{gua}), HDO selectivity (S_{HDO}), and the HDO catalytic activity (A_{HDO}) at the end of the reaction (after 30min).*

Catalyst	Characteristic	Guaiacol Conversion at 30 min (X_{gua} %)	Aromatics Selectivity at 30 min (S_{HDO} %)	Catalytic Activity A_{HDO} ($mmol.h^{-1}.g_{cat}^{-1}$)
15%Fe@ SBA-15- 1SC	Silica (pores 8 nm, 2 OH/nm^2)	82	56	5.61
15%Fe@ SBA-15-3S	Silica (pores 5-8 nm, 8 OH/nm^2)	55	0	0
15%Fe@ SBA-15-3SC	Silica (pores 5-8 nm, 2 OH/nm^2)	52	26	1.75
15%Cu@ SBA-15-3SC	Copper on Silica (pores 8 nm, 2 OH/nm^2)	71	80	7.24
15%Fe3%Cu@ SBA-15-3SC	Bimetallic Fe-Cu on Silica (pores 8 nm, 2 OH/nm^2)	87	72	7.39
15%Fe@ SBA-15-3SC-DPU	Fe(II) (controlled impregnation by DPU)	73	52	4.82

Table 5.6 *Catalysts performance at 400 °C by mean of the HDO deoxygenation degree (X_{HDO}), HDO carbon yield ($Y_{C.HDO}$), and HDO carbon selectivity ($S_{C.HDO}$) at the end of the reaction (after 30min).*

Catalyst	Deoxygenation degree at 30 min (X_{HDO} %)	Aromatics Carbon Yield at 30 min ($Y_{C.HDO}$ %)	Aromatics Carbon Selectivity at 30 min ($S_{C.HDO}$ %)
15%Fe@SBA-15- 1SC	74	40	49
15%Fe@SBA-15-3S	100	0	0
15%Fe@SBA-15-3SC	88	12	23
15%Cu@SBA-15-3SC	61	49	68
15%Fe3%Cu@SBA-15-3SC	68	54	62
15%Fe@ SBA-15-3SC-DPU	74	33	45

Figure 5.7 reminds the reaction pathways for the guaiacol hydrodeoxygenation leading to the formation of desired products (phenol, BTX, xylene) and by-products (water, CO, CH_4, CO_2). In our opinion, the representation of the products yields (mole of product/mole guaiacol injected) as a function of X_{HDO} is the best way to assess the catalyst, as presented in **Figure 5.8**. Indeed, a given catalyst can exhibit good selectivity to hydrocarbons aromatics (as benzene) as low guaiacol conversion or low X_{HDO} conversion. BTX can be formed in high yields by phenols conversion after the complete conversion of guaiacol therefore the formation of BTX as a function of guaiacol is not a good representation to assess the catalyst. It is of high importance to present the yields in products as a function of the X_{HDO}. For instance, a catalyst can exhibit an interesting product yield in BTX at low X_{HDO} but it may lead to a low selectivity in BTX at high HDO degrees due to the subsequent hydrogenation of aromatic rings or coke formation (Olcese *et al.*,[2] 2012). Therefore, such catalyst is not able to produce a high yield of target products.

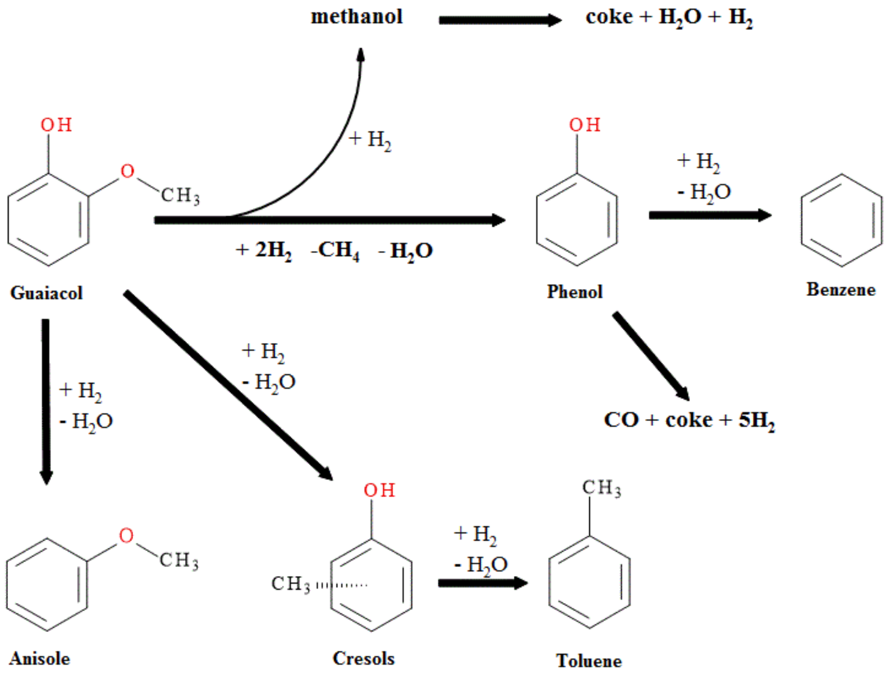

Figure 5.7 Guaiacol HDO reaction mechanisms, products and by-products.

Our materials show better performance with respect to phenol selectivity than conventional CoMo and NiMo catalysts where the main product at 60% guaiacol conversion is catechol (around 40%), and then promote hydrogenation reactions of the aromatic ring at higher HDO degree.[17] Moreover, as the interest of our study is to conserve the aromatic ring while breaking the C-O bond, comparing our catalysts to sulfided catalysts (MoS_2 and CoMoS) proved that they could be more attractive for aromatics production (phenol, cresol, BTX).[1,18] Furthermore, the pyrolysis gas presents a very low content in sulfides species therefore the sulfides catalysts are prone to deactivation without a costly addition of a sulfur additive source. For example, Fe-Cu catalyst showed better performance than CoMoS/γ-Al_2O_3 catalyst having an aromatics selectivity at 80% conversion of about 65% (25% phenol, 20% cresols, 15% catechol, 5% methyl-catechol, 2% benzene). Contrarily, CoMoS/ZrO_2 is more attractive than our catalysts, with an aromatics production of 78% (55% phenol, 20% benzene, 2% toluene) at 100% conversion of guaiacol.[1,18] Furthermore, our catalysts are more selective to phenol from noble metals Pt/MgO and Pt/γ-Al_2O_3 that showed a selectivity of 51% (at 70% conversion) and 26% (at 30% conversion) respectively.[19]

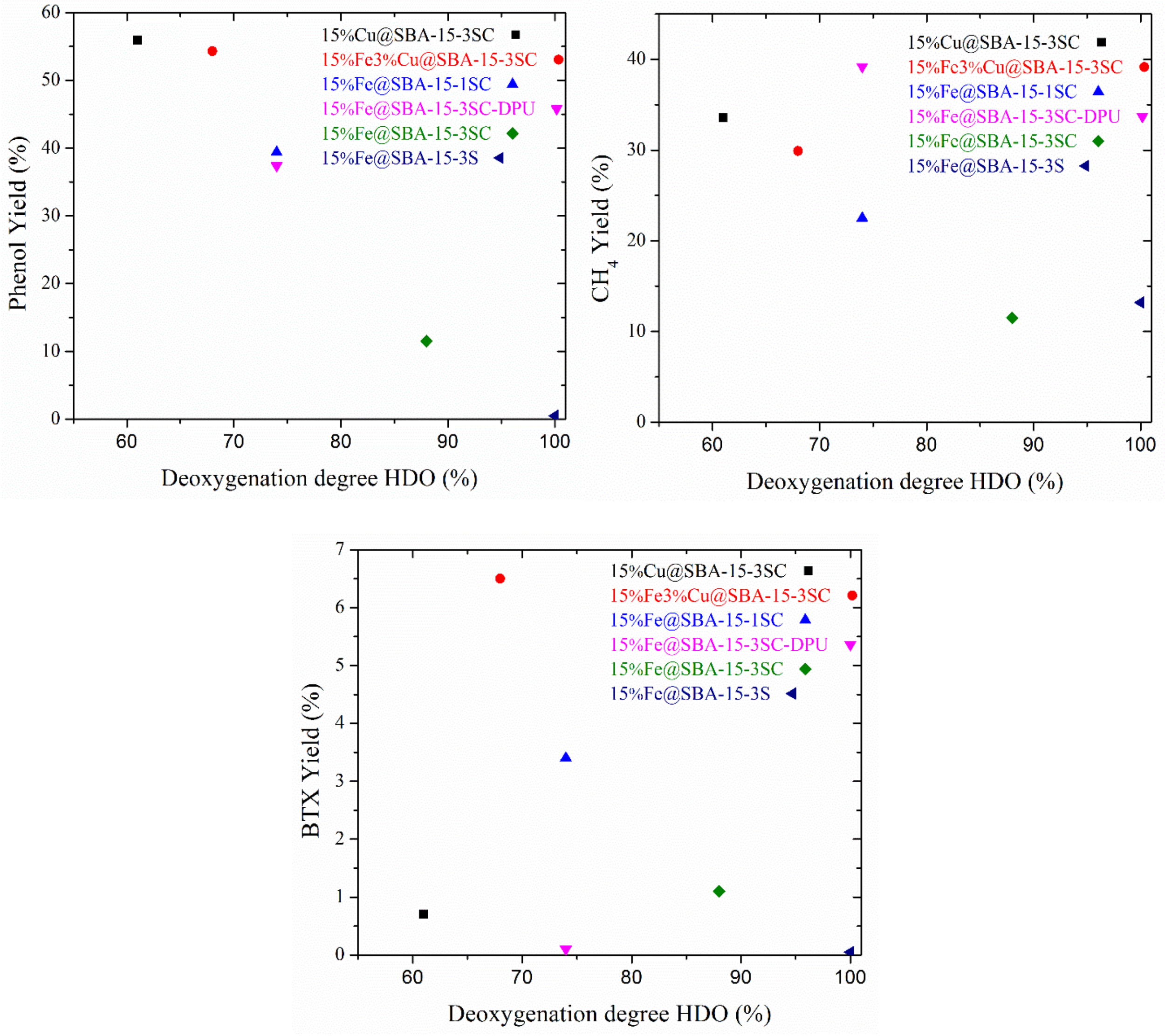

Figure 5.8 *Desired (phenol and BTX) and undesired (CH_4) products yield in function of the HDO deoxygenation degree (X_{HDO}) corresponding to different catalysts.*

Tyrone Ghampson *et al.*[20] studied guaiacol conversion over alumina and SBA-15-supported molybdenum nitrides catalysts and found that the main products are phenol and catechol. We calculated the HDO catalytic activity for their catalysts by multiplying the reaction rate ($mol.s^{-1}.g_{cat}^{-1}$) by the aromatics percentage yield (example for MoN/SBA-15-A: A_{HDO} = 6.4*10^{-6}*0.26 = 1.66 $\mu mol.s^{-1}.g_{cat}^{-1}$) and found that the bimetallic Fe-Cu catalyst is more attractive for aromatics production than those catalysts.[20] Using the same calculation method for the results obtained by Zhang *et al.*,[21] we evaluated the performance of our catalysts in comparison with Ni-Cu/ZrO_2-SiO_2 catalysts by mean of aromatics production (BTX, phenol, cresol, catechol) as showed in **Table 5.7**.

Table 5.7 *Performance of catalysts by mean of HDO catalytic activity (A_{HDO} $mol.s^{-1}.g_{cat}^{-1}$) comparing to literature.*

Catalyst	A_{HDO} (10^{-7} $mol.s^{-1}.g_{cat}^{-1}$)	**Reference**	**Conditions**
Ni5Cu/SZ-3	20.81	Zhang *et al.*[21]	T=340°C, P_{H2}=50 bar 2 hours reaction
Fe-Cu@SBA-15-3SC	20.53	This study	T=400°C, P_{H2}=1 bar 30 min reaction
Cu@SBA-15-3SC	20.11	This study	T=400°C, P_{H2}=1 bar 30 min reaction
MoN@SBA-15-A	16.64	Tyrone Ghampson *et al.*[20]	T=300°C, P_{H2}=50 bar 4 hours reaction
15%Fe@SBA-15- 1SC	15.58	This study	T=400°C, P_{H2}=1 bar 30 min reaction
15%Fe @SBA-15- 3SC-DPU	13.39	This study	T=400°C, P_{H2}=1 bar 30 min reaction
MoN@SBA-15-NH	11.44	Tyrone Ghampson *et al.*[20]	T=300°C, P_{H2}=50 bar 4 hours reaction
Ni5Cu/SZ-3	10.66	Zhang *et al.*[21]	T=300°C, P_{H2}=50 bar 2 hours reaction
CoMoN@Al_2O_3-A	5.40	Tyrone Ghampson *et al.*[20]	T=300°C, P_{H2}=50 bar 4 hours reaction
15%Fe@SBA-15- 3SC	4.86	This study	T=400°C, P_{H2}=1 bar 30 min reaction
Ni5Cu/SZ-3	3.83	Zhang *et al.*[21]	T=250°C, P_{H2}=50 bar 2 hours reaction
MoN@Al_2O_3-A	1.40	Tyrone Ghampson *et al.*[20]	T=300°C, P_{H2}=50 bar 4 hours reaction
CoMoN@SBA-15-A	0.60	Tyrone Ghampson *et al.*[20]	T=300°C, P_{H2}=50 bar 4 hours reaction
15%Fe@SBA-15-3S	0.00	This study	T=400°C, P_{H2}=1 bar 30 min reaction
Fe@SiO_2(10) with 1%Fe	0.00	This study	T=400°C, P_{H2}=1 bar 30 min reaction

5.4 X-ray and Mössbauer Measurements of Conventionally Synthetized Catalysts

It is of high importance to determine the speciation of catalytic iron sites before and after catalysis in order to interpret the catalytic performance of tested materials. Mossbauer and XRD analysis are well complementary for iron speciation analysis. They were conducted and discussed by Prof. B. Malaman at IJL. The scope of our synthesis of catalysts is to keep small nanoparticles of metallic iron as much as stable as possible and to reduce their oxidation (to promote their oxophilicity). Transmission electron microscopy (TEM) analysis are currently being performed in order to assess the size of metal nanoparticles, coke deposit and mapping of the composition by energy dispersive X-ray analysis (EDX).

Figure 5.9 shows X-ray measurements data collected at room temperature of catalysts before reduction using a X'PERT Pro PANalytical multipurpose diffractometer (MPD) over a 2θ range of 8 to 108°. Those data are acquired by exposing powder samples to Cu-K_α X-ray radiation, which has a characteristic wavelength (λ) of 1.5418 Å. X-ray radiations were generated from a Cu anode supplied with 40 kV and 40mA current.

Bimetallic Fe-Cu catalyst shows peaks corresponding to paratacamite ($Cu_2(OH)_3Cl$) and hematite (Fe_2O_3) species. The catalyst synthesized through the co-precipitation method with decomposition of urea (DPU) presents magnetite (Fe_3O_4 that can be expressed as $FeO.Fe_2O_3$); thus, as expected from its color, it contains Fe(II) species. The 15%Fe@SBA-15-1SC spectra shows two types of Fe_2O_3 species, the hematite and the maghemite. While for catalysts where silica support is washed for 3 days (15%Fe@SBA-15-3S and 15%Fe@SBA-15-3SC), only maghemite species were detected. This can indicate that the washing does not affect only the porosity, but also the types of the silanols on the silica surface and thus the interaction with iron during the impregnation.

The X-ray spectra of 15%Cu@SBA-15-3SC before reduction and after reduction at 500°C with catalysis are presented in **Figure 5.10**. Copper chloride (CuCl) and copper hydroxide chloride (CuOHCl) resulting from impregnation are reduced into metal Cu species as showed. **Figure 5.11** shows the X-ray spectra of catalysts after reduction (at 500°C) and catalysis (guaiacol + H_2 during 30min). Different peaks corresponding to metal Fe(0) species were detected in the X-ray spectra of all catalysts.

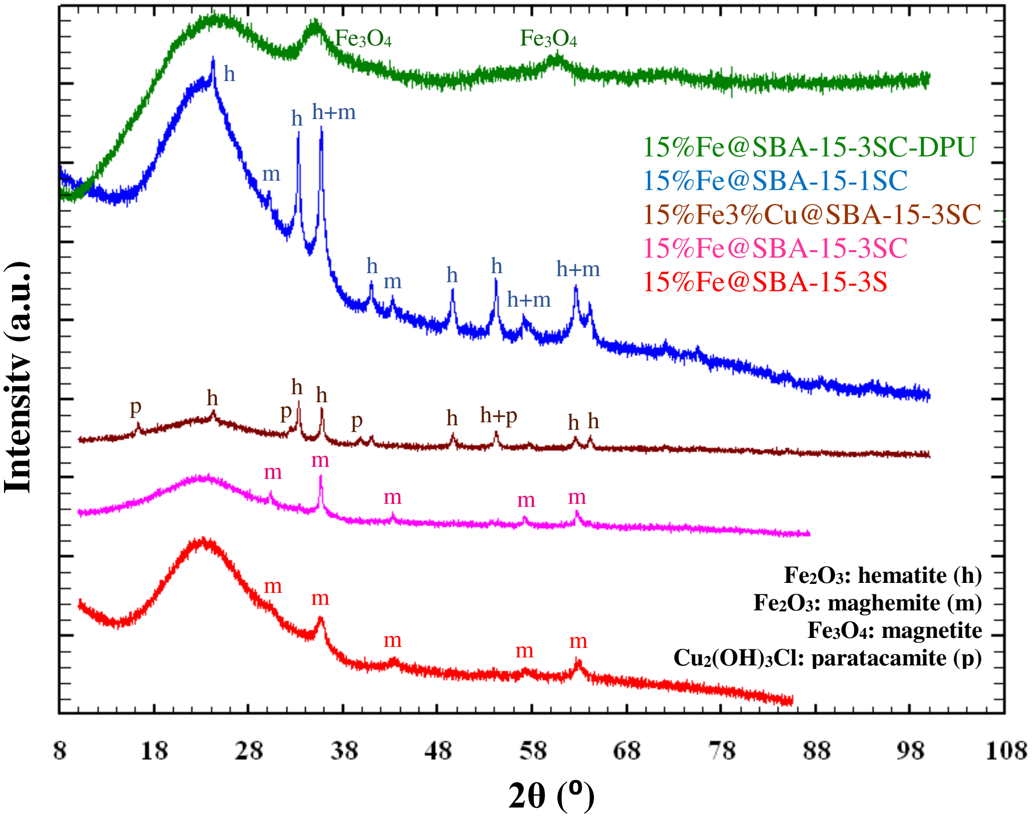

Figure 5.9 *XRD spectra of synthesized catalysts before reduction.*

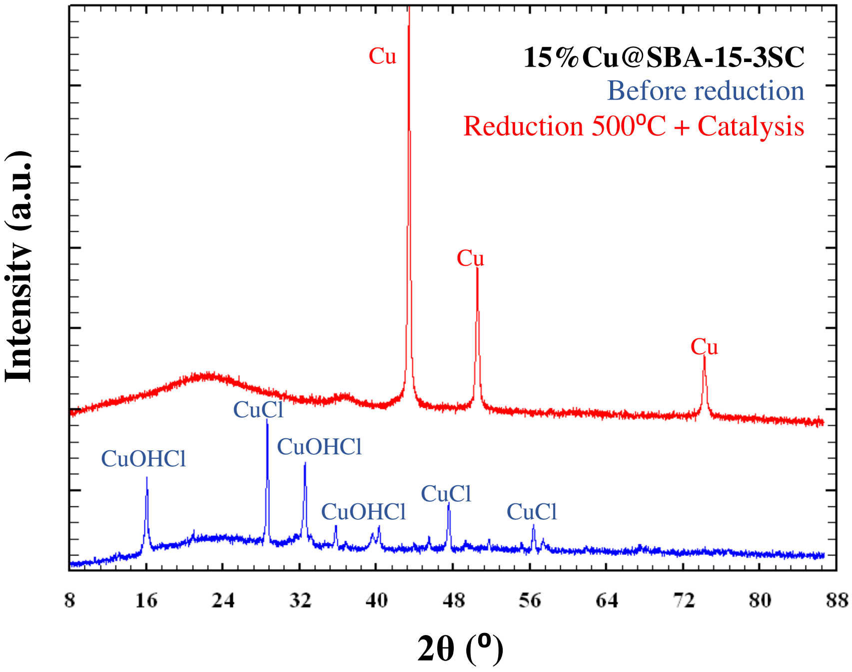

Figure 5.10 *XRD spectra of copper catalysts: (i) before reduction, and (ii) after reduction (at 500°C) and catalysis (guaiacol + H_2 during 30min).*

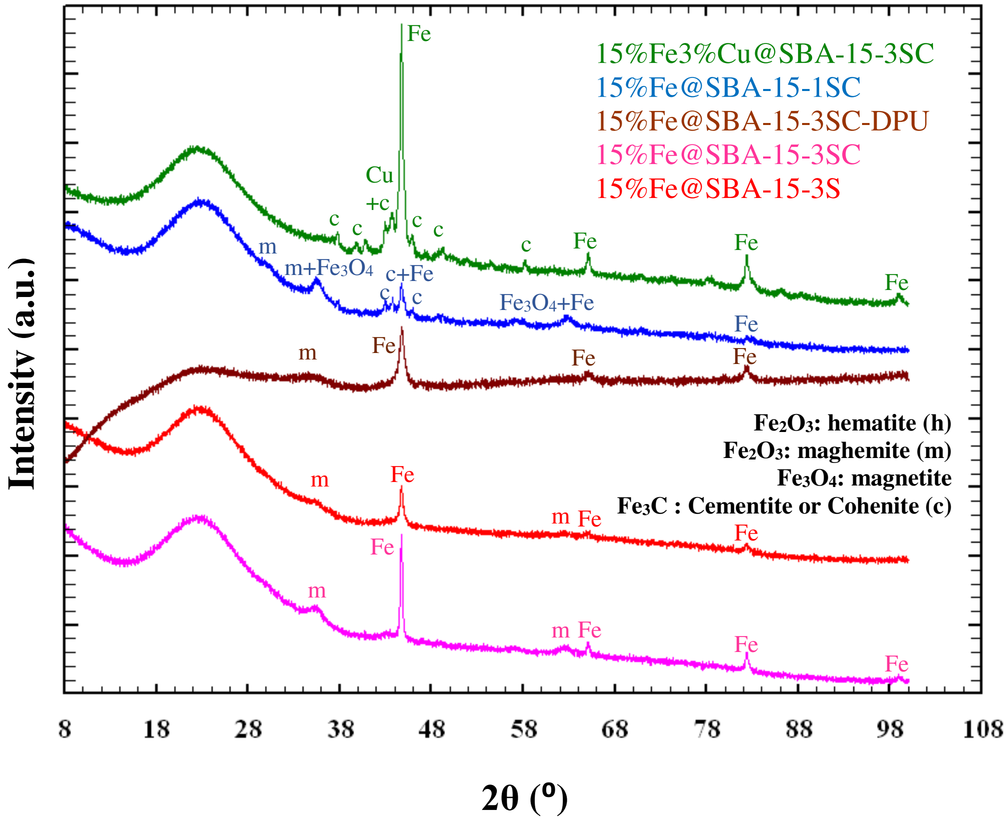

Figure 5.11 *XRD spectra of synthesized catalysts after reduction (at 500 °C) and catalysis (guaiacol +* H_2 *during 30min).*

All iron based catalysts are not reduced completely and show maghemite (Fe_2O_3) peaks with the reduced Fe(0) species. The 15%Fe@SBA-15-1SC catalyst presents additional iron carbide Fe_3C (cementite and cohenite) and magnetite (Fe_3O_4) species. While the bimetallic Fe-Cu catalyst presents peaks corresponding only to metal copper, metal iron, and iron carbide species.

Figure 5.12 shows the Mössbauer spectra of the 15%Fe@SBA-15-3SC catalyst before reduction, after reduction at 500°C, after reduction at 500°C with catalysis, and TPR at 800°C. ^{57}Fe Mössbauer measurements were performed, using a constant-acceleration spectrometer in standard transmission geometry with a ^{57}CoRh source at 300 K.[7] The corresponding Mössbauer spectrum for the reduced material at 500°C exhibits the characteristic sextuplet of α-Fe with a proportion area of 25%, a small percentage of Fe(II) species and a central doublet assigned to Fe(III) species.[22–25] Analysis after catalysis showed the same percentage of metal iron (25%), with no formation of iron carbides. X-ray results suggest that this central doublet of Fe(III) correspond to maghemite species, Mössbauer analysis at 15 K is currently performed in order to confirm that.

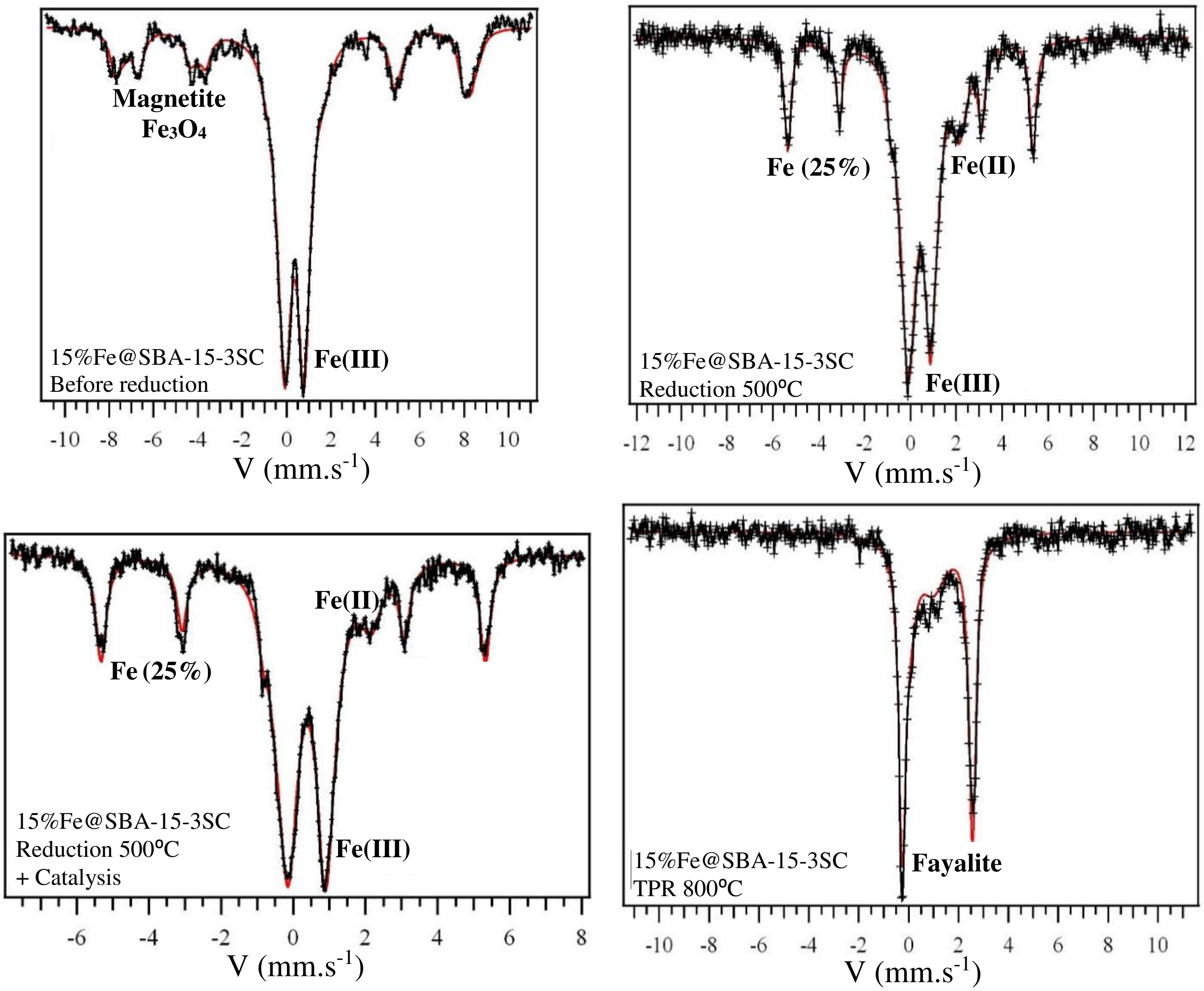

***Figure 5.12** Mössbauer spectra of 15%Fe@SBA-15-3SC catalyst: (i) before reduction, (ii) after reduction (at 500 °C), (iii) after reduction (at 500 °C) and catalysis (guaiacol + H_2 during 30 min), and (iv) after temperature programmed reduction (TPR at 800 °C).*

Furthermore, the Mössbauer spectrum corresponding to the catalyst after temperature programmed reduction (TPR) at 800°C can be fitted with the paramagnetic fayalite (Fe_2SiO_4) fitting model spectrum.[26,27] Those results are correlated with TPR results (**Figure 5.4**) where we observed that the hydrogen consumption reach a maximum at 500°C, then decreases as the temperature increase until 800°C where it increases again. This confirm that the formed Fe(0) species formed at 500°C and the remaining Fe(III) species continue their reduction into iron species that are chemically attached to the silica surface (Fe_2SiO_4).

Figure 5.13 shows the Mössbauer spectra of different catalysts after reduction at 500°C with catalysis. The 15%Fe@SBA-15-3SC-DPU presents a similar spectrum as the 15%Fe@SBA-15-3SC with the same percentage of Fe(0) species of 25%. This was expected as both catalysts are reduced under the same conditions. Thus, in order to interpret the effect of the synthesis by co-precipitation with decomposition of urea, catalysts should be reduced at lower temperature (400°C) then the percentage and size of iron nanoparticles should be compared.

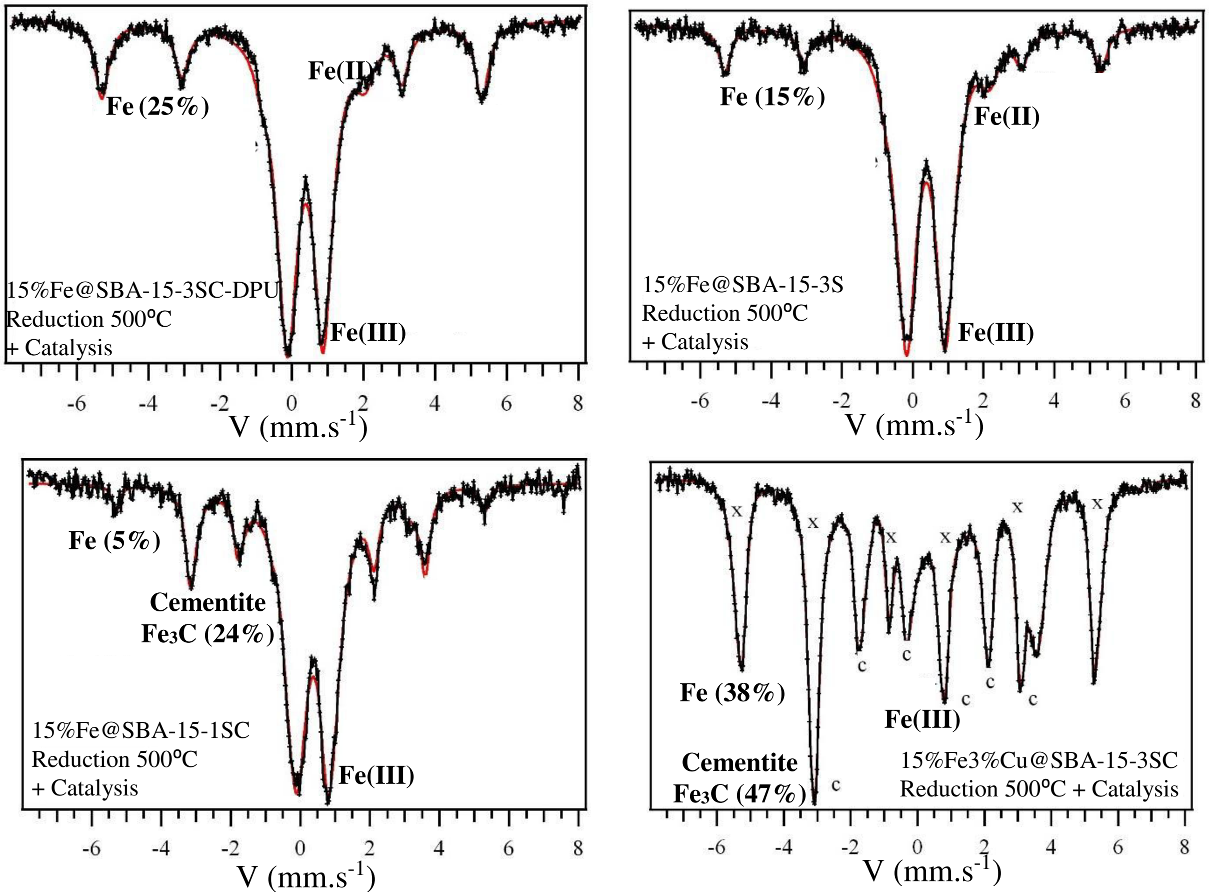

Figure 5.13 *Mössbauer spectra of catalysts after reduction (at 500 °C) and catalysis (guaiacol +* H_2 *during 30 min).*

The 15%Fe@SBA-15-1SC spectra shows in addition to the Fe(III) central doublet peak, 5% of Fe(0) species and 24% of Cementite Fe_3C species, as observed by XRD spectra. While the bimetallic Fe-Cu catalyst presented the highest percentage of Fe(0) of 38% with 47% of Cementite. Those two catalysts proved the better catalytic performance (conversion and aromatics selectivity) comparing to other catalysts. Meanwhile, Mössbauer measurements are performed for catalysts after reduction at 500°C with no catalysis in order to determine the total metal iron percentage before catalysis (before formation of iron carbides).

Interpreting catalysis, XRD, and Mössbauer measurements proved that the 15%Fe@SBA-15-3SC that showed lower catalytic performance than 15%Fe@SBA-15-1SC and Fe-Cu catalyst can be better from them for longer residence time as Fe(0) are more stable and no iron carbides where formed. However, those iron carbide species present in the 15%Fe@SBA-15-1SC and bimetallic catalysts can have a positive catalytic effect, and thus those catalysts can conserve their good performance for long residence time. Thus, to confirm those interpretations, new catalytic tests for longer residence time (4 hours) should be performed, and further temperature programmed oxidation (TPO) measures enable to determine the stability of catalysts with time.

5.5 Conclusions

HDO tests performed for the guaiacol conversion enlightened the effect of the silica support textural properties, the incorporation of a bi-metal, and the synthesis method on the catalytic performance of Fe@silica materials. Results confirmed that in SACs, iron atom are chemically attached to the silica support, which inhibit their reduction into catalytically active Fe(0) sites, and therefore unsatisfactory performance is obtained. Among catalysts synthetized by the impregnation method, Cu showed the highest selectivity to aromatics (80% with 71% conversion after 30 min), while bi-metallic 15%Fe-3%Cu showed a better conversion (87% after 30 min) and a good selectivity of 72%. However, XRD and Mössbauer spectra shows that iron carbides is formed after the catalysis residence period. Thus, the bimetallic Fe-Cu catalyst performance should be tested at longer catalysis time (up to hours) in order to interpret its stability over time. As deduced from previous studies, nickel-based catalyst have a high selectivity to benzene; Thus, a tri-metallic Fe-Ni-Cu catalyst can be optimal to obtain a good activity and benzene selectivity. The silanols density of the silica support should be low (around 2 OH/nm^2) as non-calcined materials (with 8 OH/nm^2) showed null aromatics selectivity. For instance, the catalyst with the silica support is washed for one day (15%Fe@SBA-15-1SC) showed better catalytic performance than that with the silica washed for three days (15%Fe@SBA-15-3SC). But, the most of Fe(0) sites of the former become iron carbides after 30 min reaction period, while the later conserved the same amount of Fe(0) before and after catalysis of 25%. The iron carbide sites can have a positive or a negative catalytic effect. Thus, catalytic tests for longer time should be performed in order to determine the catalyst having the optimal conversion, aromatics selectivity and stability. Finally, the co-precipitation by decomposition of urea method, that allow to obtain more easily reduced Fe(II) species, proved a good performance while conserving Fe(0) sites. Thus, further studies should be applied as the elaboration of Fe-Cu or Fe-Ni-Cu catalysts following this method, and modifying the reduction conditions (temperature) in order to reduce the size of metal nanoparticles and therefore increase the number of active sites.

References

(1) Bui, V. N.; Laurenti, D.; Delichère, P.; Geantet, C. Hydrodeoxygenation of Guaiacol. *Appl. Catal. B Environ.* **2011**, *101* (3–4), 246–255.

(2) Olcese, R. N.; Bettahar, M.; Petitjean, D.; Malaman, B.; Giovanella, F.; Dufour, A. Gas-Phase Hydrodeoxygenation of Guaiacol over Fe/SiO_2 Catalyst. *Appl. Catal. B Environ.* **2012**, *115–116*, 63.

(3) Robertson, S. Determination of Reducibility and Identification of Alloying in Copper-Nickel-on-Silica Catalysts by Temperature-Programmed Reduction. *J. Catal.* **1975**, *37* (3), 424–431.

(4) Van Der Grift, C. J. G.; Mulder, A.; Geus, J. W. Characterization of Silica-Supported Copper Catalysts by Means of Temperature-Programmed Reduction. *Appl. Catal.* **1990**, *60* (1), 181–192.

(5) Zhang, C.-H.; Wan, H.-J.; Yang, Y.; Xiang, H.-W.; Li, Y.-W. Study on the Iron-Silica Interaction of a Co-Precipitated Fe/SiO_2 Fischer-Tropsch Synthesis Catalyst. *Catal. Commun.* **2006**, *7* (9), 733–738.

(6) Bykova, M. V.; Ermakov, D. Yu.; Kaichev, V. V.; Bulavchenko, O. A.; Saraev, A. A.; Lebedev, M. Yu.; Yakovlev, V. A. Ni-Based Sol-Gel Catalysts as Promising Systems for Crude Bio-Oil Upgrading: Guaiacol Hydrodeoxygenation Study. *Appl. Catal. B Environ.* **2012**, *113–114*, 296–307.

(7) Gao, X.; Shen, J.; Hsia, Y.; Chen, Y. Reduction of Supported Iron Oxide Studied by Temperature-Programmed Reduction Combined with Mössbauer Spectroscopy and X-Ray Diffraction. *J Chem Soc Faraday Trans* **1993**, *89* (7), 1079–1084.

(8) Güvenatam, B.; Heeres, E. H. J.; Pidko, E. A.; Hensen, E. J. M. Decomposition of Lignin Model Compounds by Lewis Acid Catalysts in Water and Ethanol. *J. Mol. Catal. Chem.* **2015**, *410*, 89–99.

(9) Santiago, M. A. N.; Sánchez-Castillo, M. A.; Cortright, R. D.; Dumesic, J. A. Catalytic Reduction of Acetic Acid, Methyl Acetate, and Ethyl Acetate over Silica-Supported Copper. *J. Catal.* **2000**, *193* (1), 16–28.

(10) Sen, S.; Liu, D.; Palmore, G. T. R. Electrochemical Reduction of CO_2 at Copper Nanofoams. *ACS Catal.* **2014**, *4* (9), 3091–3095.

(11) Li, F.; Han, G.-F.; Noh, H.-J.; Kim, S.-J.; Lu, Y.; Jeong, H. Y.; Fu, Z.; Baek, J.-B. Boosting Oxygen Reduction Catalysis with Abundant Copper Single Atom Active Sites. *Energy Environ. Sci.* **2018**, *11* (8), 2263–2269.

(12) Badawi, M.; Paul, J.-F.; Cristol, S.; Payen, E. Guaiacol Derivatives and Inhibiting Species Adsorption over MoS_2 and CoMoS Catalysts under HDO Conditions: A DFT Study. *Catal. Commun.* **2011**, *12* (10), 901–905.

(13) Olcese, R.; Bettahar, M. M.; Malaman, B.; Ghanbaja, J.; Tibavizco, L.; Petitjean, D.; Dufour, A. Gas-Phase Hydrodeoxygenation of Guaiacol over Iron-Based Catalysts. Effect of Gases Composition, Iron Load and Supports (Silica and Activated Carbon). *Appl. Catal. B Environ.* **2013**, *129*, 528–538.

(14) Inui, T.; Kang, M. Reliable Procedure for the Synthesis of Ni-SAPO-34 as a Highly Selective Catalyst for Methanol to Ethylene Conversion. *Appl. Catal. Gen.* **1997**, *164* (1–2), 211–223.

(15) Newsome, D. S. The Water-Gas Shift Reaction. *Catal. Rev.* **1980**, *21* (2), 275–318.

(16) Berro, Y.; Gueddida, S.; Lebègue, S.; Pasc, A.; Canilho, N.; Kassir, M.; El Haj Hassan, F.; Badawi, M. Atomistic Description of Phenol, CO and H_2O Adsorption over Crystalline and Amorphous Silica Surfaces for Hydrodeoxygenation Applications. *Appl. Surf. Sci.* **2019**, *494*, 721–730.

(17) Laurent, E.; Delmon, B. Study of the Hydrodeoxygenation of Carbonyl, Carboxylic and Guaiacyl Groups over Sulfided CoMo/γ-Al_2O_3 and NiMo/γ-Al_2O_3 Catalyst. *Appl. Catal. Gen.* **1994**, *109* (1), 97.

(18) Bui, V. N.; Laurenti, D.; Afanasiev, P.; Geantet, C. Hydrodeoxygenation of Guaiacol with CoMo Catalysts. Part I: Promoting Effect of Cobalt on HDO Selectivity and Activity. *Appl. Catal. B Environ.* **2011**, *101* (3–4), 239–245.

(19) Nimmanwudipong, T.; Aydin, C.; Lu, J.; Runnebaum, R. C.; Brodwater, K. C.; Browning, N. D.; Block, D. E.; Gates, B. C. Selective Hydrodeoxygenation of Guaiacol Catalyzed by Platinum Supported on Magnesium Oxide. *Catal. Lett.* **2012**, *142* (10), 1190–1196.

(20) Tyrone Ghampson, I.; Sepúlveda, C.; Garcia, R.; García Fierro, J. L.; Escalona, N.; DeSisto, W. J. Comparison of Alumina- and SBA-15-Supported Molybdenum Nitride Catalysts for Hydrodeoxygenation of Guaiacol. *Appl. Catal. Gen.* **2012**, *435–436*, 51–60.

(21) Zhang, X.; Wang, T.; Ma, L.; Zhang, Q.; Yu, Y.; Liu, Q. Characterization and Catalytic Properties of Ni and NiCu Catalysts Supported on ZrO_2-SiO_2 for Guaiacol Hydrodeoxygenation. *Catal. Commun.* **2013**, *33*, 15–19.

(22) Suzdalev, I.; AFANAS'EV, A.; Plachinda, A.; Gol'Danskii, V.; Makarov, E. A Study of Spin-Lattice Relaxation on the Basis of the Hyperfine Structure of Fe^{3+} Mossbauer Spectra. *Sov. Phys. JETP* **1969**, *28* (5).

(23) Putzka, A. An Improved Method for Efficient Computation of Paramagnetic ^{57}Fe(III) Mossbauer Relaxation Spectra. *J. Phys. C Solid State Phys.* **1988**, *21* (19), 3517–3531.

(24) Sasaki, Y.; Hyakkai, M.; Kita, E.; Tasaki, A.; Tanimoto, H.; Iwamoto, Y. Magnetic Properties and Mössbauer Study of Fe Nanocrystals Prepared by the Gas-Deposition Method. *J. Appl. Phys.* **1997**, *81* (8), 4736–4738.

(25) Moura, F. C. C.; Araujo, M. H.; Costa, R. C. C.; Fabris, J. D.; Ardisson, J. D.; Macedo, W. A. A.; Lago, R. M. Efficient Use of Fe Metal as an Electron Transfer Agent in a Heterogeneous Fenton System Based on Fe^0/Fe_3O_4 Composites. *Chemosphere* **2005**, *60* (8), 1118–1123.

(26) Eibschütz, M.; Ganiel, U. Mössbauer Studies of Fe^{2+} in Paramagnetic Fayalite (Fe_2SiO_4). *Solid State Commun.* **1967**, *5* (4), 267–270.

(27) Becker, K. D.; Dreher, S.; Wißmann, S. A High-Temperature Mössbauer Study of Fayalite, Fe_2SiO_4: Cation Diffusion and Reactivity. *Berichte Bunsenges. Für Phys. Chem.* **1992**, *96* (11), 1778–1783.

Conclusions and Perspectives

Conclusions and Perspectives

This Ph.D. work has been made in the frame of several projects: the LUE Mirabelle+/Lign-In project that aims to valorize one of the largest sources of renewable energy, biomass, through the hydrodeoxygenation (HDO) of bio-oils derived from lignin pyrolysis (Université de Lorraine); and the PHC CEDRE (French Lebanon partnership) for Future Materials. The project gathers multidisciplinary researchers in a multi-scale approach: from molecular ab-initio modelling, to the synthesis of innovative catalysts, and the optimization of the HDO process. The HDO process consists of a gas phase catalytic reaction under hydrogen pressure in order to produce oxygen-free molecules. Favoring the direct deoxygenation (DDO) pathway over the hydrogenation (HYD) pathway reduce hydrogen consumption and promote non-oxygenated aromatics production.

This study treated this subject by a combined theoretical/experimental approach in order to develop new catalytic formulations to reduce H_2 consumption, conserve aromatic nuclei, and consequently obtain a better energy balance at lower cost (H_2 operational costs, storage and pressurization costs, etc.). For this purpose, we performed density functional theory (DFT) calculations in order to understand the interaction between oxygenated molecules (as well as inhibitors, water and CO) and the catalytic surface. Experimentally, we synthetized affordable materials by conventional and advanced methods, and tested them for guaiacol conversion under HDO conditions in order to compute their catalytic performance (activity and aromatics selectivity).

The adsorption of oxygenated molecules on the silica surface constitutes the first step of the reaction mechanism. However, the interaction of those molecules with the surface is dependent on the density, distribution and type of silanol groups that characterize each surface. Therefore, DFT calculations were done using the VASP code (taking into account vdW forces) to determine the adsorption energies of phenol (as a model molecule) following different interaction modes, and of inhibitor co-products (water and CO) on various amorphous and crystalline silica surfaces. Three modes of interaction of phenol with surfaces were explored: "perpendicular O-interaction", "flat π-interaction" and "flat O-interaction". Results show that on crystalline surfaces, the "flat π-interaction" mode dominates, which can favor the HYD rather than the DDO pathway. On amorphous surfaces, greater phenol adsorption energies were found following the "flat O-interaction" mode comparing to other modes. A specific interaction of phenol with SiO_2-3.3 and SiO_2-2 surfaces of 120 kJ/mol following this mode was found. It involves a C_{phenol}-$Si_{surface}$ bond leading to the deformation of the phenol molecule, which is promising for catalytic applications. The competitive effect of CO is negligible over all silica surfaces, making them more attractive than conventional sulphided catalysts according to this criterion. Water has a strong inhibitory effect over amorphous surfaces having a silanols density higher than 5 OH/nm^2. However, SiO_2-

3.3 and SiO_2-2 surfaces have very low water adsorption energies relative to phenol. Those results motivate the synthesis of amorphous silica with a density of silanols between 2 and 4 OH/nm^2 for better catalytic performance. As perspectives for theoretical work, molecular dynamics (MD) simulations should be performed in order to study the reaction kinetics and to determine the rate-limiting step, which allow proposing various mechanisms and determining the most possible one.

Mixed micelles, used as templates during the hydrothermal sol-gel synthesis of silica, were formed by non-ionic (pluronic P123) and metallic (cetyltrimethylammoniumtrichloromonobromoferrate, CTAF) surfactants. Micellar solutions with various CTAF/P123 molar ratio and concentrations were prepared and characterized in order to determine the structuring of those mixed micelles. Their critical micelle concentration (CMC) was determined using the surface tension method, while their size and zeta potential were determined using a zeta-sizer. Small angle neutron scattering (SANS) experiments on those micelles and others (mixed micelles CTAB/P123 and deuterated micelles CTAFd/P123) in H_2O, D_2O and H_2O/D_2O mixture allow determining their gyration diameters. We noticed that by adding CTAF, the micelles size decreases and their spherical shape is disturbed. Magnetic studies are performed on those micellar solutions in order to determine the percentage of high spin Fe(III) species and the interaction between them, which gives idea on the dispersion of CTAF in mixed micelles and enable to locate them. Meanwhile, SANS results are being fitted with micelles structural models using SasView in order to determine the shape depending on the CTAF/P123 ratio.

Single Atom Catalysts (SACs) were synthesized by the hydrothermal sol-gel process using mixed CTAF/P123 micelles as porogens. Four materials were prepared having a CTAF/P123 molar ratio of 1, 2, 5 and 10. The fine distribution of the iron atoms results from their distribution in the micellar structure of mixed micelles that serve as a matrix around which the silica framework polycondensation occurs. The CTAF/P123 ratio makes it possible to control the percentage of iron loading, as well the material structural properties. The absence of iron nanoparticles was confirmed by Squid magnetic measurements, nuclear magnetic resonance (NMR) measurements, per-distribution function (PDF) synchrotron measurements, and image mapping (TEM). DFT+U calculations confirm the state of oxidation of iron (III) and its state (high spin 5/2) appeared during magnetic measurements Squid. This strategy enable the preparation of SACs with improved efficiency compared to conventional catalysts due to the higher number of active sites.

Metallic (Fe and Cu) and bimetallic Fe-Cu catalysts were prepared by the simple impregnation of pre-synthesized mesoporous SBA-15-like materials in order to understand the effect of the silica support textural properties and copper incorporation on the catalyst performance. Other silica-supported iron catalysts were prepared through the co-precipitation method with decomposition of urea (DPU) through heating, which allow obtaining Fe(II) species.

Catalytic tests were performed for the HDO conversion of guaiacol (as a model molecule of bio-oils) to determine the performance of synthesized materials. An online mass spectrometer allow following qualitatively the evolution of the reaction in real time, and thus predict the catalyst deactivation period. For SACs materials, results show a difficulty in reducing Fe (III) atoms, which are strongly chemically attached to the silica surface, into active Fe(0) atoms. Thus, the catalytic performance of those materials were unsatisfactory with a null aromatics selectivity. Thus, synthetic modifications should be tried as using Fe(II) sulfate instead of $FeCl_3$ (as iron source to synthetize CTAF metallosurfactant) accompanied with replacing the calcination step by a pyrolysis in order to prevent iron oxidation, or to incorporate copper (through copper metallosurfactant) in order to facilitate the reduction of iron atoms.

The bimetallic Fe-Cu/SBA-15-3SC catalyst showed the best catalytic activity (7.39 $mmol.h^{-1}g_{cat}^{-1}$) comparing to other catalysts, with a conversion after 30 min of 87% and an aromatics selectivity of 72%. However, Cu catalyst showed the highest selectivity (80%) and aromatics carbon yield (68%) with a good conversion (70% after 30 min) and catalytic activity (7.24 $mmol.h^{-1}g_{cat}^{-1}$). The silica-supported catalysts having a silanol density of 8 OH/nm^2 showed no selectivity towards aromatics, as expected form DFT calculations. The effect of the silica pore size is important as Fe/SBA-15-3SC with small pores (porosity of 5 and 8 nm) is less active and selective than the Fe/SBA-15-1SC having a porosity of 8 nm, which can be caused by the obstruction of those pores by large molecules. The catalyst synthesized by co-precipitation with DPU proved a better performance than that synthesized by impregnation method, due to the formed Fe(II) that are reduced more easily. Our catalysts proved to be more active and selective than some conventional sulfide and nitride catalysts, and even some noble metals. As perspectives, bimetallic Fe-Cu catalysts must be synthesized through the co-precipitation method (with DPU), which facilitate more iron reduction, and enable reducing them at lower temperature thus creating smaller nanoparticles and a higher number of active sites. As our primary product is phenol and nickel proved in literature a selectivity to shift the reaction into benzene production, in our opinion the tri-metallic Fe-Cu-Ni catalyst (with small amount of Cu and Ni, 15%Fe3%Cu3%Ni) should be tested. Calculations and experimental tests will enable to compute the percentage load required for each metal and its effect on decreasing the C-O rupture energy, thus producing more benzene.

All our test were performed for a residence time of 30 min under one set of conditions and conversion were computed at the end of the reaction (30 min). Thus, future work should focus on determining the most efficient catalyst and testing its stability for longer times (8 h) and under various conditions (changing the temperature, the contact time, the H_2 partial pressure…), which permit to compute the conversion and selectivity with respect to those parameters. The HDO process should be coupled with the pyrolysis system for more realistic measures and gas feed.

Annexes

Annexes

Annex 1. Dispersion Forces (vdW) Contribution

Taking into account the vdW forces, the adsorption energy can be decomposed as the sum of the DFT and the dispersion energies. **Figure A1.1** shows the significant contribution of those forces on the adsorption energies, with an average on crystalline surfaces of 59, 52, 38, and 32 % for CO, phenol flat π-int, phenol perp O-int, and water respectively. The effect of the dispersion forces on the total adsorption energy and the promotion of the DDO or the Hyd route is further interpreted in **Figure A1.2**. As shown, the total adsorption energy is highly affected by the introduction of the dispersion forces due to their higher contribution on the π-int adsorption over all surfaces. For example, over the [101] β-cristobalite, the perp O-int adsorption mode energy was more important than the flat π-int adsorption energy but after taking into account the vdW forces, the flat π-int adsorption energy become slightly higher. This effect is mainly due to the small forces between the carbon atoms of the aromatic ring and the silica surface. In this context, under the reaction conditions we cannot state if the flat O-int adsorption mode found over the amorphous surfaces will promote the DDO or the Hyd route, because those interactions can be largely affected by the variation of the temperature and the restructuration of the surface.

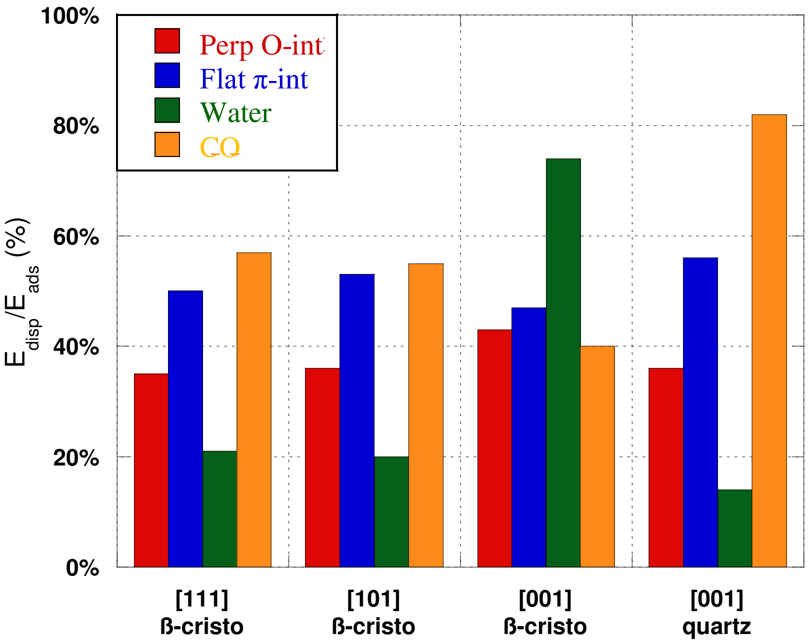

Figure A1.1 *Dispersion (vdW) forces contribution on the adsorption energies.*

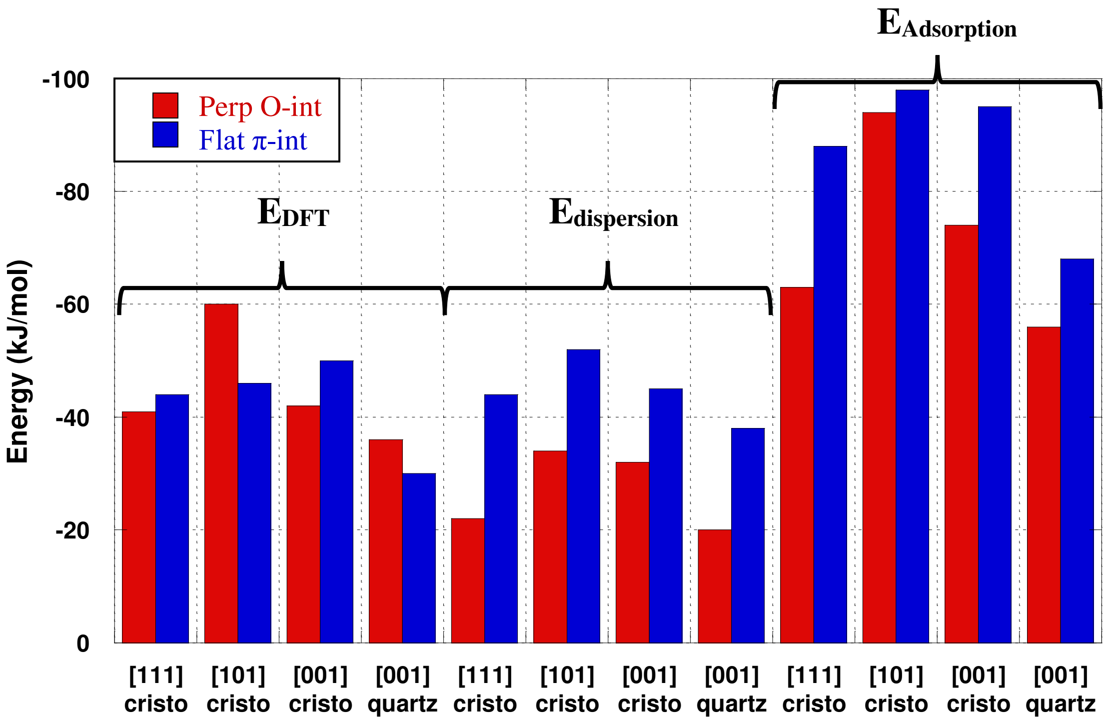

Figure A1.2 *Effect of introducing the dispersion forces on the promotion of phenol adsorption modes (perp O-int vs flat π-int).*

Annex 2. Structural Properties of Pristine SBA-15-like Material

The pristine material, synthesized in the absence of CTAF, have the structural properties of the SBA-15 silica. SAXS, BET-BJH and N_2 isotherms measurements of that material are presented in **Figure A2.1** showing ordered hexagonal mesoporous, of around 8 nm, giving rise to a pore volume of 0.984 $cm^3 \cdot g^{-1}$ and a surface area of 846 $m^2 \cdot g^{-1}$. A wall thickness of 2 nm is simply determined by the subtraction of the interlayer distance of 10nm (determined from XRD, $2\theta = 0.878^0$) from the pore diameter of 8nm (determined by the BET-BJH method).

The hexagonal structure is confirmed by the ratio of d_{hkl} of approximately $1:\sqrt{3}:2$ obtained at the three corresponding peaks using the following Bragg law:[1]

$$n\lambda = 2d_{hkl}sin\theta \qquad where\ n = 1\ and\ \lambda = 1.54\ nm$$

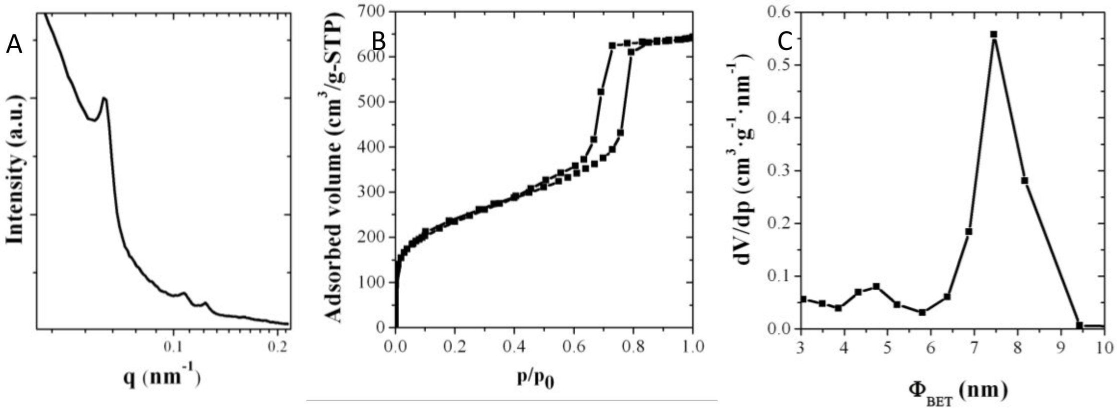

Figure A2.1 ***(A)*** *XRD pattern,* ***(B)*** *N_2 adsorption-desorption isotherms and* ***(C)*** *Pore size diameter distribution of pristine material synthesized in the absence of CTAF.*

Annex 3. Thermogravimetric Analysis (TGA)

In order to investigate the water and silanols densities, ThermoGravimetric Analysis (TGA) was performed using a Netzsch STA 449F1 thermobalance. Approximately 10 to 15 mg of each sample were heated up to 1073 K at a rate of 5 K·min^{-1} under air for the decomposition of organics.

The specific surface area data obtained from BET analysis coupled with the mass loss data obtained from TGA for $T_R < T < 476$ K, and $476 \text{ K} < T < 1073$ K are implemented in the following equations in order to determine the water, and silanols densities, respectively.[2,3]

$$H_2O\ (nm^{-2}) = \frac{2N_A \Delta m_{H_2O}}{m_{ini} M_{H_2O} S_{BET}} \qquad OH\ (nm^{-2}) = \frac{2N_A \Delta m_{OH}}{m_{ini} M_{H_2O} S_{BET}}$$

Where N_A is the Avogadro's number, Δm_{H_2O} and Δm_{OH} are the weight loss for water and silanols respectively, m_{ini} is the initial weight of the sample, M_{H_2O} is the molecular weight of water, and S_{BET} is the specific surface area.

Table A3.1 present the water and silanols mass loss, and the corresponding water and silanols densities for studied materials Fe@SiO_2(r). For all materials, the silanols density was higher than the density of a conventional SBA-15 silica (around 2.50 OH/nm^2); this may be due to the existence of iron particles that obstruct silica crosslinking during the polymerization of the framework. Comparing materials, as the CTAF surfactant content increases the density of silanols decreases, which may indicate the formation of Si-O-Fe bonds instead of Si-OH bonds.

***Table A3.1** Water and silanols mass loss, and their corresponding water and silanols densities of Fe@SiO$_2$(r) materials (r = 1, 2, 5, 10).*

	m_{total} (mg)	m_{H2O} (mg) (wt %)	$H_2O_{surface}$ density (OH/nm^2)	m_{OH} (mg) (wt %)	$OH_{surface}$ density (OH/nm^2)
Fe@SiO$_2$(1)	7.97	1.07 (13.43%)	12.31	0.84 (10.49%)	9.61
Fe@SiO$_2$(2)	9.37	0.87 (9.27%)	8.30	0.58 (6.20%)	5.53
Fe@SiO$_2$(5)	10.01	0.84 (8.33%)	5.84	0.55 (5.45%)	3.82
Fe@SiO$_2$(10)	10.72	0.91 (8.46%)	5.72	0.63 (5.90%)	3.96

Annex 4. Magnetic Measurements

4.1 Substraction of the Diamagnetic Signal

Figure A4.1 shows the temperature dependence of the magnetization of Fe@SiO$_2$(1) sample measured under an applied field of 1 kOe. It is well fitted by the sum of a constant with a Curie law as follow:

$$M(H,T) = a + \frac{CH}{T}$$

Where "a" is the contribution of diamagnetism or residual ferromagnetism, $\frac{CH}{T}$ is the paramagnetic susceptibility at low fields, and "C" is the Curie constant. From this value, the proportion "x" of high versus low spins can be calculated as follow:

$$C = x * C_{5/2} + (1 - x) * C_{1/2}$$

Where $C_{S = 1/2,\ 5/2}$ is the Curie constant per Fe weight calculated using the following equation and including the molecular weight "M":

$$C_{S= 1/2\,or\,5/2} = \frac{N_A}{M}\frac{4S(S+1)\mu_B^2}{3k_B}$$

The slope of the magnetization versus field measured at low field is indeed lower due to the diamagnetic linear contribution of P@SiO2(1) silica and sample holder. The difference between these quantities has then been used to perform the correction from diamagnetism; it is at most around 10% of the slope at low fields. The same procedure has been applied for all samples except the Fe@SiO2(5) for which the range 15-30 K have been considered for the fit.

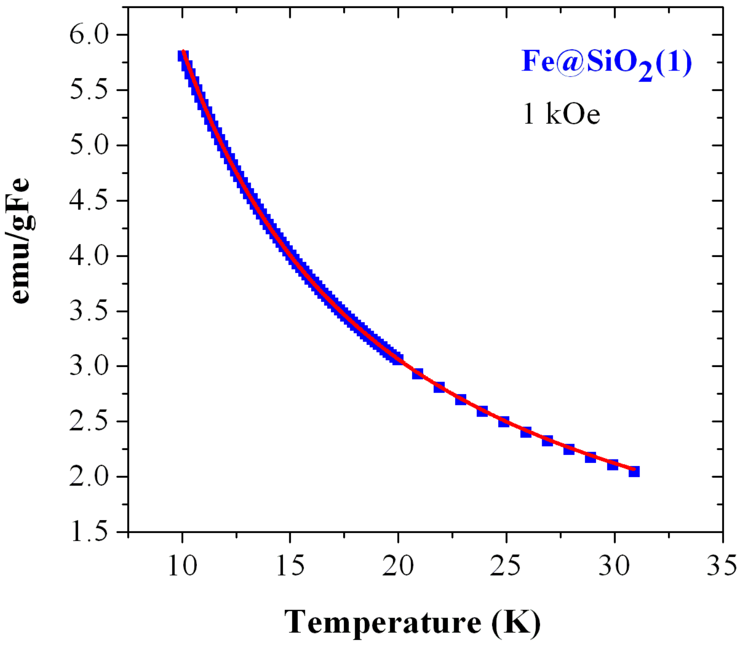

Figure A4.1 *Temperature dependence of magnetization of the Fe@SiO$_2$(1) sample measured under 1 kOe. The red line is a fit according to equation of M(H,T) in the range 10 K – 30 K.*

4.2 Low Temperature Spin Crossover

Figure A4.2 presents the temperature dependence of the magnetization of the Fe@SiO2(1) sample, it esxhibits a clear deviation from the Curie below 7 K. This deviation depends on the temperture history of the sample. It is then attributed to a high spin - low spin crossover. Such crossover has already been observed for the similar material previously studied.[4] A spin crossover is observed for the other samples below 10K, the deviation from the Curie law occurs below 15K for the Fe@SiO2(5).

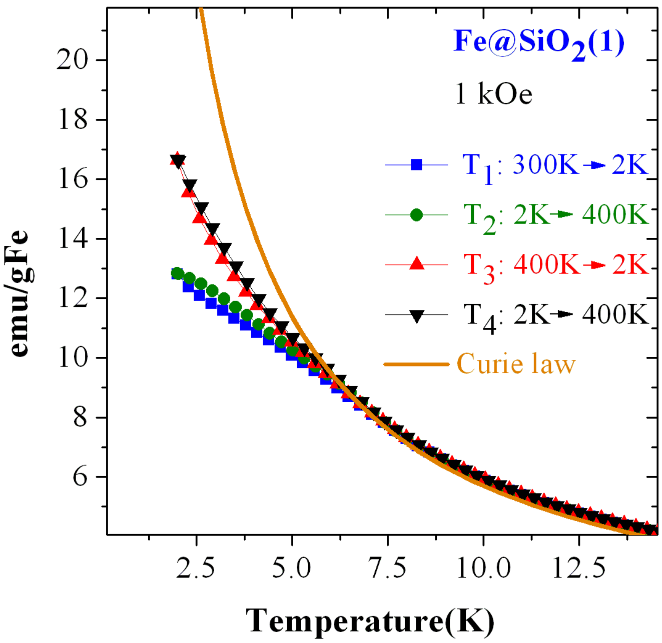

Figure A4.2 *Low temperature magnetization measured under 1 kOe magnetic field with a cooling/heating rate of ± 0.4 K·min*$^{-1}$.

References

(1) Bragg, W. H.; Bragg, W. L. The Reflection of X-Rays by Crystals. *Proc. R. Soc. Math. Phys. Eng. Sci.* **1913**, *88* (605), 428–438.

(2) Mueller, R.; Kammler, H. K.; Wegner, K.; Pratsinis, S. E. OH Surface Density of SiO_2 and TiO_2 by Thermogravimetric Analysis. *Langmuir* **2003**, *19* (1), 160–165.

(3) Peng, L.; Qisui, W.; Xi, L.; Chaocan, Z. Investigation of the States of Water and OH Groups on the Surface of Silica. *Colloids Surf. Physicochem. Eng. Asp.* **2009**, *334* (1–3), 112–115.

(4) Kim, S.; Bellouard, C.; Pasc, A.; Lamouroux, E.; Blin, J.-L.; Carteret, C.; Fort, Y.; Emo, M.; Durand, P.; Stébé, M.-J. Nanoparticle-Free Magnetic Mesoporous Silica with Magneto-Responsive Surfactants. *J. Mater. Chem. C* **2013**, *1* (42), 6930.